THERMAL PERFORMANCE OF FINGER-TYPE GAS-COOLED DIVERTORS

A Dissertation
Presented to
The Academic Faculty

By

Jordan D. Rader

In Partial Fulfillment
Of the Requirements for the Degree
Doctor of Philosophy in the
G. W. Woodruff School of Mechanical Engineering

Georgia Institute of Technology
August, 2013

THERMAL PERFORMANCE OF FINGER-TYPE GAS-COOLED DIVERTORS

Approved By:

Dr. Said I. Abdel-Khalik, Co-Advisor
School of Mechanical Engineering
Georgia Institute of Technology

Dr. Minami Yoda, Co-Advisor
School of Mechanical Engineering
Georgia Institute of Technology

Dr. S. Mostafa Ghiaasiaan
School of Mechanical Engineering
Georgia Institute of Technology

Dr. Michael Schatz
School of Physics
Georgia Institute of Technology

Dr. Thorsten Stoesser
School of Engineering
Cardiff University

Date Approved: June 21st, 2013

For Emily

ACKNOWLEDGEMENTS

First and foremost I would like to thank my advisors Drs. Said I. Abdel-Khalik and Minami Yoda. It has been a pleasure working with them on the divertor projects for the past several years. Their professionalism and respect was much appreciated. Thank you for forcing me to figure things out on my own while also providing useful feedback. I would like to thank the rest of my committee, Drs. Ghiaasiaan, Schatz, and Stoesser, for providing useful feedback and suggestions regarding the content of my thesis.

Dennis Sadowski provided a great deal of assistance when it came to operating the flow line and running the experiments. I thank him for all the time he put into getting the test sections designed and machined and leveraging his experience to this project.

To Brantley Mills, thanks for the many hours spent in the lab. Enough cannot be said about the benefits of his collaboration. I know I will be returning the favor soon.

To Lee Stokes and Andrew Polkinghorne, thanks for helping with the HEMJ experiments. Thanks go to Brandon Weathers for correspondence regarding his past work on the HEMJ. Thanks to the ARIES team for providing feedback at conferences and ARIES meetings. Thanks to the Department of Energy for funding this research. And thanks to the American Nuclear Society for providing opportunities for students to present research and receive feedback from the scientific community. Also, thanks to my friends and colleagues: Scott King, Necmettin Cevheri, Yaofa Li, Tongran Qin, Ben Chan, and Matt Golob.

I would also like to thank all of those that helped make my being at Georgia Tech for so long a memorable experience and for providing me an outlet for stress relief by participating in intramurals sports with me. This includes my wife, Emily, to whom I owe so much as well.

TABLE OF CONTENTS

LIST OF TABLES

LIST OF FIGURES

NOMENCLATURE

Variable or Abbreviation	Definition	Units (if applicable)
HEMJ	Helium-cooled multi-jet divertor	
HEMP	Helium-cooled modular divertor with integral pin array	
HCFP	Helium cooled flat plate divertor	
HEMS	Helium-cooled modular divertor with slot array	
MFE	Magnetic fusion energy	
EWT	Enhanced wall treatment	
SWF	Standard wall functions	
NEWF	Non-equilibrium wall functions	
SKE	Standard k-ε turbulence model	
RKE	Realizable k-ε turbulence model	
RNG	Renormalization Group k-ε turbulence model	
FEM	Finite-element method	
ITER	International thermonuclear experimental reactor	
LWR	Light water reactor	
BWR	Boiling water reactor	
PWR	Pressurized water reactor	
NIF	National Ignition Facility	
IEC	Inertial electrostatic confinement	

IFE	Inertial fusion energy	
CFC	Carbon fiber composite	
CFD	Computational fluid dynamics	
KIT	Karlsruher Institut für Technologie (Karlsruhe Institute of Technology)	
ppi	Pores per inch	
GPF	Gas-puffing facility	
EDM	Electro-discharge machining	
DNS	Direct numerical simulation	
RANS	Reynolds-average Navier-Stokes	
TC	Thermocouple	
BF	Bare forward	
BR	Bare reverse	
FF	Fins forward	
FR	Fins reverse	
HTC	Heat transfer coefficient	[W/m^2-K], [kW/m^2-K]
OD	Outer diameter	[m], [mm]
ID	Inner diameter	[m], [mm]
c_P	Constant pressure specific heat	[J/kg-K]
h	Heat transfer coefficient	[W/m^2-K], [kW/m^2-K]
Re	Reynolds number	[-]
Nu	Nusselt Number	[-]
Pr	Prandtl Number	[-]
$\dot{m}$	Mass flow rate	[kg/s], [g/s]

$\dot{V}$	Volumetric flow rate	[m^3/s]
T_{in}	Inlet temperature	[K], [℃]
T_{out}	Outlet temperature	[K], [℃]
p_{in}	Inlet Pressure	[Pa], [kPa], [psi]
p_{out}	Outlet Pressure	[Pa], [kPa], [psi]
p_{rot}	Rotameter Pressure	[Pa], [kPa], [psi]
Δp	Differential Pressure	[Pa], [kPa], [psi]
$\Delta p'$	Normalized pressure drop	[Pa], [kPa], [psi]
ρ_{cal}	Calibration density	[kg/m^3]
R	Specific gas constant	[J/kg-K]
ρ_{in}	Inlet density	[kg/m^3]
η	Fin efficiency	[-], [%]
ε_f	Fin effectiveness	[-]
$\tilde{\nu}$	Modified turbulent viscosity	[m^2/s]
k	Turbulence kinetic energy	[J/kg], [m^2/s^2]
ε	Turbulence dissipation rate	[m^2/s^3]
u_{avg}	Average velocity	[m/s]
ℓ	Turbulence length scale	[m]
I	Turbulence intensity	[-], [%]
V_j	Jet velocity	[m/s]
ω	Turbulence specific dissipation rate	[1/s]
K_L	Pressure Loss Coefficient	[-]
β	Pumping power fraction	[-], [%]

$\overline{T_s}$	Average heated surface temperature	[K], [℃]
q''	Heat flux	[W/m^2], [MW/m^2]
$\overline{T_c}$	Average cooled surface temperature	[K], [℃]

SUMMARY

For decades, the promise of electricity from fusion power has been elusive. Now with the construction of the International Thermonuclear Experimental Reactor (ITER) ongoing in France, the hope for the fulfillment of these promises is growing. However, even if the operation of ITER is wildly successful, further developments in heat removal and energy conversion technology will be required to operate such a device on a commercial scale. A significant factor in the balance of plant for a future magnetic fusion energy (MFE) reactor is the divertor. The divertor receives a large heat load from the fusion plasma as plasma impurities and fusion products are deposited on its surface. For an advanced MFE device, an average heat load of 10 MW/m^2 is expected at steady-state operating conditions.

Gas cooled (specifically helium-cooled) divertors have been considered for many years now. Gas cooling is one of the most effective ways to remove this heat on account of several benefits compared to other coolant types such as pressurized water, liquid metals, and molten salt: ability to operate at high temperature (>600 °C) necessary for refractory metals such as tungsten, operate at high pressure (10 MPa) resulting in more efficient pumping, low neutron interaction cross section, chemical inertness, compatibility with other reactor coolant systems such as the blanket and first wall, magnetic field indifference, lack of phase change (including concerns of critical heat flux), and the ability to operate directly in a Brayton cycle. Issues with helium cooling include: leaks, pumping power, manifolding, and tritium retention.

Several helium-cooled divertor designs have been proposed and/or studied including the T-Tube divertor, the helium-cooled flat plate (HCFP) divertor, the helium-cooled multi-jet (HEMJ) divertor, the helium-cooled modular divertor with integral fin

array (HEMP), and the helium-cooled modular divertor with slot array (HEMS). Each of these concepts requires a different number of modules to cover the expected ~100 m^2 size of the divertor. The HEMJ, HEMP, and HEMS, referred to as 'finger-type' divertors, are all of similar size (plasma-facing tungsten tile ~2-3 cm^2) and thus require on the order of 10^{5-6} modules. The HCFP is of the larger 'plate-type' variety (~1 m^2) and only on the order of 10^{2-3} modules would be required. The T-Tube is of an intermediate size (~12 cm^2) and thus would require an intermediate number of modules (10^{4-5}). All of these designs (and many other not mentioned) rely on some form of heat transfer enhancement via impinging jets or cooling fins to help improve the heat removal capability of the divertor. Other designs have been investigated that use other heat transfer enhancement mechanisms such as porous media. For all of these designs very large heat transfer coefficients on the order of 50-60 kW/(m^2-K) have been predicted.

As the conditions of a fusion reactor and associated helium flow conditions (600 ºC and 10 MPa) are difficult to achieve safely in a controlled laboratory environment, the study of these divertors often relies on computer simulations and dynamically similar experimental modeling. Studies performed at Georgia Tech in the last several years on the HEMJ, T-Tube, and HCFP have used a combination of these techniques. This thesis takes these developed techniques and applies them to a divertor test section that closely resembles the HEMP design. Also, a further study has been performed on the optimization of the fin array of the HEMP-like module as well as another study of the HEMJ. These studies were motivated by the results of a study of the HEMP that showed that the use of previous techniques involving the assumption of dynamic similarity between the experimental test sections and the prototypical divertor were flawed because the difference in conduction, versus convection, heat transfer was not considered. This thesis proposes a correction for this effect and makes performance predictions for the HEMJ and HEMP-like divertors at prototypical conditions.

CHAPTER 1: INTRODUCTION

It's important to understand the history of nuclear science and how it relates to the present thesis. Therefore, first a background of nuclear energy research will be provided followed by an introduction to nuclear fusion technology and concluded with an introduction to the purpose and state of the art of gas-cooled divertor design.

1.1. Background

For decades now, man has harnessed the power of the atom via the process of nuclear fission for the production of electricity. The nuclear fission reaction that takes place in the core of a power reactor involves the splitting of "large," fissile atoms of Uranium or Plutonium by neutrons thus producing two "daughter" nuclei and several neutrons. The extra neutrons from the reaction go on to produce further fissions and thus a chain reaction. Typically, about 200 MeV of energy is released per fission event. An example of one possible fission of the isotope ^{235}U is given:

$$ {}^{1}_{0}\mathrm{n} + {}^{235}_{92}\mathrm{U} \rightarrow {}^{135}_{53}\mathrm{I} + {}^{98}_{39}\mathrm{Y} + 3{}^{1}_{0}n + Q \quad (1) $$

The reaction energy, *Q*, is split amongst the daughter nuclei, the fission neutrons, neutrinos, and gamma rays. Typically, about 95% of the fission energy is captured when the kinetic energy of the daughter nuclei is dissipated in the structure of the fuel material resulting in heat generation which is used in an energy conversion system to create electricity. The most common type of nuclear fission reactor is the light-water reactor or LWR which uses the boiling of water at high pressure to create steam which drives a turbine connected to a generator to produce electricity. Reactors of this variety have been operating since the 1950s. Concurrent with the development of nuclear fission,

scientists developed theories regarding the combining of nuclei or nuclear fusion to release energy. As shown in Figure 1, both combining light atoms and splitting heavy atoms results in a net release of energy.

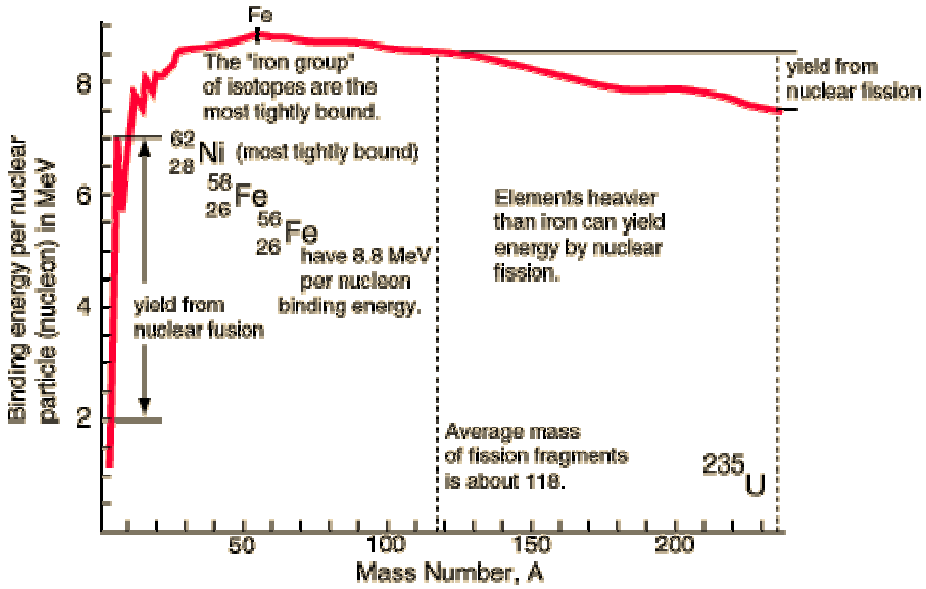

Figure 1. Binding energy per nucleon for known elements. [1]

Fusion is the process which takes place in the Sun and creating the environment for and controlling the nuclear fusion reaction has proved to be much more difficult than fission. While the general concepts and strategies for achieving nuclear fusion have been around since the 1950s, the successful demonstration of electricity production from heat generated by nuclear fusion has yet to take place. Decades of research in material science, plasma physics, magnetics, heat transfer, and superconductivity among other subjects was required. To create the conditions necessary for fusion to take place, hydrogen atoms must be stripped of their electrons and heated to several million degrees Celsius so that they have the kinetic energy sufficient to fuse. When atoms and electrons are heated to this temperature, a fourth state of matter, plasma, is created. Several methods for creating and confining a fusion plasma have been conceived.

1.2. Nuclear Fusion Concepts

Of particular interest for this dissertation is the concept of magnetic confinement fusion energy or MFE. The plasma is confined by strong magnetic fields created by superconducting current loops surrounding the plasma chamber. The magnetic fields are constructed such that the plasma is circulated in a torus. The fusion reaction itself creates heat and if a sufficient reaction rate can be achieved such that the heat from the reactions creates a self-sustaining state, the fusion reactor is said to have ignited.

Another type of controlled fusion is inertial fusion energy (IFE). These reactors use lasers or ion beams to compress and heat a small quantity of fusion fuel to the conditions necessary for fusion. Presently, the time required to charge the power systems for the lasers necessitate that this type of reactor can operate only one “shot” at a time. The National Ignition Facility (NIF) and other groups are currently trying to solve problems associated with IFE including how to operate such a machine at a repetition rate suitable for commercialization.

Inertial electrostatic confinement (IEC) fusion is yet another method developed to create a fusion environment. IEC uses electric fields created by concentric spheres to accelerate the fusion fuel towards the center of the inner sphere where they can be combined at fusion conditions. IEC reactors have proven to be a viable source of neutrons but harnessing the power from such a device large enough to create electricity has not been pursued on account of several limitations of this type of confinement as detailed in other references.

The fusion reaction that takes place inside stars like our Sun is different than that proposed by to be used in reactors on Earth. Simply, the scale required to confine atoms into a plasma is not achievable on Earth. The core of the Sun actually has a relatively

low power generation rate; however, the large scale of the Sun (333,000 Earth masses) allows for such a significant power output (3.85×10^{26} W). Also, the fusion reaction that takes place in the Sun occurs in several intermediate stages and may not be practical for a terrestrial device.

1.3. Nuclear Fusion Technology

As outlined, harnessing the power of fusion energy for electricity in a commercial scale facility has for many decades now been unattainable on account of many technical challenges both foreseen and unexpected. However, with construction underway of the International Thermonuclear Experimental Reactor (ITER) facility near Cadarache, France, the promise of fusion energy is renewed and its fulfillment impending. ITER is a tokamak design and a cutaway view of the reactor is shown in Figure 2.

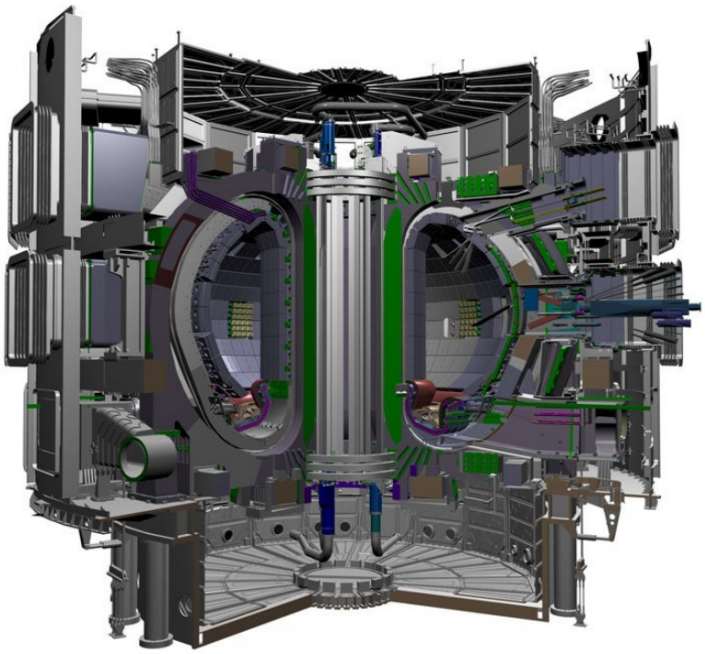

Figure 2. Cutaway view of ITER tokamak design. [2]

The tokamak was invented by Russian scientists in the 1950s. Modification made to the design of the magnetic fields confining the plasma in a torus make the tokamak unique. Toroidal MFE devices require a means to keep ion confinement times large enough to achieve controlled fusion. Like another toroidal MFE device, the stellarator, the tokamak uses current coils to create a toroidal magnetic field that causes ions to travel around the inside of the torus. Ions drift away from the center of the torus as a result of a non-uniform toroidal field. A poloidal field (orthogonal to the toroidal direction) is required to correct this drift. The stellarator addresses this problem by using external current coils or by changing the shape of the toroidal field coils to create non-uniformities that correct for the ion drift. A tokamak uses external coils to induce a current inside the plasma that then creates a poloidal field.

An important heat removal component in the tokamak device is the divertor. Shown in Figure 3, the divertor is located at the bottom of the torus and is the target of helium ash and other impurities rejected from the fusion plasma.

Figure 3. Cutaway view of the ITER divertor system. [2]

The helium comes from the Deuterium-Tritium (D-T) fusion reaction:

$$ {}_{1}^{2}\mathrm{H} + {}_{1}^{3}\mathrm{H} \rightarrow {}_{2}^{4}\mathrm{He} + {}_{0}^{1}\mathrm{n} + 17.6\ \mathrm{MeV} \tag{2} $$

There are many fusion reactions and the D-T reaction was chosen for initial fusion reactors for several reasons. Primarily, this reaction has a “low” reaction threshold energy. Deuterium is radioactively stable and present naturally on Earth accounting for approximately 0.0156 atom percent of all hydrogen. The reaction also produces a neutron that can be captured by lithium (another abundant element) placed in the “blanket” of the reactor to create more tritium as well as energy that can be used for electricity production:

$$ {}^{1}_{0}\mathrm{n} + {}^{6}_{3}\mathrm{Li} \rightarrow {}^{4}_{2}\mathrm{He} + {}^{3}_{1}\mathrm{H} + 4.8\ \mathrm{MeV} \tag{3} $$

$$ {}^{1}_{0}\mathrm{n} + {}^{7}_{3}\mathrm{Li} + 2.466\ \mathrm{MeV} \rightarrow {}^{4}_{2}\mathrm{He} + {}^{3}_{1}\mathrm{H} + {}^{1}_{0}\mathrm{n} \tag{4} $$

Capturing the kinetic energy of the neutron allows for the direct conversion of fusion energy for use in a power system. Other neutron-less fusion reactions would require a different method to remove useful heat from the plasma.

The two isotopes of lithium both can produce tritium by capturing a neutron; however, the reaction with lithium-7 requires the neutron to have sufficient kinetic energy. A neutron leaving a D-T fusion plasma has 14.1 MeV of energy so some reactions with lithium-7 are possible until the neutron slows down to energies below 2.466 MeV. As the neutron has no net charge, it travels isotropically and independent of the magnetic fields of the reactor. Blankets and neutron shielding thus need to be placed around the entire reactor as the neutron will activate structural materials and damage the superconducting magnets.

Though ITER will be an advanced device, far more capable than previous MFE devices, it is a necessary first step towards an even more advanced device capable of producing a significant amount of electricity for general consumption. As a significant fraction (~15%) of the fusion power will be incident on the divertor plates, efficient

operation of the divertor cooling system will result in significant benefits to the overall balance of plant [3]. Advanced devices, like those developed through the ARIES project, will require more sophisticated heat removal systems than will be used in ITER to achieve efficient plant operation. As such, the research and development of advanced heat removal systems is an important aspect of any future MFE device.

Each particle and its kinetic energy are deposited in the plasma-facing plate of the divertor resulting in expected peak temperatures near 3000°C and an average incident heat flux on the order of 10 MW/m^2 over the entire 100 m^2 of the divertor surface. Advanced heat removal techniques are required to adequately perform this critical task while remaining under material temperature and thermal stress limitations.

The leading divertor designs for the ARIES project focus on high temperature, gas-cooled, modular components. Namely, divertors constructed of tungsten and tungsten alloys (for their high melting and operating temperatures, and relatively high thermal conductivity) and cooled with gaseous helium (for its chemical inertness, resistance to neutron activation, compatibility with other reactor coolant systems, relatively high thermal conductivity, and high operating temperature capability) are considered the most viable options for an advanced MFE design. Often, heat transfer enhancement techniques are proposed such as cooling fins, impinging jets, or other means of increasing the cooled surface area of the divertor or the coolant velocity near the cooled surface.

Other divertor designs have been proposed using a variety of coolants including pressurized water, liquid metal, and molten salt. Other materials for the plasma facing component of the divertor such as carbon fiber composites (CFC) and beryllium have been proposed. For a post-ITER divertor with high heat loads, particle fluxes, and temperatures, a robust design is required that will be able to survive such an extreme environment. Light elements pulled off the plasma-facing side of the divertor will be

pulled into the plasma and ionized. This causes radiation losses in the plasma and can cause instabilities, disruptions, or loss of plasma confinement. Light elements radiate and self-sputter less than heavy elements so this may be an advantage over tungsten. However, the high melting points associated with tungsten and tungsten alloys cannot be overlooked.

Use of pressurized water as a coolant presents several problems including neutron activation, tritium retention, critical heat flux induced departure of nucleate boiling in the case of disruptions or loss of flow transients, and incompatibility with other proposed cooling systems for blankets and the first wall. Molten salts and liquid metals also suffer from wall detachment and boiling issues when subjected to high heat loads or loss of flow transients. Liquid metals also must overcome significant pressure loss associated with strong magnetic fields. Single phase coolants like gases avoid some of these issues.

The topic of this dissertation is the investigation of several finger-type He-cooled divertor designs. The first design was tested using experiments performed at conditions dynamically similar to those of the proposed design on test sections constructed of brass, cooled with air, and heated by an oxy-acetylene torch. These experiments were performed over a wide range of non-dimensional flow rates or Reynolds number *Re* resulting in the calculation of both non-dimensional heat transfer coefficients (HTC) or Nusselt numbers *Nu* and non-dimensional pressure loss coefficients K_L. By using air as coolant and constructing test sections out of brass, a large number of small scale experiments can be performed at relatively low temperatures. Heating the test sections with a torch provides a heat flux higher than had previously been tested using similar dynamically similar methods with electric heaters.

Data from these experiments are then compared to simulations using a commercial computational fluid dynamics (CFD) package. Verifying the numerical

models against the experiments provides a means for easily testing small modifications to the divertor design and testing operating conditions outside those easily reproduced in the laboratory. Following the verification of the model, the dynamic similarity of the experiments is explored and used to extrapolate the *Re*, K_L, and *Nu* relationships of the experiments to prototypical conditions for a divertor constructed of tungsten and tungsten alloys and cooled with high temperature and pressure helium. These results indicate that combining impinging jets with cooling fins may improve divertor performance, i.e. enhance heat transfer without significantly increasing the pressure drop. However, as the tested fin arrangement was not optimized for combining these two effects, there is still room for improving this design.

Following the recommendations of the experimental study and numerical validation, the fin arrangement of the experimentally tested design is optimized using the validated computer model of the divertor design. Beyond finding a more optimum fin arrangement than that experimentally tested, these studies serve to provide assurance to reactor designers by showing that the performance of the divertor is not significantly impacted by minor changes or inconsistencies in the fin geometry.

A second divertor design that relies primarily on impinging jets for heat transfer enhancement was also studied using experiments performed at conditions dynamically similar to those of the proposed design on tests section constructed of brass or steel and heated by an oxy-acetylene torch using methods similar to the first study. The results of these experiments were also translated to prototypical conditions for a divertor constructed of tungsten and tungsten alloys and cooled with high temperature and pressure helium. The results of these studies indicate a path forward for finger-type gas-cooled divertor research using dynamically similar experiments.

As both the potential and challenge for electricity producing fusion energy devices is great, it is imperative that thorough research and development be conducted

such that the path forward is well-defined and as many solutions as possible have been evaluated. It is for this purpose that several divertor designs have been chosen for this particular investigation. The synergistic effects of combining heat transfer enhancement mechanisms to achieve such extreme heat removal capabilities as required by a MFE divertor are not fully understood and require examination of a large number of divertor designs. Designs must be guided by fundamental heat transfer concepts and combined efficiently with the concerns of manufacturing, materials science, and economics.

The remainder of this thesis is organized as follows: Chapter 2 includes a literature review of previous work on gas-cooled divertors. The experimental apparatus and procedures used in this investigation are described in Chapter 3. Chapter 4 presents two-dimensional numerical simulations performed on one of the experimentally studied divertor test sections as well as the calculation of parametric performance curves for that design. Chapter 5 includes three-dimensional simulations performed on a divertor test section that incorporates cooling fins. An optimization of the fin array to combine the heat transfer enhancement of an impinging jet with a fin array follows. Conclusions and recommendations derived from this investigation are presented in Chapter 6. A series of Appendices that follow the main thesis body include tables of the experimental data, the experimental uncertainty calculation methodology, experimental equipment calibrations, and material properties assumptions. Appendix F includes refereed journal publications resulting from this work.

CHAPTER 2: LITERATURE REVIEW

Gas-cooled divertor technology has been developing for many years. Significant lead time is required to ensure that all design criteria for an advanced MFE facility are met. This is especially true as the requirements placed on the divertor continue to evolve, often placing further restrictions on acceptable operating parameters. As is the case, more advanced designs require more sophisticated analysis starting from an analytical model and continuing through initial experimental and numerical analysis before a prototype design can be tested. The designs presented herein represent only a few select designs that have proceeded at least into initial experimental and numerical development.

Several of the following designs are considered “finger type” as they are composed of a large number (~10^6) of small modules (~1 cm^2) bundled together and oriented facing the plasma. Finger-type designs have shown the potential to satisfy most design criteria (≥10 MW/m^2 incident heat flux while remaining under temperature and thermal stress limitations), at least after initial investigations. As required of the divertor, large average heat transfer coefficients (HTCs) (>30 kW/m^2-K) are predicted for these designs. Each of the finger-type designs presented uses either an impinging jet or array of jets and/or cooling fins to enhance heat transfer at the cooled surface of the divertor.

Alternatively to the small, finger-type designs, larger “plate-type” designs have also been proposed that require only a few thousand or even several hundred modules to cover the plasma facing surface of the divertor. Often, the relative simplicity and large size of these designs comes at the expense of lower maximum allowable heat flux. Heat transfer enhancement mechanisms that scale to the larger sizes are thus an important

part of improving the designs of plate-type divertors. Also, design optimization using computer simulations can lead to improved performance.

A review of heat transfer enhancement theory and its relation to divertor designs follows as well. Both analytical and numerical models are used to predict the performance of divertors. Often, computer simulations are used to aid in the engineering of these components as computer models validated against experiments provide an efficient path to vary design parameters in order to reach a more optimum design. Also, computer models give insight into the inner workings of a component and allow researchers to see performance parameters (e.g. temperature, pressure, velocity, stress, strain, etc.) that may not be easily measured (if at all) in an experiment.

2.1. Impinging Jets

Jet impingement is used in many industrial applications to enhance the heat transfer effectiveness of a particular system. Of particular interest for this thesis is round gas jet impingement, either from a lone, single jet or from an array of jets. Jets increase the per unit mass heat transfer performance of a system by increasing near-wall velocity and turbulence induced mixing when compared to a system with the same mass flow rate and flow parallel to the impingement surface. The increase in velocity and turbulence-induced mixing results in higher heat transfer rates as the near-wall temperature of the impinging fluid is lower on average. This increase in heat transfer performance typically comes at the cost of increased pressure drop.

As described by Incropera and Dewitt [4] and Lee and Vafai [5] jet heat and mass transfer should be analyzed by dividing the jet into four regions: the potential core, the free jet, the stagnation zone or impingement region, and the wall jet or radial flow region. A depiction of these regions is given in Figure 4. As gas exits the nozzle with a uniform velocity profile, the cross-sectional area of the jet exhibiting a uniform velocity profile (the

potential core) decreases as the edge of the jet interacts with the ambient gas. As the jet continues to spread, the entire velocity profile becomes non-uniform. This region where there is no interaction with the impingement surface is called the free jet and includes part of the potential core. The gas approaches the surface and begins to slow down axially and then accelerate radially in the stagnation zone. This is typically the area of highest heat transfer coefficient. The gas flows away from the stagnation zone radially and slows considerably in the wall jet region. In an array of round jets, the wall jets will interact with each other and can significantly affect the heat transfer performance of the jet array. Gas-cooled divertors with jet arrays thus need to be optimized for this effect by managing the array spacing between the jets.

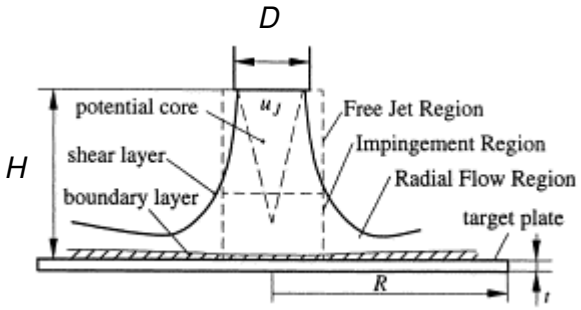

Figure 4. Impinging jet schematic. [5]

Martin [6] collected data from several sources and provides a thorough review of round jet theory. Typically, the local *Nu* value on the impingement surface takes the shape of bell with its peak at the center. For smaller values of wall spacing to jet diameter ratio, the local *Nu* may exhibit two maxima with the second maximum possibly being larger the first. This is an effect of turbulence. Gas-cooled divertors typically have small wall spacing to jet diameter ratios and thus this effect is of particular interest.

Several investigations have been performed regarding the jet-to-wall spacing and its impact on heat transfer. Jets are characterized by the nozzle hydraulic diameter at the exit *D*, the spacing from the nozzle exit to the impingement surface *H*, the ratio of the

nozzle area to the impingement area *A*, and the *Re* based on *D*. Martin [6] found that the following correlation described well the heat transfer characteristics of several previous investigations of round jets:

$$\frac{Nu}{Pr^{0.42}} = G\left(A, \frac{H}{D}\right)\left[2Re^{1/2}(1 + 0.005Re^{0.55})^{1/2}\right] \quad (5)$$

where

$$G = 2A^{1/2}\frac{1-2.2A^{1/2}}{1+0.2(H/D-6)A^{1/2}} \quad (6)$$

The above correlation is valid for

$$\begin{bmatrix} 2000 < Re < 400{,}000 \\ 2 < H/D < 12 \\ 0.004 < A < 0.04 \end{bmatrix}$$

Some divertor designs that have small *H/D* may not fall within the range of this correlation.

Meola [7] combined correlations and experimental data from several sources to create a new correlation for both single jets and arrays of impinging jets that covers a wider range of parameters. The correlation is:

$$\frac{Nu}{Pr^{0.42}} = G\left(A, \frac{H}{D}\right)\left[0.3Re^{0.68}\right] \quad (7)$$

where

$$G = A^{0.15}\left(\frac{H}{D}\right)^{-0.3} \quad (8)$$

The above correlation is valid for:

$$\begin{bmatrix} 200 < Re < 100{,}000 \\ 1.6 < H/D < 20 \\ 0.0008 < A < 0.2 \end{bmatrix}$$

Meola's correlation is shown in Figure 5.

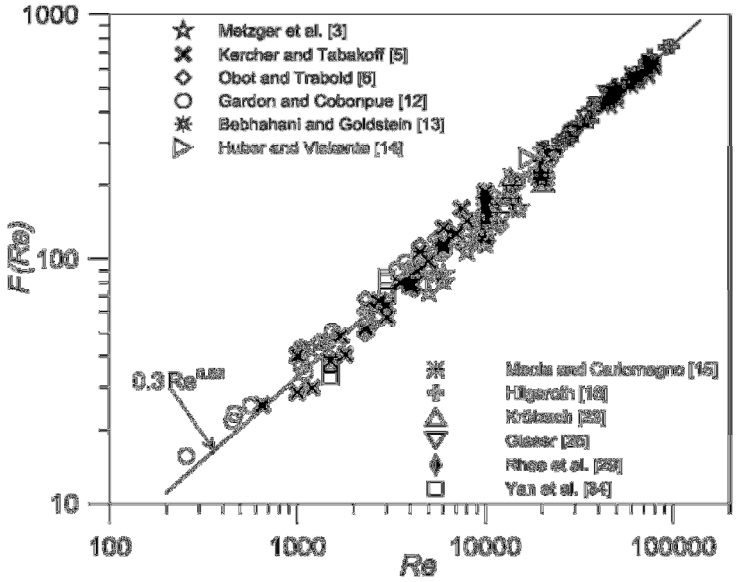

Figure 5. Jet impingement correlation of Meola (references in Figure do not correspond to this thesis). [7]

Using the correlations of Martin and Meola with dimensions commonly seen for gas-cooled divertor applications requires an extrapolation as the jet-to-wall spacing for such designs is usually small (*H/D* ≤1.5). If the value of *H/D* is chosen to vary from 1 to 2.5, then for a fixed mass flow rate of 4.95 g/s and an impingement area with diameter of 10 mm for He at 600 ℃, the resulting impingement surface averaged HTCs are shown in Figure 6 for a fixed *H* of 2 mm and thermal conductivity of 0.328 W/m-K (value for He at 600 ℃). These trends characterize the performance expected by changing just the diameter of a round jet while keeping the other parameters constant. These values range from 46 to 126 kW/m^2-K. These HTC values go outside the range predicted for He-cooled divertors which are typically estimated to be ~60 kW/m^2-K. Using values typical of a He-cooled divertor (*H/D* = 1, *Re* = 75,000, *A* = 0.04) produces HTCs of 46

kW/m^2-K by Martin and 53 kW/m^2-K by Meola. As these values are calculated from a correlation derived from experimental data from many sources, it is reasonable to assume at least ±10% uncertainty.

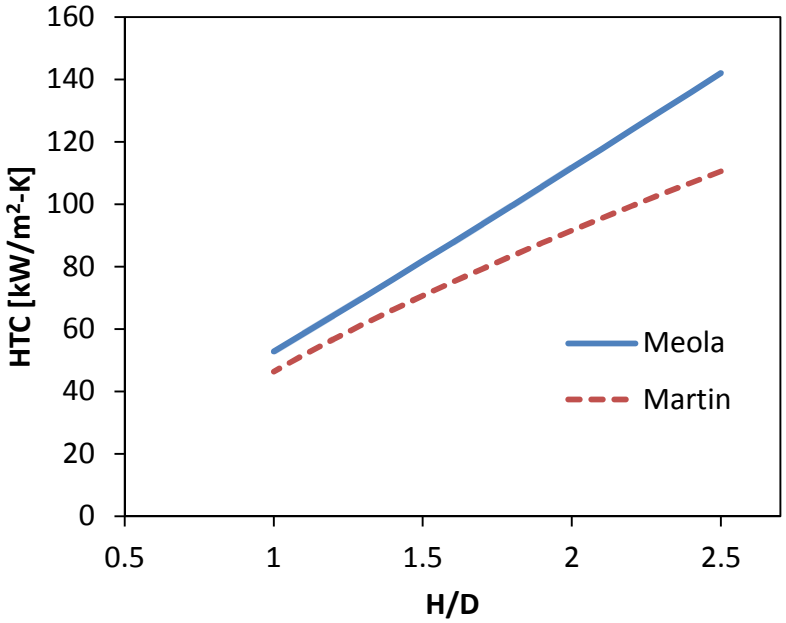

Figure 6. Trends of area averaged HTC for the correlations of Martin [6] and Meola [7] for a single round jet impinging on a surface changing just the jet diameter leaving other parameters constant.

The effect of jet-to-jet spacing for arrays of impinging jets has also been investigated by several researchers. A diagram of two impinging jets is shown in Figure 7. When the wall jets from two jets collide, they form a “fountain” that forces the coolant to flow away from the impingement surface. If the impinging jets are spaced too close together, these fountains can negatively affect the heat transfer performance of the jet array.

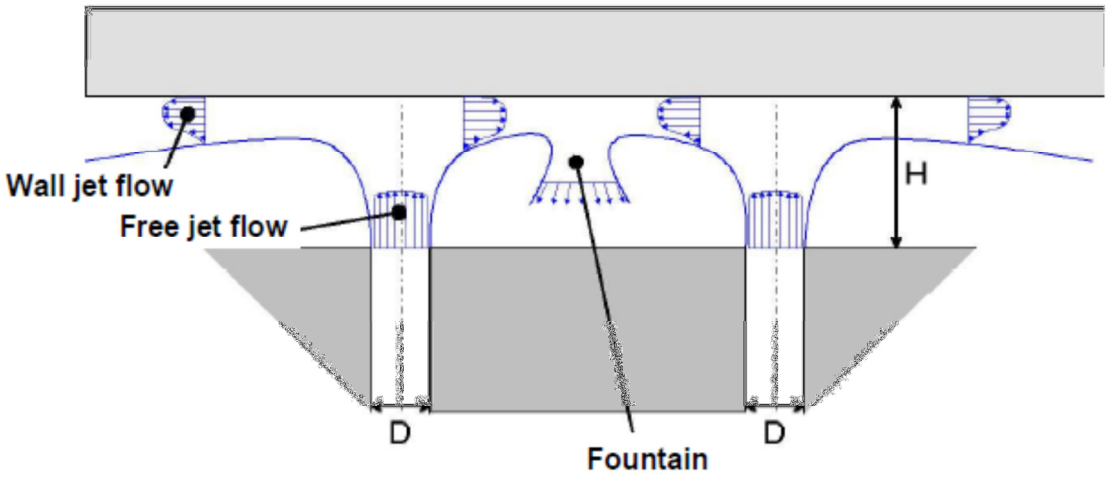

Figure 7. Interaction of two impinging jets. [8]

One study that examined the effect of jet-to-jet spacing for a staggered array of round jets was performed by San and Lai [9]. They found that there was an optimum jet-to-jet spacing that varied depending on the jet-to-wall spacing. They also observed that the *Re* of the flow may have an impact on the optimum spacing. For example, as shown in Figure 8 [left], the optimum jet-to-jet spacing (s/D) occurs near 8 for all flow rates investigated for a fixed jet-to-wall spacing (H/D = 2). Figure 8 [right] however shows that the optimum jet-to-jet spacing for a jet-to-wall spacing of 5 occurs near s/d = 6. Also, a secondary maximum occurs at higher values of s/D. These tests did not investigate jets with small jet-to-wall spacing (H/D < 2) used in some divertor designs.

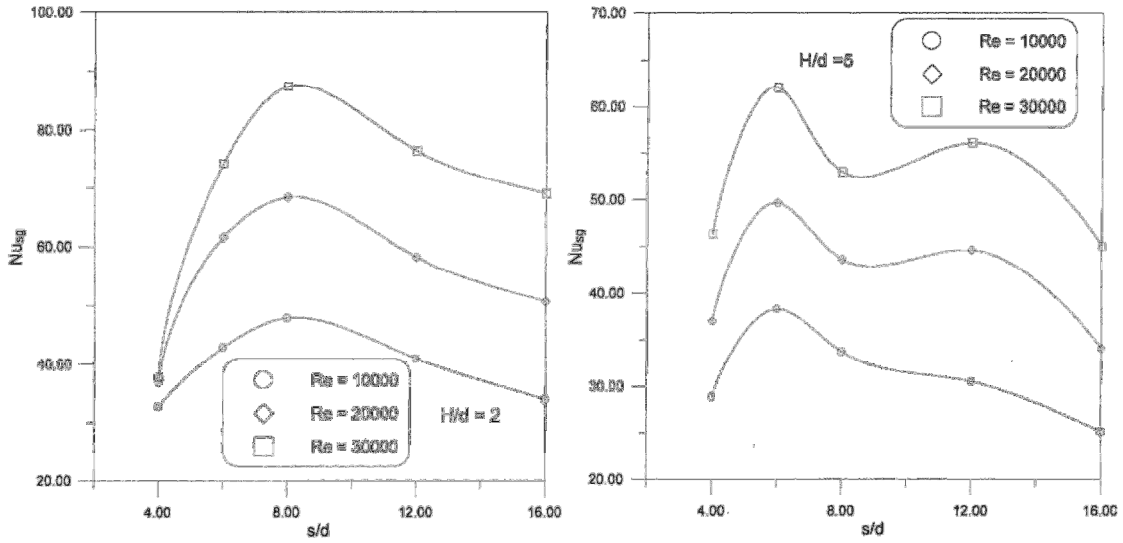

Figure 8. Effect on stagnation *Nu* (Nu_{sg}) of jet-to-jet spacing (s/D) for two fixed jet-to-wall spacings of H/D=2 [left] and H/D = 5 [right] at several flow rates (Re). [9]

Another concern is the impingement of jets or arrays of jets on a concave surface which is common to several divertor designs. One such study by Cornaro et al [10] examined experimentally the flow of a single round jet on either a flat, concave or convex semicylindrical surface (i.e. a round jet impinging on a flexible plate formed into a flat, concave, or convex shape). They found a strong effect on the behavior of the jet based on the jet-to-wall spacing. This study, however, focused on qualitative behavior including vortex generation and propagation and thus heat transfer performance was not emphasized.

An earlier study that examined the cooling of an airfoil from a jet engine by Chupp et al [11] produced heat transfer correlations particular to that scenario. They correlated the *Nu* to *Re* as well as geometric properties including jet-to-wall spacing, jet-to-jet spacing, and the jet diameter to cooled surface diameter ratio (*Pr* effects were ignored as all of the experiments were performed with air). They found that, in general for their particular configuration, small values of the jet-to-wall spacing resulted in larger values of *Nu*. Thus both the geometry and the flow rate play an important role in

determining the behavior and heat transfer performance of a system incorporating jet impingement.

2.2. Cooling Fins and Tube Bundles

Heat transfer enhancement can also be achieved by passing the coolant over extended surfaces (fins) or through arrays of tube bundles. These methods achieve heat transfer enhancement by increasing the heat transfer area and turbulent mixing of the flow.

For the case of cylindrical tube bundles in a staggered or triangular array, the first row of tubes acts similar to a single cylinder in cross flow. In successive rows, eddies (as shown in Figure 9) produced by the rows before it leads to heat transfer enhancement. However, depending on the *Re* of the flow, the entirety of the tube may not be participating in meaningful heat transfer as the backside of the tube is subjected to very low coolant velocities and thus low heat transfer coefficient with increasing *Re*. The flow-facing side of the tubes thus sees the highest heat transfer coefficients. Of course, tubes with non-circular cross sections can be used to optimize this effect.

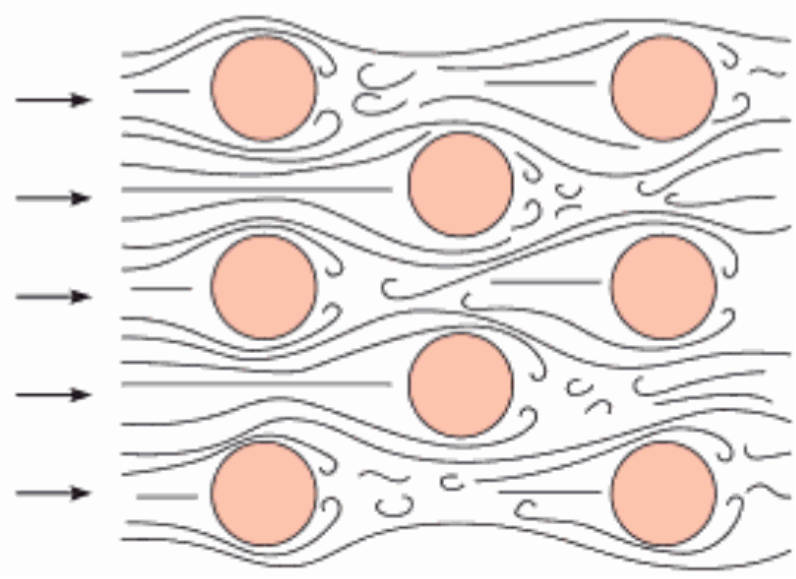

Figure 9. Cross section of cylinders in cross flow. [4]

Tube bundles also need to be optimized for pressure drop. The spacing between tubes can greatly impact the pressure drop across an array of tubes. A small spacing to tube size ratio typically results in a larger pressure drop as the coolant is forced into tumultuous flow paths. However, spacing the tubes out too far results in decreased heat transfer enhancement and therefore an optimization must be made between the heat transfer enhancement and the pressure drop across an array of tubes.

Also, it must be considered that the coolant temperature increases as it passes through successive rows of tubes thus decreasing the heat transfer rate. Therefore, the number of rows of tubes needs to be optimized to account for this effect along with the size and spacing of the tubes.

Using extended surfaces or fins is another common method of enhancing heat transfer by increasing the heat transfer area. Typically, a highly conductive material is used for the material of the fin to maximize its efficiency. High heat transfer coefficients can be achieved when the temperature difference between the conductive surface and the bulk temperature of the coolant is great. A high thermal conductivity for the fin allows the temperature drop across the length of the fin to be minimized. This maximizes the difference between the fluid and solid temperature over the majority of the surface and thus the heat transfer rate.

Two measures of the performance of a particular fin are the fin effectiveness, ε, and the fin efficiency, η. As defined by Incropera and Dewitt [4], the fin effectiveness is the "ratio of the fin heat transfer rate to the heat transfer rate that would exist without the fin" and is defined as:

$$\varepsilon = \frac{q}{hA_c\Delta T_b} \tag{9}$$

where q is the fin heat transfer rate, h is the heat transfer coefficient, A_c is the cross sectional area of the fin at its base, and ΔT_b is the temperature difference between the coolant and the base of the fin. A large value of ε is desired, and typically values greater than 2 make the use of fins justifiable [4]. For the case of a fin with finite length L and an adiabatic boundary condition at its tip, the fin effectiveness is:

$$\varepsilon = \frac{k}{h}\, m \tanh mL \tag{10}$$

where k is the thermal conductivity of the fin, and m is defined as:

$$m^2 = \frac{hP}{kA_c} \tag{11}$$

where P is the perimeter of the fin (circumference in the case of cylindrical fin). It is apparent that for the case of a finite length fin with adiabatic tip and uniform diameter D ($P/A_c = 4/D$) that the particular characteristics that cause large fin effectiveness come from different factors. The only thing that can be said for certain is that small diameter and large length fins will result in higher ε. The effects of the high HTC/high thermal conductivity of the fin are self-opposing as they appear in the denominator/numerator of the coefficient and the numerator/denominator of the hyperbolic tangent quotient, respectively. The effect of the thermal conductivity and HTC on the fin effectiveness would thus vary for a given geometry.

The fin efficiency is the ratio of the heat removal rate of the actual fin to the heat removal rate of the same fin with infinite thermal conductivity. The fin efficiency for a cylindrical fin with adiabatic tip is:

$$\eta = \frac{\tanh mL}{mL} \tag{12}$$

As an increase in the *mL* will both cause an increase and decrease in the value of η, an optimization of geometry and flow characteristics around the fin is necessary, inasmuch as the presence of the fins themselves will impact the heat transfer coefficient.

As cylindrical fins in a staggered array are necessarily of finite length, the two heat transfer enhancement mechanisms must be combined to calculate the enhancement effect of an array of fins. Analytical calculations can be used to guide a design and make performance estimates, but experimental and CFD studies are needed for verification especially if unusual fin geometries and arrangements are proposed.

2.3. Porous Media

Another method of increasing heat transfer area is by passing the coolant through a porous medium such as metallic foam. This method results in a significant increase in heat transfer area as well as turbulent mixing. A particular foam specimen is characterized by its average pore density which is given in terms of pores per inch (ppi). Foams with large pore density have larger heat transfer area and thus higher effective heat transfer coefficients but typically result in larger pressure drop. An optimization of the pore size and the coolant *Re* is thus required for an effective porous medium application. Several proposed divertor designs use a porous medium to enhance heat transfer. One such design investigated at Georgia Tech will be discussed in Section 2.8. Other gas-cooled divertor designs such as the porous foam-in-tube (PFIT) and the short flow path foam-in-tube (SOFIT) have been proposed as well. These designs were estimated to withstand a heat flux of 5.5 MW/m^2. [12] [13]

2.4. Helium-Cooled Multi-Jet Divertor Design

The Helium-Cooled Multi-Jet (HEMJ) [14] divertor design was proposed by Karlsruhe Institute of Technology (KIT) and is depicted in Figure 10. The HEMJ cools the inner surface of a tungsten alloy endcap (also referred to as the pressure boundary) with an array of 25 round jets. Helium enters a steel jet cartridge at 600 ℃ and 10 MPa before passing through an array of twenty-four 0.6 mm OD round jets centered about one 1 mm OD round jet. The helium impinges upon the curved tungsten alloy endcap, cooling the tungsten tile brazed onto the endcap. As shown in Figure 10, each hexagonal tungsten tile is 18 mm flat-to-flat covering 280.6 mm^2. As the endcap has an outer diameter of 15 mm, heat flux incident on the tile is focused onto the endcap. By actively cooling the curved inner surface of the endcap with area 194.4 mm^2, the focusing effect is lessened; however, the cooled surface heat flux is still nearly 44% higher than the heat flux incident on the plasma-facing tile based on the difference in areas.

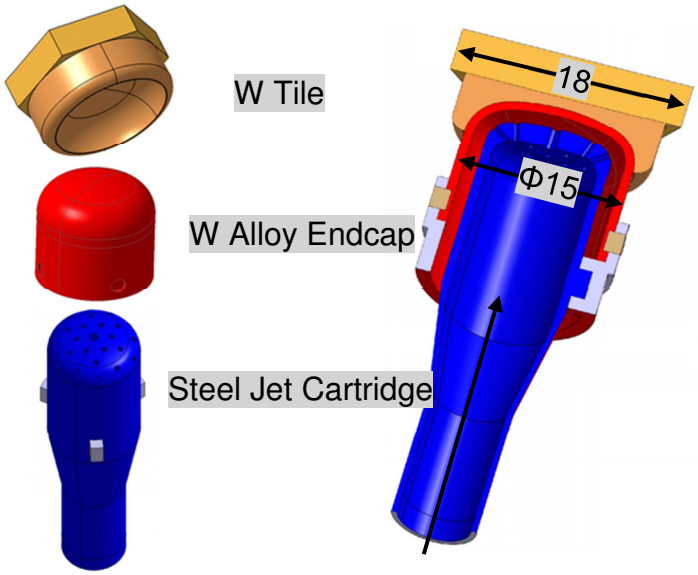

Figure 10. The HEMJ divertor. Exploded view (left) and cross section of assembled module (right). Dimensions in mm. [15]

Approximately 350,000 HEMJ modules of this size will be required to cool a 100 m^2 divertor. If each HEMJ uses 6.8 g/s of He, the total flow rate for the divertor system will need to be 2380 kg/s. If the recirculation time of He in the divertor system is on the order of a few minutes, the amount of He required for the divertor system is on the order of several hundred tonnes.

The HEMJ has been studied both experimentally and numerically by groups at both Georgia Tech [16] [17] [18] [19] and KIT with the Efremov Institute [8] [14] [20] [21]. An experimental and numerical study by previous researchers at Georgia Tech used an electrically heated HEMJ module made of C36000 brass and cooled with air. They were able to achieve heat fluxes up to 0.9 MW/m^2 based on a control volume energy balance. They validated a numerical model to their experimental results and used the numerical model to make performance predictions for the HEMJ operating at an elevated heat flux with helium coolant. Crosatti and Weathers used ANSYS® FLUENT® to perform their CFD analyses. The results of the work by Crosatti can be seen in Figure 11. These results show that the *Nu* is not strongly dependent on the incident heat flux.

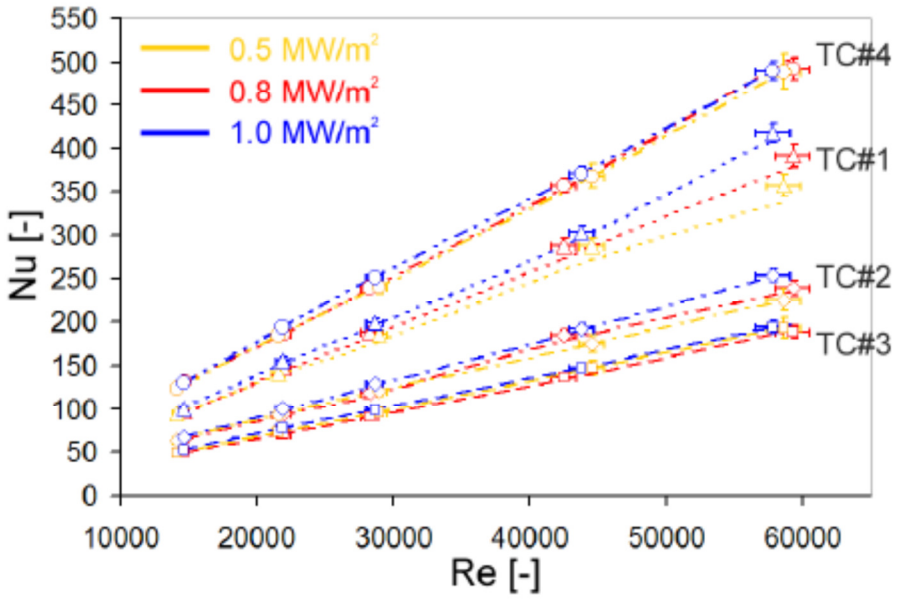

Figure 11. *Nu* v. *Re* at different locations for different heat fluxes for the air-cooled HEMJ. [16]

Part of this previous study was a combined effort with researchers at KIT to predict the HEMJ's behavior in the HEBLO test facility (helium test loop operating at 8 MPa). Tests performed at HEBLO and at a gas-puffing helium loop indicated the HEMJ could withstand 12.5 MW/m^2 incident heat flux. Further experimental studies by KIT at the Efremov Institute on a single HEMJ module as well as a cluster of nine HEMJ modules agreed with these results.

The high heat flux for these tests was achieved in one of two ways: a "reverse" heat flux method, and an electron beam. The reverse heat flux method relies on the fact that the *Nu* or heat transfer coefficient will be the same for a given *Re* or $\dot{m}$ regardless of the sign of the temperature difference between the surface of the structure and the bulk temperature of the gas. By heating the gas before it enters the divertor test section and cooling what would normally be considered the heated surface, a calculation of the heat flux through the divertor can be made based on the decrease in the temperature of the gas from inlet to outlet and from temperature measurements of the divertor material.

High heat fluxes can be simply achieved this way by cooling an area with water and focusing the cooling into the divertor piece. Alternatively, the divertor can be heated by accelerating and collimating electrons into beam. When the electrons reach the divertor tile, they begin to slow down thus depositing their kinetic energy. Helium is pumped though the divertor and the heat flux can be calculated using an overall energy balance. An infrared image of a bundle of nine HEMJ modules being heated by an electron beam is shown in Figure 12.

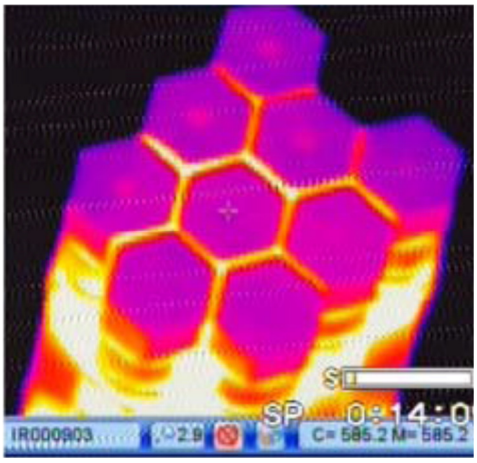

Figure 12. Infrared image of a bundle of nine HEMJ modules during high heat flux tests at Efremov Institute. [22]

The HEMJ has gone through several design iterations and have been tested both experimentally and using computer simulations. The aforementioned gas-puffing tests [8] used several combinations of jet-wall spacing and jet diameters. The researchers compared the results of the gas-puffing tests for several different HEMJ configurations to find the optimum design in terms of both maximum heat flux and pressure loss. The results of this test are shown in Figure 13 and Figure 14. As shown by the two performance figures, the HEMJ designs have both a higher maximum heat flux and lower pressure drop than the helium-cooled modular divertor with slot array (HEMS) [Section 2.6].

Another test of the HEMJ used a thermo-mechanical computer simulation to create a better design for attaching the different components of the HEMJ [23]. A concern for the construction of the HEMJ is that the large temperature gradients (necessitated by large heat flux) will create thermal stresses exceeding acceptable limits for either the primary components (tile, thimble or cartridge) or the brazing material used the bond the components together. The study by Widak and Norajitra [23] found that the design depicted in Figure 15 was a more optimized version of the HEMJ for minimizing the effects of thermal stress. The design has been tested successfully at the Efremov Institute and survived over 100 load cycles.

Another method to reduce the mechanical stress on the HEMJ module is how it is assembled, as shown in Figure 16. The effects of high stress caused by temperature gradients can be alleviated by using a cap with a thinner wall and using intermediate pieces that relocate the points of highest stress to locations away from brazings and onto metal pins. The differences in the two depicted designs would obviously need to be reconciled before manufacturing.

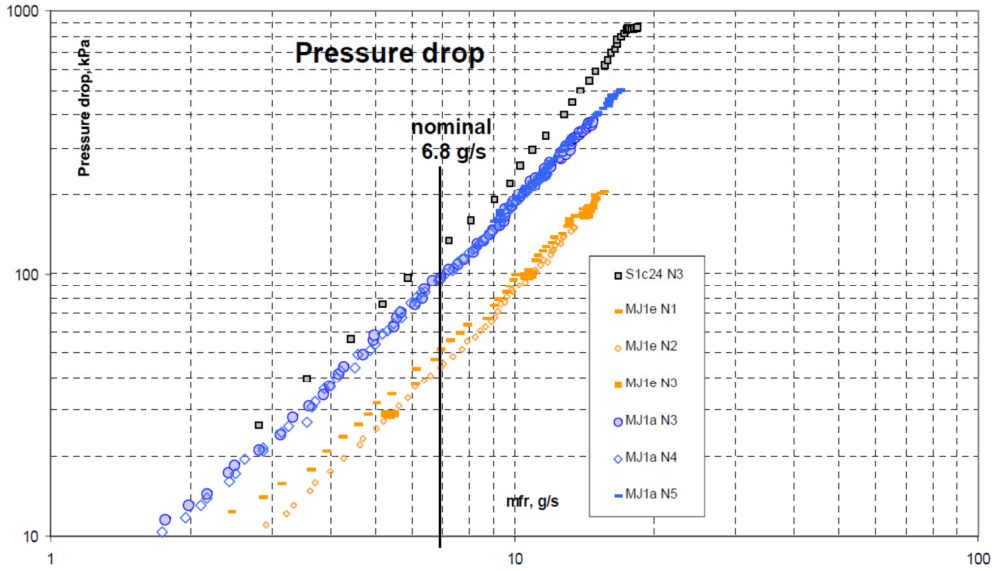

Figure 13. Pressure drop vs. mass flow rate for GPF experiments performed by KIT on variants of the HEMJ (blue and orange) and HEMS (black). [8]

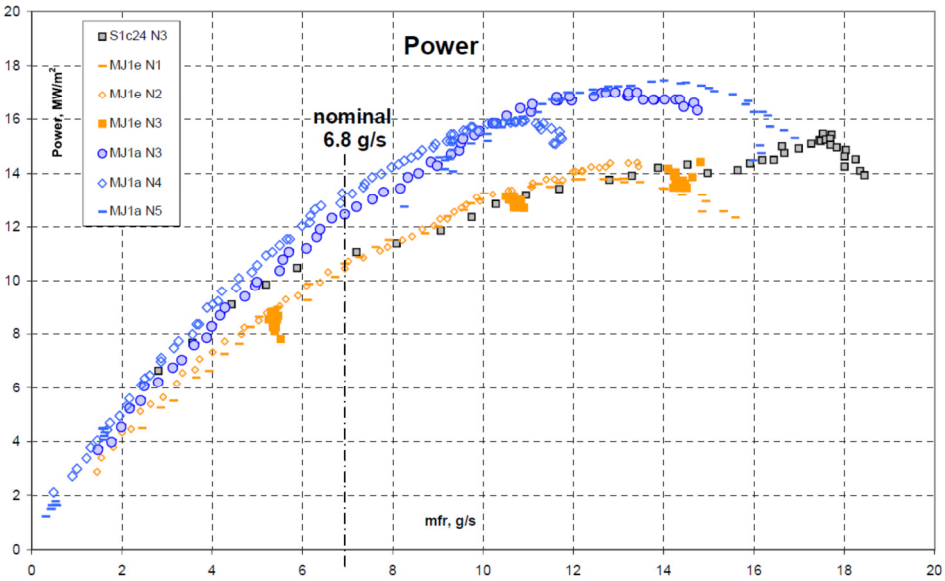

Figure 14. Maximum heat flux vs. mass flow rate for GPF experiments performed by KIT on variants of the HEMJ (blue and orange) and HEMS (black). [8]

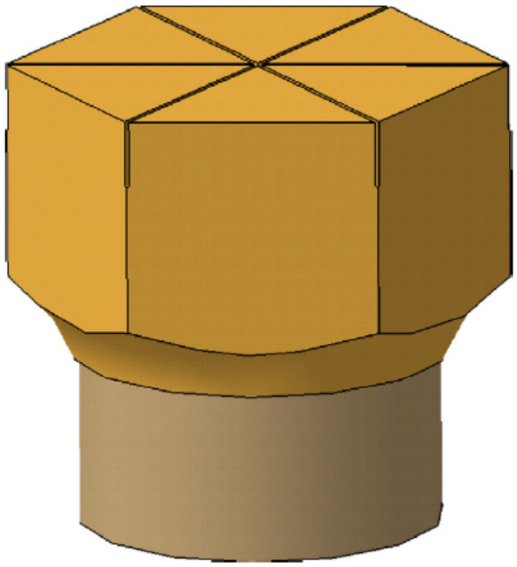

Figure 15. Reduced thermo-mechanical stress optimized HEMJ assembly [23].

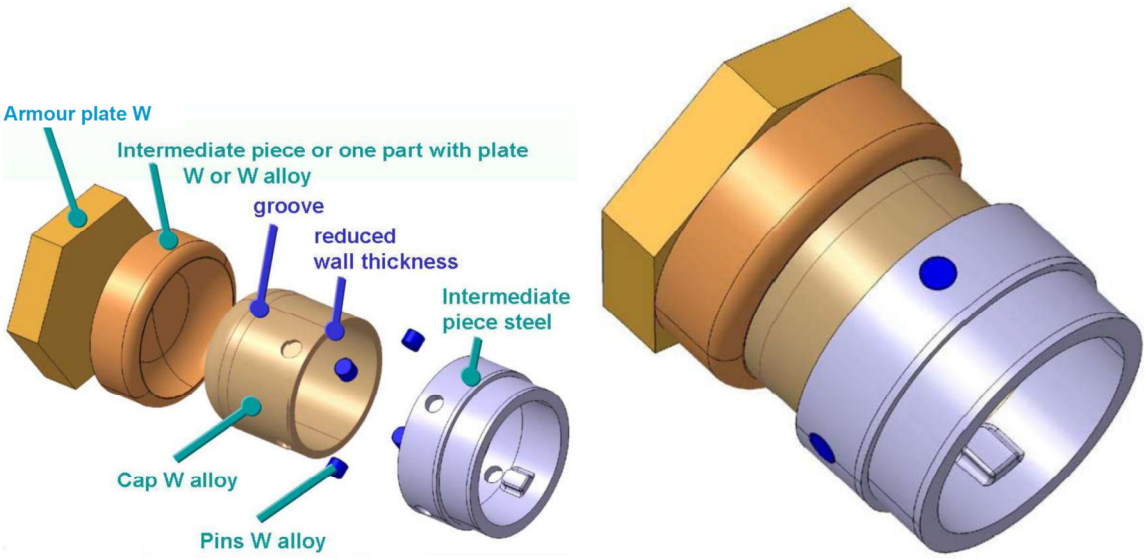

Figure 16. Proposed design of reduced stress HEMJ. Exploded (left) and assembled (right). [8]

2.5. Helium-Cooled Modular Divertor with Integral Pin Array

The Helium-cooled modular divertor with integral pin array (HEMP) was proposed by KIT [24] and is depicted in Figure 17. Instead of using impinging jets like the HEMJ, the HEMP relies on an array of integral fins on the cooled surface of the tungsten alloy pressure boundary for heat transfer enhancement. Helium enters in an annular channel at 600 ℃ and 10 MPa before reaching the cooled surface and passing through an array of cooling fins. Similar to the HEMJ, a 249.6 mm^2 square tungsten tile is brazed onto the pressure boundary and receives up to 10 MW/m^2 heat flux from the fusion plasma. Like the HEMJ, there is a focusing of the heat flux from the tile to the cooled inner surface of the pressure boundary. The fins increase the cooled surface area to help offset this effect. As the design of the fin array for the HEMP divertor has proven difficult to manufacture, the HEMP has yet to be tested experimentally. As shown in Figure 18, the EDM (electro-discharge machining) process, even after several electrodes were consumed, was not able to produce a usable HEMP module with the original design geometry.

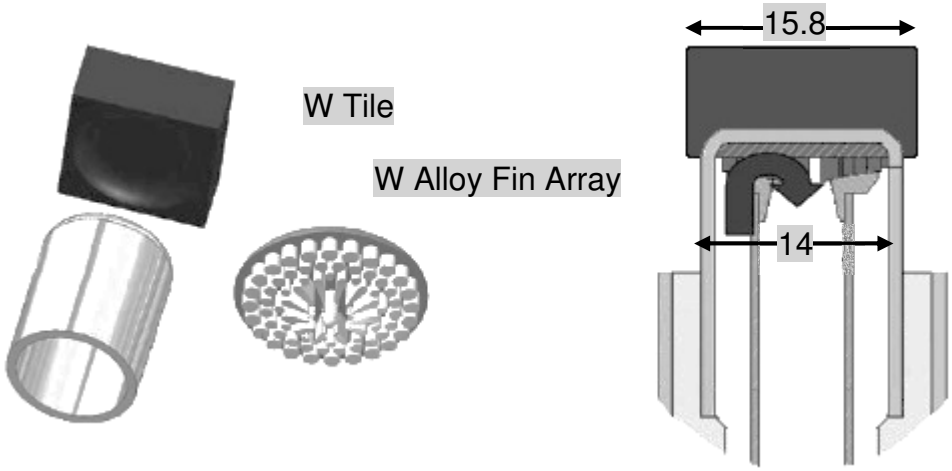

Figure 17. The HEMP divertor. Exploded view with fin array (left) and cross section of assembled module (right). Dimensions in mm. [24]

Initial performance predictions for the HEMP estimated effective HTCs as high as 60 kW/m^{2}K with a pumping power below 5% of thermal power. This corresponds to a heat removal rate of up to 15 MW/m^2 while remaining within mechanical stress limits [24]. As stated by the original designers, however, the HEMP design needs to be optimized using CFD codes to potentially increase performance margins and verify initial performance predictions.

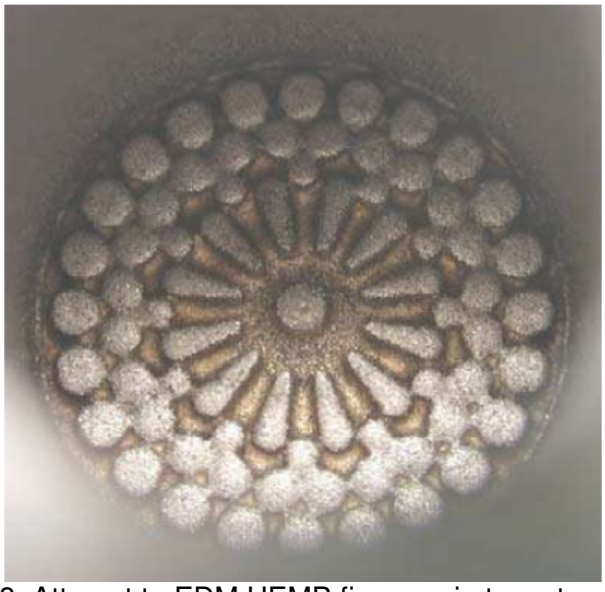

Figure 18. Attempt to EDM HEMP fin array in tungsten alloy. [8]

2.6. Helium-Cooled Modular Divertor with Slot Array

The helium-cooled modular divertor with slot array (HEMS) was designed by KIT as part of a similar project to the HEMP [25]. Instead of using fins to increase the cooling surface area, the coolant would pass radially through slotted channels. Depending on the relative performance of the HEMS and HEMP, inserts created in the shape of each design could be brazed onto the cooled surface of a common divertor module. Another variant of the HEMS with curved channels was also designed. The three so-named heat transfer promoters and the divertor module can be seen in Figure 19. As mentioned in Section 2.4, the straight slot HEMS was crafted and tested alongside several HEMJ variants. Its performance in terms of both maximum heat flux and reduced pressure drop was not as good as the HEMJ so development has not continued since.

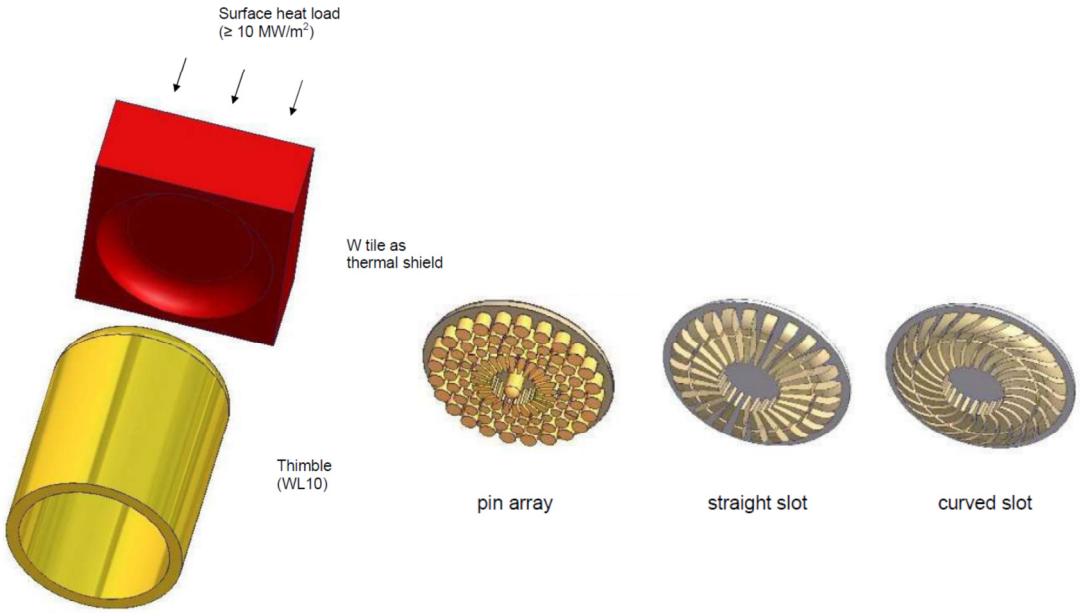

Figure 19. HEMP and HEMS inserts (right) next to generic divertor module (left). [25]

2.7. Helium-Cooled Flat Plate

The Helium-cooled flat plate divertor (HCFP) was designed by a group at KIT [26] to withstand a peak heat flux of 10 MW/m^2. The HCFP is referred to as a plate-type design as it consists of large channels within a plate configuration. As compared to aforementioned finger-type designs, a relatively few number of HCFP modules would be required to cover the entire plasma-facing surface of the divertor. The HCFP cools the inner surface of a plate or tiles of tungsten armor by a long slot jet that extends the length of the channel. Helium enters each inlet channel at 10 MPa and 600 ℃ from a common reservoir, flows through the slot as a planar jet, retreats over the curved inner surface of the plate thus removing heat from the tiles, and enters an outlet channel. As the HCFP consists of several large components, thermal stress issues have always been a concern. However, given its relatively simple design and construction, development of the HCFP has continued.

Since its initial development, an optimization of the HCFP has been performed by to reduce thermal stresses [27]. As shown in Figure 20 and Figure 21, the HCFP consists of several long channels that share common inlet and outlet manifolds. The optimization study served to reduce the thermal stresses on the structure which allows the HCFP to accommodate a higher heat flux from the plasma.

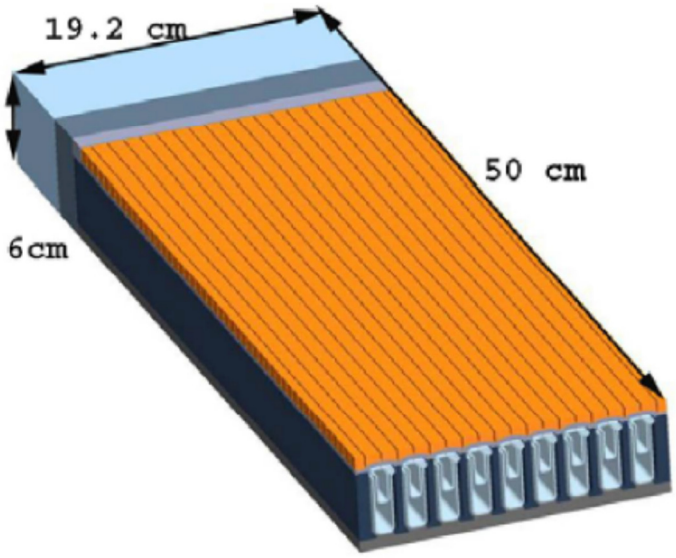

Figure 20. Half of HCFP assembly. Actual length 1 m. [27]

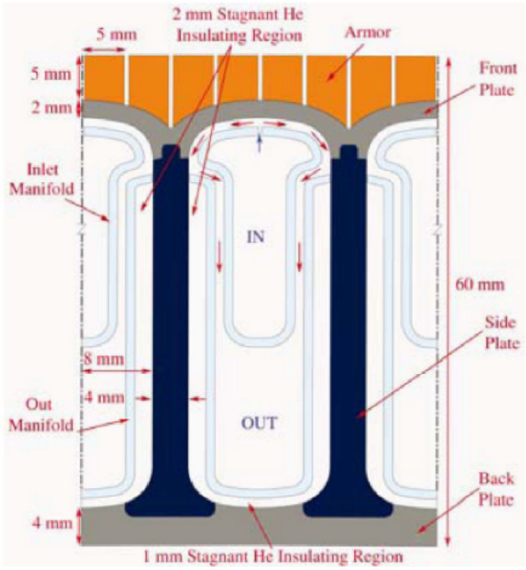

Figure 21. Close up of the arrangement of HCFP channels. [27]

There have been several variations of HCFP-like designs studied at Georgia Tech as well, albeit at low temperatures [28] [29] [30] [31]. Each of the test modules used various aluminum cartridges placed inside brass shells with air near 700 kPa and ambient temperature at a *Re* dynamically similar to the helium-cooled design. A diagram of the cartridge-in-shell design is given in Figure 22. The shell was heated electrically

using three cartridge heaters up to 0.8 MW/m^2. Gayton studied two modifications to the standard slot-jet design: the use of an array of round jets like the HEMJ instead of the central slot jet, and the use of a metallic foam insert placed in the gap between the cartridge and the shell to increase turbulence and heat transfer area. Gayton also performed numerical simulations on a half model of the HCFP-like test section. Hageman studied the variation of the slot width with the combination of an array of cylindrical fins integral to the cooled surface of the shell.

Both Hageman and Gayton also calculated the pressure drop and heat transfer coefficient at different flow rates and heat fluxes for each combination of jet design and heat transfer promoter. Hageman found that a 2 mm slot width had a lower pressure drop and at least as high heat transfer coefficient compared to a 0.5 mm width slot. Pins on the cooled surface increase the heat transfer coefficient three-fold for air; however, the effect of the pins when helium is the coolant is lessened because of the lower fin efficiency. He predicted that the HCFP-like design with pins could withstand up to 18 MW/m^2 near its prototypical operating *Re*.

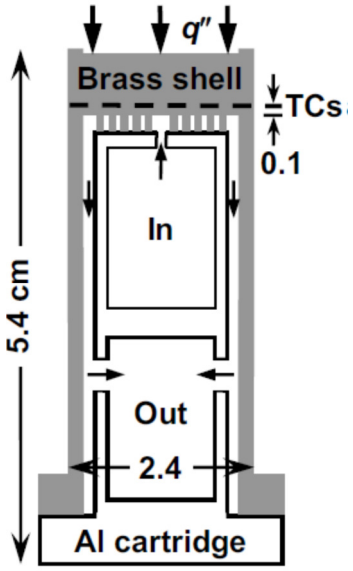

Figure 22. HCFP-like cartridge-in-shell design used by Hageman and Gayton at Georgia Tech. [29]

Gayton determined that the array of round jets resulted in lower shell temperatures for a given flow rate and heat flux compared to a 2 mm width slot jet but with a significant increase in pressure drop. The presence of foam also decreases the shell temperature but at the expense of much increased pressure drop. Gayton tested three foams with pore sizes of 45, 65, and 100 ppi and found that the foam with 100 ppi had the greatest increase in HTC (Figure 23). She also found that this increase in HTC came with a significant increase in pressure drop.

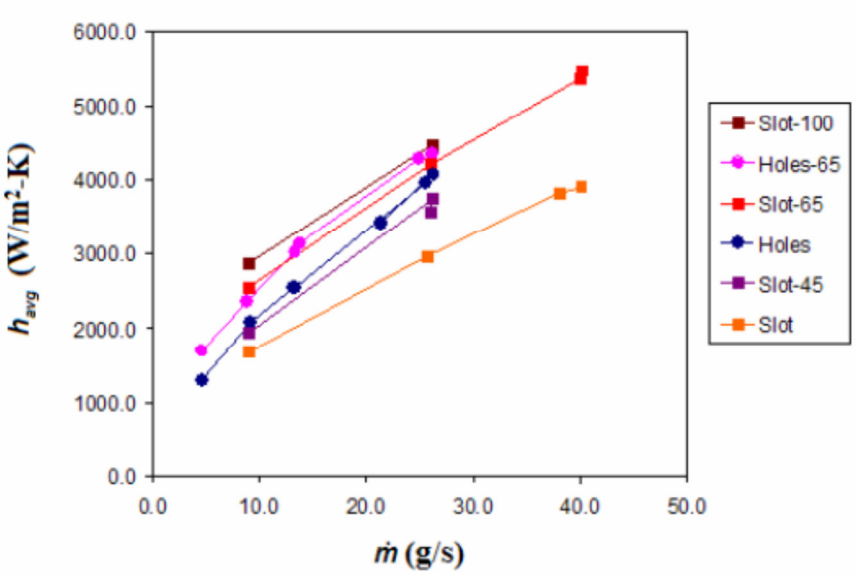

Figure 23. Comparison of several HCFP configurations tested by Gayton. [30]

2.8. T-Tube

The T-Tube divertor was designed as part of the ARIES-CS study to accommodate heat fluxes up to 10 MW/m^2. Several studies of the T-Tube at both Georgia Tech [16] [32] [33] [34] and KIT [3] [35]have been performed. As shown in Figure 24 and Figure 25, the T-Tube uses jet impingement to cool a layer of tungsten armor. The T-Tube is larger than the HEMJ or HEMP but smaller than the HCFP having a length of approximately 100 mm. By having an intermediate size, the T-Tube was

designed to have the benefits of simple manifolding and construction of large divertors and improved heat flux removal of small divertors.

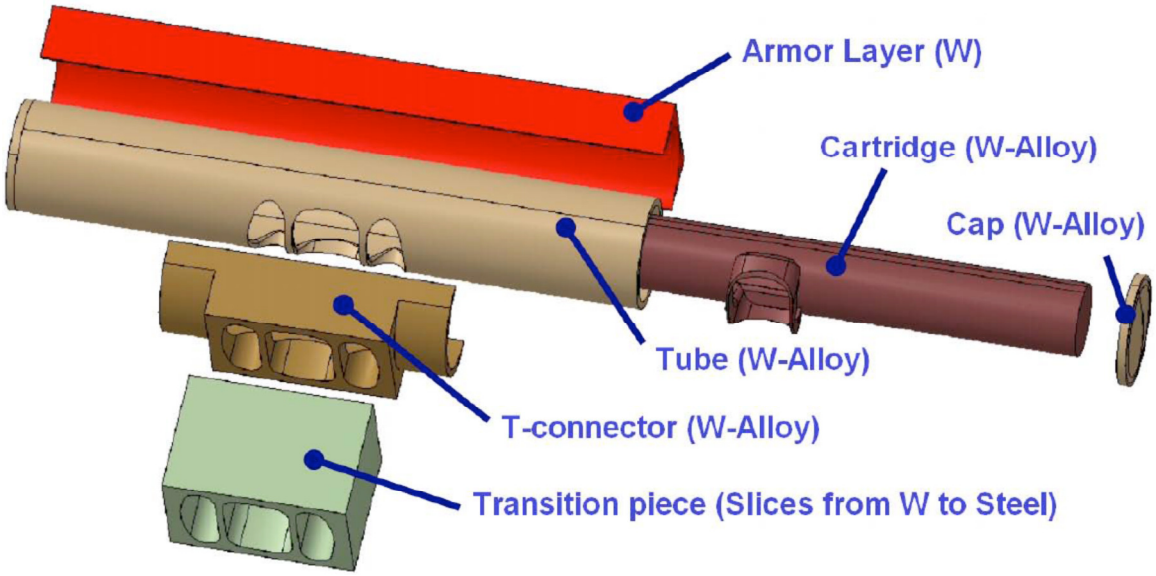

Figure 24. The T-Tube divertor. [35]

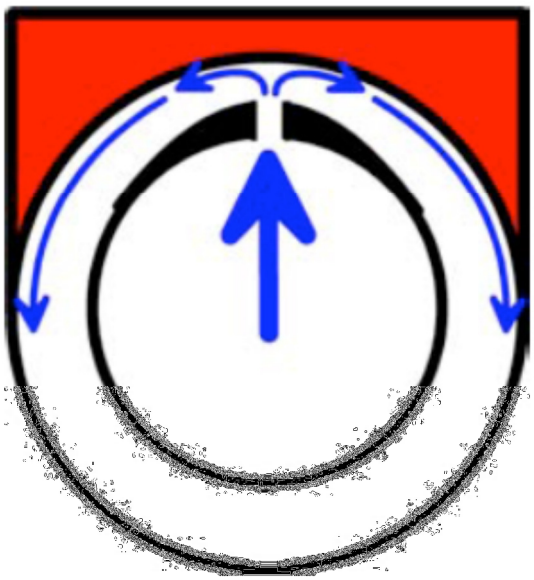

Figure 25. Cross section of the T-Tube showing slot jet impingement. [35]

Researchers at KIT performed simulation studies of the T-Tube at prototypical temperatures and heat fluxes to determine if the T-Tube was a viable option for a tokamak or stellarator divertor. Their simulation results were obtained using ANSYS®

FLUENT® and Workbench®. Both CFD and mechanical studies were performed. They found that the T-Tube under uniform loading should be able to withstand 10 MW/m^2. However, under non-uniform loading caused by plasma disruptions or flow transients, the T-Tube on account of length may be subject to stresses beyond recommended levels.

The group at Georgia Tech performed two studies of the T-Tube. The first was a scoping study of a T-Tube like geometry (though longer) intended to compare a numerical model to experimental calculations. A 220 mm T-Tube module was electrically heated and cooled with air over a range of *Re* spanning those expected in the prototypical divertor. The experimental apparatus was designed so that different flow configurations could be tested. This study found that the simulation predictions of wall temperature and heat transfer coefficient matched well those obtained from experimental data [34]. The simulations for these studies were based on those by KIT used to calculate the original prototypical performance of the T-Tube. The second study used a T-Tube test section of nearly prototypical length electrically heated up to 0.8 MW/m^2. Using modeling techniques based on the successful first study, numerical simulations were compared to experimental data of the second study. These results also showed good agreement as shown in Figure 26. The researchers thus recommended the use of similar CFD and experimental techniques for the study of high heat flux components and divertors.

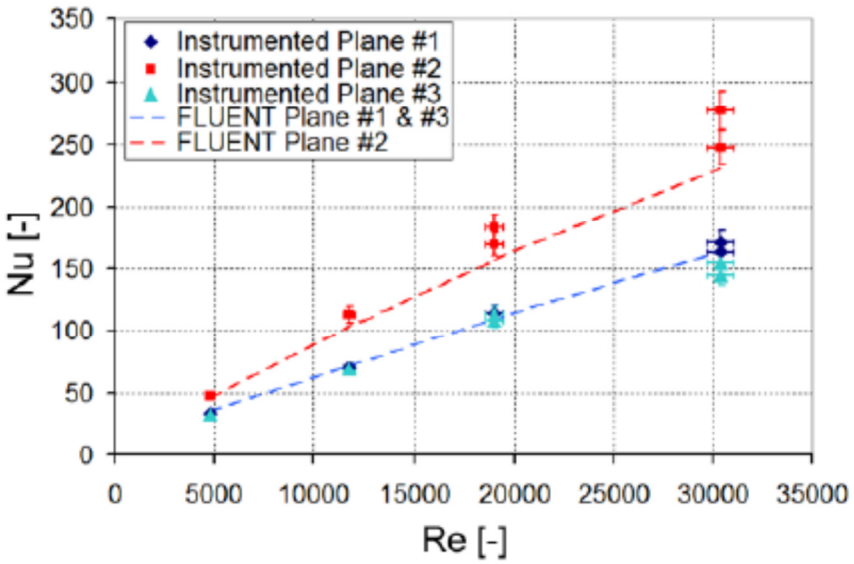

Figure 26. *Nu* v. *Re* for T-Tube experiments performed by Crosatti at Georgia Tech showing comparison of experiments to simulations. [16]

2.9. Integrated Designs

As shown in Figure 27, the divertor is expected to receive a non-uniform heat flux over its surface. In order to maximize the performance of the divertor, more effective cooling should be delivered to the part of the divertor with the highest heat flux.

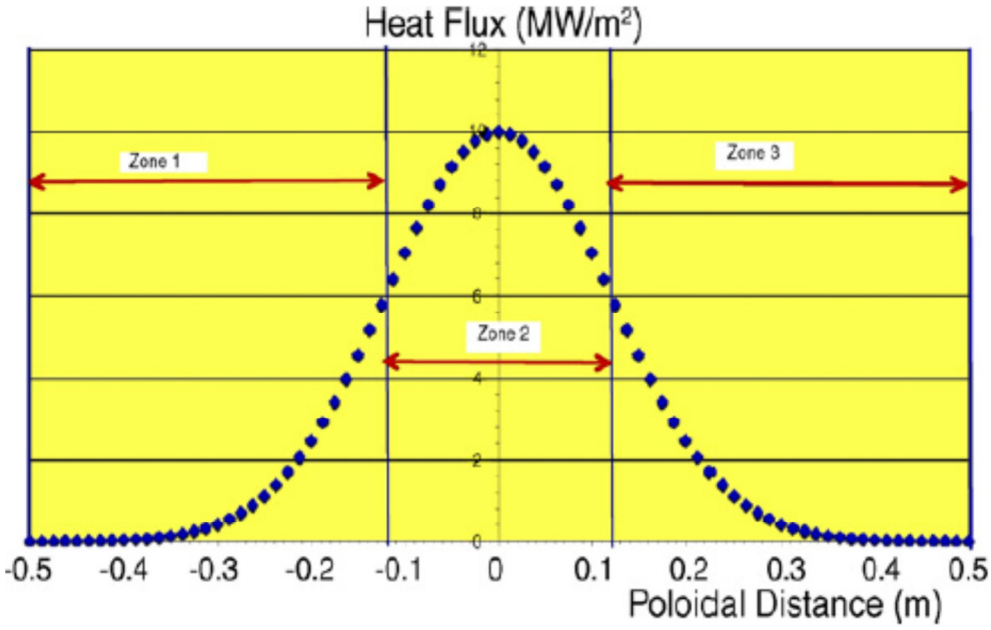

Figure 27. Heat flux distribution along the divertor plate. [3]

The HCFP has been proposed to be combined with the HEMJ in a hybrid divertor scheme where HEMJ modules would be placed in areas of high heat flux and the HCFP plates would be located in areas of low heat flux [36]. As shown in Figure 28 and Figure 29, the HCFP and HEMJ concepts can be combined to receive helium from a common manifold. This design should give several benefits: reduced thermal stress by having small modules in areas of high heat flux, reduction in number of units needed to cover the divertor surface, and simplification in design as opposed to designing to separate manifold (one each for the HCFP and HEMJ components).

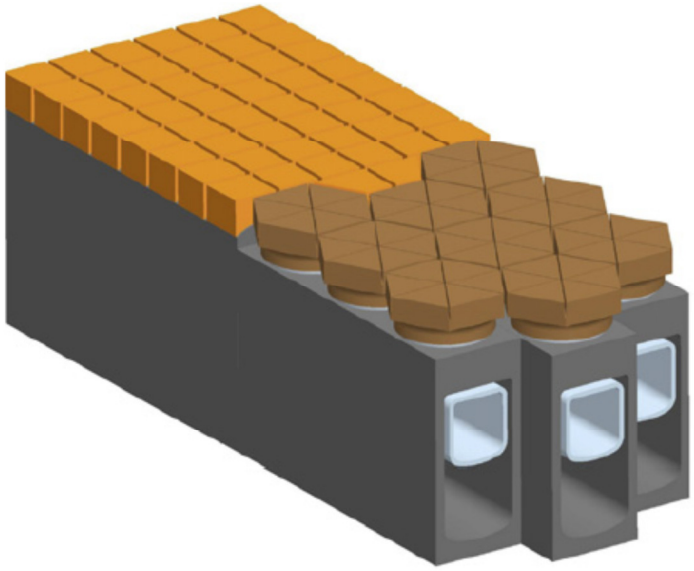

Figure 28. Combined design of HCFP and HEMJ. [36]

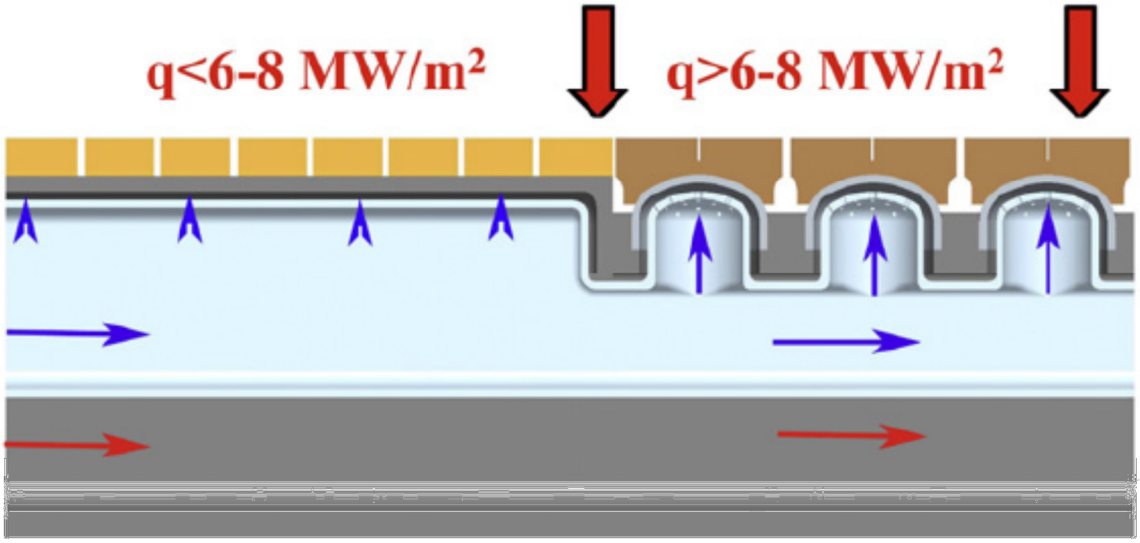

Figure 29. Areas with high heat flux using the HEMJ and areas with low heat flux use the HCFP. [36]

2.10. Heat Transfer and Fluid Flow Simulations

Predicting the behavior of non-isothermal turbulent fluid flow has been a challenge in engineering for many decades now. The advent of the computer age allowed for the calculation and prediction of fluid behavior that is not possible using analytic techniques alone. However, given the complicated nature of solving the 3-D

Navier-Stokes equations, only recently with the continued increase of computing power have direct numerical simulations (DNS) of isothermal turbulent flows for simple geometries become reasonable. For most situations, approximations must be made to the governing equations to account for turbulent behavior of fluid flow, the geometry, and boundary conditions. Several such examples relevant to this thesis will be discussed. The theses of Crosatti [16], Weathers [18], and Gayton [30] used similar methods as those to be presented to model divertors with good results.

There are many different techniques for simplifying fluid flow calculations. One of the most commonly employed methods is the use of symmetry. Many divertor designs exhibit some type of geometric symmetry that can be exploited when constructing a model. For example, the HCFP and T-Tube have a lateral symmetry plane that crosses through the center of the slot jet and runs the length of the inlet and outlet channels. Using a half-model of these divertors saves significant computing resources and time. Similarly, the HEMP, HEMS, and HEMJ have rotational symmetry. Some designs may even exhibit axisymmetry or other 2D symmetry that can be used to save computational resources. The use of symmetry should be carefully applied however, as fluid flows may not behave symmetrically. Checking a single model that does not use symmetry against an otherwise identical symmetric model is one way to verify the use of symmetry boundary conditions.

When modeling experiments in heat transfer, oftentimes thermal insulation can be approximated as boundary conditions instead of modeling the entirety of the insulation. When modeling experiments in a laboratory setting, natural convection, adiabatic, or temperature boundary conditions may be appropriate.

Modeling turbulent flows is an ongoing and ever-evolving field of fluid mechanics research. Many techniques exist in industry and academia for performing these types of calculations. The behavior of turbulent flows is inherently time-dependent, though not

always on a scale accessible with experimental measurements. As there is no true steady-state condition, Reynolds-averaged Navier-Stokes (RANS) equations were developed to account for these oscillations [37]. The RANS forms of the continuity and balance of linear momentum in Cartesian tensor notation are as follows:

$$\frac{\partial \rho}{\partial t} + \frac{\partial}{\partial x_i}(\rho u_i) = 0 \tag{13}$$

$$\frac{\partial}{\partial t}(\rho u_i) + \frac{\partial}{\partial x_j}(\rho u_i u_j) = -\frac{\partial p}{\partial x_i} + \frac{\partial}{\partial x_j}\left[\mu\left(\frac{\partial u_i}{\partial x_j} + \frac{\partial u_j}{\partial x_i} - \frac{2}{3}\delta_{ij}\frac{\partial u_l}{\partial x_l}\right)\right] + \frac{\partial}{\partial x_j}\left(-\rho\overline{u_i' u_j'}\right) \tag{14}$$

The term $-\rho\overline{u_i' u_j'}$ is known as the Reynolds stress tensor. This is therefore a system of four equations with ten unknowns, which are the pressure, the three components of the velocity, and the six components of the Reynolds stress tensor. The challenge of determining six additional equations to completely specify the six unknown components of the Reynolds stress tensor is known as the "turbulence closure problem," and a wide variety of turbulence models, or "turbulence closures," have been developed over the last century to model the Reynolds stress tensor. To close these equations by providing expressions for the Reynolds stresses, turbulence models have been developed. There are many such examples of turbulence models, each developed with a particular purpose in mind. For the purposes of this thesis and to be consistent with previous research performed on gas-cooled divertors by groups at both Georgia Tech and KIT, only a select few turbulence models will be reviewed.

Each of the models discussed hereafter employs the Boussinesq hypothesis [38] which relates the Reynolds stresses to the velocity gradients by a parameter known as the turbulent (or eddy) viscosity, μ_t and the turbulence kinetic energy, *k*:

$$-\rho\overline{u_i' u_j'} = \mu_t\left(\frac{\partial u_i}{\partial x_j} + \frac{\partial u_j}{\partial x_i}\right) - \frac{2}{3}\left(\rho k + \mu_t \frac{\partial u_k}{\partial x_k}\right)\delta_{ij} \tag{15}$$

This introduces μ_t as a parameter that links turbulence (*k*) with momentum (*u*). The Boussinesq approach has the advantage that it allows for the calculation of μ_t at a relatively low computational cost. As will soon be discussed, only one or two additional equations are required. The disadvantage of the Bousinnesq approach is that it assumes that μ_t is an isotropic scalar quantity. This is a good approximation for many flows. The alternative is to use Reynolds Stress Models (RSM) which can handle anisotropy in μ_t. However, these models introduce five additional equations in 2-D flow and seven additional equations in 3-D flow. The increase in computational resources required to use these models may not be worth the benefit these models provide.

Commonly used turbulence models for industrial flows are the semi-empirical, two-equation *k-ε* models. Many variants have been derived including: the standard model (SKE) [39], the re-normalized group (RNG) model [40], and the realizable model (RKE) [41]. These models solve two equations for turbulence (beyond those for temperature/energy, mass, and momentum) and describe the flow away from the wall. The two extra equations are for the turbulence kinetic energy, *k*, and the turbulence dissipation rate, *ε*. For the SKE model, the governing equations for *k* and *ε* are:

$$\frac{\partial}{\partial \mathrm{t}}(\rho k) + \frac{\partial}{\partial x_i}(\rho k u_i) = \frac{\partial}{\partial x_j}\left[\left(\mu + \frac{\mu_t}{\sigma_k}\right)\frac{\partial k}{\partial x_j}\right] + G_k + G_b - \rho\varepsilon - Y_M \quad (16)$$

$$\frac{\partial}{\partial \mathrm{t}}(\rho \varepsilon) + \frac{\partial}{\partial x_i}(\rho \varepsilon u_i) = \frac{\partial}{\partial x_j}\left[\left(\mu + \frac{\mu_t}{\sigma_\varepsilon}\right)\frac{\partial \varepsilon}{\partial x_j}\right] + C_{1\varepsilon}\frac{\varepsilon}{k}(G_k + C_{3\varepsilon}G_b) - C_{2\varepsilon}\rho\frac{\varepsilon^2}{k} \quad (17)$$

where σ_k, σ_ε, $C_{1\varepsilon}$, and $C_{2\varepsilon}$ are model constants, $C_{3\varepsilon}$ is calculated from the orientation of the flow in relation to the gravity field and ranges from 0 to 1, G_k represents the production of *k* due to velocity gradients, G_b represents the production of *k* due to buoyancy, and Y_M represents the dissipation of *k* due to compressibility effects.

To link the turbulence equations back to the momentum equation the turbulent viscosity is a function of both *k* and *ε*:

$$\mu_t = \rho C_\mu \frac{k^2}{\varepsilon} \tag{18}$$

where C_μ is a model constant. The *k*-*ε* models thus require a total of five model constants.

Although the three models have similar formulations for *k*, they differ in their equations for *ε*. The RNG model has additional terms in the *ε* equation that account for swirling and rapidly strained flows. The RKE model contains mathematical limits on the calculation of the Reynolds stresses which prevent the calculation of negative Reynolds stresses (thus the 'realizable' description) when the flow is highly strained as well as a modification to the *ε* equation that removes a singularity if *k* goes to 0.

Each of the governing equations must be adapted to account for near-wall effects as they were derived to be applicable away from the wall and are not necessarily valid in the near-wall region. The governing equations for the *k*-*ε* model are only valid in fully turbulent regions and not suitable near the wall where the flow may be laminar. Often, turbulence models are adapted for wall-bounded flows using wall functions. The options available to the user in ANSYS® FLUENT® for *k*-*ε* models are standard wall functions (SWF) [42], non-equilibrium wall functions (NEWF) [43], and enhanced wall treatment (EWT). The two wall function approaches (SWF and NEWF) are necessary when the model is not resolved with a high enough resolution to capture effects near the wall. If the mesh is appropriately refined, the flow near the wall can be resolved using EWT.

The EWT of ANSYS® FLUENT® combines the strategies of several researchers [44] [45] [46] [47] [48] [49] and allows for flexibility in modeling by adapting the governing equations of *k*-*ε* to extend to the wall. As near-wall behavior is necessarily related to the

Re of the flow, by using EWT a researcher may use the same model over a wide range of *Re* without having to give thought as to which near-wall modeling approach would be most suitable and without changing the generated mesh.

Another turbulence model was developed by Spalart and Allmaras (S-A) [50]. It differs from the *k-ε* models in that it is a one-equation model for the turbulent kinematic viscosity, $\tilde{\nu}$. The original S-A model did not use or recommend wall functions, thus requiring fine resolution down to the wall. However, it has been extended by ANSYS to use an approach similar to EWT. The expression for μ_t for the S-A model is:

$$\mu_t = \rho\tilde{\nu}f_{\nu 1} \tag{19}$$

where $f_{\nu 1}$ is a viscous damping function given by:

$$f_{\nu 1} = \frac{\chi^3}{\chi^3 + C_{\nu 1}^3} \tag{20}$$

where $C_{\nu 1}$ is a model constant equal to 7.1 and χ is ratio between the turbulent kinematic viscosity and the molecular kinematic viscosity, ν:

$$\chi = \frac{\tilde{\nu}}{\nu} \tag{21}$$

Other turbulence models such as the *k-ω* and Reynolds stress models (RSM) as well as other variants of the *k-ε* model are also available to users of ANSYS FLUENT. However, as these were not used significantly in this thesis, their details will not be discussed. In the instances when the *k-ω* model and the *k-ε* model of Abe, Kondoh, and Nagano [51] [52] were used to model divertors for this thesis, the results were not significantly different enough from the results obtained using either the S-A or *k-ε* models to warrant additional inspection.

Heat transfer is an important part of this thesis and the details of the modeling of heat transfer in FLUENT should be discussed. The modeled energy equation in a stationary solid region used by FLUENT is:

$$\frac{\partial}{\partial t}(\rho h) = \nabla \cdot (k \nabla T) + S_h \tag{22}$$

where ρ is the density of the solid, h is the enthalpy, k is the thermal conductivity, T is the temperature, and S_h is a volumetric heat source. The enthalpy is defined as the integral of the constant pressure specific heat from a reference temperature of 298.15 K to the temperature T. The equation for the total energy E in a turbulent fluid region is defined as:

$$\frac{\partial}{\partial t}(\rho E) + \frac{\partial}{\partial x_i}[u_i(\rho E + p)] = \frac{\partial}{\partial x_j}\left(k_{eff}\frac{\partial T}{\partial x_j} + u_i\left(\tau_{ij}\right)_{eff}\right) + S_h \tag{23}$$

where ρ is the density of the fluid, h is the enthalpy defined as the integral of the constant pressure specific heat from a reference temperature of 298.15 K to the temperature T, k_{eff} is the effective thermal conductivity (which depends on the turbulence model), T is the temperature, and S_h is a volumetric heat generation source term. The term $u_i\left(\tau_{ij}\right)_{eff}$ represents the viscous heating where $\left(\tau_{ij}\right)_{eff}$ is the deviatoric stress tensor. All simulations performed as part of this thesis include this term which can be significant in compressible flows. The term $\left(\tau_{ij}\right)_{eff}$ is defined as:

$$\left(\tau_{ij}\right)_{eff} = \mu_{eff}\left(\frac{\partial u_j}{\partial x_i} + \frac{\partial u_i}{\partial x_j}\right) - \frac{2}{3}\mu_{eff}\frac{\partial u_k}{\partial x_k}\delta_{ij} \tag{24}$$

The value of k_{eff} is determined by the particular turbulence model used. For the SKE, RKE, and S-A models, it has the form:

$$k_{eff} = k + \frac{c_p \mu_t}{Pr_t} \tag{25}$$

where k is the thermal conductivity, and Pr_t is the turbulent Prandtl number which is set to a constant default value of 0.85. For the RNG model, k_{eff} is defined as:

$$k_{eff} = a c_p \mu_{eff} \tag{26}$$

where a is calculated from:

$$\left|\frac{a-1.3929}{a_0-1.3929}\right|^{0.6321} \left|\frac{a+2.3929}{a_0+2.3929}\right|^{0.3679} = \frac{\mu}{\mu_{eff}} \tag{27}$$

where

$$a_0 = \frac{1}{Pr} = \frac{k}{\mu c_p} \tag{28}$$

The effective viscosity is the sum of the laminar and turbulent viscosities. At high-Reynolds numbers, it can be approximated as μ_t. Near the wall, however, where laminar conditions may exist, there can be a significant difference in μ_{eff} and μ. Accounting for this effect in the calculation of k_{eff} is one of the advantages of the RNG model.

The equation of state for the modeling of gases can impact the solution in some instances. ANSYS FLUENT has available several options including both the ideal gas law and 'real' gas equations of state such as Redlich-Kwong [53]. For most conditions, the ideal gas law is an appropriate approximation and was used in all instances for this thesis.

The discretization scheme and method for calculating derivatives and gradients of a particular transport variable has an impact on the accuracy of the solution. In ANSYS FLUENT there are several options available for determining gradients. The method used for this thesis is referred to as the Least Squares Cell-Based method. This method uses information from each of the cell's neighbors to form a gradient calculated from a weighted vector sum of the differences between the values of a particular variable at each cell center and each of its neighboring cell centers. This method is considered to be both the most accurate and computationally efficient of the methods available in ANSYS FLUENT for calculating the gradient of unstructured grids.

As ANSYS FLUENT uses a finite volume approach, grids are constructed with cells with corresponding faces attached to each cell. For example in a 3-D grid, each tetrahedral cell has information associated at both its cell center and on each of its four faces. Values at the vertices or nodes of the cells can also be interpolated. Convective terms must be calculated at cell faces. To calculate these values several schemes are available each with advantages and disadvantages. The simulations performed for this thesis used the second-order upwind scheme [54]. Quantities on cell faces are calculated using the cell-centered value and gradient of the corresponding upstream cell.

Pressure-velocity coupling is achieved using the SIMPLE algorithm [55]. Other pressure-velocity coupling methods such as SIMPLEC [56] are available in ANSYS FLUENT, but were not investigated as they are unlikely to speed convergence for simulations of compressible, turbulent flows.

Solution initialization can have an impact on how quickly the solution converges. ANSYS FLUENT utilizes a hybrid initialization scheme. The hybrid initialization scheme differs from a traditional initialization scheme (where all velocities are set to a constant value) in that a prediction of the expected fluid flow direction is quickly calculated and used to initialize the velocities. This is beneficial for flow geometries where specifying a

constant, unidirectional velocity in all cells would lead to velocity vectors initially pointing in the wrong direction relative to the boundaries. Near-wall velocity is set to zero. Pressure information specified at the boundaries is used to make a smooth transition in the pressure form the inlet to the outlet in a similar fashion as the velocity initialization. Turbulence parameters and temperature are initialized to constant values in the entire domain.

All simulations performed as part of this thesis assume a steady-state condition. Though no time-dependence was assumed, the solution still requires many iterations to converge. A convergence criterion is required for each transport variable which describes the change in the calculated value of a particular quantity from one iteration to the next. Convergence criteria for continuity, velocity, and turbulence parameters were set to 10^{-5}. The convergence criterion for energy was set to 10^{-10}. The rate of convergence varies depending upon several factors including the *Re* of a simulation, the turbulence model, and the discretization scheme. For some cases, the convergence criteria were not reached. In these cases, the solution was monitored to ensure that relevant solution quantities such as the cooled surface temperature or the inlet pressure were not changing.

2.11. Literature Review Summary

Many gas-cooled divertors have been proposed. A thorough review of leading He-cooled, W-alloy divertors was performed by Tillack, et al [12]. The finger-type designs show much promise as they have large HTCs and thus are capable of effectively removing the heat flux incident on the divertor tiles. Also, their relatively small size makes them less susceptible to thermal stress issues than larger divertor cooling designs. As many thousands of these modules will be needed to cover the divertor area, the analysis of these designs needs to be thorough. Two finger designs, the HEMJ and

HEMS, have been tested at near prototypical conditions and the HEMJ has been tested as conditions dynamically similar to prototypical in the laboratory as well.

Alternatively, plate-type designs use far fewer modules and thus would require less complication in manufacturing and construction. However, this simplification comes at the expense of thermal performance. The T-Tube design is an “intermediate” size option between the HCFP and the finger designs. The HCFP and T-Tube have been tested at conditions dynamically similar to prototypical conditions in a laboratory setting as well as undergone several series of CFD and FEM investigations. As such, a hybrid design has been proposed that uses the best of both the plate- and finger-type designs in order to efficiently and effectively cool the divertor tiles. In order to verify the operating capability of this design, both types of divertors need to be studied.

Experimental investigation and numerical validation of divertor performance is critical to producing divertor cooling designs that are robust and reliable, and behave predictably. Using methods presented in this thesis will result in a path forward for divertor research that is both practical and effective.

CHAPTER 3: EXPERIMENTAL PROCEDURES AND RESULTS

This chapter details the experimental procedure used in this investigation, along with the results, for divertor test modules that closely resemble the HEMP and HEMJ designs presented in Chapter 2.

3.1. HEMP-Like Divertors

3.1.1. HEMP-Like Experimental Apparatus

Experiments were performed on a test module that closely resembles the HEMP divertor presented in Section 2.5. Several hundred experiments were completed over the course of this study resulting in a significant amount of experimental data. A listing of all relevant experiments for this Chapter can be found in Appendix A. Details on instrument calibrations can be found in Appendix D.

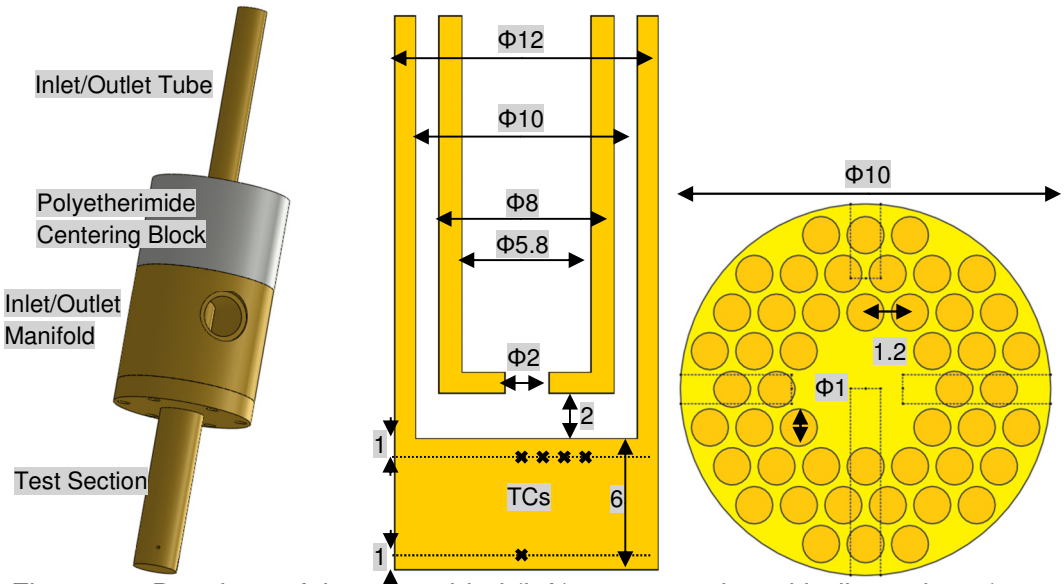

Figure 30. Drawings of the assembled (left), cross section with dimensions (center) and fin array (right) of the HEMP experiment with TC position and size indicated by dashed lines. Dimensions in mm.

Though the test module used in this experiment most closely resembles the HEMP design, it is smaller in diameter (12 mm vs. 14 mm) and the fin array is not as intricate. As shown in Figure 30 and Figure 31, two HEMP-like test sections were designed, constructed, and instrumented, one each with and without fins (also called 'bare'). Both test sections were machined from C36000 brass and instrumented with OMEGA Type E thermocouples (TCs) in the heated end of the finger. The pin-fins of the finned test section were created using electric discharge machining. The HEMP experiment can be configured in four unique ways by pairing one of two flow paths, 'forward' and 'reverse' flow, with one of the two test sections. The cases are abbreviated as bare forward (BF), bare reverse (BR), fins forward (FF) and fins reverse (FR). Nomenclature of relevant experimental parameters follows the direction of the flow, i.e. inlet pressure for forward flow is measured at the same physical location as outlet pressure for reverse flow. Material properties assumed for this study can be found in Appendix E.

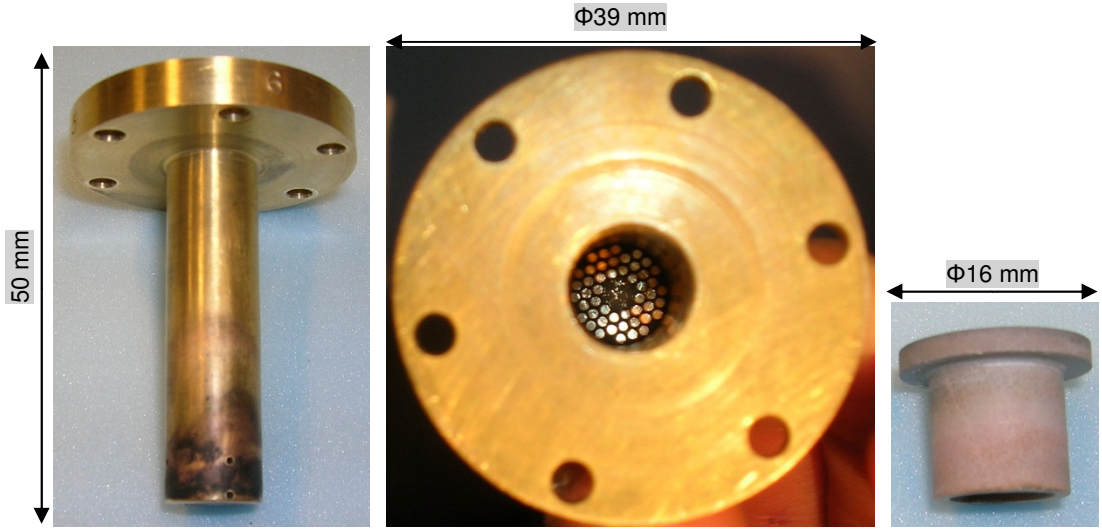

Figure 31. Pictures of outside of test section (left) and inside of finned test section (center) and ceramic sleeve (right).

As shown in Figure 30 and Figure 32, the test section was attached to an inlet/outlet manifold and a polyetherimide block used for centering of the inlet/outlet tube. The tube was positioned in all cases such that the central port was 2 mm from the cooled surface. To maintain this position, the tube was compressed onto the tops of the fins and locked in place with a collar. By leaving this collar on the tube at all times, the cooled surface of bare test section would always be placed 2 mm from the central port. Heat is applied to the test section using an oxy-acetylene torch. The finger is insulated by Marinite blocks and protected from the torch by a ceramic sleeve (Figure 31). The rest of the experiment is insulated with pipe foam and Rockwool (Figure 33).

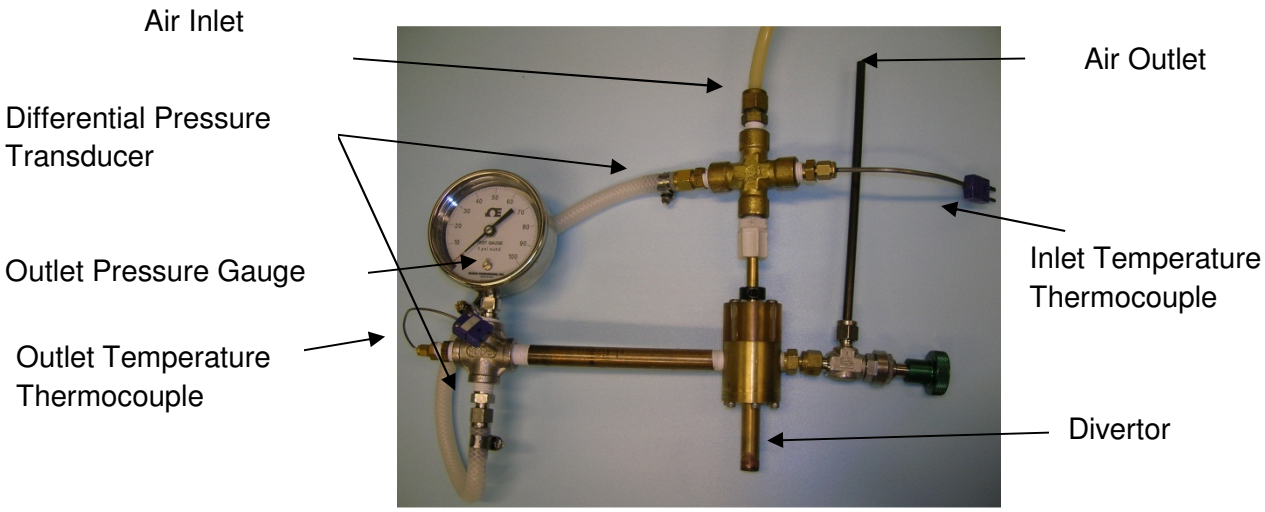

Figure 32. Picture of experiment in forward flow configuration removed from insulation.

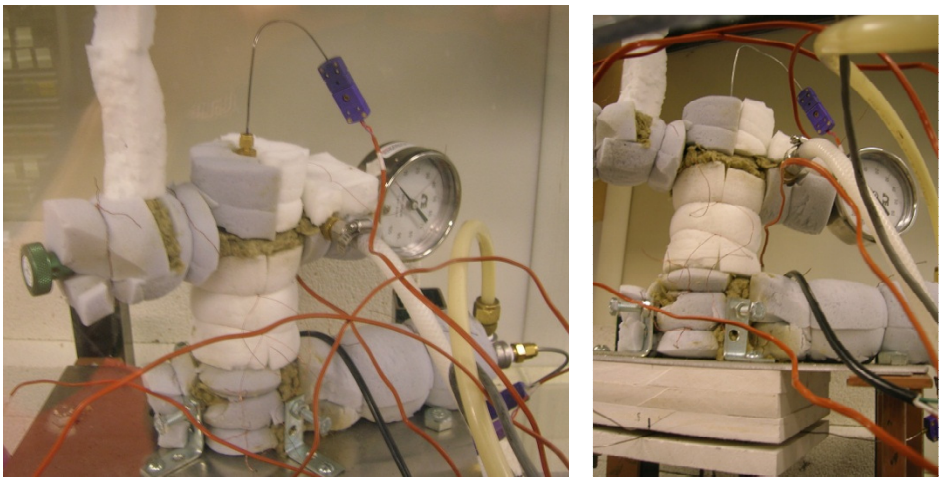
Figure 33. Pictures of insulated experiment in reverse flow configuration.

House air with gage pressure up to 0.7 MPa is used as the coolant. The volumetric flow rate, $\dot{V}$, into the test section is measured using a calibrated variable area flow meter (Brooks 1110). After flowing through the flow meter and the test section, the hot air is discharged into a fume hood. Air flow into the test section was controlled either by a pressure regulator on the wall or a plug valve on the outlet of the test section. OMEGA Type E TCs in the flow line measure the temperature of the air at the inlet, T_{in}, and the outlet, T_{out}, of the test section. Pressure transducers attached to the flow line provide measurements at the inlet (OMEGA PX302-300AV) of the test section, p_{in}, and the outlet of the flow meter (Keyence AP-15SK), p_{rot}. A differential pressure transducer (OMEGA PX26-100DV) is attached to both the inlet and the outlet of the test section flow lines and provides a direct measurement of the pressure drop, Δp. The outlet pressure is calculated as the difference $p_{out} = p_{in} - \Delta p$. Since the cases are often performed at different p_{in}, the adjusted pressure drop $\Delta p'$ is used to compare the cases across the entire range of tested mass flow rates and operating pressures:

$$\Delta p' = \frac{\Delta p}{p_{nom}} \frac{p_{in}+p_{out}}{2} \tag{29}$$

where p_{nom} is an arbitrary common pressure equal to 500 kPa.

The mass flow rate of air, $\dot{m}$, is found using the density, ρ_{rot}, calculated from the absolute pressure in Pa, p_{rot}, and temperature in K measured at the outlet of the flow meter and the calibration density, ρ_{cal}:

$$\rho_{rot} = \frac{p_{rot}}{R_{air}T_{in}} \tag{30}$$

where R_{air} is the ideal gas constant for air, 287 J/(kg-K). The mass flow rate, $\dot{m}$, is given by

$$\dot{m} = \dot{V}\sqrt{\rho_{cal}\rho_{rot}} \tag{31}$$

where the calibration density is that of dry air at 101.325 kPa and 21.11 ℃, 1.198 kg/m^3. Mass flow rates for the experiments ranged from 0.2-4.8 g/s.

The test sections were heated with an oxy-acetylene torch (Smith Equipment "The Little Torch") as shown in Figure 34. The heat flux into the test section, $\overline{q''}$, is calculated using an overall energy balance on the coolant:

$$\overline{q''} = \frac{\dot{m}\overline{c_P}\Delta T}{A_h} \tag{32}$$

Here $\dot{m}$ is the mass flow rate, $\Delta T = T_{out} - T_{in}$ is the change in air temperature, where $\overline{c_P}$ is the temperature dependent specific heat of air based on the average of T_{in} and T_{out} and A_h is the area of the heated surface, 113.1 mm^2.

Figure 34. Test section being heated by torch. Ceramic sleeve is glowing red hot.

Thermocouples in the test sections were arranged as shown in Figure 35. Each test section had four TCs placed one mm from the cooled surface at 90° intervals spaced 0, 1, 2, and 3 mm from the center. There was one TC one mm from the heated surface of each test section used to measure the maximum brass temperature, T_h. Experiments were performed such that the maximum brass temperature remained below 400 ℃. The readings of the TCs nearest the cooled surface were extrapolated Δz (1 mm) through the brass using $\overline{q''}$:

$$\overline{q''} = \frac{\int_{T_i'}^{T_i} k(T)dT}{\Delta z} \tag{33}$$

where T_i is the reading of the TC, T_i' is the extrapolated TC reading, and $k(T)$ is the temperature dependent thermal conductivity of the brass, approximated by the power law:

$$k(T) = 11.611 \times T^{0.4006} \tag{34}$$

where T is in Kelvin, and k is in W/m-K. The correlation is derived from tabular data provided in Incropera and Dewitt [4] and should not be used outside the range 100-600 K. See Appendix E for more details on assumed material properties.

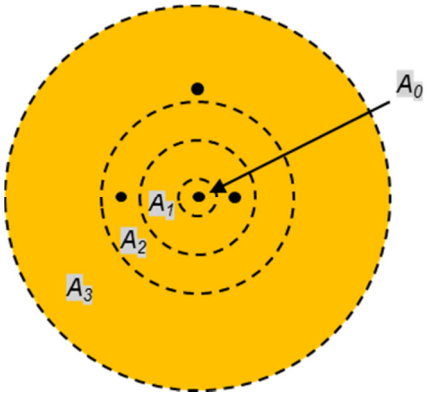

Figure 35. Arrangement of TCs near the cooled surface. Weighting areas indicated.

The extrapolated TC readings are area averaged over the cooled surface assuming axisymmetry to calculate the average cooled surface temperature $\overline{T_c}$:

$$\overline{T_c} = \frac{\sum_i T_i A_i}{\sum_i A_i} = 0.01T_0 + 0.08T_1 + 0.16T_2 + 0.75T_3 \tag{35}$$

where index i indicates the radial position of the TC. The weights are based on the concentric circular and annular areas calculated based on the midpoint radii between the TCs. That is, the weight on T_0 is based on the area of circle with radius 0.5 mm. The weight of T_1 is based on the annular area with inner radius 0.5 mm and outer radius 1.5 mm. The weight for T_3 is based on the area from 2.5 mm to 5 mm (Figure 35).

An area averaged heat transfer coefficient (HTC) over the cooled surface, $\overline{h}$, is calculated assuming that all of the heat incident on the divertor is absorbed into the air through the cooled surface with a cooled area, A_c = 78.5 mm^2:

$$\overline{h} = \frac{\overline{q''}}{\overline{T_c} - T_{in}} \frac{A_h}{A_c} \tag{36}$$

For the finned cases, $\overline{h}$ is an effective HTC in that the actual HTC is lower as the heat is removed over the entire area of the fin surface. An effective HTC is the HTC that would exist if the fins were not present and the cooled surface temperature was the same. The net effect on the fin effectiveness and efficiency which will be discussed a later section.

Data for each experiment was collected using an Agilent 34970A Data Acquisition unit connected to a computer running BenchLink Data Logger 3. Data was captured at 1 sec intervals. Each experiment reached steady state conditions defined as TC readings of the air remaining within ±1 ℃ and no heating or cooling trends over a three minute period. The TCs embedded in the test section showed small oscillations due to the slightly unsteady flame provided by torch. Thus the experimental data was collected over a period of at least three minutes and time averaged after “steady-state” conditions were reached. The experimental uncertainties in measured and calculated quantities were calculated using standard methods as detailed in Appendix C.

3.1.2. HEMP-like Experimental Procedure

In order to operate the experiment most efficiently, experiments were typically performed in sets. That is, steady-state operating points would be reached sequentially by changing the flow rate and allowing the experiment to reach a new steady-state condition. For example, several experiments performed with a similar heat flux could be performed in this manner by leaving the torch turned on and directed at the test section and either changing the air supply pressure or the position of the outlet valve. An example procedure follows for performing the variable inlet pressure experiments with a constant heat flux.

1. Initiate airflow by opening valves on the house air supply line and the test section. Typically, a pressure of 60 psig (~414 kPa) was chosen. Care should be taken to avoid fluid hammer (open all valves slowly and turn up pressure from the house air pressure regulator slowly). At this time a check of instrument readings (specifically the pressure sensors) using the data acquisition system should be performed.
2. Start the torch directed away from the test section. Adjust the flow rates of O_2 and C_2H_2 to get a bright, blue-white flame. Ensure that pressure in flow lines of combustion gases corresponds to the manufacturer's recommended values.
3. Move the torch in position and direct it on the test section. Care should now be taken to ensure that the torch is centered on the test section tip and not directed onto the ceramic sleeve.
4. Adjust the flow rates of O_2 and C_2H_2 to achieve desired heat flux. Depending on the size of the flame, the distance from the torch to the test section tip may need to be adjusted to prevent the torch from blowing itself out.
5. Adjust the air supply pressure to achieve desired air flow rate. Typically, sets of experiments were performed starting at the highest flow rate and decreasing down to the lowest flow rate. Check $\dot{m}$, Re_j and $\overline{q''}$ manually.
6. Allow experiment to reach steady-state. This may take several minutes depending on the flow rate. Typically, lower flow rate experiments take longer to reach steady-state. Ensure that temperature limits are not reached. Pressure sensors and plastic tubing should be kept below 120 ℃ (check T_{out}). The C36000 finger should be kept below 400 ℃ (check T_h).

7. When steady-state is reached, record timestamps and scan numbers given by data acquisition system over which the steady-state period will be time-averaged.
8. Repeat steps 5-7 to reach and record a new operating point.
9. When the experiments have been completed, cut off the C_2H_2 then the O_2. Then move the torch away from the test section and allow the test section and insulating blocks about an hour to cool by leaving on the air flow through the test section.

The constant inlet pressure experiments were performed similarly except that the house air supply regulator pressure was fixed at 700 kPa (100 psig) and the coolant flow rate was controlled by changing the position of the test section outlet valve. Safety precautions were taken when adjusting the outlet valve as the outlet valve would get hot during cases with large coolant ΔT. Two people were required to run these experiments as both a matter of safety and out of necessity in order to monitor the various components required to successfully complete a set of experiments.

3.1.3. HEMP-Like Experimental Results

The effective HTC for all four experimental configurations are shown in Figure 36. The FF and BF cases show similar results while BF outperforms BR. Comparing just the bare cases, BF shows a higher $\overline{h}$ on account of the impinging jet and BR has no heat transfer enhancement from either fins or a jet.

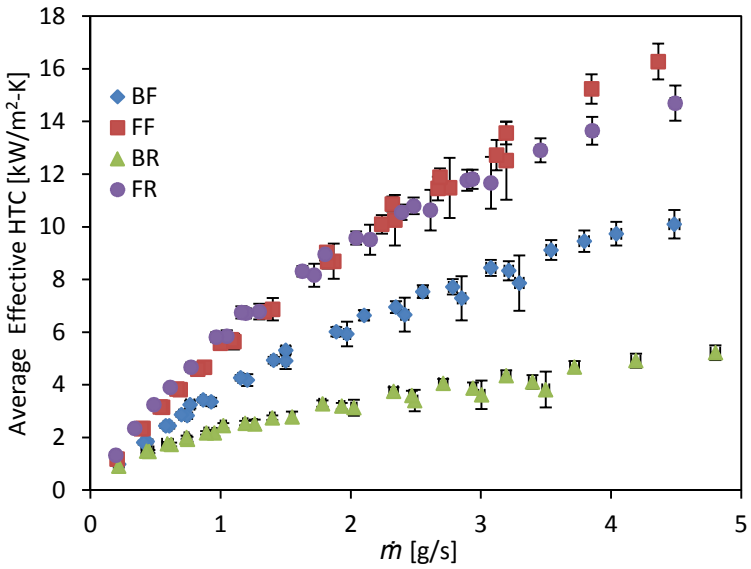

Figure 36. Average cooled surface HTC vs. mass flow rate.

Though $\overline{h}$ for the fins cases with forward and reverse flow is similar, $\Delta p'$ for FF is lower than FR (Figure 37) even though FF includes the pressure drop of both the fins and the impinging jet. For the FR case, the air is at a higher temperature and thus has a higher viscosity when flowing through the orifice leading to an increase in $\Delta p'$. The pressure drop and HTC need to be converted to non-dimensional parameters so that the experimental results can be translated to prototypical conditions.

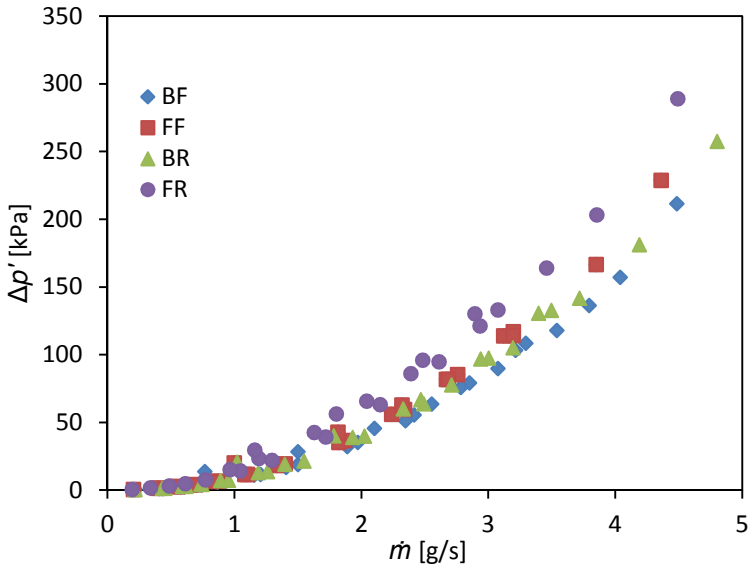

Figure 37. Normalized pressure drop vs. mass flow rate.

The $\dot{m}$ for each experiment was converted into non-dimensional mass flow rate, or Reynolds number, based on the diameter of the jet or exit orifice, Re_j:

$$Re_j = \frac{4\dot{m}}{\pi \mu_j D_j} \tag{37}$$

where D_j is the 2 mm diameter of the jet (or exit orifice) and μ_j is the dynamic viscosity of the air at the jet based on T_{in} for forward flow and T_{out} for reverse flow.

The Δp for each experiment was converted into a non-dimensional pressure loss coefficient, K_L. As it is assumed that majority of the pressure drop occurs at the inlet/outlet orifice, the density, ρ_L, and velocity, V_L, used for the calculation of K_L were evaluated at the exit of the jet (i.e. p_{out} and T_{in} for forward flow and T_{out} and p_{out} for reverse flow):

$$K_L = \frac{\Delta p}{\frac{1}{2}\rho_L V_L^2} \tag{38}$$

The definition here of K_L is based on the difference in static pressure as measured by the differential pressure transducer. The loss coefficient for compressible flows should be determined using the difference in the total pressure [57] which is the sum of the static pressure and the dynamic pressure. As the differential pressure measurements were taken as locations with relatively large diameters, the dynamic pressure at the pressure measurement locations was small. It was found that the difference in the calculated Δp based on total pressure was at most 1% different than the Δp calculated from the static pressure difference. As the difference in the total and static pressure difference was very small, this effect was assumed to be negligible.

This assumption will be investigated using the numerical models in Chapters 4 & 5. Figure 38 shows K_L for each of the four flow configurations. The trends are correlated to just Re_j as the loss coefficient is a purely hydraulic parameter assuming a power law plus a constant trend:

$$\begin{aligned}
&\text{BF} \quad K_L = 0.413\left(\frac{Re_j}{10^4}\right)^{-1.18} + 1.05 \quad R^2 = 0.95 \\
&\text{FF} \quad K_L = 0.652\left(\frac{Re_j}{10^4}\right)^{-1.07} + 1.18 \quad R^2 = 0.98 \\
&\text{BR} \quad K_L = 0.184\left(\frac{Re_j}{10^4}\right)^{-1.59} + 1.05 \quad R^2 = 0.91 \\
&\text{FR} \quad K_L = 0.716\left(\frac{Re_j}{10^4}\right)^{-0.99} + 1.26 \quad R^2 = 0.99
\end{aligned} \tag{39}$$

The quality of the fits is greatly impacted by the large experimental uncertainties encountered at low flow rates and thus the value of R^2 is not near unity for all configurations.

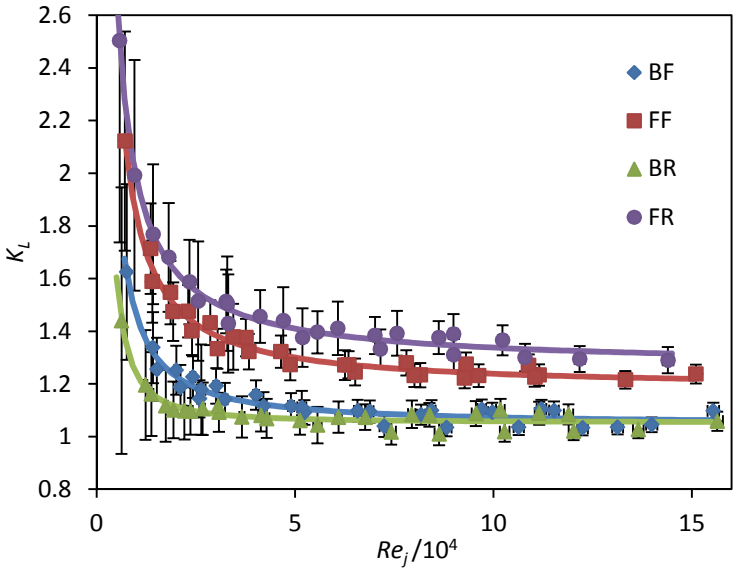

Figure 38. Pressure loss coefficient vs. jet Reynolds number.

The $\overline{h}$ is converted into a non-dimensional HTC or Nusselt number, $\overline{Nu}$. This is a simple process for BF and BR as $\overline{h}$ was calculated over the actual cooled surface.

$$\overline{Nu} = \frac{\overline{h} D_j}{\overline{k_g}} \tag{40}$$

To accomplish this for the finned surface cases (FF and FR), however, the effective HTC must be corrected to an actual HTC, $\overline{h_a}$, to account for the extra surface area and efficiency of the fins η. The following series of equations shows this process. First a guess is made of η allowing for the calculation of $\overline{h_a}$. This value of $\overline{h_a}$ is in turn used to calculate new values of α and η. This process repeats several times until

converged values are reached. Typically, three to four iterations were required to reach convergence of 10^{-5}.

$$\overline{Nu} = \frac{\overline{h_a} D_j}{\overline{k_g}} \tag{41}$$

$$\overline{h_a} = \frac{\overline{h} A_c}{A_p + \eta A_f} \tag{42}$$

$$\eta = \frac{\tanh(\alpha)}{\alpha} \tag{43}$$

$$\alpha = L_f \sqrt{\frac{4\overline{h_a}}{k_f D_f}} \tag{44}$$

where $\overline{k_g}$ is the average thermal conductivity of the air, A_p is the cooled surface area not covered by the fins 40.8 mm^2, A_f is the fin-coolant contact area 314 mm^2, and L_f, D_f, and k_f are the length, diameter, and thermal conductivity of the fins, respectively. As η depends on $\overline{h_a}$, the solution is iterative. The formula for η is based on an adiabatic fin tip assumption. As mentioned earlier, the center tube was compressed onto the tops of the fins, however, perfect contact on all fins could not be assured, so this conservative assumption was made. The fin tip condition will be discussed further in Chapter 5 regarding the numerical modeling of the FF and FR configurations. Also, the implications of fin tip boundary condition on prototypical performance will be addressed in Chapter 5.

As described in Chapter 2, the fin efficiency is the ratio between the actual heat transfer rate through the base of the fin to the heat transfer rate that would be expected if the entire surface of the fin was at the same temperature as the base. The fin effectiveness is the ratio of the fin heat transfer rate to the heat transfer rate that would exist without the fin. [4]

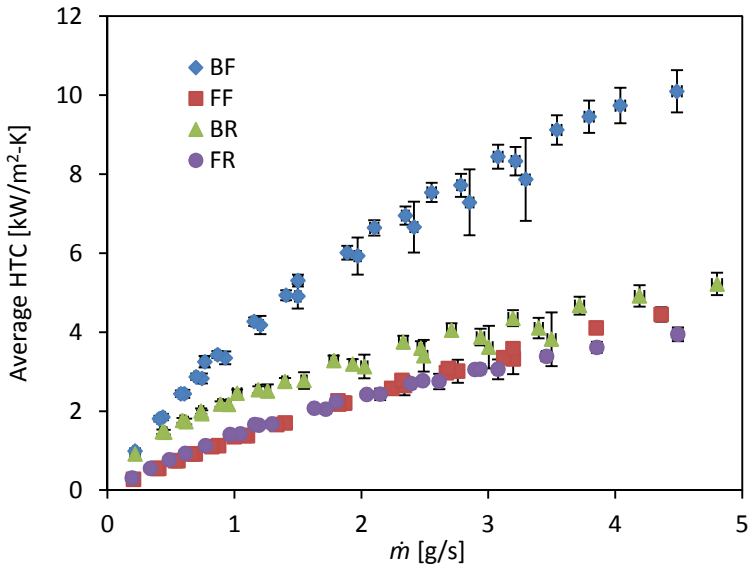

Figure 39. Actual HTC vs. mass flow rate.

The values of are $\overline{h_a}$ are presented against $\dot{m}$ in Figure 39. As $\overline{h}$ increases with $\dot{m}$, it is expected that η decreases with $\dot{m}$. This trend is presented in Figure 40. This result has significant implications for the effect of the fins at prototypical conditions as $\overline{h_a}$ for He-cooled cases is expected to be much higher, and hence, the fin efficiency should be much lower.

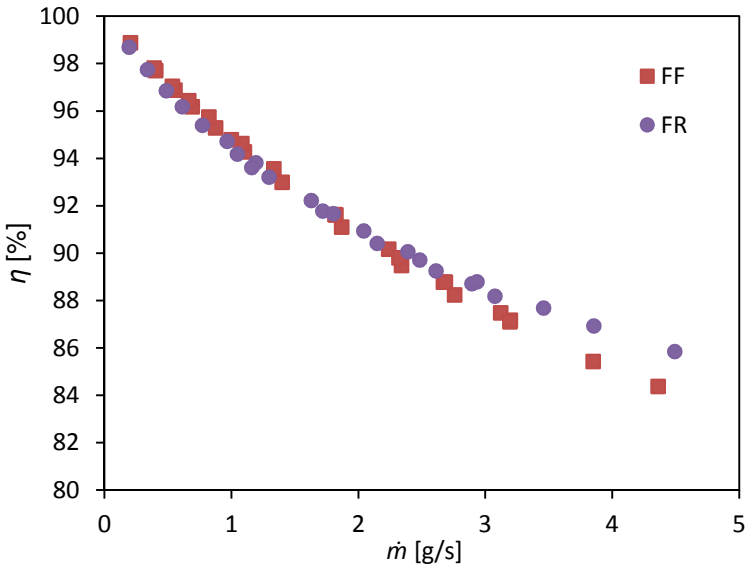

Figure 40. Fin efficiency for FF and FR configurations vs. mass flow rate.

The fin effectiveness was also calculated for FF and FR configurations. These trends are plotted against $\dot{m}$ in Figure 41. The fin effectiveness for a cylindrical fin with uniform cross sectional area and with an adiabatic fin tip is:

$$\varepsilon_f = \sqrt{\frac{4k_f}{\overline{h_a} D_f}} \tanh(\alpha) \tag{45}$$

where variables are defined as before. The observed trend in the effectiveness is as it would be expected, i.e. the effectiveness decreases as $\dot{m}$ (and thus $\overline{h_a}$) increases. At all flow rates, the fin effectiveness is greater than 2, which is the suggested minimum for incorporating fins [4].

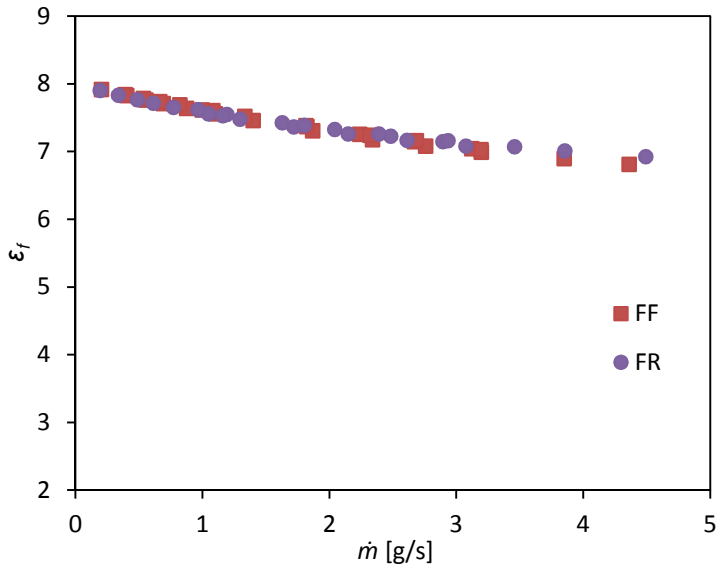

Figure 41. Fin effectiveness for FF and FR configurations vs. mass flow rate.

To check for effects of compressibility, the Mach number M based on the average velocity at the jet V_j was calculated for each case.

$$M = \frac{V_j}{\sqrt{\gamma R T_j}} \tag{46}$$

where V_j is calculated based on conditions at the exit of the jet (outlet pressure and inlet temperature for forward flow and outlet pressure and outlet temperature for reverse flow), γ = 1.4 is ratio of the specific heats for air, R = 287 J/kg-K is the gas constant of air, and T_j is the absolute temperature of the air at the outlet of jet (T_i for forward flow and T_o for reverse flow). A set of experiments was performed for each configuration at both variable inlet pressure and fixed inlet pressure (~700 kPa). As shown in Figure 42-Figure 45, there is significant variation in M for the low $\dot{m}$ cases. As these cases do not show appreciable changes in $\overline{h}$, the effect of M over the ranges studied is deemed inconsequential to the performance of the divertor.

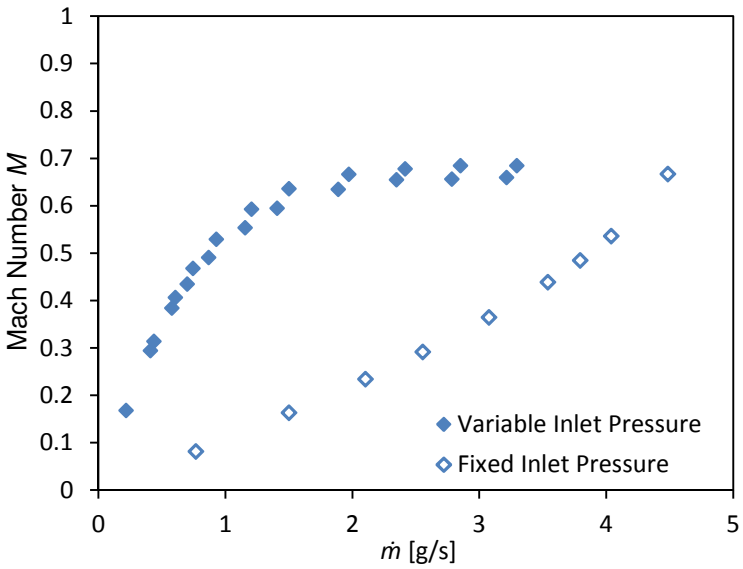

Figure 42. Mach number versus mass flow rate for BF.

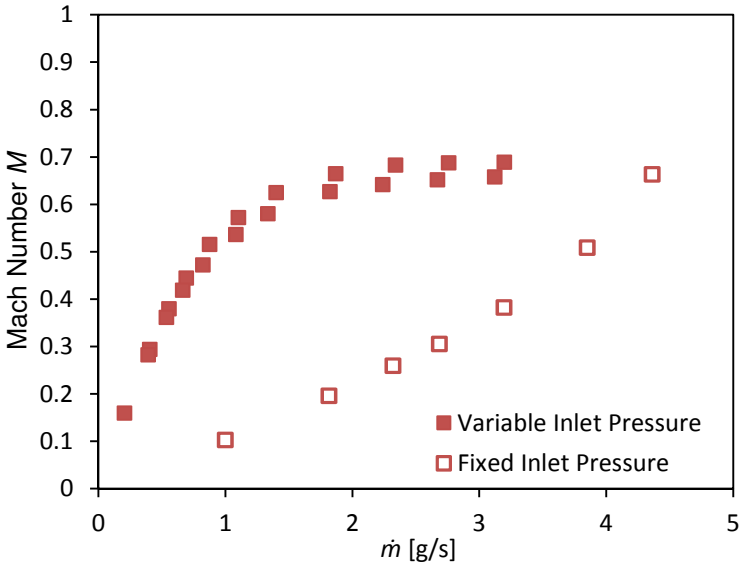

Figure 43. Mach number versus mass flow rate for FF.

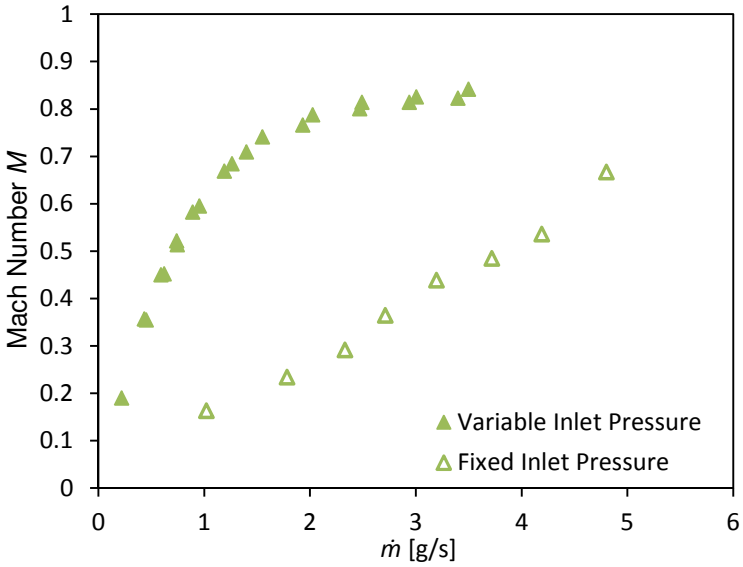

Figure 44. Mach number versus mass flow rate for BR.

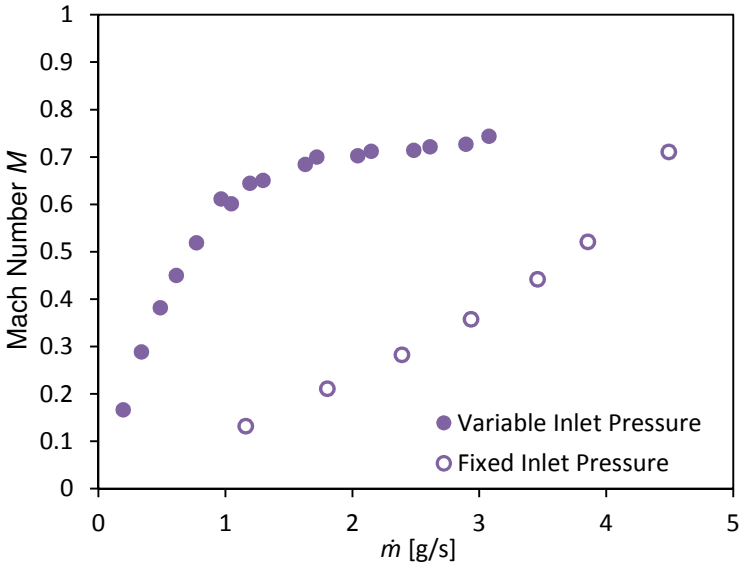

Figure 45. Mach number versus mass flow rate for FR.

3.2. HEMJ Divertors

3.2.1. Motivation for New HEMJ Experiments and Discussion of Previous HEMJ Experiments

A series of experiments was performed on test modules that closely resemble the HEMJ divertor described in Section 2.5. Namely, a series of experiments was performed to quantify the thermal performance of the HEMJ divertor using several different divertor structure and coolant combinations. The new experiments were performed at higher heat fluxes and were carried out to verify the dynamic similarity of the experiments.

The theses of Crosatti and Weathers detail previous experiments performed on the HEMJ at Georgia Tech. These experiments were performed on a brass test section that was heated electrically and cooled with air. Crosatti and Weathers performed a series of tests over a range of flow rates and heat fluxes. The mass flow rates tested ranged from 2.01-8.39 g/s corresponding to Re_j of 14,600-61,000. The prototypical Re_j for the HEMJ is 21,400. The basic assumption used in these experiments was that dynamic similarity can be achieved by only matching the Re_j. This assumption was found to be untrue as the Nusselt number was found to also depend on the ratio of the solid to the coolant thermal conductivities. To this end, additional experiments with other coolants and test section materials were performed in this study in order to fully characterize the thermal performance of the HEMJ divertor.

Their work focused on confirming the rotational symmetry of the test section and heat transfer coefficients as well as verifying their numerical models. Their experiments are thus divided into two campaigns. The first is a series of fifteen experiments performed at five different flow rates repeated three times. The first two runs were

performed with an electrical power input corresponding to a heat flux of 0.8 MW/m^2. The third run was performed using an electrical power input corresponding to a heat flux of 1.0 MW/m^2. These tests were performed to verify the repeatability and heat flux independence of the experiment. These are the experiments referenced in this thesis.

In the second campaign, the rotational symmetry of the HEMJ was confirmed by rotating the jet cartridge inside of the thimble while the experiment was operating. While these tests were useful for confirming the rotational symmetry of the HEMJ, they are not useful for the purposes of this thesis. Relevant experimental data from the first campaign was thus reprocessed to be consistent with the formulations and nomenclature presented hereafter.

3.2.2. HEMJ Experimental Apparatus

The HEMJ experiments were performed in a manner similar to the HEMP-like divertor experiments with the primary exception being the method of introducing coolants other than air (helium or argon) into the flow line using compressed gas cylinders. The HEMJ test section is made up of two primary components: the jet cartridge and the thimble. Coolant flows into the jet cartridge through a tube sealed with epoxy then into an array of round jets impinging on the curved inner surface of the thimble before exiting at elevated temperature through the outlet flange of the jet cartridge. House air is supplied up to 0.7 MPa. Helium or argon from gas canisters is supplied up to 1.4 MPa. Up to five gas canisters were connected to the flow line using a set of flexible rubber-in-steel hoses and two pressure regulators to step down the up to 18 MPa gas to 1.4 MPa suitable for use in the flow line.

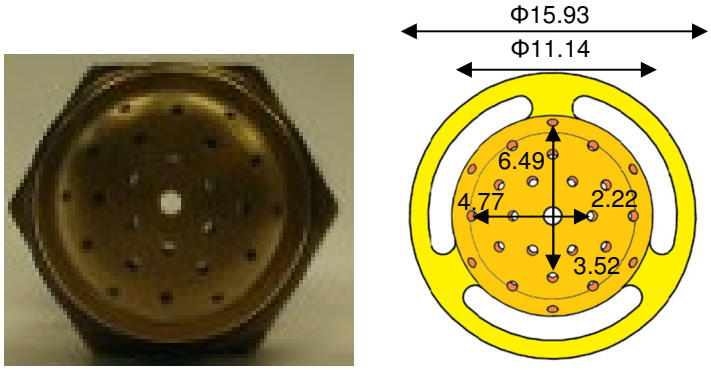

Figure 46. Picture (left) and drawing (right) of the HEMJ jet cartridge. Dimensions in mm.

The jet cartridge, shown in Figure 46 (left), was machined out of C36000 brass. Twenty-four 0.6 mm diameter round jets are arranged in four concentric rings around a central 1 mm OD jet [Figure 46 (right)]. The total area of the round jets A_j is 7.57 mm^2. The jet cartridge has a curved face (parallel to the cooled surface) and thus the jets point away from each other. The radii of the jets is based on their projection to the same plane as the central jet as shown in Figure 46 (right). A stainless steel tube was inserted into and glued to the bottom of the jet cartridge with the epoxy Devcon FasMetal 10. The epoxy is rated up to 121 ℃. The outer surface of the jet cartridge and the cooled surface of the thimble are kept at a constant 0.9 mm distance by contact made between the thimble and the outlet flange on the bottom of the jet cartridge. A drawing of the jet cartridge inserted into the thimble is shown in Figure 47 (center).

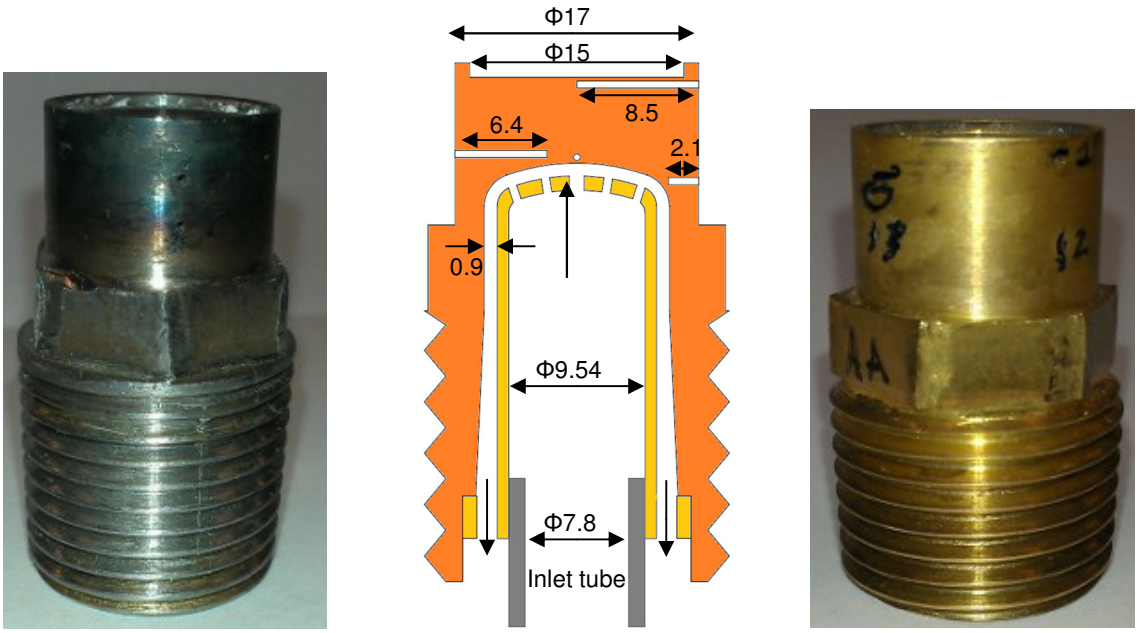

Figure 47. Drawing of the HEMJ thimble with inserted jet cartridge (center). Steel thimble (left), brass thimble (right). Dimensions in mm.

Two thimbles were machined - one out of C36000 brass [Figure 47 (right)] and the other from AISI 1010 carbon steel [Figure 47 (left)]. The thimbles have ½" NPT threads so they can attach to pipe fittings. The thimbles were attached to a ½" NPT tee and sealed with SWAK® sealant which is rated up to 176 °C. Six holes for 0.5 mm OMEGA Type E or Type K TCs were drilled into each of the thimbles. Their insertion depth and axial position relative to the top of the thimble are given in Table 1.

Table 1. Location of HEMJ TCs

TC	Depth [mm]	Distance from top of thimble [mm]
0	8.5	6.25
1	6.4	6.36
2	4.2	6.88
3	2.08	8.26
4	8.5	4.2
5	8.5	1.5

Three of the TCs are positioned on the center axis of the thimble. Of these, one is located 0.5 mm from the heated surface to measure the maximum temperature of the

thimble (for operational safety) denoted T_5. One of these is placed 0.5 mm from the cooled surface (T_0) and the other is placed directly in the center of these two (T_4). Their readings were used to provide an estimate of the uniformity of the heat flux coming from the oxy-acetylene torch. A uniform heat flux is expected if both the heat flux calculated between the TCs closest to the heated surface ($q''_{4,5}$) is equal to the heat flux calculated between the TCs closest to the cooled surface ($q''_{0,4}$):

$$q''_{a,b} = \frac{\int_{T_a}^{T_b} k(T)dT}{\Delta z} \tag{47}$$

where $k(T)$ is the thermal conductivity of the thimble and Δz is the distance between the TCs (2.375 mm). The conductivity of AISI 1010 carbon steel is approximated as:

$$k(T) = 77.467 - 0.046915 \cdot T \tag{48}$$

where T is in Kelvin, and k is in W/(m-K). The correlation is derived from tabular data provided in Incropera and Dewitt [4] and should not be used outside the range 300-1000 K. The same value used in Section 3.1 (Eq. 34) for the thermal conductivity of C36000 was assumed. See Appendix E for more details on material properties assumptions.

Including the TC on the center axis 0.5 mm from the cooled surface, four of the TCs are positioned 0.5 mm from the cooled surface and used to calculate HTCs and average cooled surface temperature, $\overline{T_c}$. The cooled surface has a cross sectional area A_{cs} of 131.5 mm^2 based on a diameter of 6.47 mm. Accounting for the curvature of the surface, its total area is A_c = 194.4 mm^2. The test sections were insulated with Marinite blocks. Powdered Marinite was placed around the test section in the area near the TC holes to accommodate the varying axial locations of the TCs. A graphite shield, that served a similar purpose to the ceramic sleeve of Section 3.1, was placed on the top of

the thimble to protect the heated surface TC and the Marinite from direct contact with the torch. A picture of the graphite shield is shown in Figure 48. A channel was ground out of the shield to go around the heated surface TC and can be seen in the photograph.

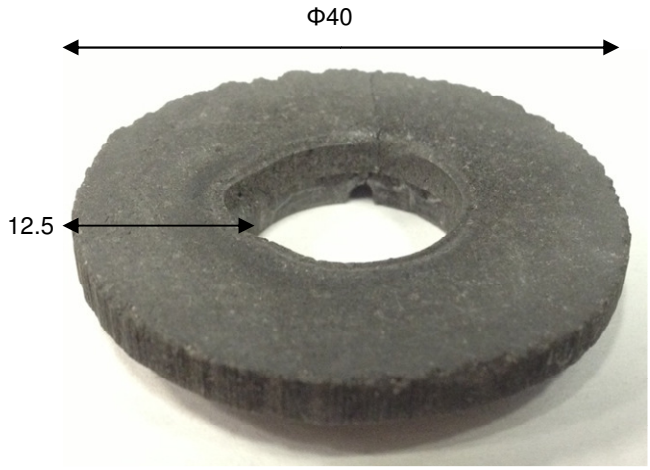

Figure 48. Graphite flame shield used in HEMJ experiments. Dimensions in mm.

Coolant volumetric flow rate $\dot{V}$ is measured using a calibrated Brooks variable area flow meter (Model 1110). The calibration was performed using a Lambda Square Venturi meter (serial #27872) as described in Appendix D. Temperature T_{rot} and pressure p_{rot} at the outlet of the flow meter were measured using an OMEGA Type E TC and OMEGA PX302-2KGV pressure transducer, respectively. The pressure at the inlet of the divertor p_{in} was measured using an OMEGA PX302-300AV pressure transducer and the pressure difference across the divertor Δp was measured directly using an OMEGA PX26 differential pressure transducer. The outlet pressure was calculated from the difference in p_{in} and Δp. For each gas, p_{in} was kept approximately constant and the mass flow rate, $\dot{m}$, was controlled using a valve on the outlet of the flow line. Details on instrument calibrations can be found in Appendix D.

The mass flow rate $\dot{m}$ was calculated using the calibration density of the flow meter, which is calculated from air at 101.325 kPa and 21.1 ℃, and the density of the coolant at the flow meter ρ_{rot}:

$$\rho_{rot} = \frac{p_{rot}M}{RT_{in}} \tag{49}$$

where M is the molar mass of the gas and R is the universal gas constant. The formulation for $\dot{m}$ assumes any change in the dynamic viscosity of the flowing gas to calibration gas is negligible:

$$\dot{m} = \dot{V}\sqrt{\rho_{cal}\rho_{rot}} \tag{50}$$

As before, TCs inserted into the flow line measure the inlet and outlet temperature of the coolant, T_{in} and T_{out}, respectively. Assuming that all of the heat into the thimble enters through the heated surface with area A_h = 227.0 mm^2, the average heat flux $\overline{q''}$ can be calculated using the change in temperature of the coolant, ΔT:

$$\overline{q''} = \frac{\dot{m}\overline{c_P}\Delta T}{A_h} \tag{51}$$

where $\overline{c_P}$ is the temperature dependent specific heat of gas based on the average of T_{in} and T_{out}. Using $\overline{q''}$, the readings of the TCs near the cooled surface can be extrapolated to the cooled surface (Δz = 0.5 mm) assuming one-dimensional conduction:

$$\overline{q''} = \frac{\int_{T_i'}^{T_i} k(T)dT}{\Delta z} \tag{52}$$

where T_i is the reading of the TC, T_i' is the extrapolated TC reading and $k(T)$ is the thermal conductivity of the thimble. The extrapolated temperature readings are area averaged over the cooled surface to arrive at $\overline{T_c}$. As the surface is curved, the calculation is approximated using a similar method as in Section 3.1 based on the weights on circular and annular areas with radii based on the midpoints between the radial locations of the TCs:

$$\overline{T_c} = \frac{\sum_i T_i A_i}{\sum_i A_i} = \frac{1.05^2}{6.47^2} T_0 + \frac{3.2^2 - 1.05^2}{6.47^2} T_1 + \frac{5.36^2 - 3.2^2}{6.47^2} T_2 + \frac{6.47^2 - 5.36^2}{6.47^2} T_3 \quad (53)$$

where the weights are based on radii of 1.05, 3.2, 5.36, and 6.47 mm.

The average cooled surface HTC $\overline{h}$ is calculated based on the assumption that all of the energy convected by the coolant is absorbed through the cooled surface:

$$\overline{h} = \frac{\overline{q''}}{\overline{T_c} - T_{in}} \frac{A_h}{A_{cs}} \quad (54)$$

Data for each experiment was captured at 1 sec intervals using an Agilent 34970A data acquisition system attached to a computer running BenchLink Data Logger 3. Experimental data was captured at steady state conditions defined as less than ±1 ℃ change in TC temperatures and no heating or cooling trends. Data was also time averaged over at least three minutes to account for oscillations in the readings of the TCs caused by the flame. The steady state condition was often difficult to reach for the Ar and He cooled experiments as the expansion of the gas from the canisters resulted in changing T_{rot} and T_{in}. To expedite the process, the Ar and He experiments would be pre-heated to the expected steady state conditions by adjusting the air flow rate and/or the flame strength. A three-way valve before the flow meter allowed for the near instantaneous switch from air to Ar or He. After the switch, the flame and flow rate could

then be finely adjusted to reach steady state conditions. Experimental uncertainty was calculated using standard methods as detailed in Appendix C.

3.2.3. HEMJ Experimental Procedure

The air-cooled experiments for the HEMJ were performed in a similar manner to those on the HEMP-like test section. The Ar- and He-cooled experiments required several modifications to the experimental procedure outlined in Section 3.1.2. The primary difference was the procedure used to switch from air to Ar or He quickly without interrupting the cooling of the heated thimble. The equipment and procedure used for those experiments will now be discussed.

A photograph of the assembly used to connect the gas cylinders is shown in Figure 49. As depicted, there are five rubber-in-steel hoses that connect to a series or crosses and then to a high pressure regulator. The high pressure regulator steps the pressure from the tanks (~2700 psi or 18 MPa) down to an acceptable level for use in the flow line (~200 psi or 1.4 MPa). The flow meter houses a glass tube and is connected to the test section with plastic tubing and should not be used with high pressure fluids. The three-way valve was installed such that either the Ar-He line or the air would be connected into the flow meter. In its current position shown in the figure it is in the “air” position. As there were always two people performing these experiments, one of the researchers could operate the torch and the other could operate the high pressure flow line.

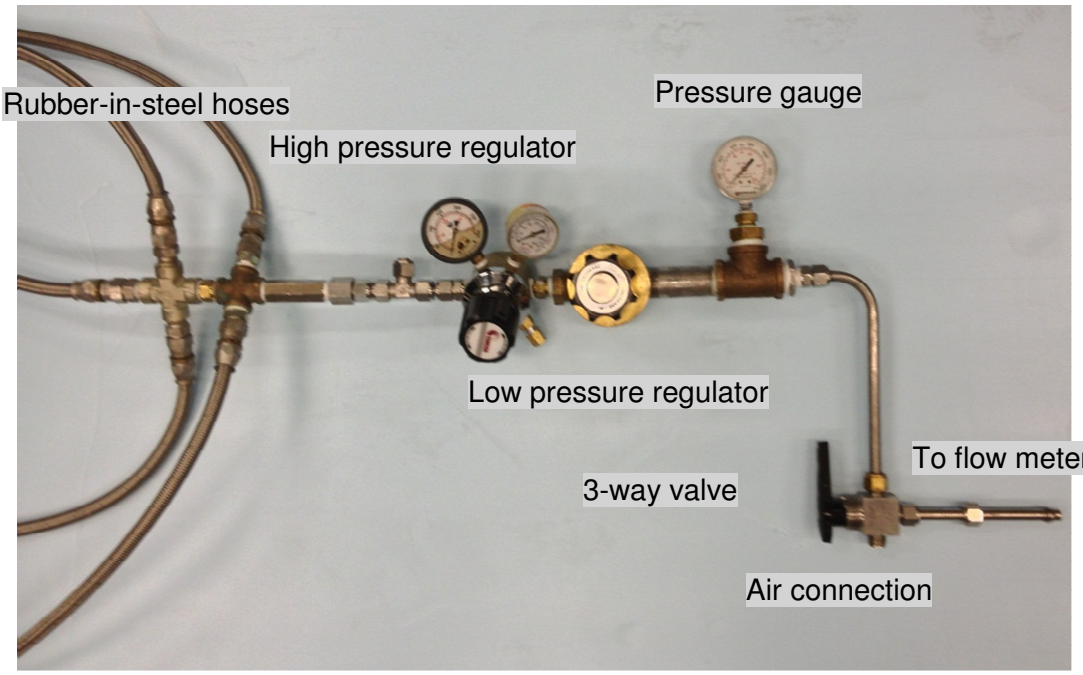

Figure 49. Apparatus used to connect to Ar and He gas cylinders for HEMJ experiments.

The process for performing an Ar or He cooled experiment will now be detailed:

1. Follow procedure from Section 3.1.2 to establish a steady-state air-cooled experiment.
2. Use T_{out} and $\overline{T_c}$ to estimate the $\dot{m}$ of He or Ar required. In order to use as small of an amount of He or Ar as possible, the temperature in the test section and the flow loop should be kept nearly constant to achieve steady-state conditions faster.
3. Adjustments to the torch and/or the air flow rate may be necessary to achieve conditions that can be matched by Ar or He. As He has a much larger $\overline{c_P}$ than air (~5193 J/(kg-K) compared to ~1009 J/(kg-K)), it requires large heat fluxes to achieve appreciable coolant ΔT. Oftentimes the air flow rate would need to be very high and the torch set to a lower setting to match the temperatures discussed in the previous step. This is especially true when trying to achieve high flow rate He-cooled cases.

4. Prepare the high pressure line. To avoid damaging the pressure transducers, the low pressure side of the low pressure regulator should be set to a similar pressure to that of the air line.
5. When both experimenters are ready, quickly switch the three-way valve to begin Ar or He flow. Then turn up the pressure on the on the low pressure regulator to 1.4 MPa while positioning the test section outlet valve to achieve the desired flow rate.
6. If necessary, simultaneously change the torch power to reach the desired heat flux level. If the torch blows out, and cannot be immediately restarted, switch back to air. This is especially important for He-cooled cases as the gas cylinders drain very fast as each of the five cylinders has ~1.5 kg of He. Only about 90% of this is usable as the cylinders must be above 300 psi (2.1 MPa) to run an experiment. This gives a total experiment runtime of ~30-45 minutes when using He.
7. Make small adjustments to the flow rate and the torch to quickly achieve a steady-state condition.
8. While gathering the steady-state data, change the air pressure to ~40 psi to avoid damaging the pressure transducers when switching back to air.
9. When sufficient data has been captured, make the switch back to air while simultaneously decreasing the torch power, if necessary. If no other experiment is to be performed the torch can be extinguished by cutting off the C_2H_2 then the O_2. Otherwise, go back to Step 1.

As described, the HEMJ experiments cooled with Ar or He were quite difficult to perform under the current arrangement. Using a continuous loop of He would greatly simplify the process of running He-cooled experiments. As such a loop would be

expensive to construct, these experiments serve a valuable purpose identifying the need for such a facility.

3.2.4. HEMJ Experimental Results

First, the $\overline{h}$ for the different cases versus $\dot{m}$ is shown in Figure 50. The results of Crosatti and Weathers are shown for comparison. As expected, the cases cooled with He showed significantly higher $\overline{h}$ than the air and Ar cooled cases. Furthermore, the Ar-cooled cases had the lowest $\overline{h}$. The experiments of Crosatti [16] and Weathers [18] are shown on the figure for comparison. They line up closely with the present Air-Brass experiments. However, the cases for the individual gasses using the different thimbles are not consistent. One would expect that if dynamically similar conditions were achieved, the cases with the same coolant and different thimble material would have the same $\overline{h}$. The validity of the dynamic similarity of the experiments must be investigated.

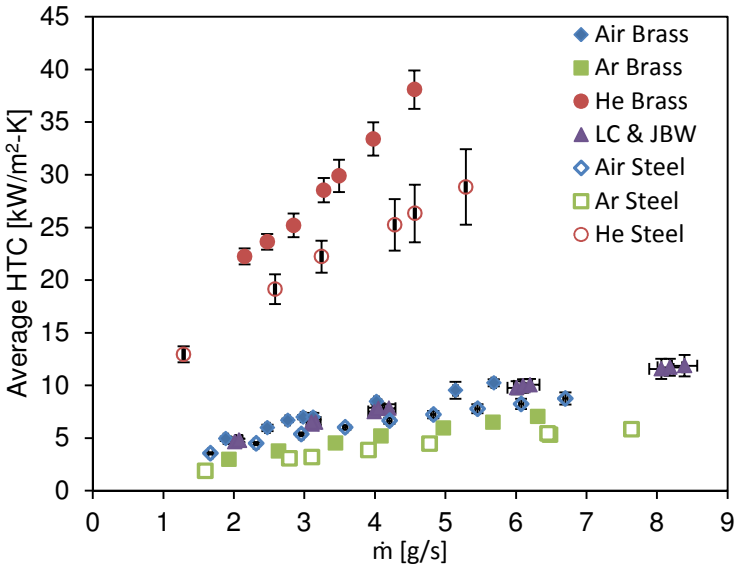

Figure 50. Average HTC vs. mass flow rate.

The non-dimensional pressure loss coefficient K_L is calculated in a similar manner to the HEMP-like divertor module (Section 3.1). The density, ρ_L, and velocity, V_L, used for the calculation were evaluated at the exit of the jet array (i.e. p_{out} and T_{in}):

$$K_L = \frac{\Delta p}{\frac{1}{2}\rho_L V_L^2} \tag{55}$$

Like the HEMP-like experiments the definition here of K_L is based on the difference in static pressure as measured by the differential pressure transducer. The difference in the Δp calculated based on static and total pressure values is small and considered to be negligible.

Figure 51 shows K_L for each of the six cases. The trend is correlated using MATLAB 2011 with Re_j as the only independent variable as the loss coefficient is a purely hydraulic parameter (i.e. no dependence on solid or coolant thermal conductivities is expected). The correlation is performed assuming a power law plus a constant trend. The Re through the jet array Re_j is calculated based on the average mass flux through the all of the jets and the diameter of the central jet D_j.

$$Re_j = \frac{\dot{m} D_j}{A_j \mu_i} \tag{56}$$

where μ_i is the dynamic viscosity of the coolant at T_{in}. The correlation for K_L is:

$$K_L = 1.39 \cdot \left({Re_j}/{10^4} \right)^{-0.50} + 1.32 \tag{57}$$

with fitting parameter R^2 = 0.66. With this correlation, the pressure drop of the experiments can be extrapolated to prototypical conditions.

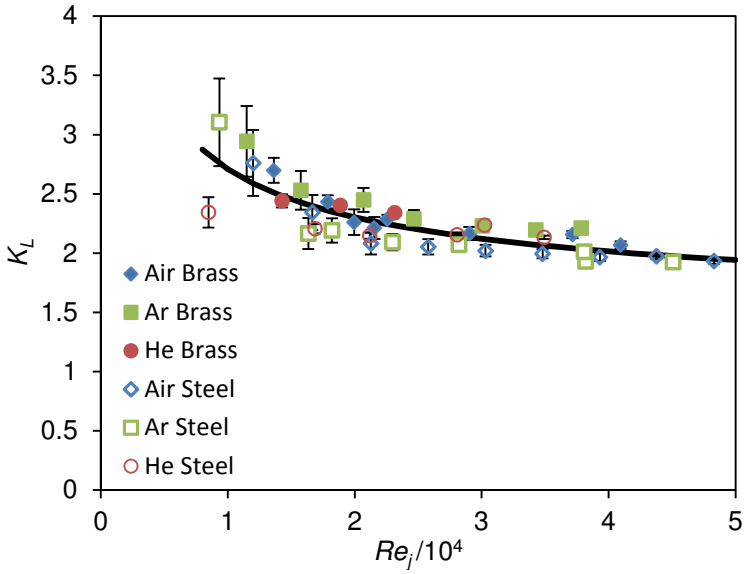

Figure 51. Pressure loss coefficient vs. jet Reynolds number, HEMJ.

3.3. Summary

Experiments have been performed on brass test sections that resemble the HEMP divertor. These experiments combined two test sections, one with and one without an array of fins integral to the cooled surface (fins and bare, respectively), and two flow configurations, one with and one without an impinging jet (forward and reverse flow, respectively) on the cooled surface. These four flow configurations (bare forward, BF; bare reverse, BR; fins forward, FF; and fins reverse, FR) were tested over a wide range of flow rates and at several heat fluxes to characterize their performance.

A new experimental study was performed to evaluate the thermal performance of the HEMJ over a wider range of operating conditions than before. The experiments used six combinations of coolants and structural materials and were designed to investigate the dynamic similarity assumptions of previous HEMJ experiments. The experiments showed that the previous assumption that dynamic similarity can be achieved by only matching the Reynolds number is not valid and should be investigated further.

Since the HEMJ and HEMP-like divertors share similar geometric properties, the dynamic similarity of the HEMP-like divertor should be investigated as well. Numerical simulations performed on the HEMP-like divertor discussed in Chapter 4 will be used for this purpose. With further understanding of the HEMP-like divertor, questions about the dynamic similarity of the HEMJ divertor will be addressed. This analysis too will be presented in Chapter 4.

CHAPTER 4: TWO-DIMENSIONAL SIMULATIONS AND PROTOTYPICAL PERFORMANCE PREDICTIONS

This Chapter details the two-dimensional numerical modeling of the HEMP-like test sections without fins. Of specific interest is the examination of the requirements for dynamic similarity and whether the Reynolds number alone can be used to correlate the heat transfer data for a specific geometry. Here, we will focus on axisymmetric geometries amenable to two-dimensional simulations. Geometries requiring three-dimensional simulations (e.g. HEMP-like test sections with fins) will be discussed in Chapter 5. The implications of the results of the simulations are investigated and applied to both the HEMP-like and the HEMJ divertors experimentally tested in Chapter 3.

4.1. 2-D HEMP-like Numerical Model

By producing numerical results that are close to those demonstrated experimentally, a model is said to be verified. Verified numerical models of divertors allow for testing conditions beyond those achievable in the laboratory. Beyond that, using consistent methodology in subsequent simulations that cannot be tested experimentally provides confidence in any numerical results that fall outside of the range of verification. Furthermore, the results of verified numerical simulations provide insight into the finer details of the thermal-hydraulic behavior of the divertor beyond those observable in standard experiments.

As the HEMP-like divertor experiments cover a range of length scales, only the most important part of the divertor will be numerically modeled. Since the bottom 50 mm of the bare test section ideally exhibits axisymmetric behavior, a two-dimensional (2D) axisymmetric model was constructed. The model was created with ANSYS® 14 and tested with ANSYS FLUENT® 14 [58]. The model was composed of three “faces”

representing the three relevant parts of the test section: tube, air, and finger. Unstructured grids were generated of quadrilaterals with cells of sizes 25, 50, and 100 μm for both forward and reverse flow. A 12.5 μm (or smaller) grid was not constructed as it would go beyond the limit of the available computational resources. An example of these models is shown in Figure 52. All material properties for the simulations were assumed to be the same as those used for the experimental calculations (see Appendix E).

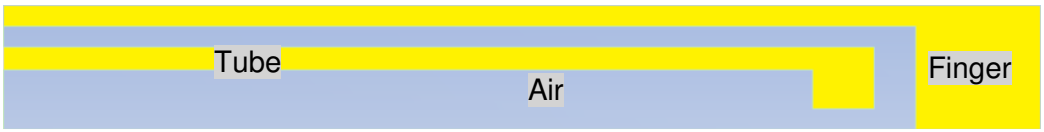

Figure 52. 2D Model used for convergence and turbulence model study.

For the fluid flow, each model has three boundaries: inlet, outlet, and axis of symmetry. Experimentally measured values were used to set the boundary conditions in the numerical simulations. At the inlet, the mass flow rate and temperature are specified according to the experiment being modeled using $\dot{m}$ and T_{in}. Also, as described in more detail in later sections, turbulence parameters are specified at the inlet. At the outlet, the outlet pressure is specified as p_{out}. A uniform heat flux is specified at the heated surface equal to the average experimental value calculated using an overall energy balance, $\overline{q''}$. All other solid boundaries are assumed to be adiabatic.

A series of grid tests was performed to ensure that accurate results were generated. Both grid independence and turbulence model studies were performed to see which conditions best modeled the bare test section. For both forward and reverse flow, a reference case was chosen at a flow rate in the middle of the range tested (~2.3 g/s). Parameters of the reference case for each of the two flow configurations without fins are given in Table 2. The reference cases were chosen based on the incident heat flux and

mass flow rate. The cases were chosen so that the mass flow rate value corresponds to a Re_j close to the prototypical value of ~7.5×10^4. Cases with high heat flux were chosen as higher heat flux cases have a smaller uncertainty in the calculated heat flux because the difference in T_{in} and T_{out} is larger. The case number as tabulated in Appendix A is given as a reference.

Table 2. Parameters of reference cases used for 2D numerical simulations

Case #	Configuration	$\dot{m}$ [g/s]	Re_j [×10^4]	$\overline{q''}$ [MW/m^2]
414	BF	2.35	8.18	0.987
291	BR	2.47	7.94	0.691

The average heat transfer coefficient was chosen as the metric to compare the numerical results to experimental data. For comparing a set of experiments, $\overline{h}$ was based on $\overline{T_c}$ calculated by an area-weighted average of the surface temperature over the entire cooled surface. For the turbulence model study, the standard *k*-*ε* (SKE), RNG *k*-*ε*, realizable *k*-*ε* (RKE), and Spalart-Allmaras (S-A) models were considered. All simulations were performed with enhanced wall treatment as this is a simple way to ensure that effect of the near wall resolution is accounted for. The model that gives the closest results to the experimental values was then tested with the different resolution grids to confirm convergence. Each of the simulations included effects due to buoyancy and viscous heating. Near-wall pressure gradient and heat transfer effects are accounted for using the methods proposed by [48] and [49].

The turbulence model study for forward flow was performed with the 50 μm grid; the results are shown in Figure 53 and Figure 54. Results indicate that the S-A model predicted more closely the experimental cooled surface temperatures. Not only is the magnitude of the cooled surface temperature closest for the S-A case, the shape of the temperature distribution is closely matched by the S-A model as well. Each of the *k*-*ε*

models tested showed similar average cooled surface temperature predictions while producing dramatically different cooled surface HTC profiles. This suggests that the *k-ε* models may not be suitable for configurations involving jet impingement such as the BF configuration examined here.

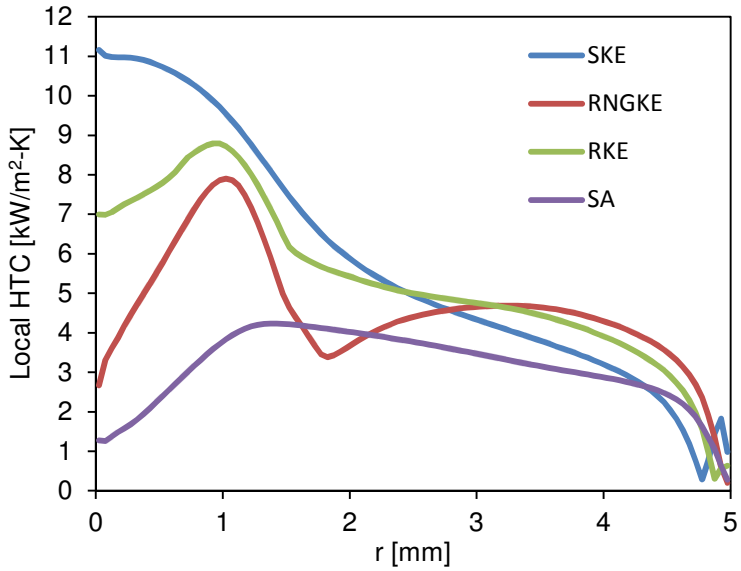

Figure 53. BF turbulence model study, local HTC vs. radial position on the cooled surface, BF reference case.

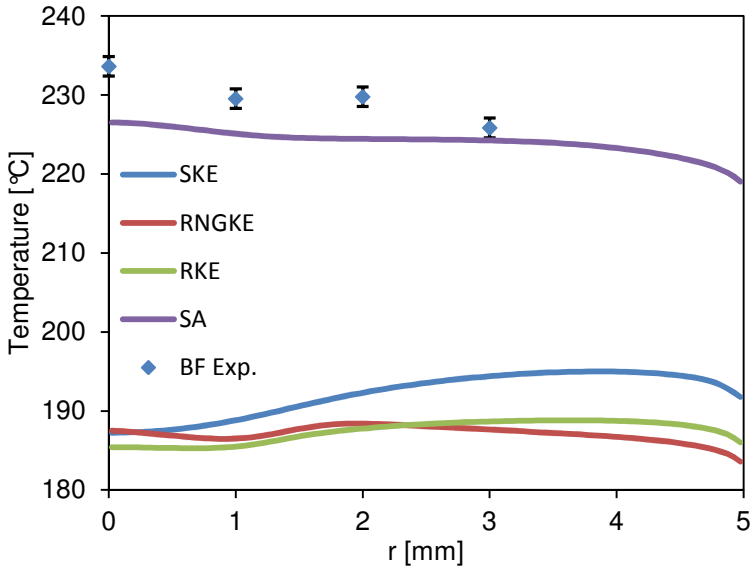

Figure 54. BF turbulence model study, cooled surface temperature vs. radial position on the cooled surface, for BF reference case.

The S-A model [50] is a one-equation turbulence model solving for the turbulent viscosity, $\tilde{\nu}$. At the inlet, the boundary condition for $\tilde{\nu}$ is:

$$\tilde{\nu} = \sqrt{\frac{3}{2}} u_{avg} I l \tag{58}$$

where u_{avg} is the average velocity of air at the inlet, I is the turbulent intensity, and l is turbulence length scale:

$$u_{avg} = \frac{\dot{m}}{\rho_{in} A_{in}} \tag{59}$$

$$I = 0.16(Re_L)^{-1/8} \tag{60}$$

$$l = 0.07L \tag{61}$$

where $\rho_{in}$is the density of the air at the inlet:

$$\rho_{in} = \frac{p_{in}}{R_{air} T_{in}} \tag{62}$$

and A_{in} is the area of the inlet, 26.42 mm^2 for forward flow and 28.27 mm^2 for reverse flow, and Re_L is the Reynolds number of the air based on the hydraulic diameter of the inlet, L, 5.8 mm for forward flow and 2 mm for reverse flow:

$$Re_L = \frac{\rho_{in} u_{avg} L}{\mu_{in}} \tag{63}$$

where μ_{in} is the dynamic viscosity of the air at the inlet temperature. A different method than originally proposed by Spalart and Allmaras for calculating the turbulent viscosity was developed by Dacles-Mariani et al [59] and is included as an option in ANSYS FLUENT listed as 'Strain/Vorticity-based' turbulence production. This variant avoids

calculating nonphysical values in the turbulence production rate in situations that the original model might (such as inside vortices). This option was used for the simulations presented here.

Using the S-A model, each of the grids was tested for grid independence using the BF reference case. The local HTC is shown in Figure 55 and the local cooled surface temperature compared to the experimental data is shown in Figure 56. As shown in Figure 55, the cooled surface local HTC shows grid dependence for the two coarsest cases even though the predicted cooled surface temperature is nearly the same for both grids. In reality, one is more interested in the average HTCs over the cooled surface, inasmuch as the effects of variations in the local HTCs would likely be "smoothed" by conduction within the solid wall. The 25 μm grid captures more of the important features of the cooled surface local HTC variations (small peak at center, larger second peak at 1.2 mm, and recirculation zone at outer edge). As the detail of the solution changes significantly from the 50 μm to the 25 μm solution, the grid should not be considered converged. Performing a further simulation with a grid of 12.5 μm would be computationally prohibitive.

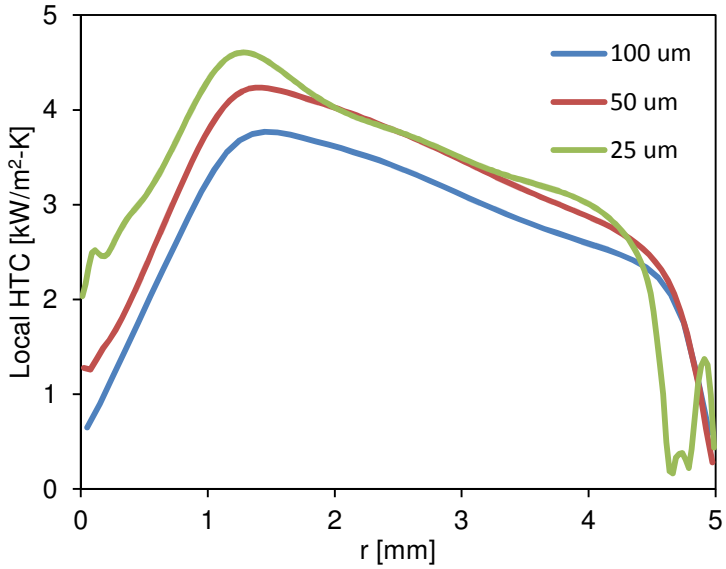

Figure 55. BF grid dependence, local HTC vs. radial coordinate, BF reference case.

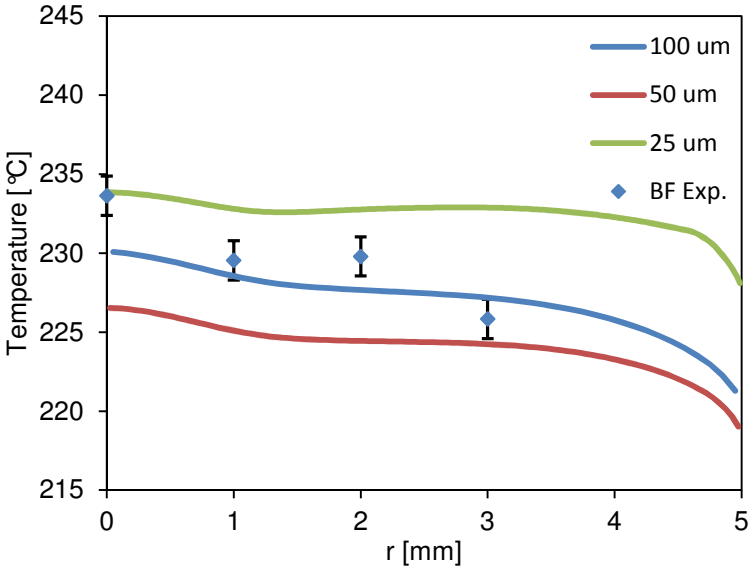

Figure 56. BF grid dependence, surface temperature vs. radial coordinate of cooled surface, BF reference case.

Following this test, the 25 μm grid was chosen to perform a complete study for the entire set of experiments. As shown in Figure 57, this model showed good agreement for the average HTC over the entire range of $\dot{m}$, often falling within the experimental uncertainty. The difference between the simulation and experimental values of average HTC ranged from a 39% overprediction at the lowest flow rate to a 3% underprediction for Case 489 (2.55 g/s). The average deviation was 7.9%. Most cases overpredict the average HTC and were within ±10% of the experimental value.

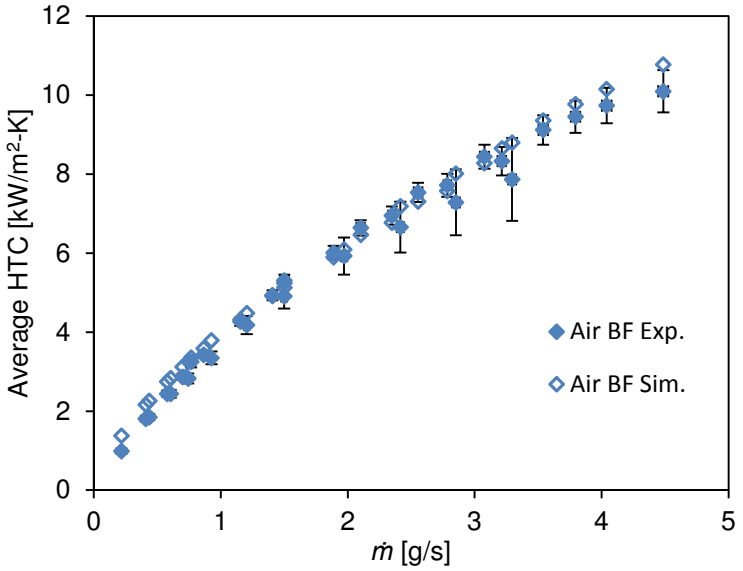

Figure 57. Comparison of numerical and experimental effective HTC results, BF.

The percent difference in HTC versus $\dot{m}$ is given in Figure 58. There appear to be two trends shown in Figure 58 as indicated. The experimental values for BF correspond to one of three categories: The first differentiating characteristic the heat flux at which the tests were operated. Eleven experiments were performed a "low" heat flux (~0.3 MW/m^2). Nineteen experiments were performed at a "high" heat flux (~1.0 MW/m^2). Of those nineteen, nine are denoted as the fixed inlet pressure experiments which were used to test the experiment for the effects of compressibility as mentioned in Section 3.1. On the chart, the lower data set corresponds to the nineteen experiments performed at the higher $\overline{q''}$. The trends converge at low $\dot{m}$ because the heat flux had to be lowered at those flow rates in order to not exceed equipment temperature limits. The difference in the trends could be the result of the accuracy of the brass thermal conductivity values assumed for the simulations. As this was not measured independently, it is recommended that temperature-dependent values of the thermal conductivity for C36000 be determined.

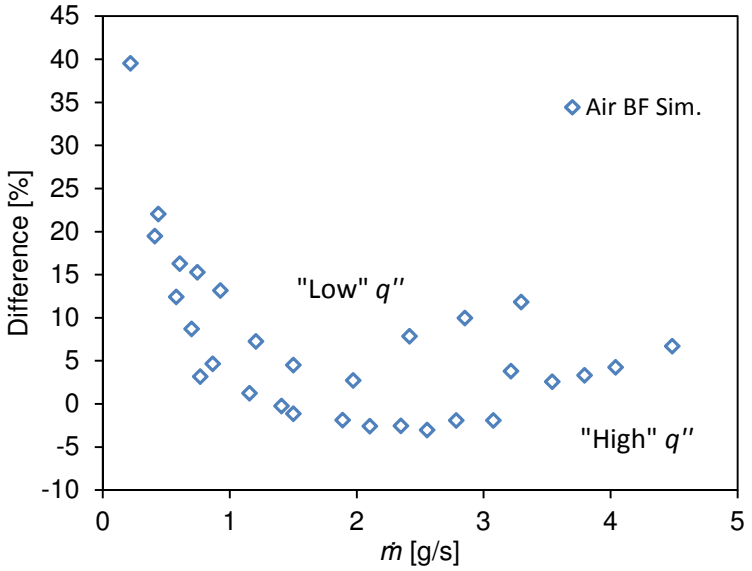

Figure 58. Percent difference in the average HTC for simulations from experiment vs. mass flow rate, BF.

The normalized pressure drop for the simulations was also calculated and compared to the experiments as shown in Figure 59. The calculation is similar that used for the experiments (Eq. 29). The values of p_{in} and p_{out} are calculated using a mass weighted average of the static pressure on the flow inlet and outlet boundaries, respectively. Compared to the experimental study, the pressure drop is overpredicted for most of the flow rates by typically ~40% as shown in Figure 60.

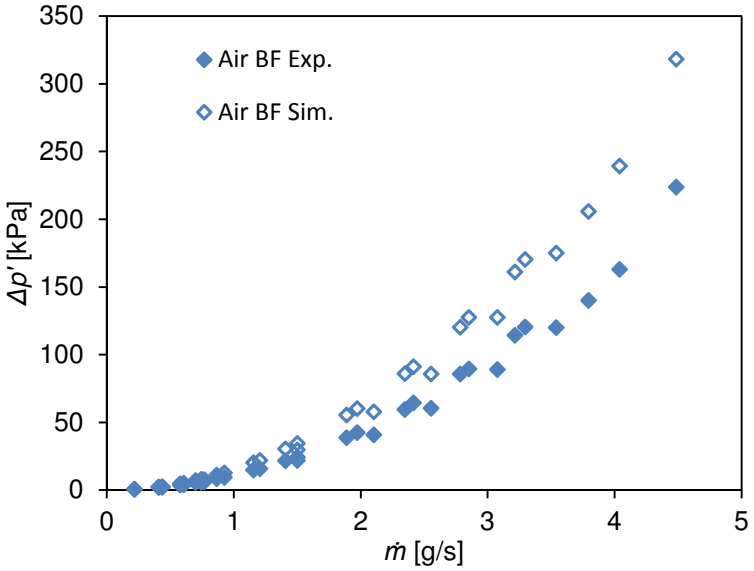

Figure 59. Comparison of numerical and experimental normalized pressure drop, BF.

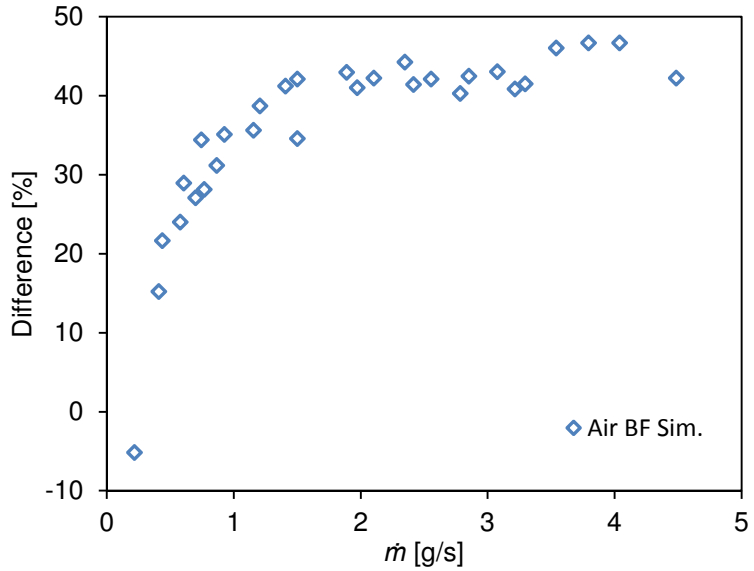

Figure 60. Percent deviation of the normalized pressure drop for simulations from experiment vs. mass flow rate, BF.

Analyses similar to those presented above were performed for the BR configuration. The effects of turbulence model on the local HTC and the cooled surface temperature profile using the 50 μm grid for the BR reference case are shown in Figure 61 and Figure 62, respectively. Though none of the present models predicts the performance exactly, these results show that the BR configuration experiments are most

closely modeled using the RKE model. This result is counter to that obtained for the BF configuration examined earlier where jet impingement was the dominant heat transfer enhancement mechanism. The RKE model [41] is a two equation turbulence model solving for the turbulent kinetic energy, *k*, and the turbulent dissipation, *ε*. At the inlet, these are defined as:

$$k = \frac{3}{2}\left(u_{avg} I\right)^2 \tag{64}$$

$$\varepsilon = C_\mu^{3/4} \frac{k^{3/2}}{l} \tag{65}$$

where u_{avg}, I, and l are defined as before and the C_μ is an empirical constant for *k*-*ε* turbulence models ≈ 0.09. Note that the RKE model uses a non-constant value for C_μ, as recommended by Reynolds [60], but it can be approximated as 0.09 for defining the inlet condition. The dynamic value of C_μ used by the RKE model is a function of both *k* and *ε* and allows the model to avoid calculating nonphysical values of the Reynolds stresses.

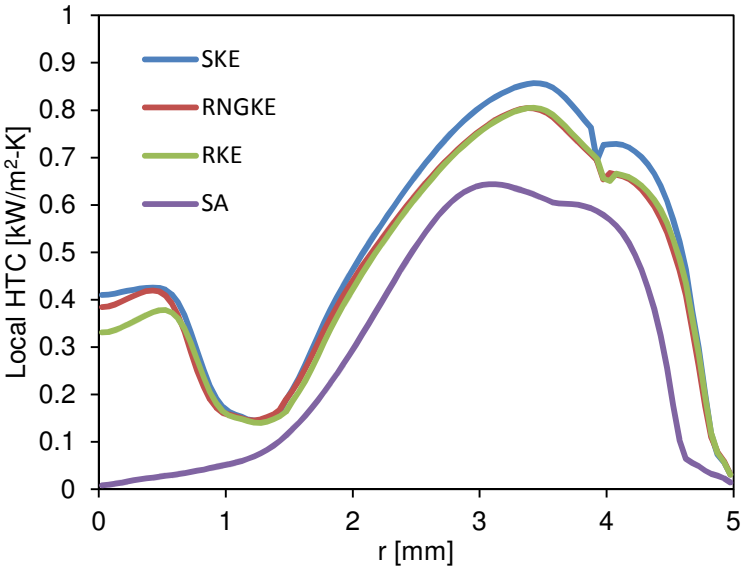

Figure 61. BR turbulence model study, local HTC vs. radial coordinate along the cooled surface, BR reference.

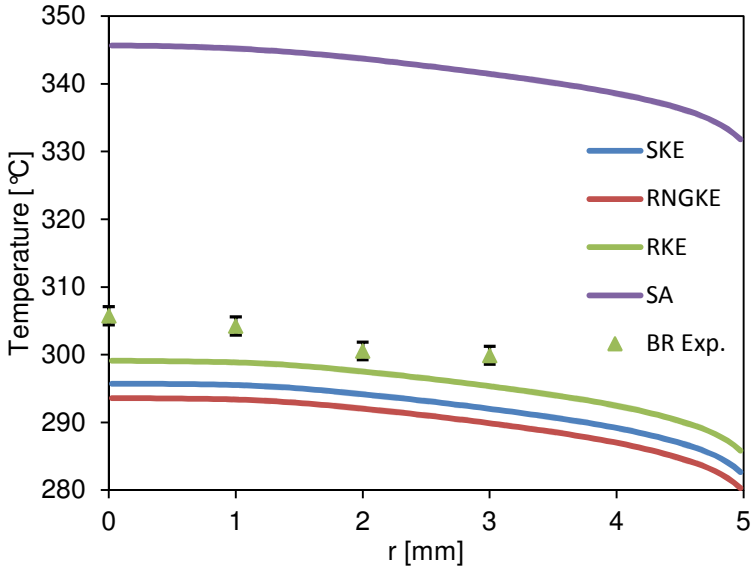

Figure 62. BR turbulence model study, cooled surface temperature vs. radial coordinate, BR reference case.

Similar to the forward flow models, the reference case was tested with different grid resolutions. As shown in Figure 63 and Figure 64, the highest resolution grid better captures the significant features of the flow and provides a smoother profile for HTC. While none of the tests predicted the cooled surface temperature exactly, both the 50 μm and the 25 μm cases showed about the same deviation (~7 °C at r = 0). As the 25 μm grid produces additional fine-scale features, it was chosen to perform the simulations over the entire range of mass flow rate. Like the BF simulations, the grid should not be considered converged as there were significant differences in the solutions of the 50 μm to the 25 μm simulations.

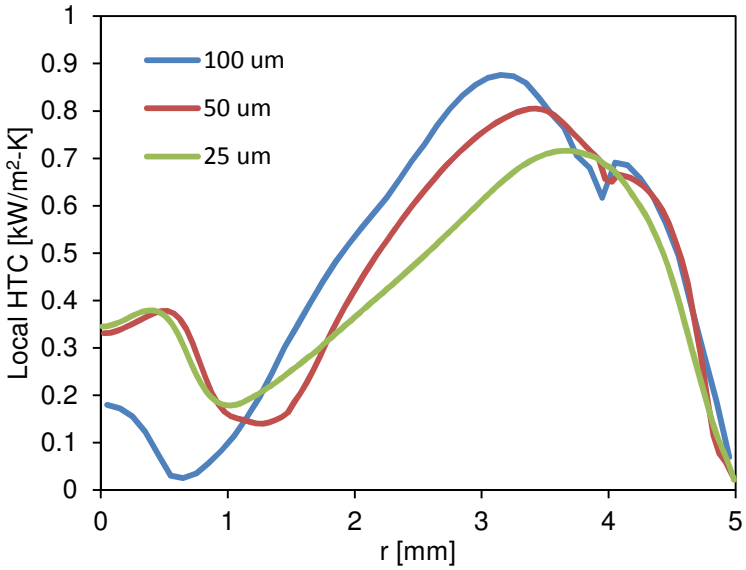

Figure 63. BR grid dependence, local HTC vs. cooled surface radial coordinate, BR reference case.

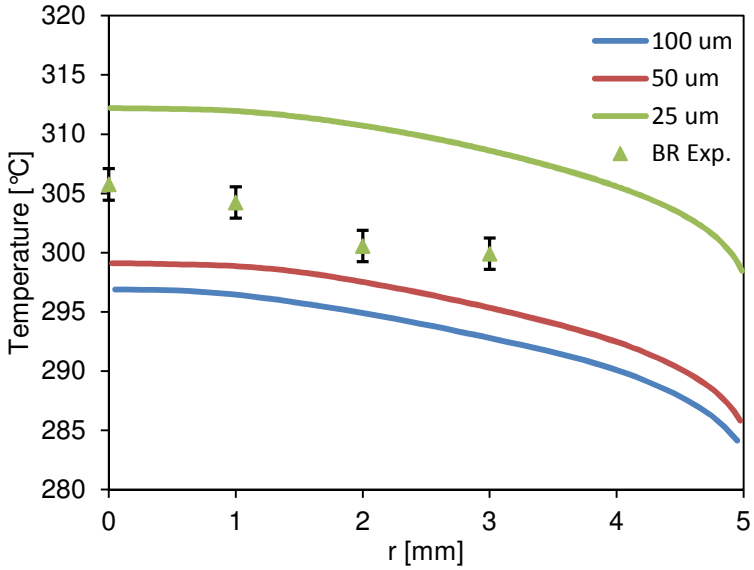

Figure 64. BR grid dependence, cooled surface temperature vs. radial coordinate, BR reference case.

The results of this test are shown in Figure 65. The model performed well over the entire range of $\dot{m}$, often falling within the experimental uncertainty when comparing the average HTC.

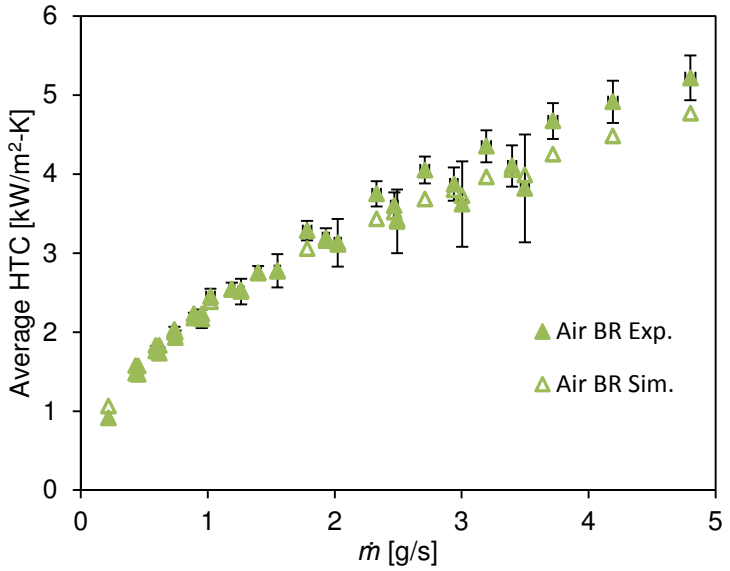

Figure 65. Comparison of numerical and experimental effective HTC results, BR.

The difference in the average HTC predicted by the simulations for BR is shown in Figure 66. The difference in the simulation and experimental values of average HTC ranged from a 16% overprediction at the lowest flow rate to a 9% underprediction for Case 554 (2.71 g/s). The average difference was 4.4%. Most cases were within ±5% of the experimental value and all but one case is within ±10%. As with the BF configuration, there are different trends among the simulations; however the trends are not arranged just according to the heat flux. For the BR configuration, the "high" heat flux corresponds to ~0.75 MW/m^2, and the "low" heat flux corresponds to ~0.25 MW/m^2. The fixed inlet pressure cases also showed a separate trend in HTC deviation. The difference in the "high" and "low" *q''* trends is likely the same as the BF configuration, i.e. the assumed temperature-dependent value of the thermal conductivity of the brass may not be accurate. And while the fixed inlet pressure cases were performed at an elevated heat flux (~1.0 MW/m^2), the observed difference is not large enough to be attributed to that effect alone.

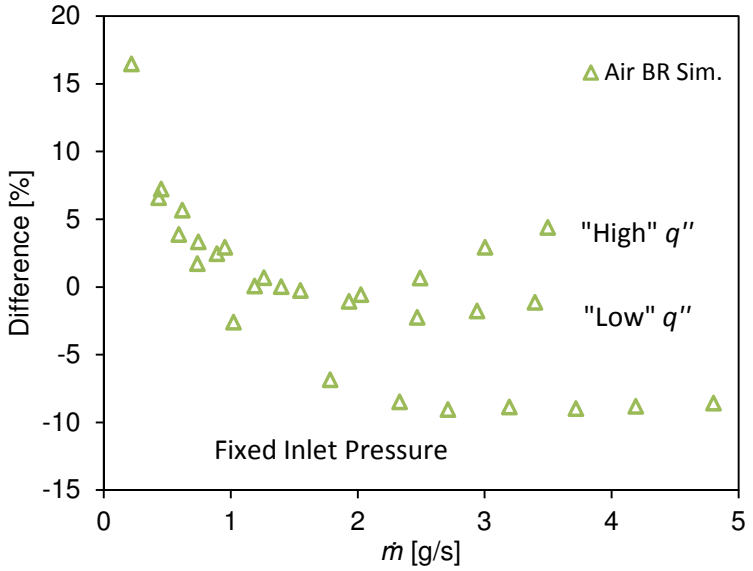

Figure 66. Percent difference of the average HTC for simulations from experiment vs. mass flow rate, BR.

The experimental and predicted pressure drop values were also compared (Figure 67). Similar to the BF simulations, the pressure drop was overpredicted for most of the BR cases.

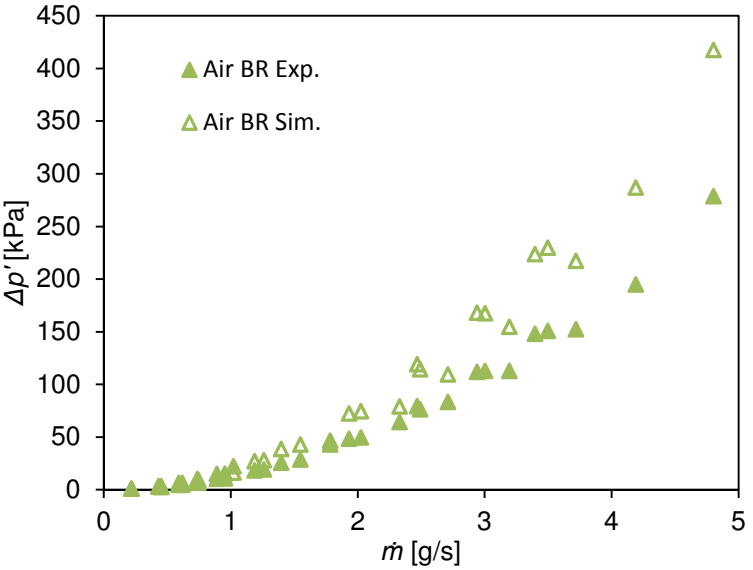

Figure 67. Comparison of normalized pressure drop for simulations and experiments, BR.

For many cases, the pressure drop was overpredicted by about 50% as shown in Figure 68. There are two trends observed in the deviation of the pressure drop. The fixed inlet pressure cases show a significantly different trend in terms of the magnitude of the percent deviation in the pressure drop compared to the variable inlet pressure cases. As the HTC deviation also shows a different trend for the fixed inlet pressure cases, there may be a common cause for both phenomena. The BF configuration did not show a similar effect based on the system pressure though a small heat flux dependence was observed. However, as the BF configuration has poor thermal performance this effect was not investigated in any detail.

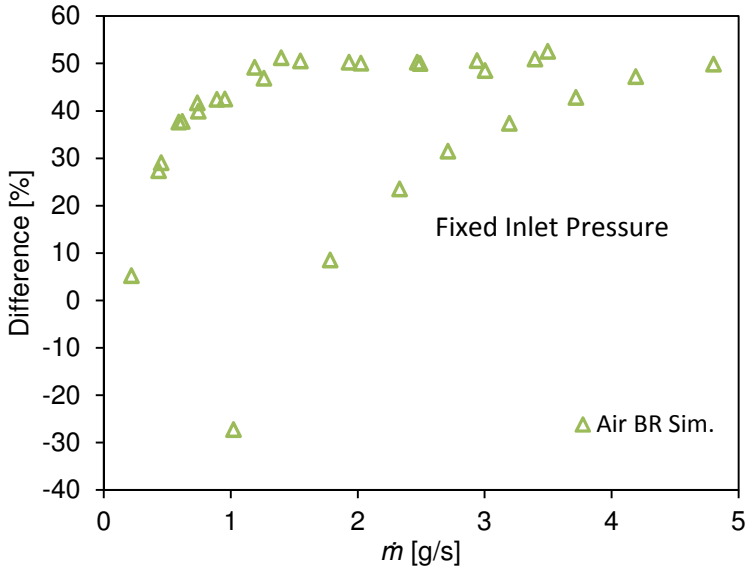

Figure 68. Percent difference of the normalized pressure drop for simulations from experiment vs. mass flow rate, BR.

The simulations provide an opportunity to look more closely at the details of the divertor behavior. The calculated (and experimental) values of temperature and pressure shown in this section and later are the static values. As was shown in Chapter 3, the experiments reached Mach numbers up to 0.8 which means that compressibility effects are non-negligible and can be significant though they were shown not to affect the heat

transfer performance of the modules. When analyzing compressible flow, it is useful to differentiate between the total (also called stagnation) temperature or pressure and the static temperature or pressure. For 1D, steady, isentropic flow the ratio of total temperature, T_t, to static temperature, T, is defined in terms of the specific heat ratio, γ, and the Mach number, M:

$$\frac{T_t}{T} = 1 + \frac{\gamma - 1}{2} M^2 \tag{66}$$

And the corresponding ratio of total pressure, p_t, to static pressure, p, is:

$$\frac{p_t}{p} = \left[1 + \frac{\gamma - 1}{2} M^2\right]^{\frac{\gamma}{\gamma - 1}} \tag{67}$$

These definitions imply that there will be a decrease in both p and T for 1D, steady, isentropic flow through an orifice in the range of M covered in the experiments of Chapter 3. For air with γ = 1.4, and M = 0.7, the expected decrease in T is 26.3 K for T_t = 295 K. The corresponding decrease in p is 112 kPa for p_t = 400 kPa. The reference temperature and pressure values used in the previous calculations are representative of the values for the BF reference case.

Contours of static pressure for the BF reference case are shown in Figure 69. The Figure shows how the pressure is changing as the coolant passes through the orifice and near the cooled surface. The stagnation zone of the impinging jet is clearly visible. Also, nearly all of the pressure drop is a result of the orifice. Optimizing the orifice diameter and shape to reduce pressure drop while still providing heat transfer enhancement would be beneficial to this design. As the air in the experimentally investigated flows is transonic, the optimum shape for reducing pressure drop may not be the same as the optimum shape for reducing pressure drop at prototypical conditions

(600 ℃ He at 10 MPa). Thus any port optimization should be performed using simulations at prototypical conditions before being tested experimentally.

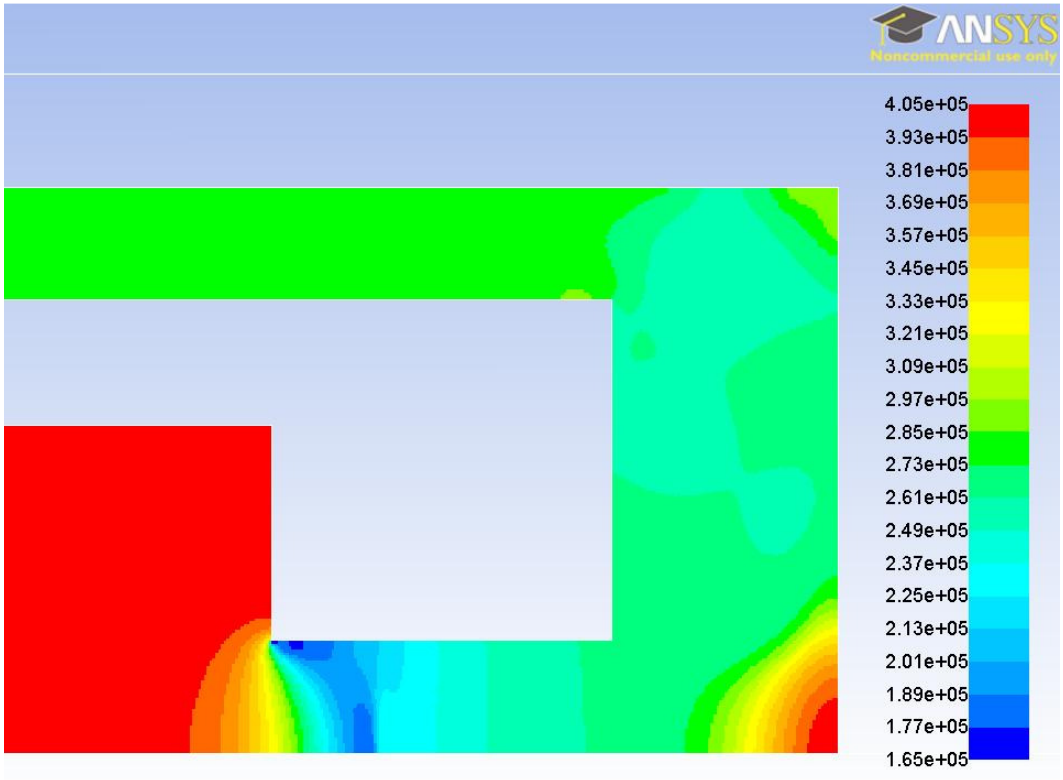

Figure 69. Close-up of static pressure contours near the cooled surface, BF reference case. Scale in units of Pa.

Temperature contours for the end of the BF model are shown in Figure 70. The figure shows that there is significant temperature gradient in the finger shell up the sides of the divertor module indicating the importance of conduction as a heat removal mechanism. Hence, the assumption that the BF configuration removes nearly all of the heat by convection through the cooled surface is likely invalid. This fact impacts any performance predictions made regarding the performance of the BF configuration at prototypical conditions. The implications of this observation will be discussed in more detail in later sections.

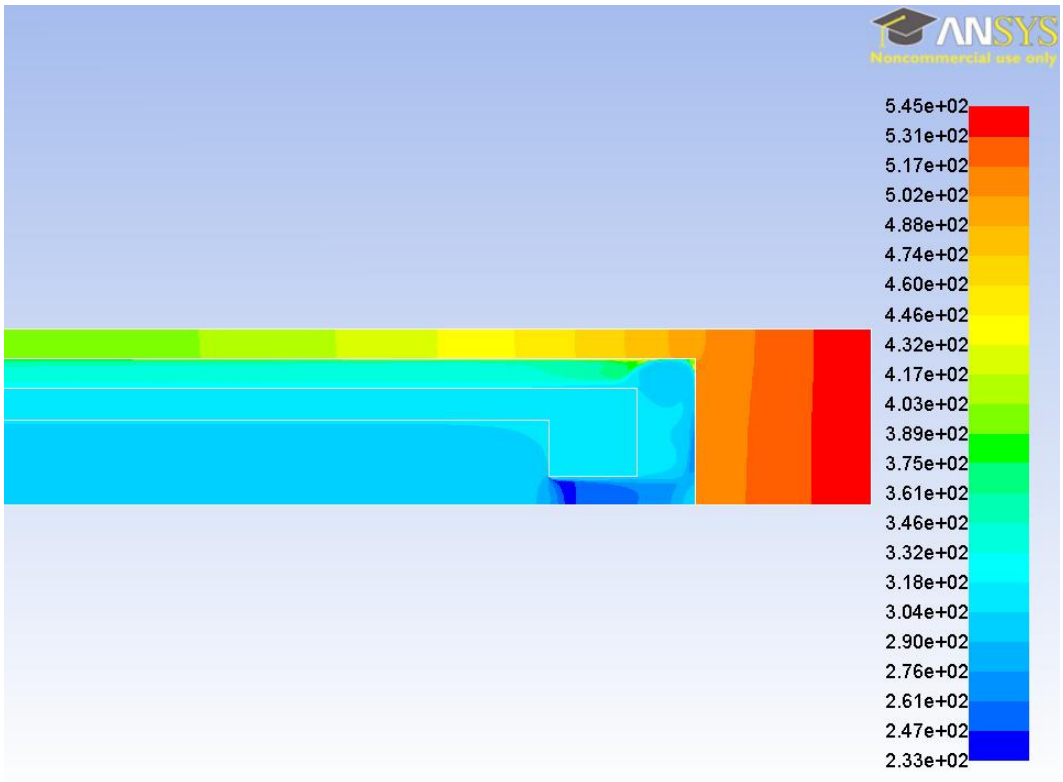

Figure 70. Static temperature contours, BF reference case. Scale in units of K.

The 1D assumption of Eqs. 66 and 67 are not valid for this flow configuration as there are obvious radial variances in the pressure and temperature through the orifice though the static temperature and pressure do decrease..

Velocity contours within the jet and near the cooled surface for the BF reference case are shown in Figure 71. The speed of sound of air at inlet temperature (22 ℃) is near ~345 m/s. For a small section of the jet, the air appears to reach sonic velocities. The average velocity through the nozzle at any fixed axial location is below the speed of sound so this does not contradict the Mach number predictions shown in Figure 42 which are based on the average velocity. The prediction of nearly sonic velocities likely leads to some of the increased pressure drop predicted by the simulations as shown in Figure 59.

Also of interest is the secondary jet impact made on the wall of the finger by the radially propagating wall jet emerging from the central jet. This creates a zone of elevated HTC and also enhances heat transfer up the side of the finger. A small zone of low velocity is seen in the corner of the finger. Smoothing out this corner may result in a larger zone of increased HTC on the wall.

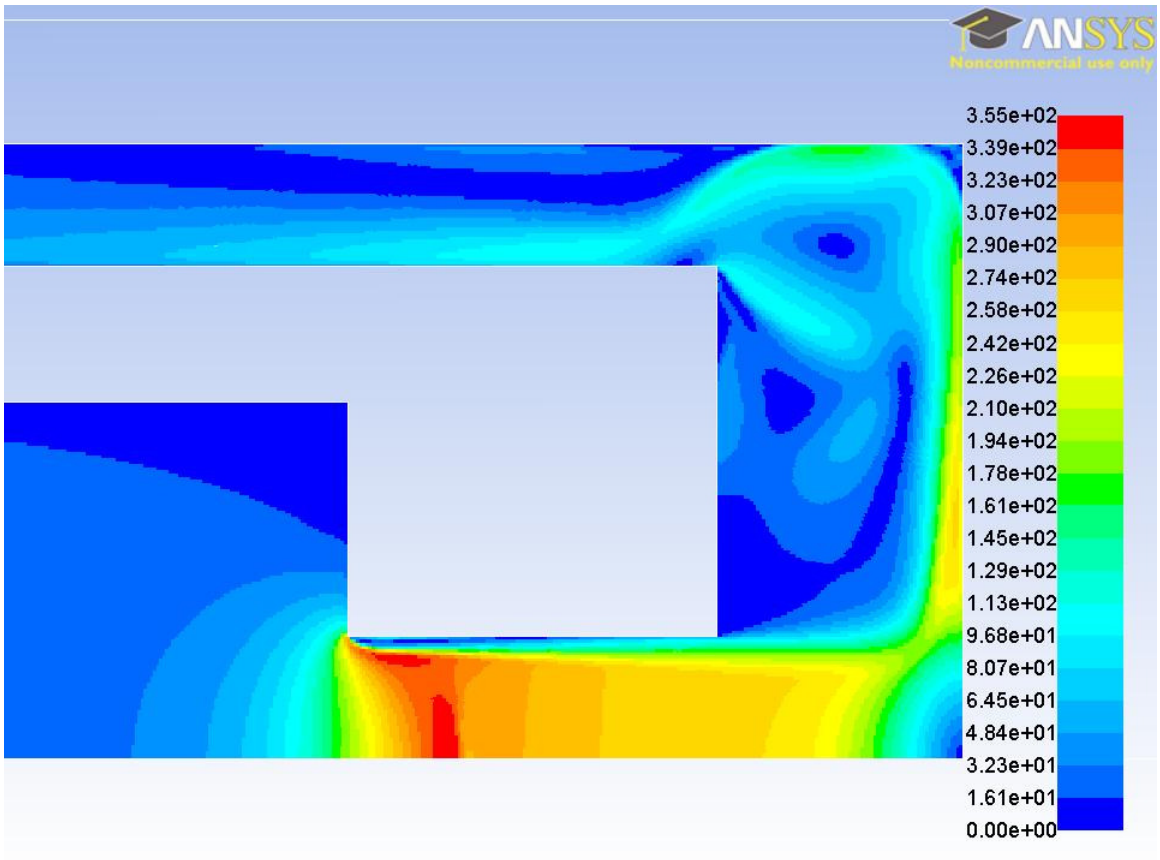

Figure 71. Contours of velocity magnitude, BF reference case. Scale in units of m/s.

The pressure contours shown in Figure 72 for the BR configuration reference case show that the majority of the pressure drop occurs through the inlet/outlet tube orifice. The orifice does not aid in the heat transfer for the BR configuration so perhaps an increase in its diameter could improve the BR configuration's performance. However, since the BR configuration has extremely poor thermal performance compared to the BF configuration, such an optimization would not be a worthwhile endeavor.

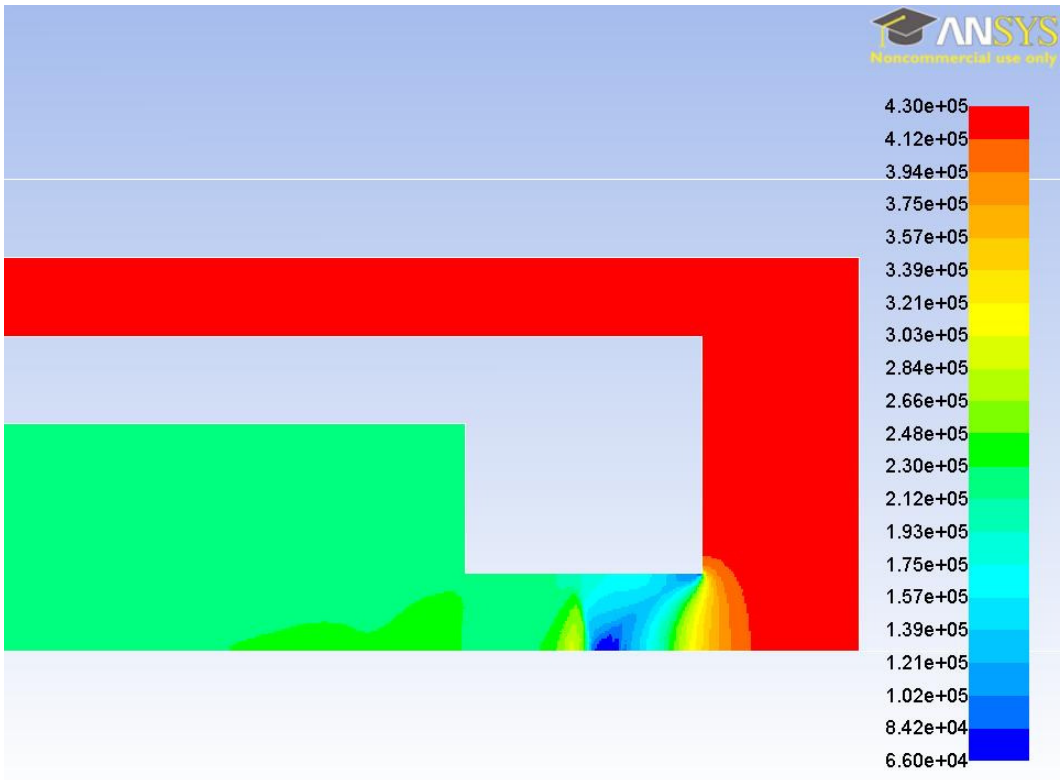

Figure 72. Close-up of static pressure contours near cooled surface, BR reference case. Scale in units of Pa.

As shown in Figure 73, for the BR configuration, the inlet air has already been heated significantly by the time it reaches the cooled surface. Very little change is observed in the temperature of the air as it passes over the cooled surface. Obviously, most of the heat into the coolant is being added somewhere other than at the cooled surface. One can clearly observe that there is a significant amount of conduction up the sides of the finger shell. The large thermal gradients in the outer region of the finger indicate that convection at the cooled surface is not a significant contributor to the overall heat removal capability of the BR configuration. This fact will play a key role in the development of performance predictions in subsequent sections.

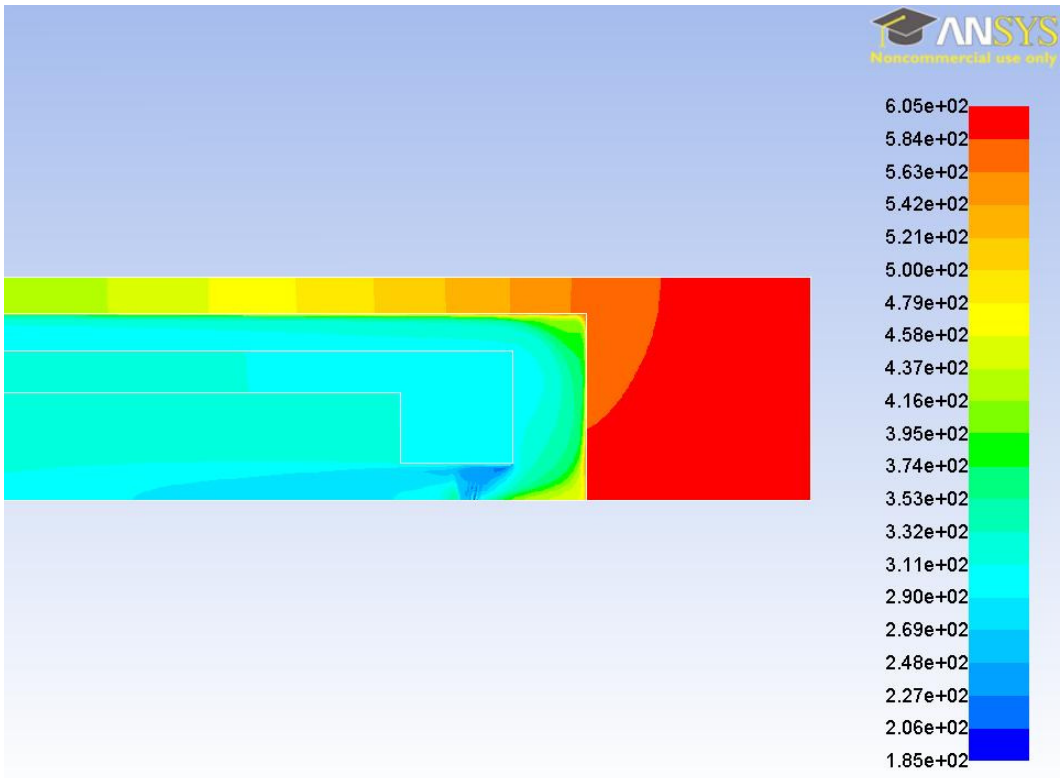

Figure 73. Close-up of static temperature contours for air near cooled surface, BR reference case. Scale in units of K.

4.2. HEMP-like Divertor: Convection vs. Conduction Contributions

A basic assumption originally used in analyzing the experimental data was that all or at least the vast majority of the heat incident on the finger tip is transferred to the air by convection through the cooled surface. This comes into play in the calculation of the average HTC in Section 3.1.2. However, the figures from the previous section indicate that some heat is being added to the air in places other than the cooled surface (parallel to the plasma facing surface). Determining how much of the total energy is removed at the cooled surface can be determined using the simulation data. The simulations allow for the determination of the convective heat removal fraction by comparing the heat removed through the cooled surface compared to the total heat input for each case. As shown in Figure 74, this fraction varies significantly for each

configuration, as well as over the range of $\dot{m}$. The cases with fins (to be discussed in Chapter 5) remove more heat through the cooled surface and thus have higher convective removal percentages. The impinging jet of BF produces significantly higher convective heat removal rates from the cooled surface compared to BR. The impinging jet of FF results in higher heat transfer through the cooled surface than FR at low flow rates. Flow rates above ~2 g/s exhibit nearly the same cooled surface heat removal rate for FF and FR. This implies that the impinging jet does not play as significant role in heat transfer enhancement at high flow rates for the cases with fins. The simulations of the FF and FR configurations will be detailed in Chapter 5.

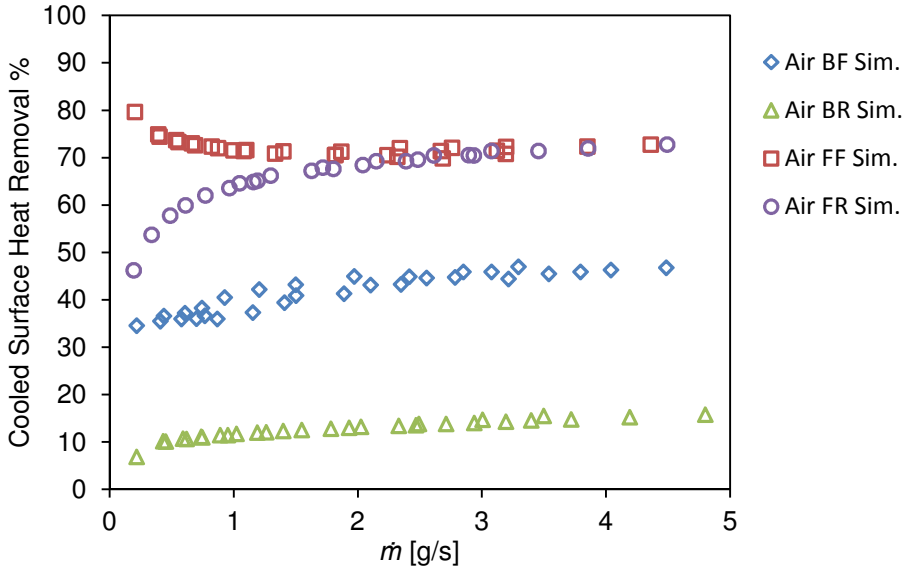

Figure 74. Cooled surface heat removal percentage vs. mass flow rate for all flow configurations.

To learn more about the relative contributions of convection and conduction to the total heat removal rate, a series of simulations were performed for the BF geometry using helium or argon (instead of air) as coolant at operating points that span the experimentally tested Re_j values. Also, another wall material was investigated to determine the effect of the thermal conductivity of the finger. All three coolants were

tested with a new structural material with thermal conductivity set to that of AISI 1010 carbon steel (material properties in Appendix E). It has a thermal conductivity approximately 40% of C36000 brass. The value of $\overline{q''}$ was set to 1.5 MW/m^2 for the He-cooled cases and 0.5 MW/m^2 for the Ar-cooled and air-steel cases. The cooled surface convective heat removal percentage of these simulations is shown in Figure 75 and compared to the previously discussed air-brass simulations.

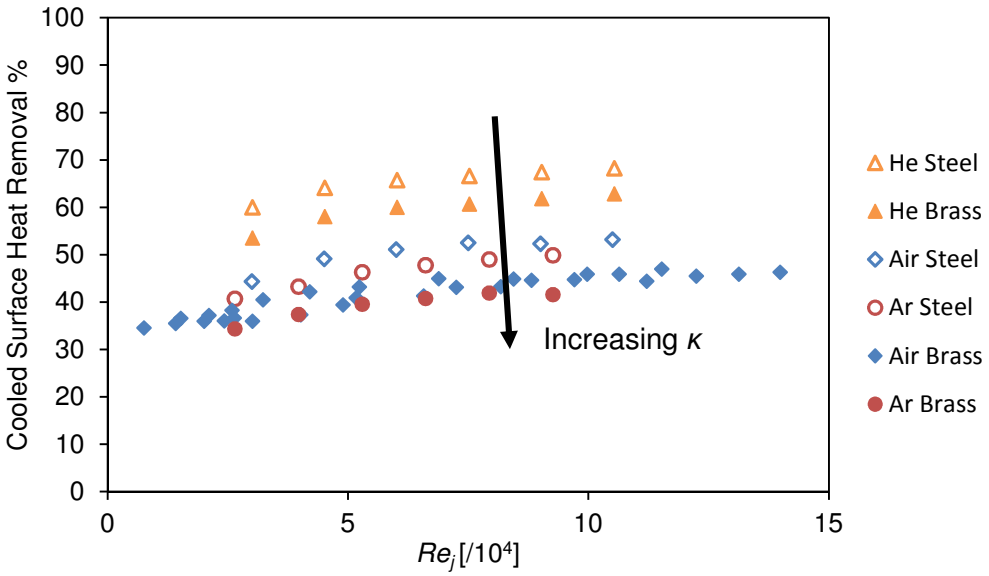

Figure 75. Convective heat removal percentage for different structure/coolant combinations versus jet Reynolds number, BF simulations.

As shown, the cooled surface heat removal percentage is not dependent solely on Re_j. As indicated on Figure 75, the trends are arranged by the thermal conductivity ratio, κ, of the structure, k_s, to the coolant, k_g:

$$\kappa = \frac{k_s}{k_g} \tag{68}$$

The Biot number, $Bi = \frac{hL}{k_s}$, was considered another possible non-dimensional parameter that would characterize the relative contributions of convection to conduction

heat transfer for the finger. However, as the formulation for *Bi* requires the value of the HTC at the cooled surface, it is not suitable for analyzing this problem as knowledge of the real HTC is unknown when performing the experiments. What is known, however, is the temperature of the solid and the coolant thus allowing for the calculation of the thermal conductivities using just experimental data.

Table 3 gives approximate value of κ for the simulations. The values change for the gases and structural materials from case to case because the thermal conductivities are temperature dependent. The values for k_g were evaluated at the average of the inlet and outlet temperature, while the values of k_s were evaluated at the average cooled surface temperature. Values shown in Table 3 are for the case with Re_j nearest the prototypical value of 75,000.

Table 3. Approximate values of thermal conductivity ratio, κ, used for BF simulations in decreasing order of κ. Values taken from cases with jet Reynolds number near 75,000.

Structure	Coolant	k_s [W/m-K]	k_g [mW/m-K]	κ [-]
Brass C36000	Ar	136	19	7230
Brass C36000	Air	140	28	5080
AISI 1010 Steel	Ar	54	19	2870
AISI 1010 Steel	Air	58	28	2040
Brass C36000	He	125	158	787
AISI 1010 Steel	He	60	158	376

The uncorrelated values of $\overline{Nu}$ are plotted vs. Re_j in Figure 76. It can be clearly seen that the values of $\overline{Nu}$ cannot be correlated only with Re_j as the independent variable. As indicated on the figure, the trends, though internally consistent, vary with κ.

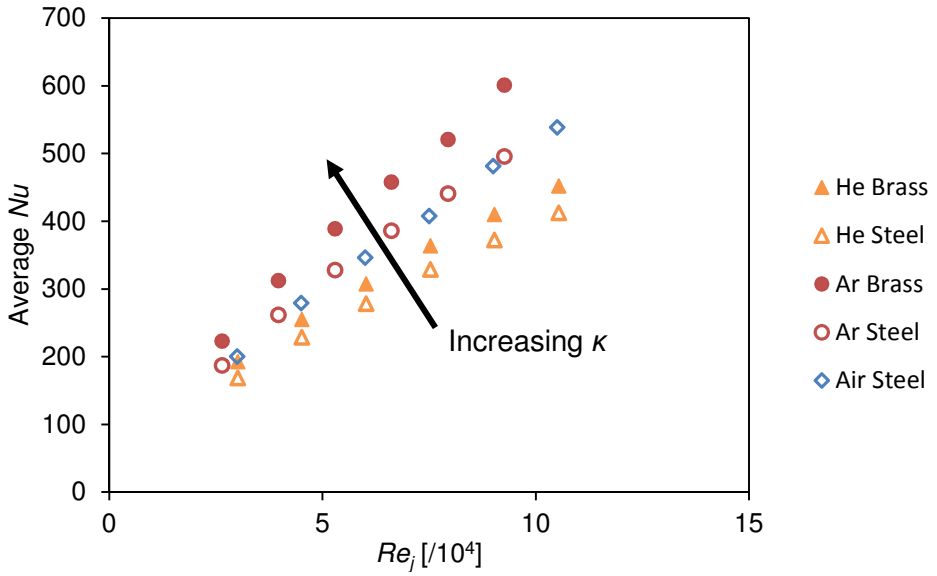

Figure 76. Average Nusselt number vs. jet Reynolds number, uncorrelated, BF.

Next, the values of $\overline{Nu}$ for the five new cases only (Air-Steel, Ar-Steel, Ar-Brass, He-Steel, He-Brass, not Air-Brass) were correlated as a function of both κ and Re_j. A power law correlation was assumed to relate $\overline{Nu}$ to κ and Re_j. The fit (based on just the new simulations) and the data for all of the simulated cases (both the new simulations and those of actual experiments) is shown in Figure 77. By plotting the air-brass data points alongside the correlation produced from the new simulations, it is shown that the experimentally tested configuration agrees with the $\overline{Nu}$ prediction of the correlation based solely on the numerical simulations. In this way, the correlation is shown to predict the actual behavior of the experiment for a combination of materials that was not included when constructing the correlation. The correlation for the BF configuration assuming a power law is:

$$\overline{Nu} = 0.0369 \cdot Re_j^{0.736} \kappa^{0.139} \tag{69}$$

with fitting parameter R^2 = 0.996. The correlation was found using multi-linear curve-fitting in Microsoft Excel 2010.The values of $\overline{Nu}$ calculated from the simulations of all six material combinations is plotted against the correlation as shown in Figure 77. Dashed lines showing ±10% of the correlation are shown as well. Nearly all of the data points lie within the dashed lines indicating that the correlation describes all of the material combinations well over a wide range of flow rates.

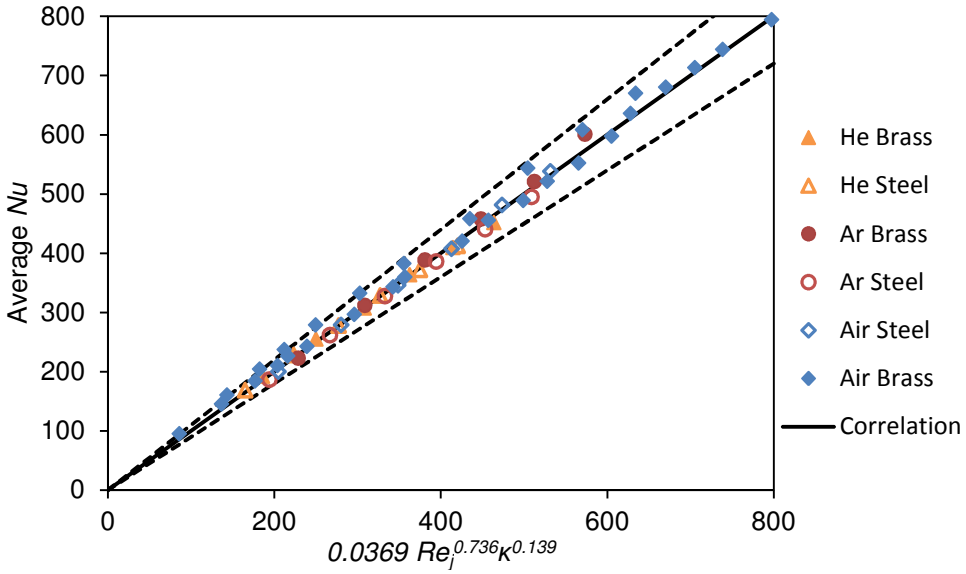

Figure 77. Average Nusselt number vs. correlation calculated from BF simulations using multiple coolants and structural materials. Dashed lines indicate ±10% of correlation.

The results of the simulations for these HEMP-like divertor geometries suggest that the thermal performance of the HEMP divertor should be characterized by both the non-dimensional mass flow rate of the coolant (i.e. the Reynolds number) as well as the thermal conductivity ratio of the divertor structure to the coolant. This implies that other finger-type divertors may show a similar effect. This hypothesis will be tested on the HEMJ divertor in later sections. Other similar designs should be tested as well, such as the HEMP-like divertors with fins (FF and FR).

The local Nusselt number should be confirmed to be similar for the five new material combinations tested. Variation of the local *Nu* as a function of radial position on the cooled surface is shown in Figure 78. The Re_j for the five cases shown in the figure are all near 75,000. Obviously the values are very similar as it is difficult to distinguish between the curves.

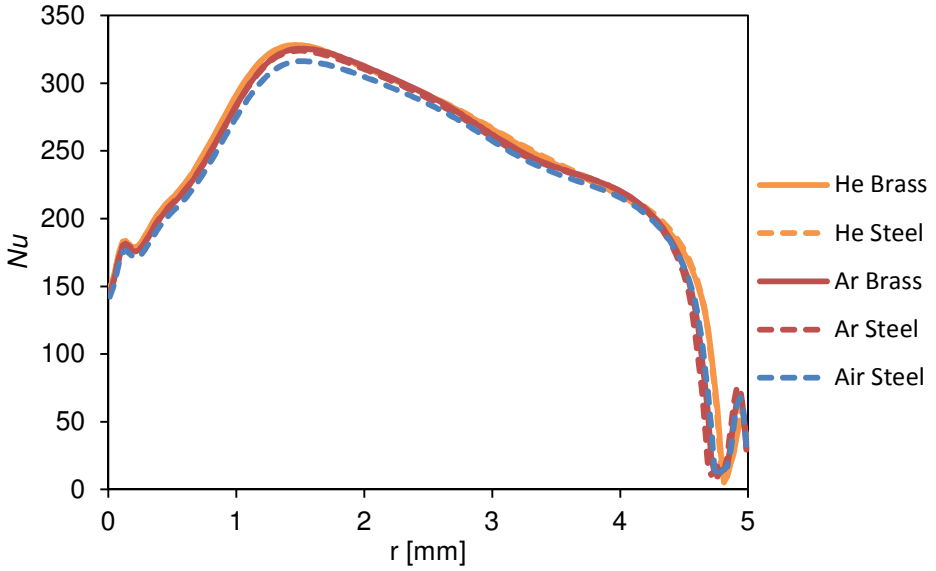

Figure 78. Local Nu for BF simulations.

For comparison, the local HTC is plotted in Figure 79. As expected, the HTC for the He-cooled cases is significantly higher than those cooled by air or Ar because of its higher thermal conductivity.

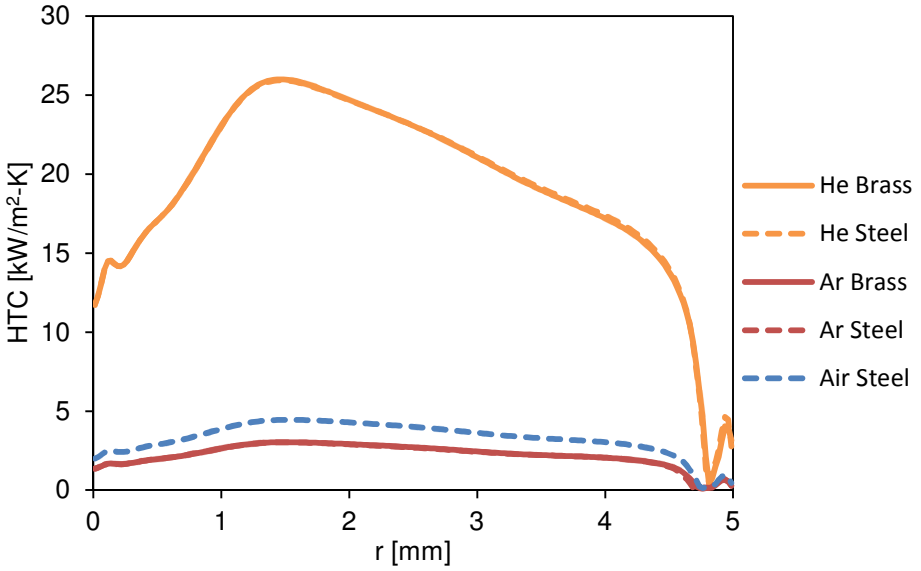

Figure 79. Local HTC for BF simulations.

The pressure loss coefficient should also be checked to ensure that it is not affected by the convective heat removal fraction. The pressure loss coefficient as a function of Re_j is shown in Figure 80. As expected, there is no apparent effect of κ on K_L as it is a purely hydraulic parameter not directly affected by the heat conducted in the finger walls.

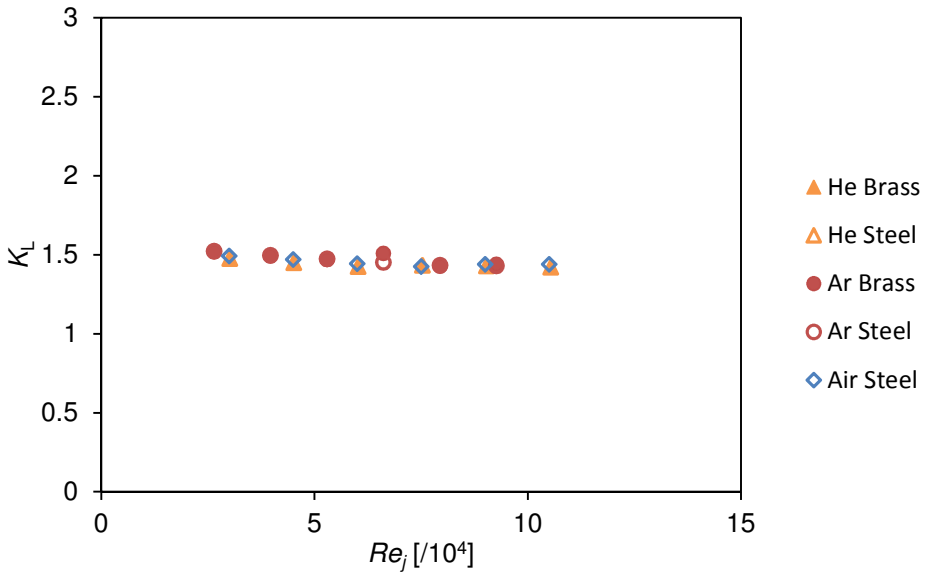

Figure 80. Pressure loss coefficient for BF simulations.

4.3. Effect of Incident Heat Flux Uniformity

The extent of non-uniformity of the heat flux from the torch is unknown. The numerical simulations were therefore used to investigate the effect of non-uniform incident heat flux on the predictions of cooled surface temperatures by varying the peak to average ratio of the incident heat flux while maintaining the same average heat flux (i.e. the same total power input). The BF reference case was chosen for this initial investigation.

The peak to average ratio, *F*, is defined as the ratio of the peak heat flux, q_0'', to average heat flux, $\overline{q''}$:

$$F = \frac{q_0''}{\overline{q''}} \tag{70}$$

The heat flux was varied assuming a Gaussian distribution with its peak at the center. The Gaussian distribution is characterized by a spreading constant σ, and coefficient, α. The formulation for the incident heat fluxas a function of radial position, r, is:

$$q''(r) = \overline{q''}\frac{\alpha}{\sigma\sqrt{2\pi}}e^{-\frac{r^2}{2\sigma^2}} \tag{71}$$

The parameters that were chosen to give values of *F* that vary from one to four are shown by Table 4. The normalized profiles of the heated surface incident heat flux for the four cases tested are shown in Figure 81.

Table 4. Parameters for Heat Flux Uniformity Study

F	σ	α
1	-	-
2	0.003362	0.01685
3	0.002526	0.01899
4	0.002143	0.02148

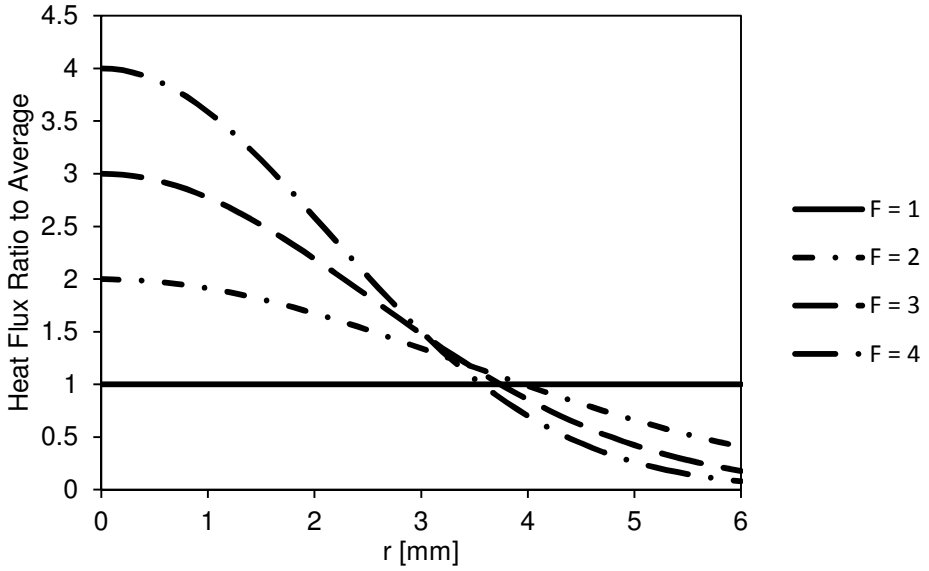

Figure 81. Normalized heated surface heat flux profiles.

The calculated cooled surface temperature as a function of radial position for the four heat flux profiles is shown in Figure 82; the cooled surface HTC is shown in Figure 83, while the axial heat flux on the axis of symmetry is shown in Figure 84.

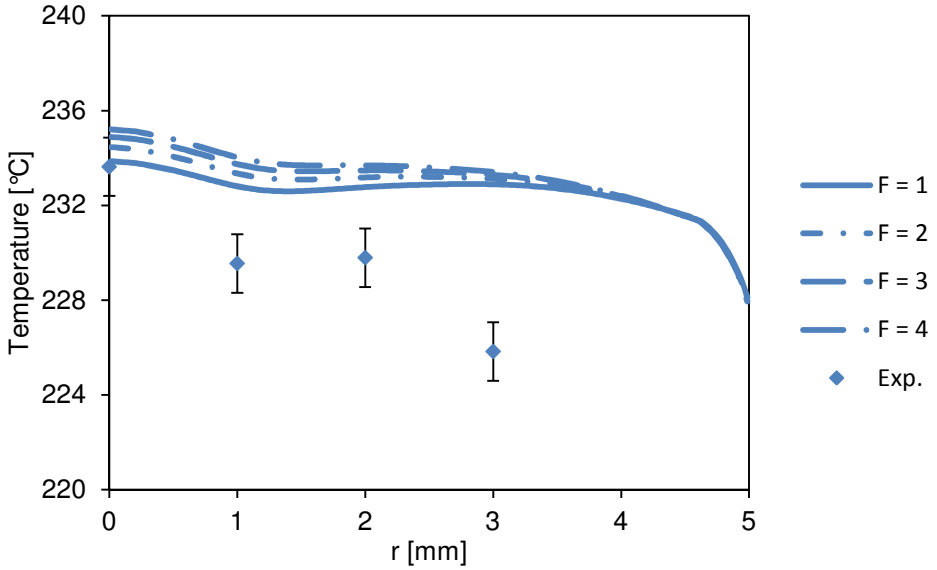

Figure 82. Cooled surface temperature for different heated surface heat flux peaking factors, BF reference case.

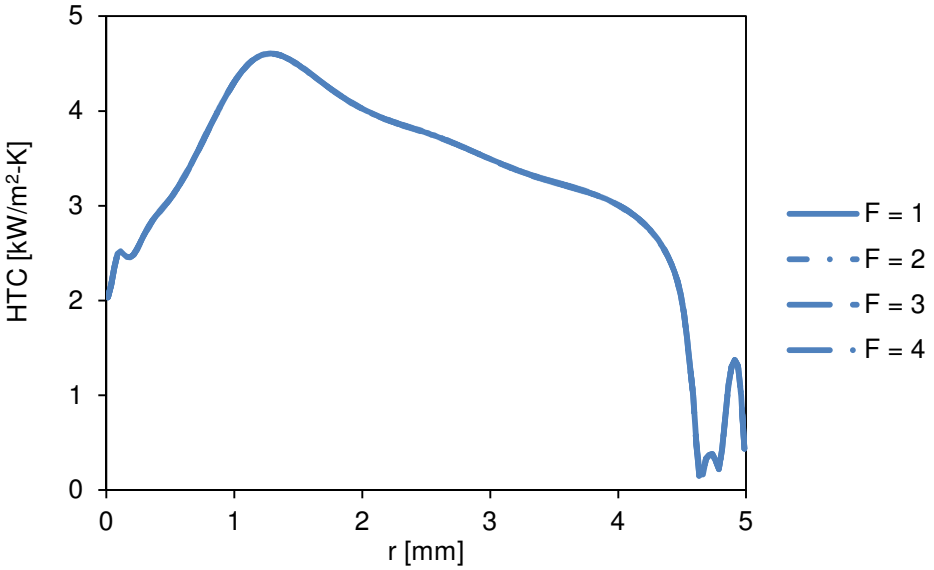

Figure 83. Cooled surface heat transfer coefficient for different heated surface heat flux peaking factors, BF reference case. The curves are indistinguishable as they nearly overlap completely.

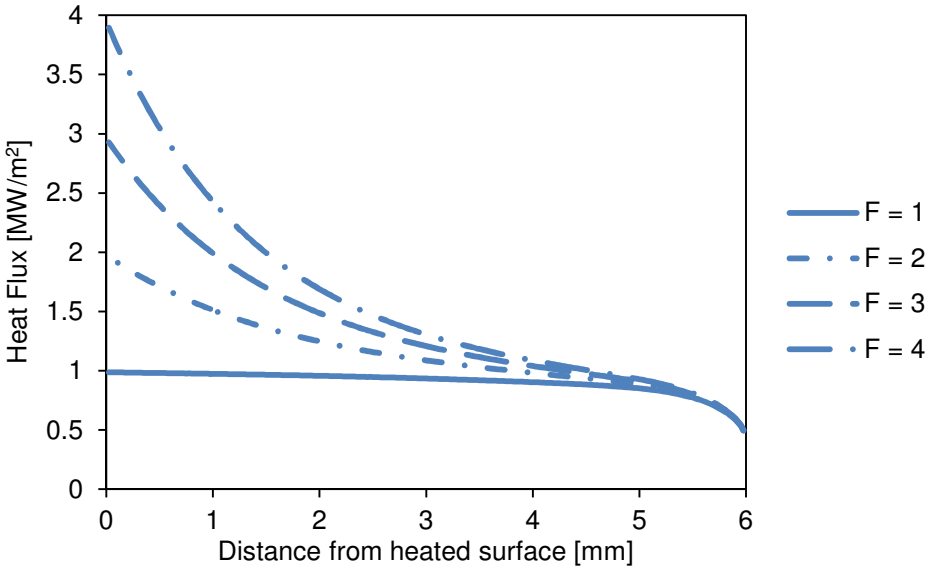

Figure 84. Axial heat flux along the axis of symmetry for different heated surface heat flux peaking factors, BF reference case.

Even for the largest value of *F*, the cooled surface temperatures are very similar to the uniform heat flux assumption. The six mm thick “finger-tip” of brass allows for sufficient conduction to occur and even out the heat flux profile. The cooled surface

HTCs for the four cases are nearly identical. The axial heat flux levels out to nearly the same value for all four cases by the time it reaches the cooled surface.

Following the study of the heat flux peaking on the air-brass BF configuration, a similar study was performed on the He-steel BF model used as part of the convection vs. conduction study of Section 4.2. The case with Re_j closest to the prototypical value was chosen as the operating point to test the four heat flux profiles. As κ is the lowest (Table 3) for this material combination, the two should nearly bound the effect of the variation of incident heat flux peaking on the divertor behavior. The cooled surface temperature, cooled surface HTC and axial heat flux for the BF He-steel reference case are shown in Figure 85, Figure 86, and Figure 87, respectively.

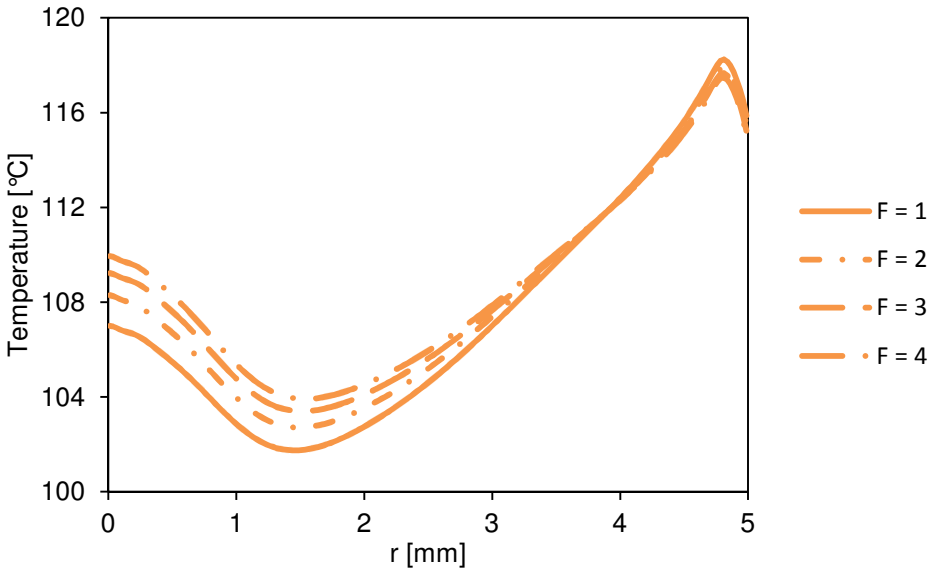

Figure 85. Cooled surface temperature for different heated surface heat flux peaking factors, He-steel BF.

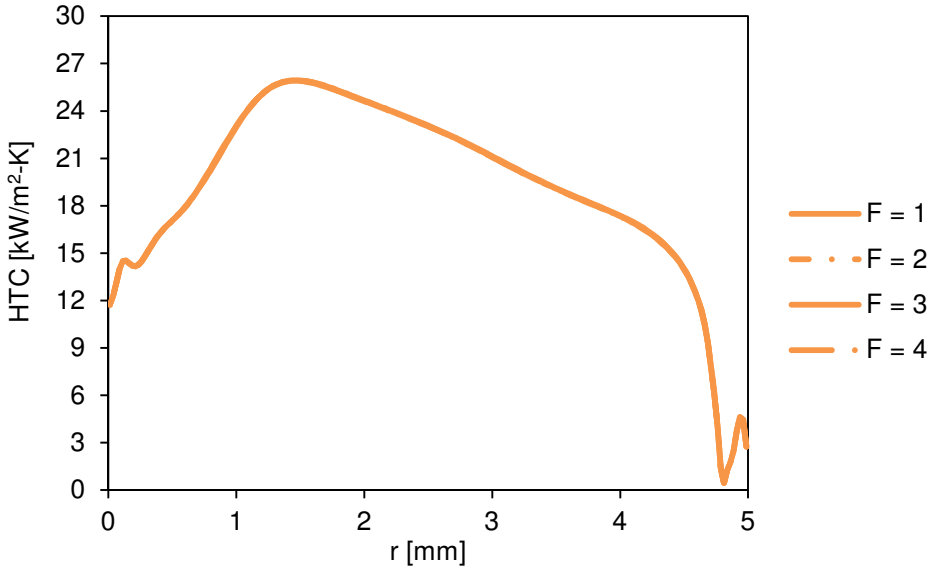

Figure 86. Cooled surface heat transfer coefficient for different heated surface heat flux peaking factors, He-steel BF. The curves are indistinguishable as they nearly overlap completely.

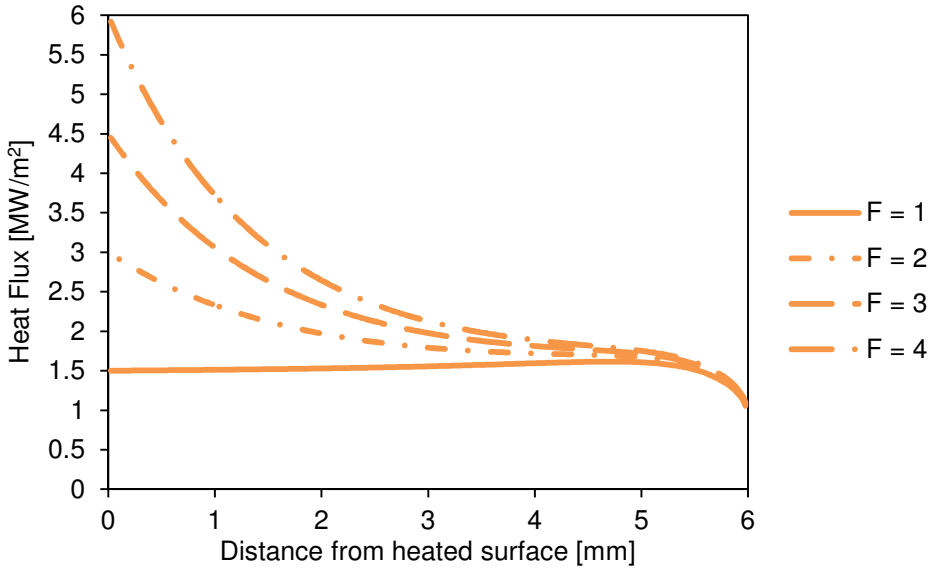

Figure 87. Axial heat flux along the axis of symmetry for different heated surface heat flux peaking factors, He-steel BF.

As shown in the Figures, the behavior for the He-steel configuration is not significantly different than the air-brass configuration in terms of the effect that the heated surface heat flux peaking factor has on what is observed near the cooled surface. Over the range of peaking factors tested, the calculated cooled surface

temperature varies by less than 3 ℃, while the cooled surface HTC for each case is nearly identical. The axial heat flux along the axis of symmetry reaches nearly the same value 1 mm from the cooled surface for each of the configurations. The cooled surface temperatures vary more than those observed for the air-brass simulations. A longer finger-tip would help dampen this effect. The above results suggest that the uncertainty in the extent of non-uniformity in the incident heat flux provided by the oxy-acetylene torch should have little impact on the predicted thermal performance and that use of the average incident heat flux (calculated from an overall energy balance) is sufficient to characterize the test conditions.

4.4. HEMJ Dynamic Similarity

Following the results of the BF simulation on the HEMP-like divertor, the observed lack of dynamic similarity for the HEMJ experiments with different coolants and thimble materials presented in Chapter 3 can be explained. Dynamic similarity predicts that flows at the same Reynolds number Re should have the same Nusselt number Nu (ignoring Prandtl number effects as it is similar for these three ideal gasses). The Nu averaged over the cooled surface $\overline{Nu}$ is also calculated based on D_j as well as the thermal conductivity of the gas at the average of T_{in} and T_{out}, $\overline{k_g}$:

$$\overline{Nu} = \frac{\overline{h} D_j}{\overline{k_g}} \tag{72}$$

As shown in Figure 88, the trend of $\overline{Nu}$ to Re_j is similar to that shown in Figure 50 in that the different material combinations show internally consistent trends but do not conform to trends expected of dynamically similar experiments.

This result was anticipated based on the predictions of the previous Section. However, these experiments are not dynamically similar using the current formulation, i.e. assuming that all of the heat into the thimble is convected away by the coolant through the cooled surface. As indicated on Figure 88, the cases are layered according to the thermal conductivity ratio of the structure to the gas, κ. Values of κ for the different experimental conditions are given in Table 5.

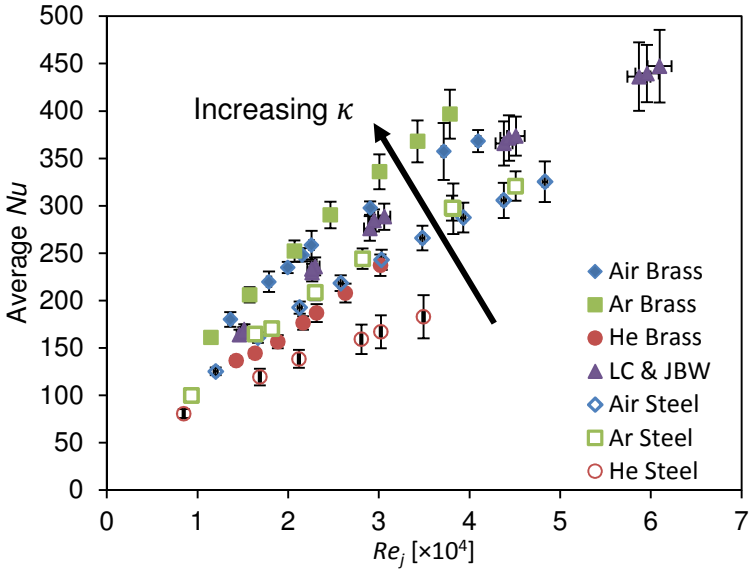

Figure 88. Average Nusselt number vs. jet Reynolds number.

Table 5. Approximate values of thermal conductivity ratio for different conditions

Structure	Gas	k_s [W/m-K]	k_g [W/m-K]	κ
Brass	Ar	135	0.018	7000
Brass	Air	135	0.026	5000
Steel	Ar	56	0.018	3000
Steel	Air	56	0.027	2000
Brass	He	135	0.16	850
Steel	He	56	0.16	370
WL-10	He (650 ℃)	115	0.33	340

As in Section 4.2, the $\overline{Nu}$ is correlated to both κ and Re_j assuming a power law using multi-linear fitting in Microsoft Excel 2010:

$$\overline{Nu} = 0.0586 \cdot Re_j^{0.669} \kappa^{0.190} \tag{73}$$

with a fitting parameter R^2 = 0.94. The $\overline{Nu}$ is plotted versus the fit in Figure 89. The correlation is shown as a solid line and the dashed lines indicate ±10% from the correlation. Nearly all of the data points fit within these bounds. The data of from Crosatti and Weathers also line up with the present data for this correlation.

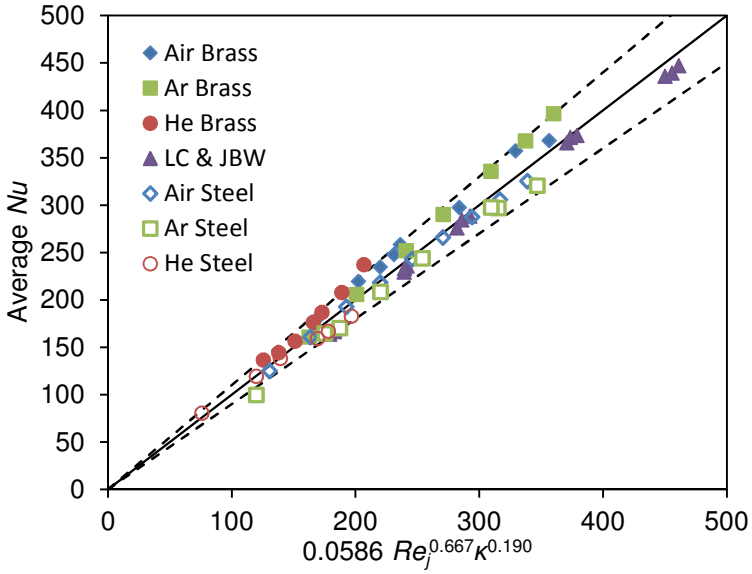

Figure 89. Average Nusselt number vs. jet Reynolds number and thermal conductivity ratio correlation. Dashed lines indicate ±10% of correlation.

4.5. Prototypical Nusselt Number

The prototypical value of κ is 340 for He at 650 ℃ and tungsten alloy WL-10 at 1100 ℃. By fixing the value of κ and plotting the above $\overline{Nu}$ correlations (Eqs. 69 and 73), the performance can be evaluated at prototypical conditions for both the HEMP-like BF configuration and the HEMJ. As shown in Figure 90, the performance prediction is significantly different when the effect of κ (i.e. conduction) is taken into account for HEMP-like BF. Near the prototypical flow rate, when conduction is ignored, the Nusselt number would be overpredicted by nearly 48%. Obviously, the importance of considering

the proportion of convective heat transfer should not be underestimated. The prediction in Figure 90 for the case without κ is based on the results of the BF air-brass simulations. Similarly, using only the air-brass experiments for the HEMJ, the *Nu* is overpredicted by at the prototypical flow rate by ~65% as shown in Figure 91.

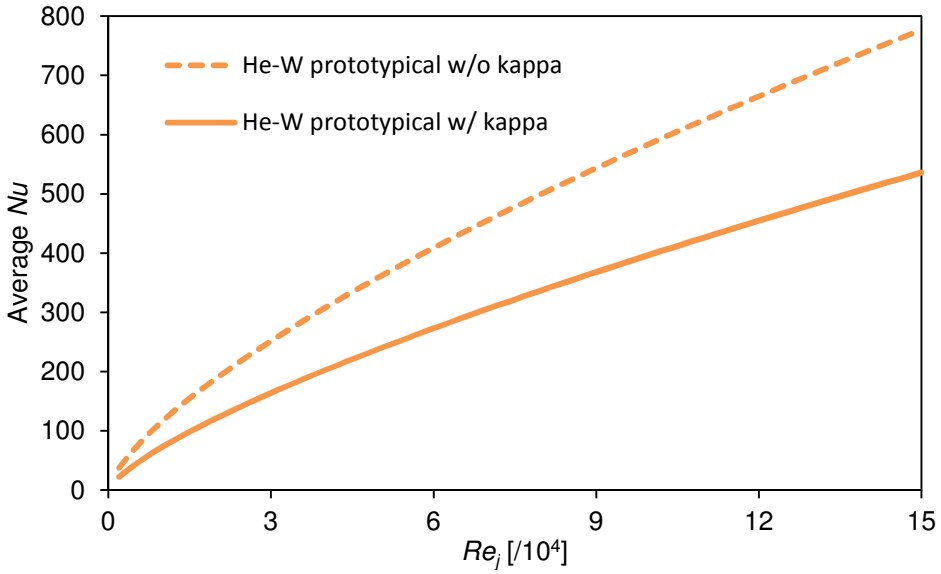

Figure 90. Average Nusselt number at prototypical κ. Calculated using correlations with and without considering the effect of κ, HEMP-like BF.

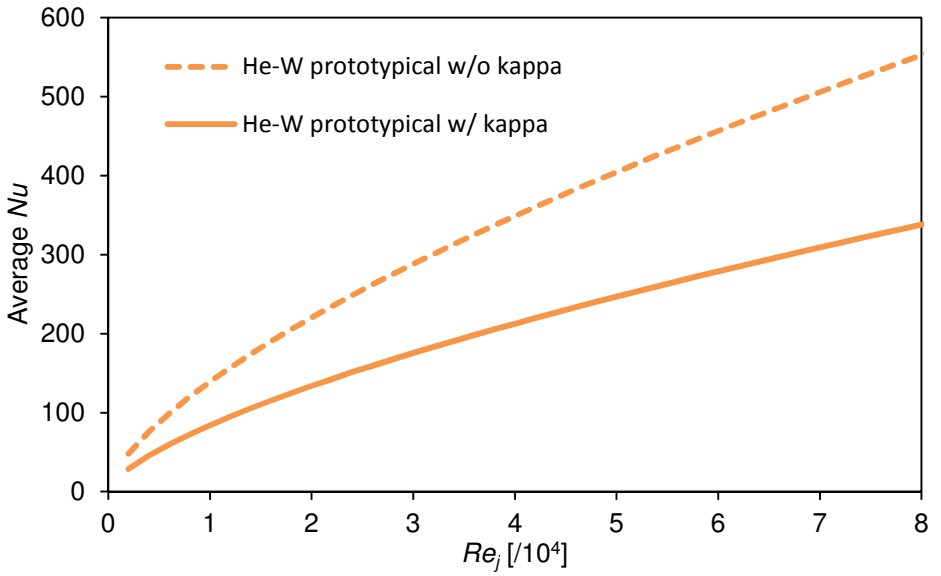

Figure 91. Average Nusselt number at prototypical κ. Calculated using correlations with and without considering the effect of κ, HEMJ.

4.6. Parametric Performance Curves

Performance curves for the HEMP-like BF configuration and the HEMJ at prototypical conditions can be generated using the correlations for $\overline{Nu}$ (Eqs. 69 and 73, respectively) and K_L (Eqs. 39 and 57, respectively). Performance predictions are presented based on three metrics as they relate to Re_j: the maximum pressure boundary temperature $\overline{T_s}$, the pumping power of the divertor system as a fraction of incident thermal power β, and the heat flux $\overline{q''}$ (either through the pressure boundary or incident on the divertor tile). The performance curves were generated assuming T_{in} of 600 ℃.

By first fixing Re_j, T_{in}, and $\overline{T_s}$, and making a guess of T_{out} and $\overline{T_c}$ (650 ℃ and 900 ℃, respectively), the value of κ is calculated and used with Re_j to calculate $\overline{Nu}$. In turn, the $\overline{h}$ is calculated followed by $\overline{q''}$, resulting in another guess of T_{out} and $\overline{T_c}$. This process, as illustrated in the flow chart of Figure 92, is repeated several times until the values in red rectangles converge. Typically, only five iterations are necessary to achieve convergence to less than 10^{-6}.

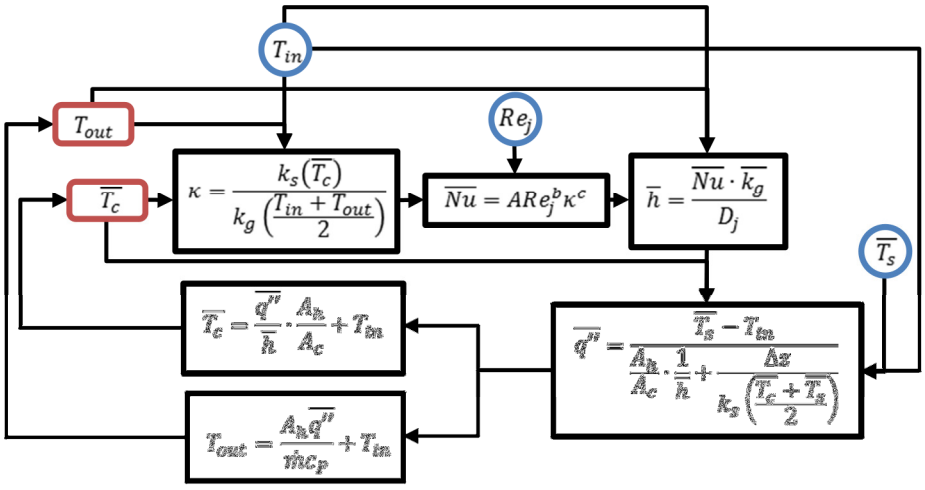

Figure 92. Lines of constant temperature flow chart for BF and BR. Fixed values are blue and initial guesses are red.

Similarly, by fixing Re_j (and thus $\dot{m}$ and K_L) and making a guess of ρ_L (5.51 kg/m^3), both V_L and Δp can be calculated. This generates a new guess for ρ_L (as $\rho_L$depends on p_{out}) based on a fixed inlet pressure of 10 MPa (the nominal operating pressure). The process, as illustrated in the flow chart of Figure 93, is repeated until the values converge. Using a fixed value of β and the calculated value of Δp, a guess is made for $\overline{\rho}$ (5.4 kg/m^3) and thus $\overline{q''}$ and T_{out} can be calculated. This process, as shown in Figure 93, is repeated until the values in red rectangles converge. As mentioned previously, only five iterations are required for convergence.

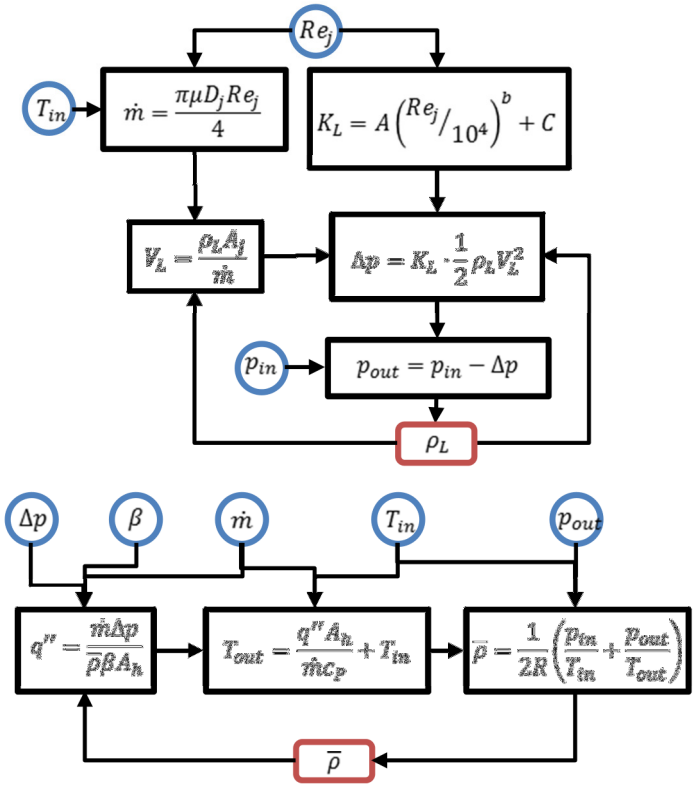

Figure 93. Flow chart for making lines of constant pumping power fraction. Fixed values are blue and initial guesses are red.

The curves are generated for fixed values of $\overline{T_s}$ 1100 ℃, 1200 ℃, and 1300 ℃ and β 5%, 10%, 15%, and 20%. The peak $\overline{T_s}$ values are dictated by the need to prevent

tungsten embrittlement by recrystallization at elevated temperatures. Figure 94 depicts the performance curves for the BF HEMP-like configuration. Lines of constant $\overline{T_s}$ are shown as solid black lines. Lines of constant β are dashed red lines.

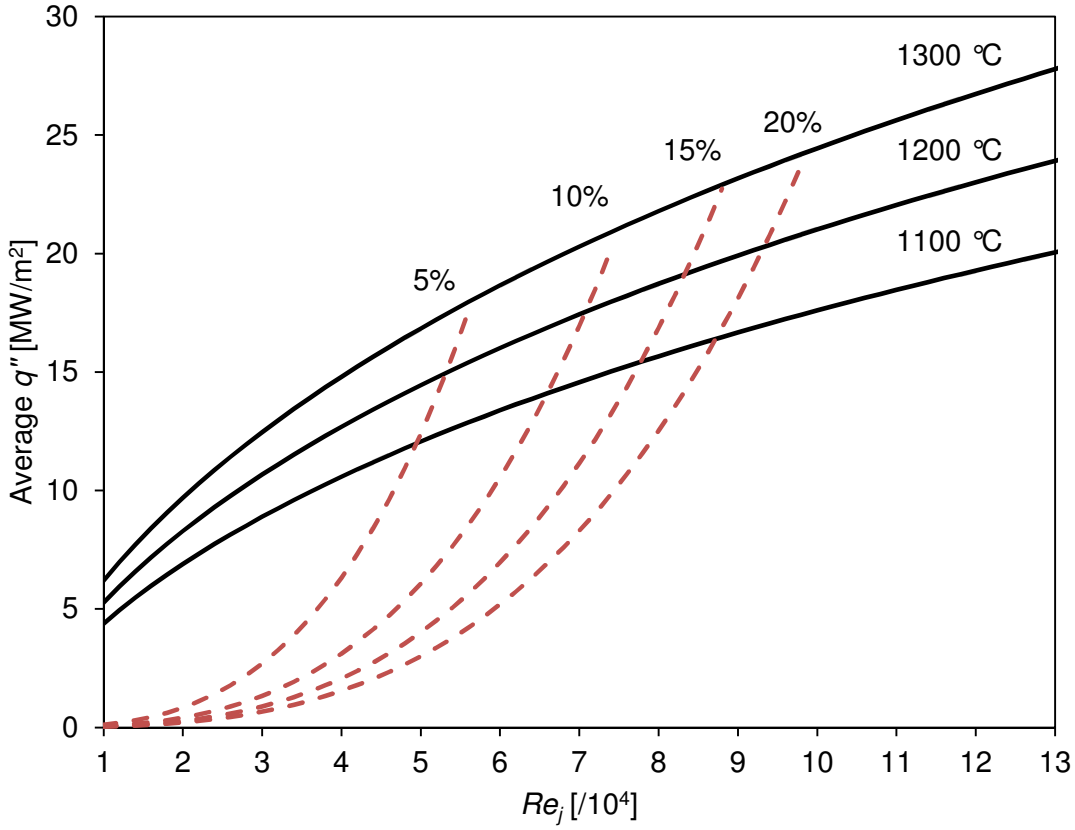

Figure 94. Prototypical performance curve, BF for He at 600 ℃ and 10 MPa at the inlet. Lines of constant heated surface temperature are black and lines of constant pumping power fraction are dashed red.

At the prototypical Re_j of 76,000, the maximum $\overline{q''}$ predicted for a $\overline{T_s}$ of 1200 ℃ is 18.2 MW/m^2. This heat flux is what is coming through the surface of the 12 mm OD finger. The prediction needs to be adjusted for the larger area of the tungsten tile to get the limiting value for the heat flux incident on the divertor. Assuming a divertor tile to finger cross sectional area ratio of 1.4, the associated heat flux incident on the divertor tile would be 13 MW/m^2. The corresponding value of β for this Re_j and $\overline{T_s}$ is ~13%.

The design curves for the HEMJ are shown in Figure 95. At the prototypical flow rate of 6.8 g/s (Re_j=21,400) and for $\overline{T_s}$ of 1200 ℃, the value of β is 8% and the predicted maximum q'' is 14.1 MW/m^2 based on the cross sectional area of the pressure boundary or 11.4 MW/m^2 based on the tile area of a hexagonal tile with flat to flat distance of 18 mm. The effect that other tile sizes would have on the divertor performance could be examined without changing the performance curves presented here. The value of q'' predicted by the curves would just have to be adjusted for the area ratio of the tile to the endcap.

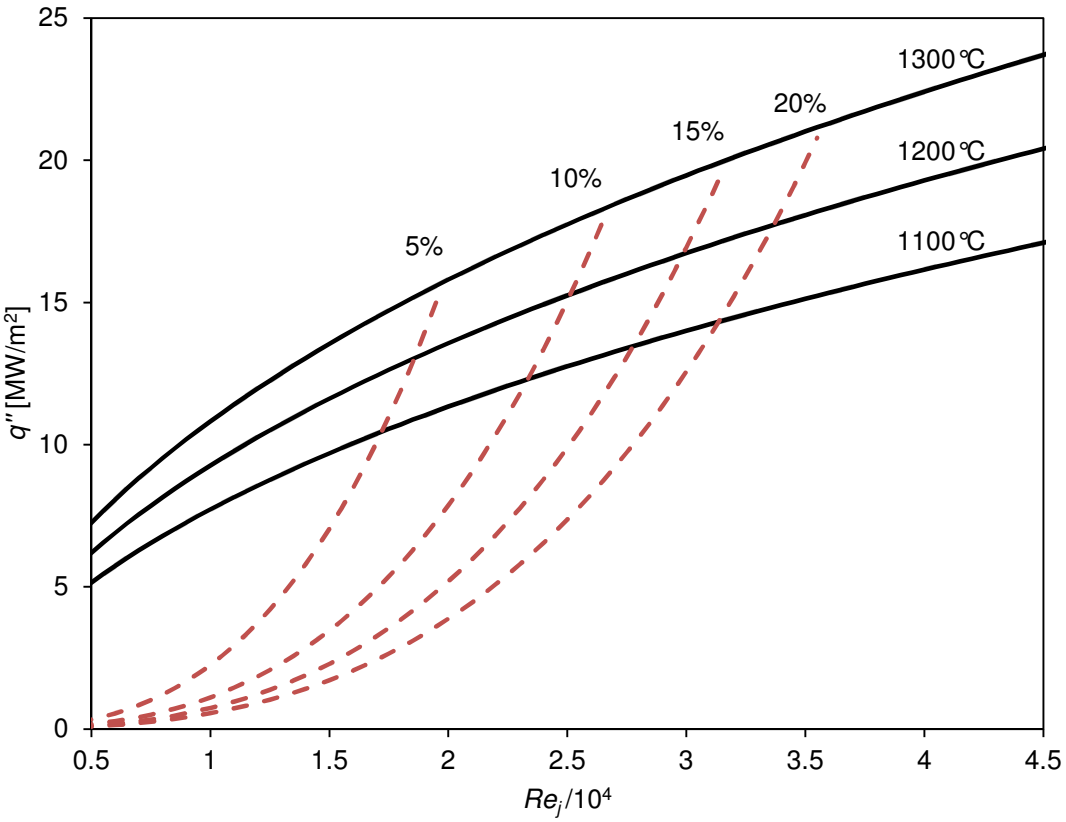

Figure 95. Prototypical performance curves for HEMJ for He at 600 ℃ and 10 MPa at the inlet. Lines of constant average heated surface temperature in solid black and lines of constant β in dashed red.

It should be noted that the values of $\overline{q''}$ referenced here do not account for effects such as reradiated power from the divertor tile. These correlations are designed to be independent of these effects and thus only use the OD of the finger itself for calculating the performance. This leaves it up to the designer for the entire divertor system to choose the tungsten tile area. The performance correlations for the BF HEMP-like and HEMJ finger designs could thus be used with tungsten tiles of varying size. Areas of the divertor with lower predicted heat fluxes could possibly use larger tiles. This recommendation ignores effects of thermal stresses which tend to limit the size of the tungsten tiles.

4.7. Effect of Inlet Temperature

As the proposed prototypical operating conditions for the divertor continue to evolve, the methods used to produce the performance curves for these divertor designs can be used to analyze the effect of changing system parameters. One useful example is the effect that raising the operating inlet He temperature from 600 °C to 700 °C would have on the thermal performance of the divertor. Changing the inlet temperature affects several parameters used in the calculation of the prototypical performance curves. For example, the viscosity of He increases with temperature which affects the calculation of Re_j, which in turn affects K_L and $\overline{Nu}$. The result is a decrease in the value of $\overline{q''}$ that can be accommodated at a fixed $\overline{T_s}$ compared to an inlet temperature of 600 °C. Performance curves were generated assuming a He inlet temperature of 700 °C and are shown in Figure 96.

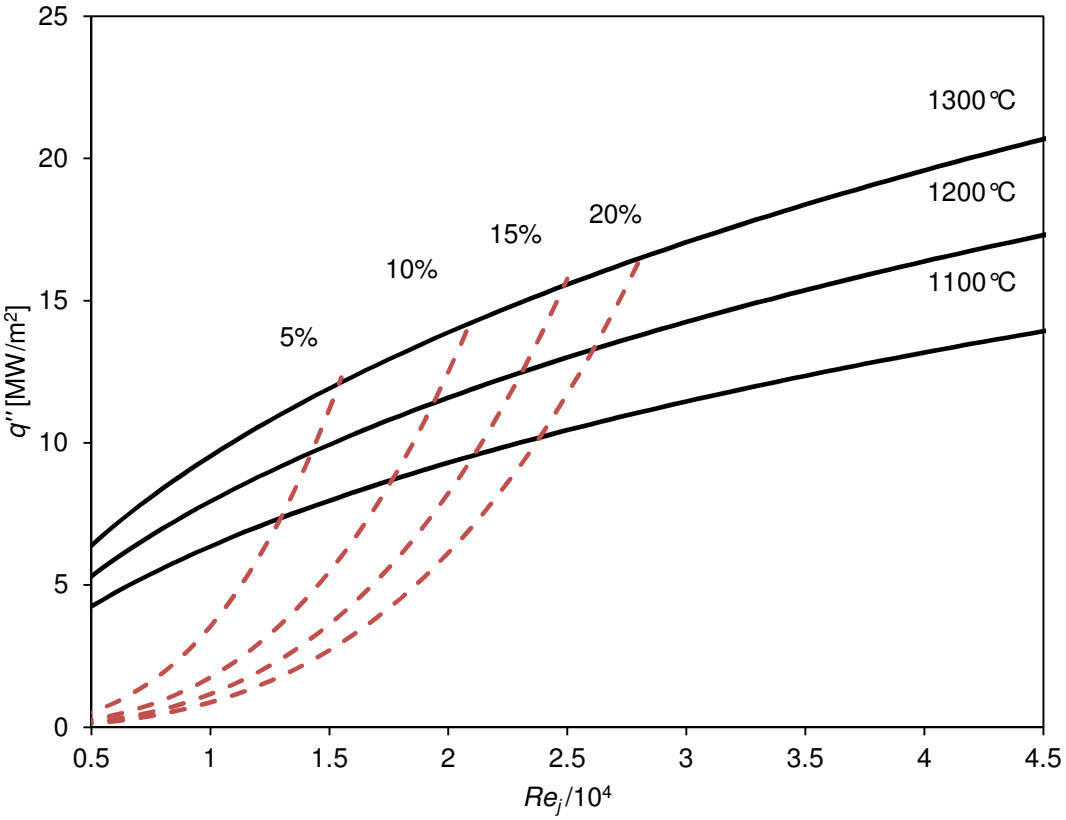

Figure 96. Prototypical performance curves for HEMJ for He at 700 ℃ and 10 MPa at the inlet. Lines of constant average heated surface temperature in solid black and lines of constant β in dashed red.

The increase in viscosity translates to a decrease in the prototypical Re_j from 21,400 to 19,840 assuming the same $\dot{m}$ of 6.8 g/s. Now, at the prototypical flow rate assuming a $\overline{T_s}$ of 1200 ℃, the maximum accommodated $\overline{q''}$ is ~11.5 MW/m^2. This corresponds to a tile heat flux of 9.3 MW/m^2. The corresponding value of β is ~11%. Compared to the 600 ℃ inlet condition, this is a 18.5% decrease in $\overline{q''}$ and a 37.5% increase in β (3% when comparing 8% and 11%). Increasing the inlet temperature is thus a significant factor concerning the thermal performance of the divertor. The minimum Re_j required to accommodate 10 MW/m^2 tile heat flux for $\overline{T_s}$ of 1200 ℃ is 22,800, which corresponds to a $\dot{m}$ of 7.8 g/s (a 14.7% increase).

4.8. Summary

Numerical simulations were performed to examine the details of the HEMP-like divertors without fins. The simulations show that a significant portion of the heat removed by the coolant is added at locations other than the cooled surface after it had been conducted through the divertor walls. The percentage varies depending on the flow rate and the particular flow configuration. The performance predictions for the BF configuration with an impinging jet and without fins show that not accounting for the conduction up the walls of the finger will result in nearly a 50% overprediction of the convective heat transfer coefficient of the divertor. Numerical simulations showed that the HEMP-like divertor performance can be evaluated using both the non-dimensional mass flow rate, Re_j, and the thermal conductivity ratio of the structure to the coolant, κ. The implications of the numerical study on the HEMP-like divertor require that previously studied, finger-type divertors be reevaluated to account for heat conduction and subsequent convection to the coolant along the sides of the finger. As this result has implications for other divertor designs, the HEMJ divertor, studied previously at Georgia Tech, was reexamined using the updated methodology.

Overall, the study of the HEMP-like divertor configurations resulted in several key developments. Firstly, 2D models have been verified against the experiments for the BF and BR configuration. Using the Spalart-Allmaras model, many of the simulations showed average HTCs within the experimental uncertainty for the BF configuration. The BR configuration was modeled best with the RKE model. Many of the HTCs predicted by the BR simulations fell within the experimental uncertainty as well. The pressure drop predicted by both the BF and BR simulations often overpredicted the pressure drop observed experimentally. This is not inconsistent with previous work using FLUENT to model pressure drop for the T-Tube, HCFP, and HEMJ divertor designs. Using details

extracted from the results of the simulations, it appears that the pressure drop for the BR configuration can be significantly reduced by optimizing the diameter of the inlet/outlet orifice, where most of the pressure drop for the BR configuration occurs. However, the poor thermal performance of the BR configuration makes the importance of such study very low. The BF configuration would also benefit from a port geometry optimization in order to minimize the pressure drop while maintaining thermal performance.

Also, the HEMP-like design needs to be studied with further experiments to confirm the results obtained using the numerical model regarding the effect of the thermal conductivity ratio between the coolant and finger. Specifically, experiments should be performed using various combinations of coolant and structural materials to cover a wide range of thermal conductivity ratio. Further numerical simulations should be performed using the models with fins to determine the effect on the finned geometries. It is likely that the effect will be different as the fins draw more energy through the cooled surface. As the air cooled experiments of Chapter 3 showed that the combination of impinging jet and fin array did not lead to significant performance improvements (compared to the finned configuration without an impinging jet), perhaps under prototypical conditions, the results would be different. Quantifying this difference and extrapolating to prototypical conditions will have a significant impact on the viability of the HEMP and designs like it as a divertor. It is likely that different effects would be seen as the fins tend to increase the heat transfer rate from the cooled surface than the finless configurations, i.e. conduction effects along the side walls will likely be less important. Also, a helium cooled design would be expected to have low fin efficiency as the HTCs anticipated for a helium-cooled design are much larger than those of the experimentally tested air-cooled design.

The effect of the heated surface heat flux peaking factor on two material combinations that are at either end of the range of κ proposed to be experimentally

tested show that the effect of peaking factor on the predicted surface temperatures, and average HTCs are small. The 6 mm of brass or steel on the closed end of the finger allows for sufficient conduction to even out of the incident non-uniform heat flux profile. A longer finger-tip may be useful for any steel HEMP experiments as the extra length allows for more heat flux smoothing to occur on account of AISI 1010 steel having a lower thermal conductivity than C36000 brass. This result shows that uncertainty regarding the extent of non-uniformity in the heat flux provided by the oxy-acetylene torch will have little impact on the experimentally measured values of average HTCs.

Prototypical performance curves have been generated for the BF configuration using the results of the simulations based on the experiments and further experiments used to characterize the effect of κ on the thermal performance. The results shows that near the prototypical flow rate, a maximum heated surface temperature of 1200 °C can be accommodated with a heat flux of 18.2 MW/m^2 and a coolant pumping power ratio of ~13%. This heat flux does not consider the plasma-facing tungsten tile area which can be adjusted to give the desired performance. The performance curves allow fusion reactor system designers to easily incorporate the HEMP-like divertor. After the other HEMP-like configurations are investigated in more detail, performance curves for those designs can be generated as well.

Further analysis on the HEMJ divertor confirmed the predictions made regarding the change in heat transfer path through the divertor based on the ratio of the thermal conductivity of the structure to the coolant. Following the correlation of the thermal performance of the HEMJ to the flow rate (i.e. Reynolds number) and conductivity ratio, prototypical performance curves were created that allow the designers of MFE reactor divertor cooling systems to better predict the performance of the HEMJ. These performance curves predict HEMJ cooling capability quite similar to that already achieved in other experimental studies.

Now that the predictions following the HEMP-like divertor study have been extended successfully to another divertor design, further studies on other previously studied divertors should be performed. These include the T-Tube and the HCFP. As these test sections are larger and require a higher mass flow rate than is achievable using the experimental methods of Chapter 3 (namely a once-through flow line from gas cylinders), a CFD study could be performed to determine each design's specific characteristics. Following these studies, prototypical performance curves for these designs to predict the maximum allowable heat flux and the corresponding pumping power fraction for various operational and design constraints could be developed.

CHAPTER 5: THREE-DIMENSIONAL SIMULATIONS AND FIN ARRAY OPTIMIZATION

This Chapter details the numerical modeling of the HEMP-like divertor test modules with fins. Also, a fin array optimization is performed at prototypical conditions using modified versions of the same model.

5.1. 3-D HEMP-like Numerical Model

Modeling of the divertor modules with fins requires a three-dimensional (3D) model. Similar to the 2D models of Chapter 4, the 3D models include the 50 mm of the test section nearest to the heated surface and were created with ANSYS 14 and tested with ANSYS FLUENT 14. As the 3D models have a large number of cells, they necessitate the use of a variably sized and unstructured grid with the highest resolution in the area of the cooled surface and the fins in order to better resolve the near wall behavior and heat transfer performance of the fins. Similar to the 2D cases, the models use enhanced wall treatment. The grids reach a resolution of 50 μm on the surface of the fins and the cooled surface area not covered by the base of the fins and expands to a resolution of 250 μm near the inlet and outlet. Even with care taken to decrease the resolution of the grid in areas of least importance, the grids have ~1M cells. The 2D simulations used a resolution of 25 μm. Making a 3D grid with a 25 μm resolution near the cooled surface would result in too many cells for the computational resources available. As the results of the 2D simulations with a 50 μm grid were not very different from the 25 μm grid in predicting the average values of cooled surface temperature and HTC, the 50 μm resolution was assumed to be acceptable for the 3D study. The minimum cell volume for the 3D grid was 2.49×10^{-16} m^3 which is near the limit of a double precision calculation of $2^{-52} \approx 2.22\times^{-16}$.

Cells near fluid/solid interfaces were constructed using ANSYS's inflation algorithm. This creates cells aligned with the expected direction of the flow in the boundary layer. Resolving the flow behavior in the boundary layer is critical to accurately predict the heat transfer from the cooled surface and the fins as well as the pressure drop through the narrows gaps between fins. The Advanced Sizing Function of ANSYS was also used to ensure that cells near two or more volumes were properly resolved. A screen capture of one of the symmetry faces of the grid is shown in Figure 97 focusing on the area near the fins. The small cells attached to the fluid/solid boundaries are clear. The same grid was used for all of the flow rates tested even though the near wall behavior may be different. This was done for consistency yet may result in increased departure from the experimental predictions especially at higher flow rates where the effects of near wall turbulence are more significant.

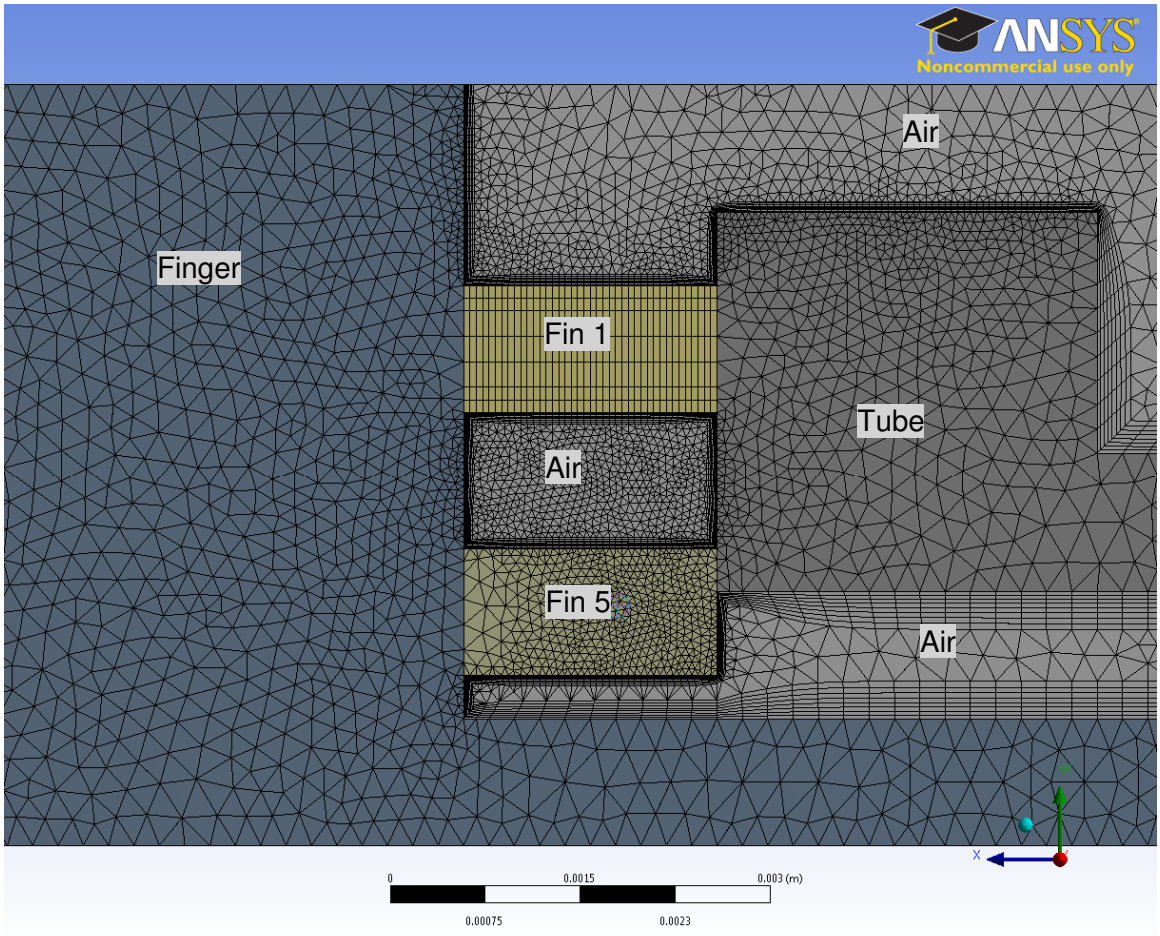

Figure 97. 3D fins grid along a 30° symmetry line (see Figure 98).

Figure 97 shows that the end of the tube is assumed to be in perfect contact with the tops of the fins. All simulations assumed that the fin tips were in direct, physical contact with the tube, though the amount of heat transfer allowed to occur from the fins to the tube was chosen to be either perfectly conducting or adiabatic. The implications of this assumption are discussed in more detail later in the section. The uncovered portions of the tops of the outermost fins (4, 5, & 6) were allowed to participate in heat transfer for all simulations.

As shown in Figure 97, the 'Air' volume appears to be split though it is actually continuous as shown in Figure 98. The locations of all of the 'Fin' volumes can be clearly

seen as well in Figure 98. The ‘Tube’ and ‘Air’ volumes have been removed from Figure 98 to make it easier to see the Fin volumes. Figure 98 also serves to shows the other symmetry plane not depicted in Figure 97. It is clear that there are some small gaps between the fins that must be resolved with many cells to accurately predict the flow field and heat transfer.

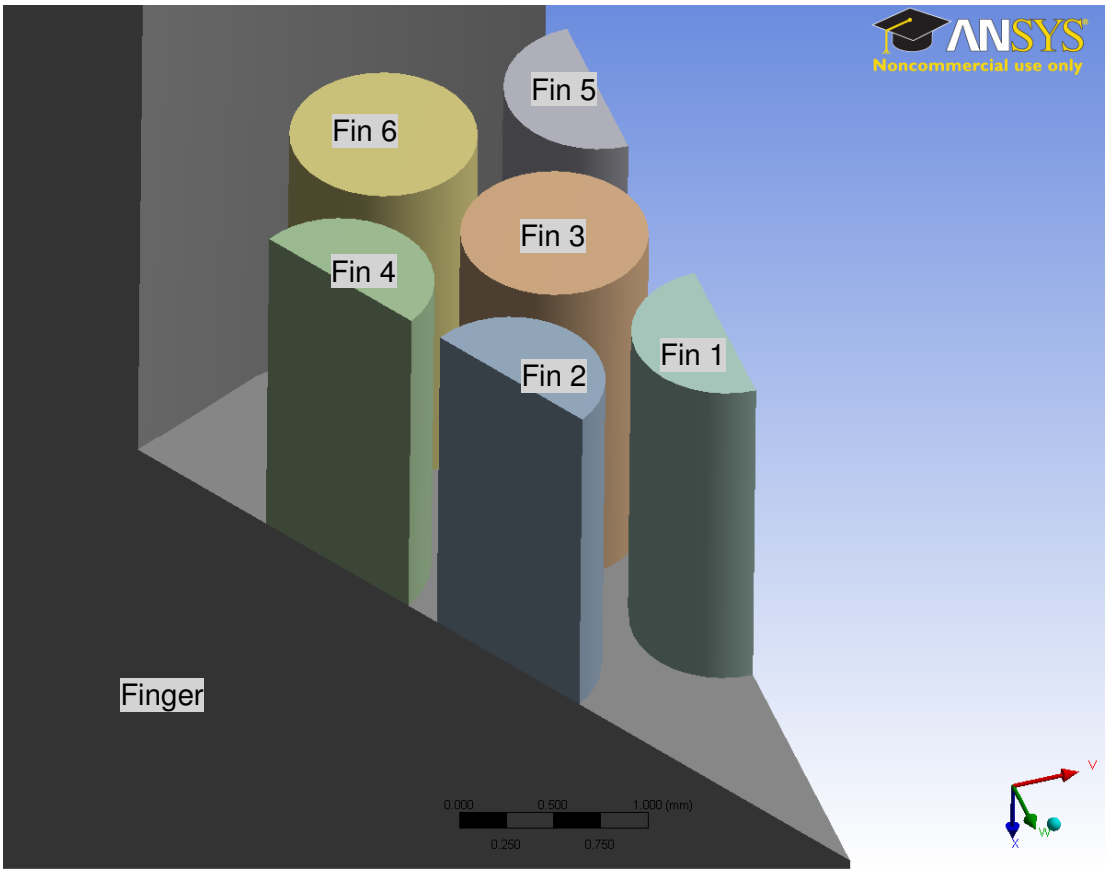

Figure 98. View of all of the fins attached to the finger.

The geometry of the fin array allows for a 30° symmetric model. The boundary conditions for the 3D model are similar to the 2D model except that symmetry conditions are required on the symmetry boundaries. Also, a mass flux boundary condition is used at the inlet instead of mass flow rate. The fins are assumed to be in perfect contact (though non-conducting) with the inlet tube for these initial tests. Results of each 3D simulation were compared to the experiments using the average cooled surface

temperature including the base of the fins. For an entire spectrum of tests, the results were compared using the effective average heat transfer coefficient as if the fins were not present. Figure 99 provides a visual explanation of the areas used in this calculation. The temperature was averaged over the prime and fin base areas. The sides and tops of the fins were not considered when calculating the effective heat transfer coefficient. However, the temperature and heat flux through the sides of the fins can be used to calculate the fin efficiency or fin effectiveness.

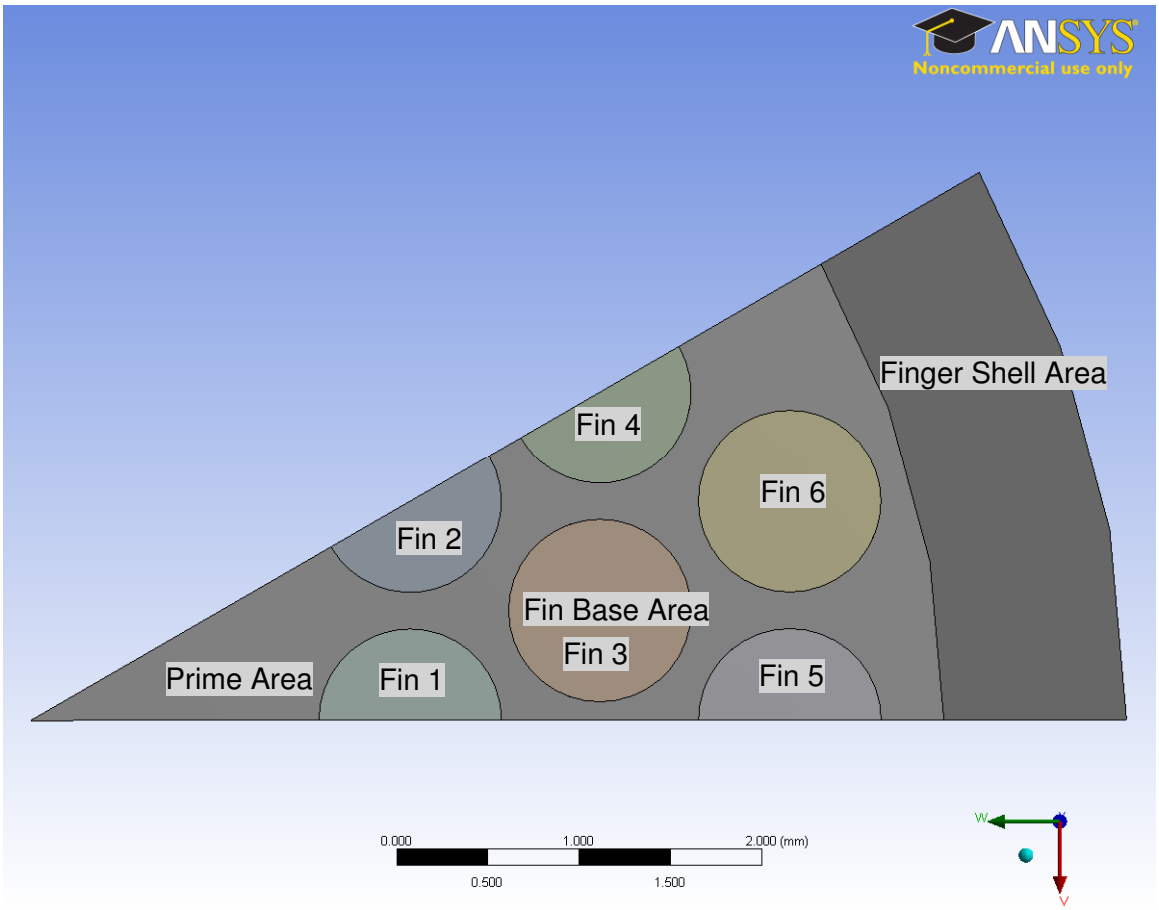

Figure 99. Area definitions for FF and FR models at the cooled surface.

The tops of the fins are shown in Figure 100. The line marking the outside of the tube is shown on the tops of Fins 4, 5, and 6. It is apparent that the outer fins (4, 5, and 6) do not make complete contact with the tube. That is, the tube only covers some of the

fin tip. The tips of fins 5 and 6 in fact make hardly any contact with the tube at all. This plays an important role in the heat transfer predictions of the FR configuration, as the inlet air stream impacts directly on top of these fins.

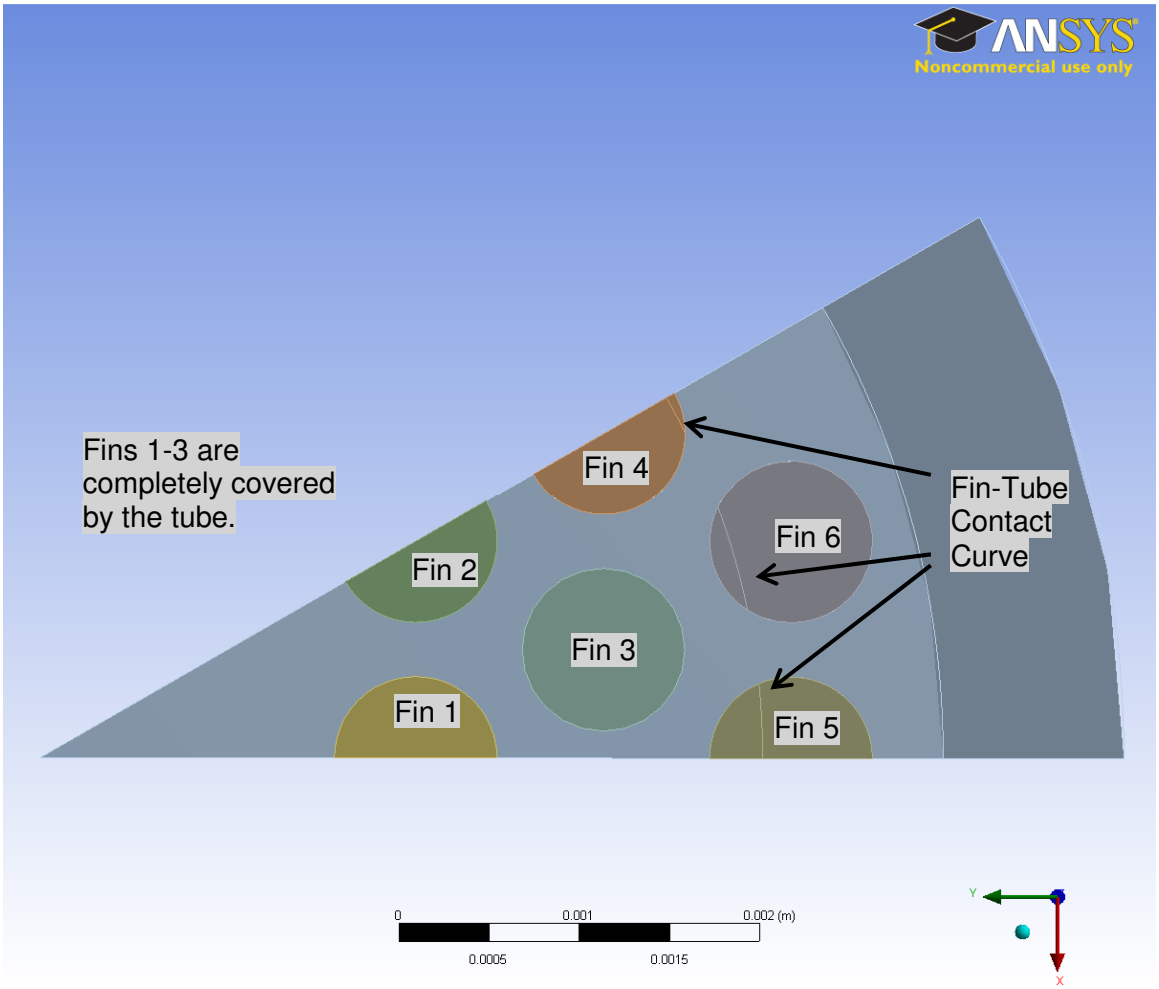

Figure 100. Top view of the fins showing the amount of fin tip to tube contact.

Figure 101 shows the boundary conditions of the 3D simulations. At the inlet, the mass flux, inlet temperature, and turbulence parameters are set. The outlet pressure is set on the face of the outlet. A symmetry condition is used for the faces of the air, fins, tube, and finger volumes on the symmetry planes. The fin tip condition can be adjusted manually using the 'coupled wall' boundary condition in FLUENT. As with the 2D simulations, all 3D simulations included effects due to buoyancy and viscous heating.

Near-wall pressure gradient and heat transfer effects are accounted for using the methods proposed by [48] and [49].

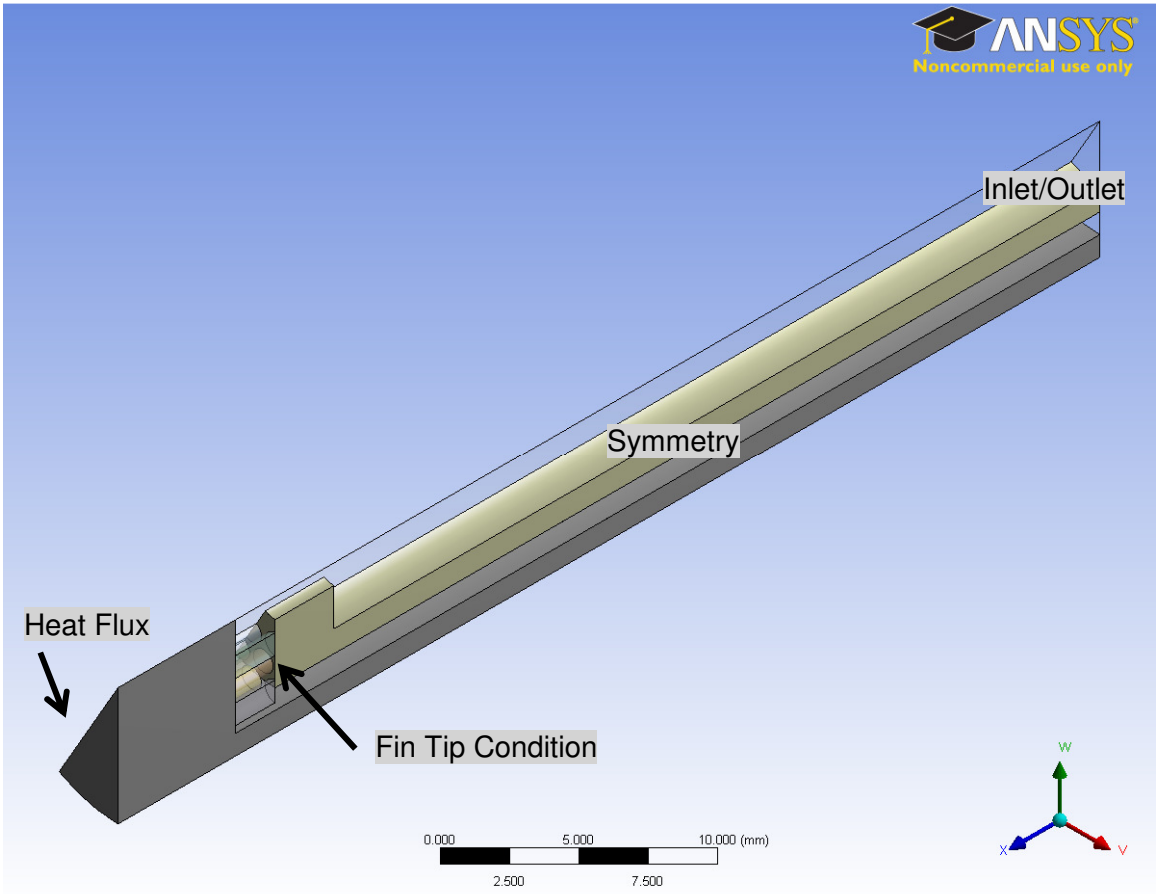

Figure 101. Entire 30° model with boundary conditions.

A turbulence model study was completed similar to that performed on the 2D model but for the FF reference case. The reference cases for FF and FR are given in Table 6. The results of the forward flow turbulence model study are shown in Figure 102. The RKE model predicted temperatures closest to the experimental values compared to the SKE and RNG models. It could be argued, however, that none of the models represent the experimental results well as the experimental cooled surface temperatures are in the range 150-155 °C.

Table 6. Parameters of reference cases used for 3D numerical simulations

Case #	Configuration	$\dot{m}$ [g/s]	Re_j [×10^4]	$\overline{q''}$ [MW/m^2]
393	FF	2.24	7.80	0.920
273	FR	2.48	7.57	1.227

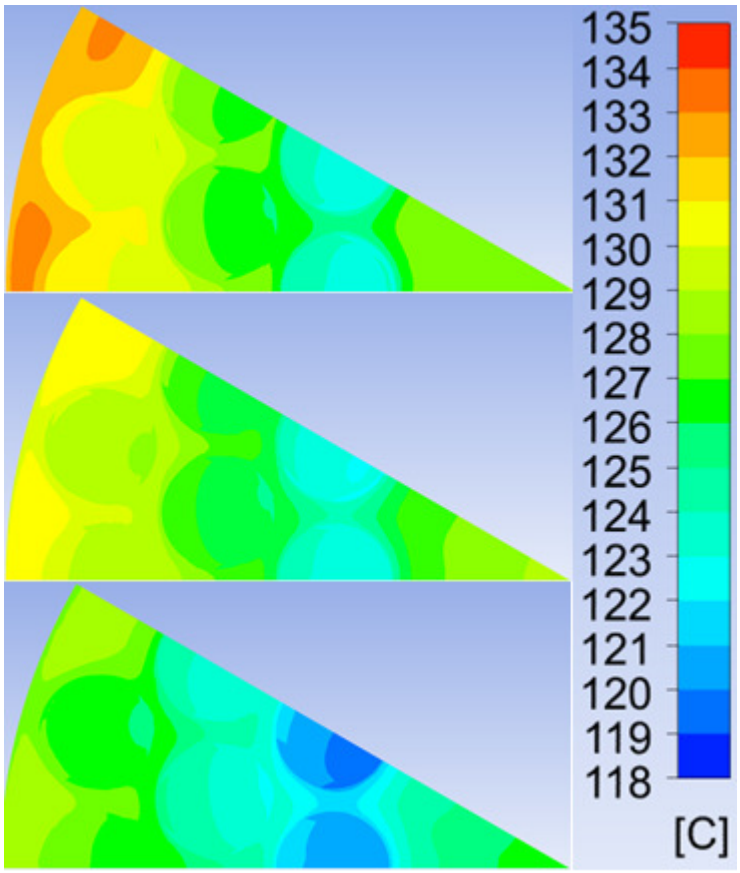

Figure 102. Cooled surface temperatures from turbulence model study FF. The figures from top to bottom are RKE, SKE, and RNG.

The results of the reverse flow study for the FR reference case are shown in Figure 103. Similar to the FF model the RKE model compared best for the FR configuration (though all of models produced reasonably close results with the cooled surface temperatures from the experiments ranging from 184-189 ℃). The S-A numerical solutions for the finned configurations were oscillatory and was not considered as they could not be relied upon to produce consistent results. The simulations modeled

with S-A never converged (and were not converging) after even 9000 iterations whereas the other simulations usually took less than 5000 iterations to converge.

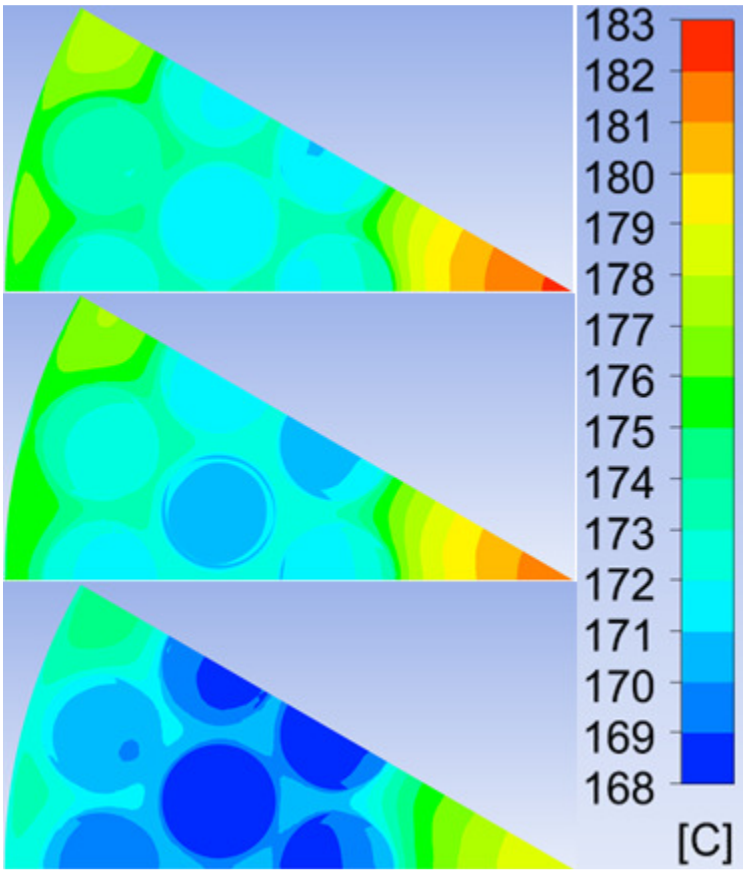

Figure 103. Cooled surface temperatures from turbulence model study FR. The figures from top to bottom are RKE, SKE, and RNG.

The RKE model was thus selected for the FF and FR studies over the entire range of $\dot{m}$. The two reference cases were chosen as they have similar mass flow rates (2.2-2.4 g/s) compared to the reference cases for BF and BR (Table 2), and that are in the middle of the range of mass flow rates tested, which in turn means their Re_j is similar to the prototypical value. All turbulence model studies shown in Figure 102 and Figure 103 assumed the fin tips to be adiabatic.

An important part of modeling the cases with fins is the fin tip condition. Contact between the fins with the tube in the test section (Chapter 3) was examined by coating

the tip of the inlet tube with soot and then assembling the test section. The tube was compressed onto the fins so that contact would be indicated with smudging of the soot. The tube was removed and the amount of smudging of the inlet tube tip was observed. A photograph of this test is shown in Figure 104.

Figure 104. Photograph of sooted tube tip after compressing onto fin tips.

The results indicate that perfectly conducting fin tips is not a good assumption; however, some amount of contact should be assumed. By performing simulations with both perfectly conducting and adiabatic fin tips, it was hoped that the two sets of results would bracket the experiments. For the simulations covering the entire spectrum of $\dot{m}$ the fins were left in perfect (though non-conducting) contact with the tube. The effective HTC versus $\dot{m}$ for the two fin tip conditions for FF and FR are shown in Figure 105 and Figure 106, respectively. As shown, the fin tip condition makes a significant difference when modeling the FF and FR configurations.

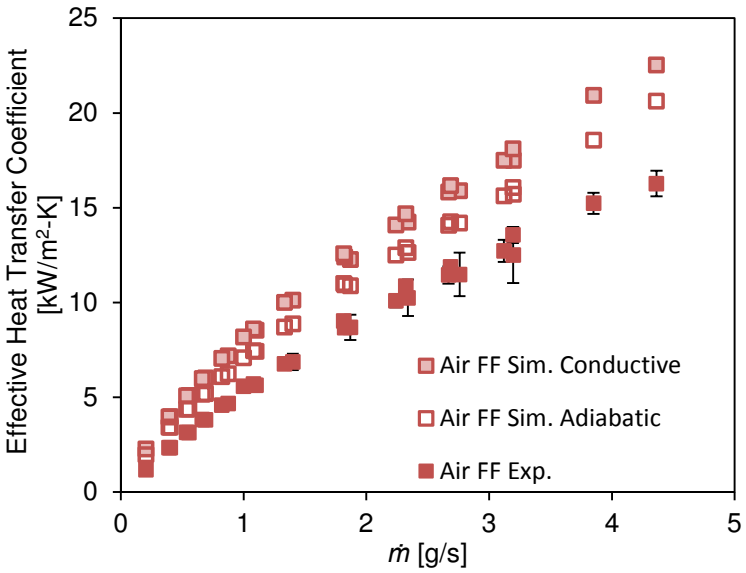

Figure 105. Adiabatic and perfectly conducting fin tip comparison for FF.

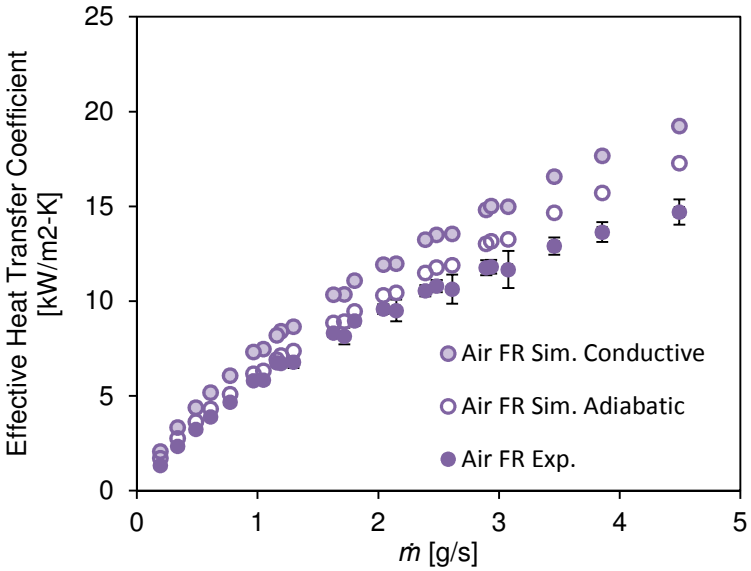

Figure 106. Adiabatic and perfectly conducting fin tip comparison for FR.

The percent difference in the prediction of the average effective HTC for the adiabatic fin tip simulations is shown in Figure 107 for FF and Figure 108 for FR. As shown, the percent difference for FF levels out near 20% for higher flow rates. The FR simulations do not show the same effect. Unlike the BF and BR simulations, there is no apparent trend between the “high” and “low” heat flux or fixed inlet pressure cases

comparing the trends in the predicted deviation of the effective average HTC predicted by simulations compared to the experiments.

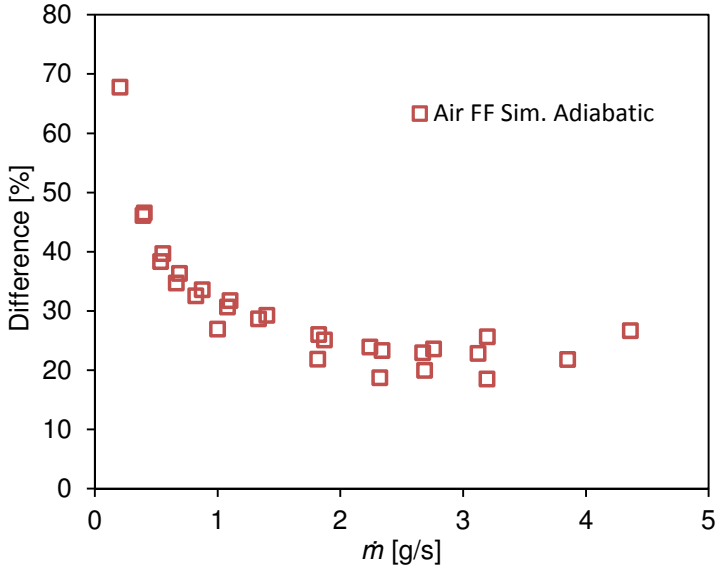

Figure 107. Percent difference in the average effective HTC for simulations from experiment vs. mass flow rate, FF.

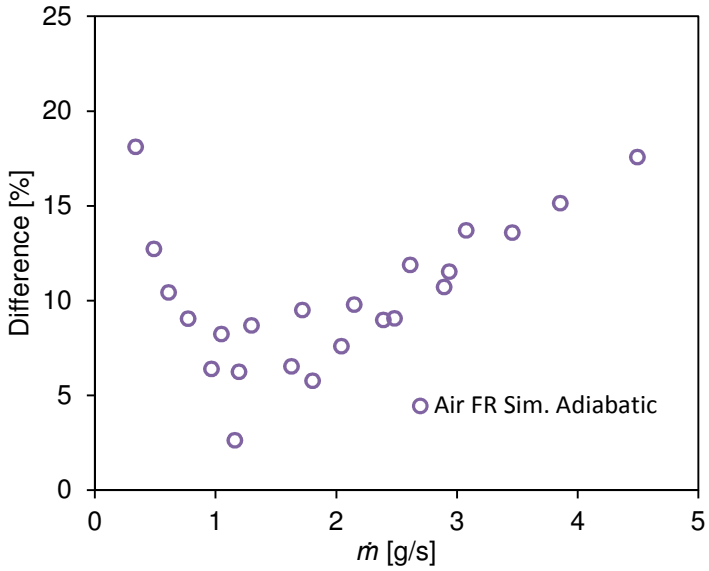

Figure 108. Percent difference in the average effective HTC for simulations from experiment vs. mass flow rate, FR.

The normalized pressure drop, $\Delta p'$, was also calculated for the simulations and compared to the experiments. The comparison between the experiments and simulations for FF and FR can be seen in Figure 109 and Figure 110, respectively.

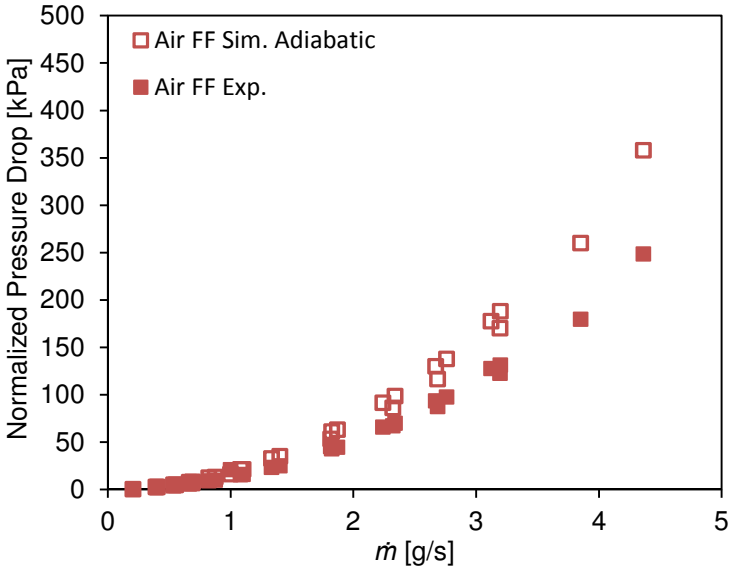

Figure 109. Normalized pressure drop comparison, FF.

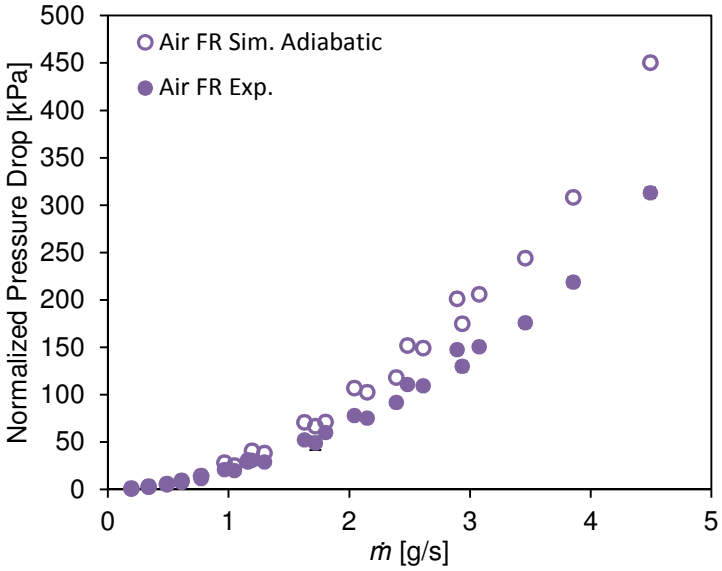

Figure 110. Normalized pressure drop comparison, FR.

The pressure drop is typically over-predicted by the simulations. For the FF configuration, an overprediction of up to 45% is seen at high flow rates as shown in

Figure 111. For the FR configuration, the simulations range from an 11% underprediction at low flow rates to a 44% overprediction at high flow rates as shown in Figure 112. For comparison, FLUENT simulations performed by Gayton [30] on the HCFP showed an over prediction of pressure drop by as much as 400%. Crosatti's [16] FLUENT model underpredicted the pressure drop through the HEMJ by 12-25%. As shown previously in the BR simulations, there is a dependence on the deviation predicted in the pressure drop based on the inlet pressure for the FF and FR configurations.

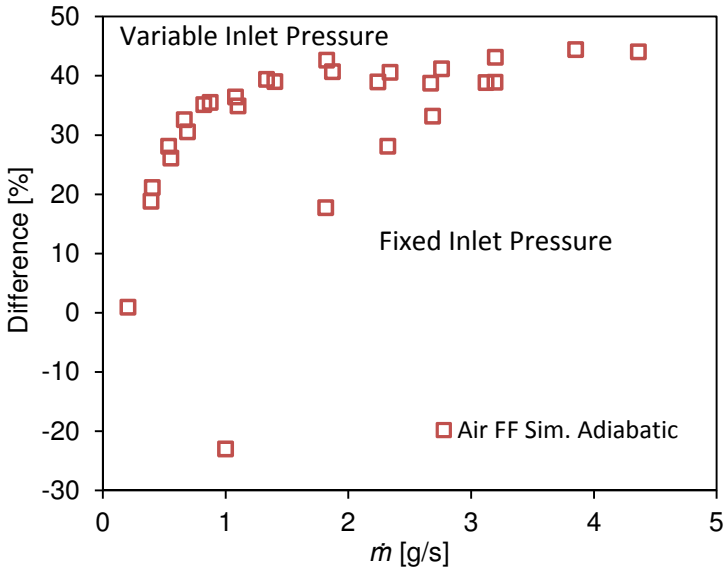

Figure 111. Percent difference of the normalized pressure drop for simulations from experiment vs. mass flow rate, FF.

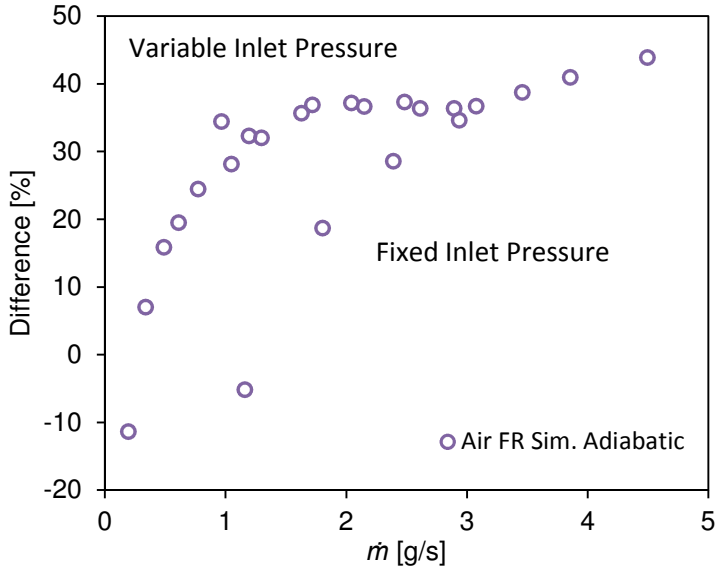

Figure 112. Percent difference of the normalized pressure drop for simulations from experiment vs. mass flow rate, FF.

The effective HTC for the FF configuration on the cooled surface is shown in Figure 113. It should be noted that the HTC values shown in the figure are not the "true" HTC values. Those data points represent the effective HTC, i.e. the HTC that would be present if the fins did not exist and surface temperature and heat flux were the same. The peak HTC for the region before fins 1 and 2 is similar to that seen for the BF reference case which has a very similar mass flow rate. However, once the air reaches the fins it is accelerated between fins 1 and 2 and a second maximum in HTC that is higher than the first is observed.

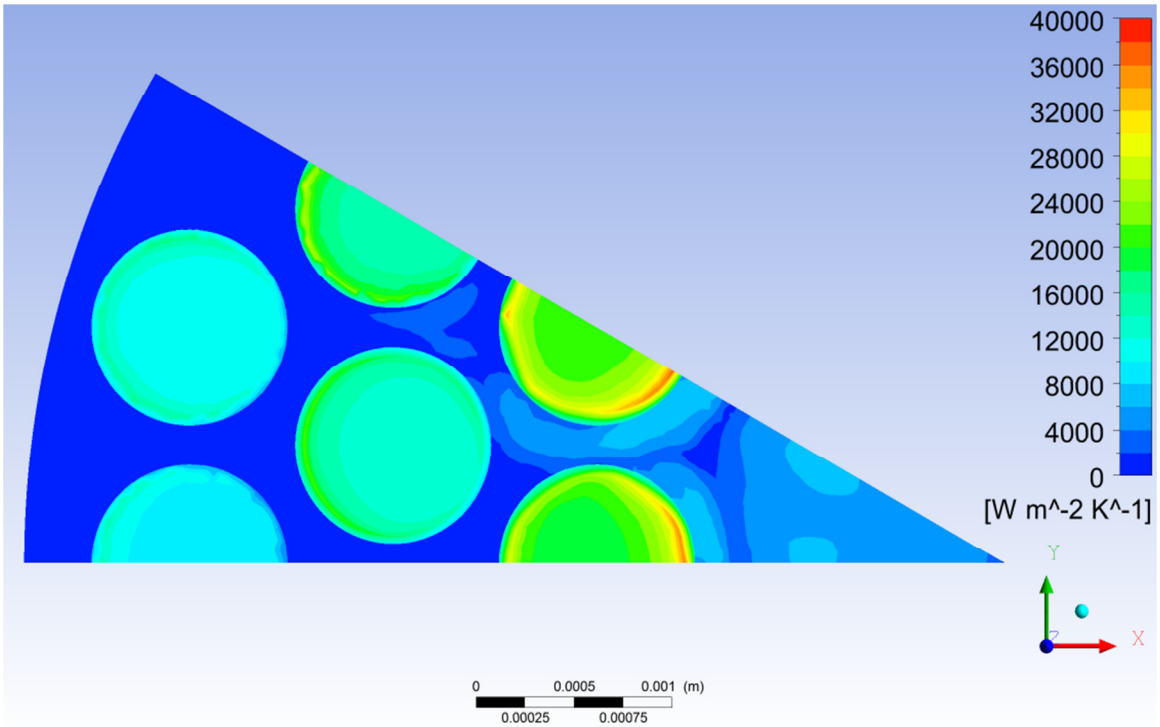

Figure 113. Effective HTC for cooled surface vs. radial coordinate, FF reference case.

The temperature distribution and local HTC on the surface of fins #1, 3, and 5 for the FF reference case is shown in Figure 114 and Figure 115, respectively. The high conductivity of the fins keeps the thermal gradients smooth on the surface of the fins. The front surfaces of Fins 1 and 3 show elevated HTC with the maximum occurring on Fin 1 where the wall jet impacts it. The regions at the base of fins 2, 4, & 6 were left out of Figure 115 as only fluid-solid interfaces are shown. The effective HTC at the base of the fins is so much larger than the actual HTC on the surface of the fins, the scale would have to be skewed too much in order to cover the entire range of HTC and still have the Figure be informative. Subsequent Figures of the local HTC values on the fin surfaces take a similar approach.

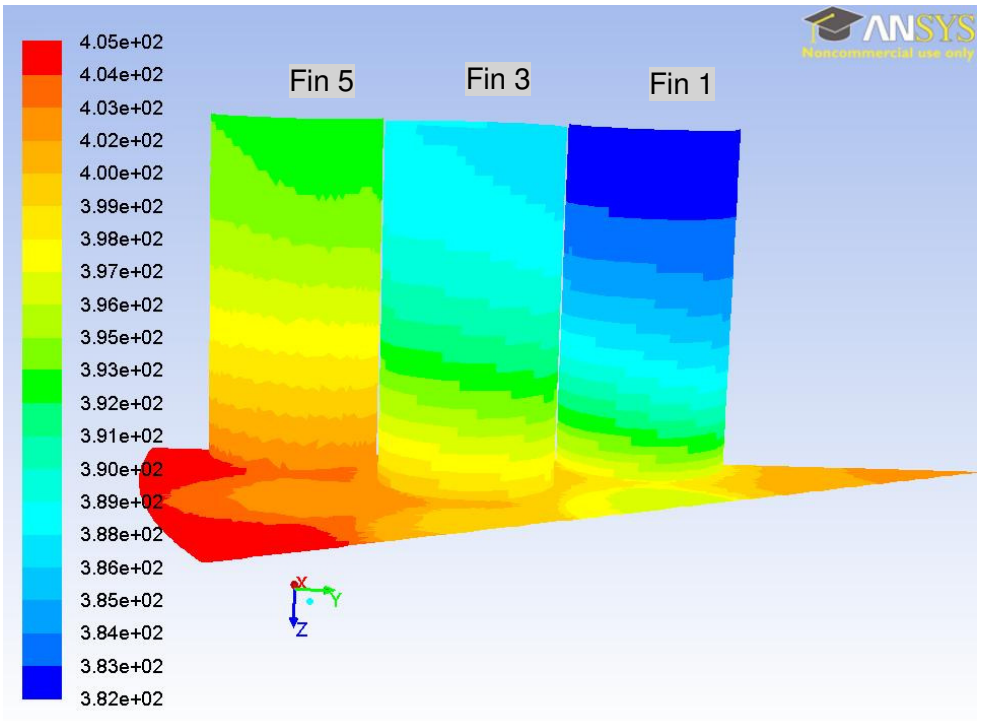

Figure 114. Surface temperature distribution of cooled surface and fins 1, 3, & 5, FF reference case. Scale in units of K.

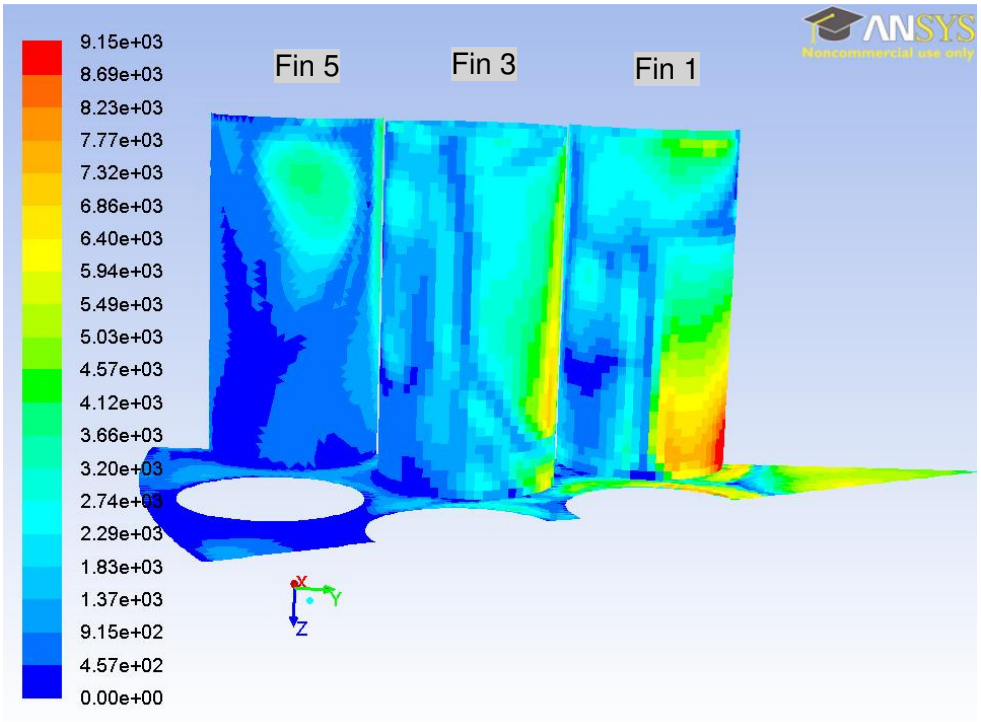

Figure 115. Surface HTC distribution of cooled surface and fins 1, 3, & 5, FF reference case. Scale in units of W/m^2-K.

The temperature distribution and local HTC for fins #2, 4, & 6 are shown in Figure 116 and Figure 117. Like Fin 1, Fin 2 shows a peak in the HTC where the wall jet emerging from the central orifice impacts the side of the fin. The HTC over the entire front surface of Fin 2 is elevated. Some of the air that goes between Fins 1 and 2 impacts Fin 4 which also shows elevated HTC. Only a small part of Fin 6 shows elevated areas of HTC. This is also apparent in the temperature of Fin 6 which is the highest of the three fins depicted. Additionally, the air impacting Fin 6 is at an elevated temperature, having passed several fins, thereby reducing the surface heat flux and thus the HTC.

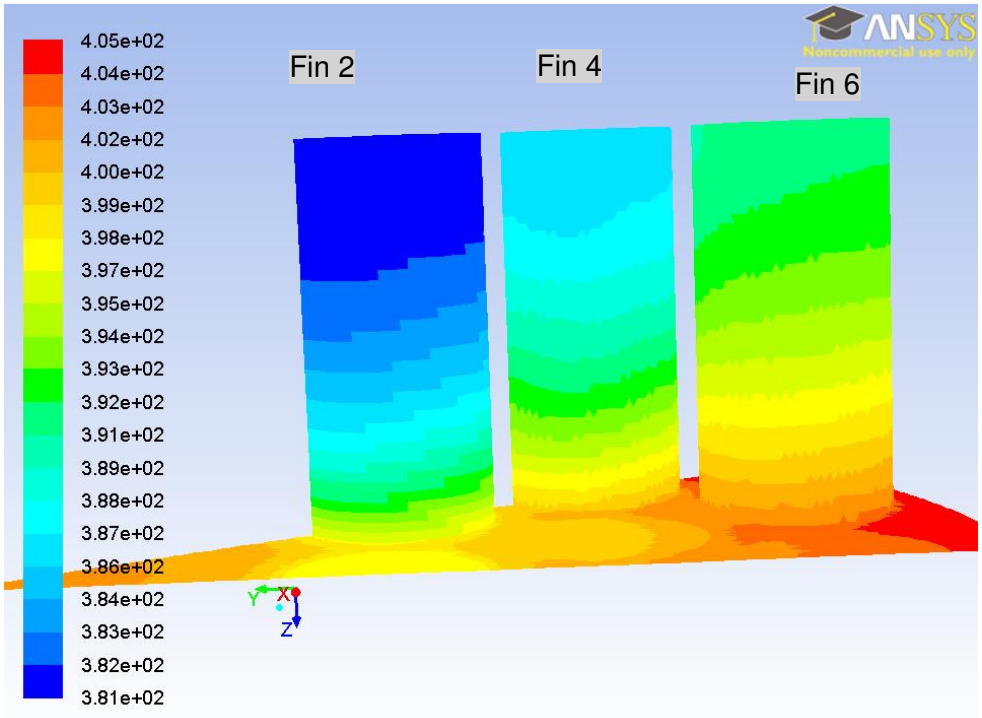

Figure 116. Local temperature distribution for cooled surface and fins 2, 4, & 6, FF reference case. Scale in units of K.

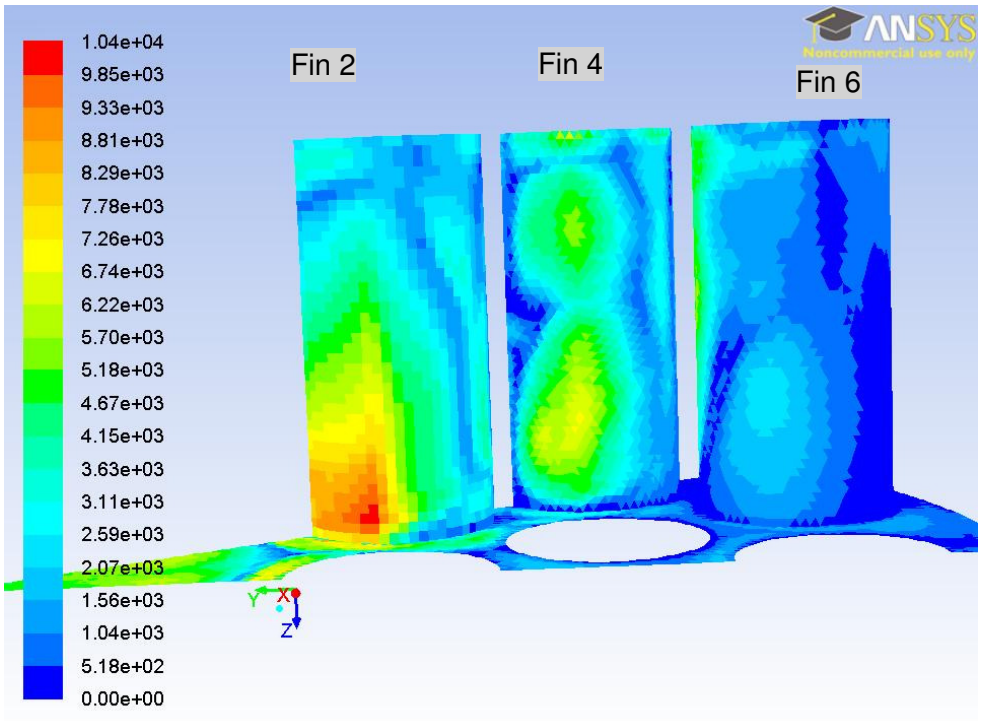

Figure 117. Surface HTC for cooled surface and fins 2, 4, & 6, FF reference case. Scale in units of W/m^2-K.

Similar to the previous figures for FF, Figure 118 shows the effective HTC for the FR reference case. As previously mentioned, the effective HTC is calculated using the local heat flux through the cooled surface and the temperature difference between the cooled surface and the coolant inlet temperature as though the fins were not present. The maximum effective HTC is thus in the locations of the fins as the heat flux through the base of the fins is much larger than the heat flux into the air in areas not covered by the fins. Though the maximum HTC values are lower than the reference case for FF, the effective HTC is much more uniform in that each of the fins exhibits a similar range in HTC values whereas the innermost fins for the FF case showed significantly higher effective HTC values than the outermost fins. The uniformity in HTC allows for uniform heat removal from the tip of the finger and may result in less thermal stresses. An investigation into the thermal stress imposed on the FF and FR configurations would be an interesting project for future researchers.

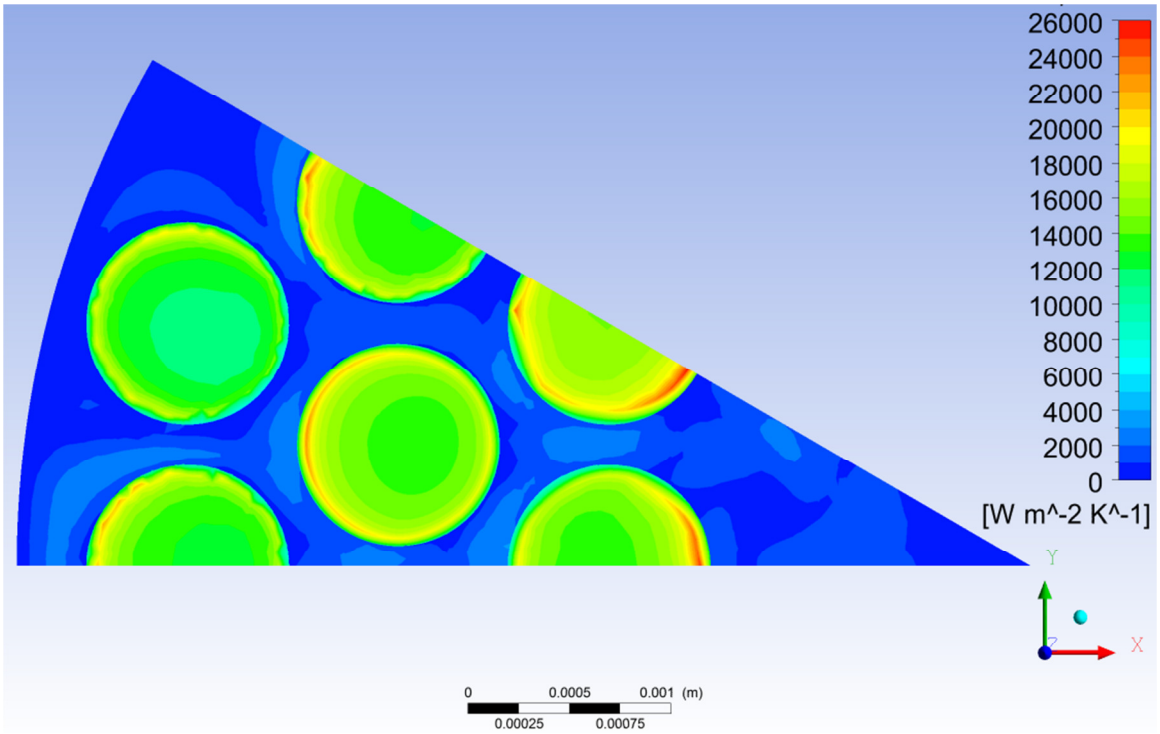

Figure 118. Contour plot of effective HTC at the cooled surface, FR reference case.

Figure 119 shows the temperature distribution, while Figure 120 shows the HTC distribution for the FR reference case for fins 1, 3, and 5. Compared to the previous figures shown for the FF reference case (which has a similar mass flow rate and overall effective HTC) the temperature drop across the length of the fins is much more uniform. For the FF reference case, the fins near the center (closest to the round jet) show much greater temperature drop along their length indicating a much larger heat flux at the base of the fin. Similarly, the HTC distribution for the fins is much more uniform for the FR configuration. Without the impinging jet, the peaks in HTC are not as dramatic. Some peaking can be observed at the top of Fin 3 and on Fin 1, however, the maximum is nearly a third less than the FF reference case. As mentioned earlier, this enhanced uniformity may be a benefit to the FR configuration when considering thermal stress analysis.

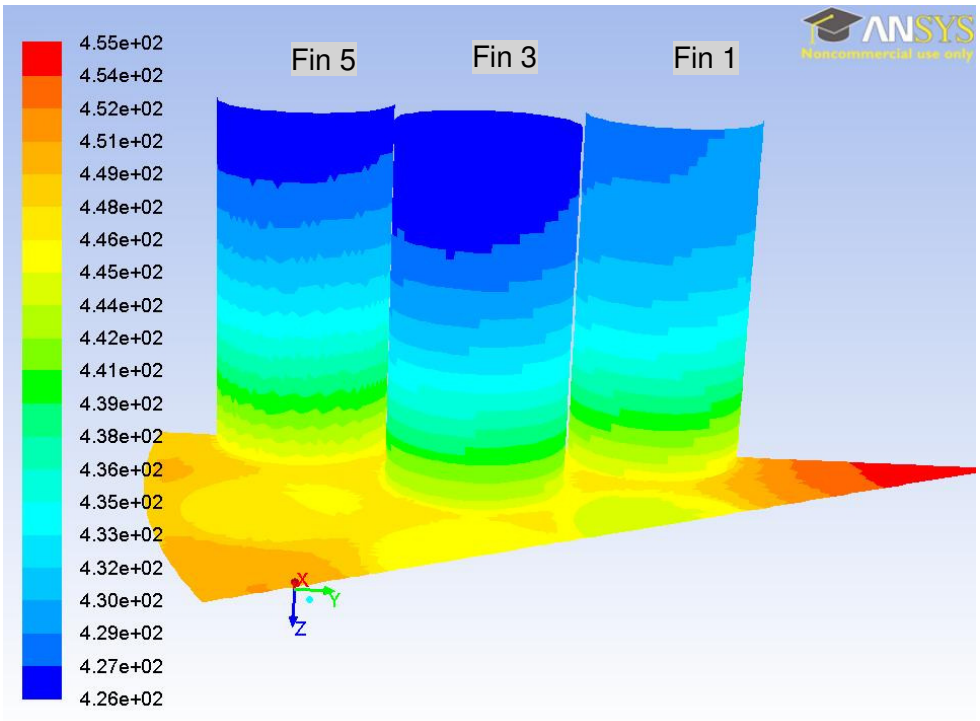

Figure 119. Surface temperature distribution of cooled surface and fins 1, 3, & 5, FR reference case. Scale in units of K.

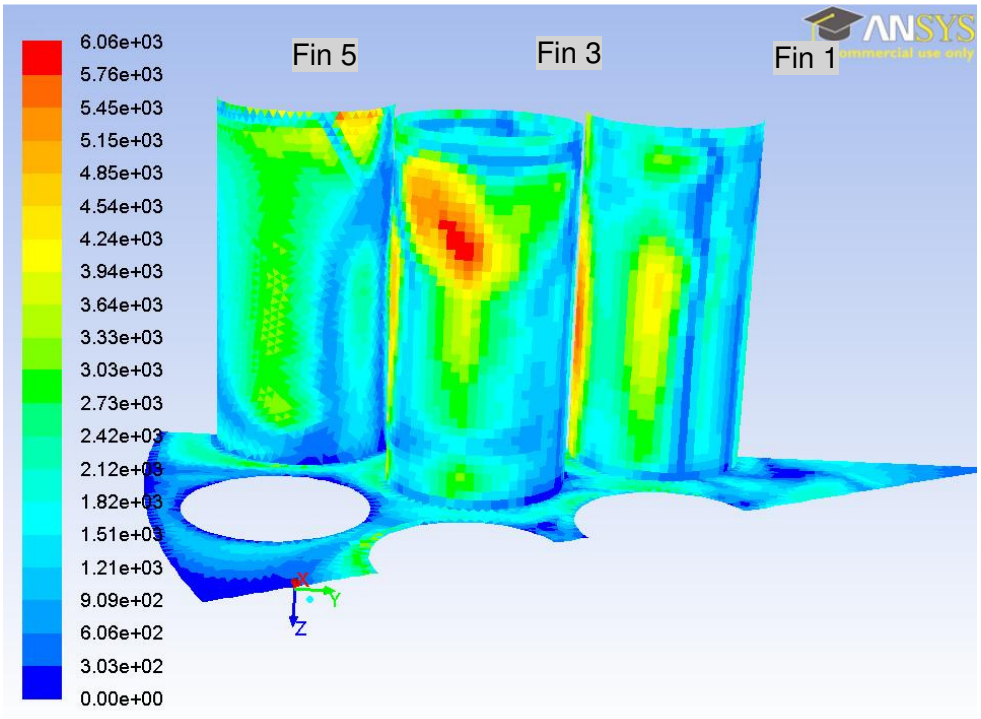

Figure 120. Surface HTC distribution of cooled surface and fins 1, 3, & 5, FR reference case. Scale in units of W/m^2-K.

Similar figures were produced for the other fins, 2, 4, and 6, as shown in Figure 121 and Figure 122. Similar to the results for fins 1, 3, & 5, these figures show the HTC for the fins in the FR configuration is much more uniform than in the FF configuration.

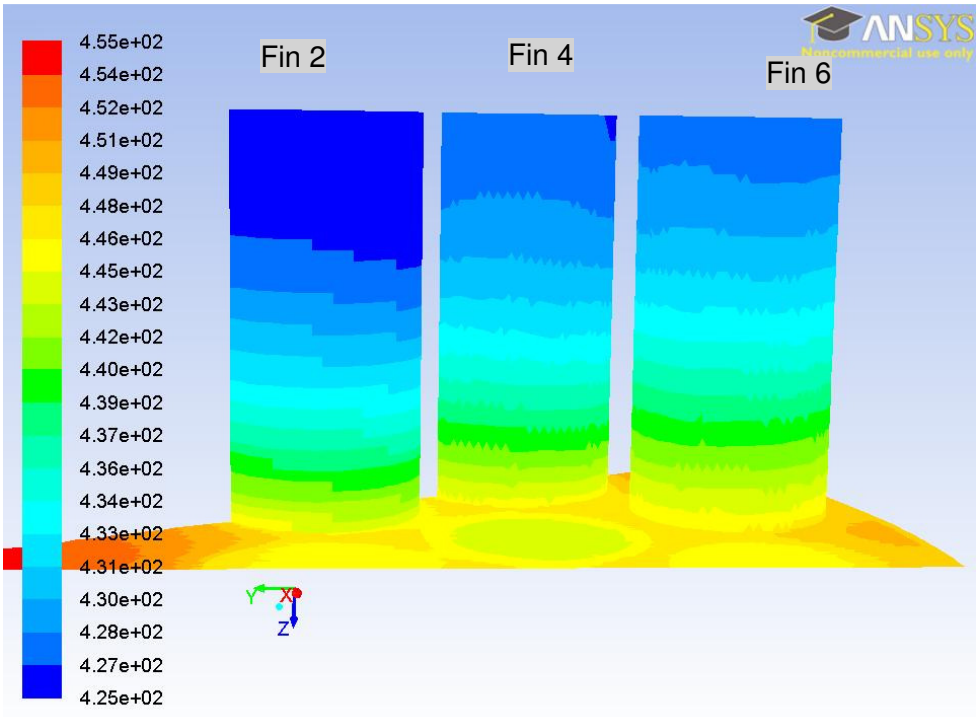

Figure 121. Local temperature distribution for cooled surface and fins 2, 4, & 6, FR reference case. Scale in units of K.

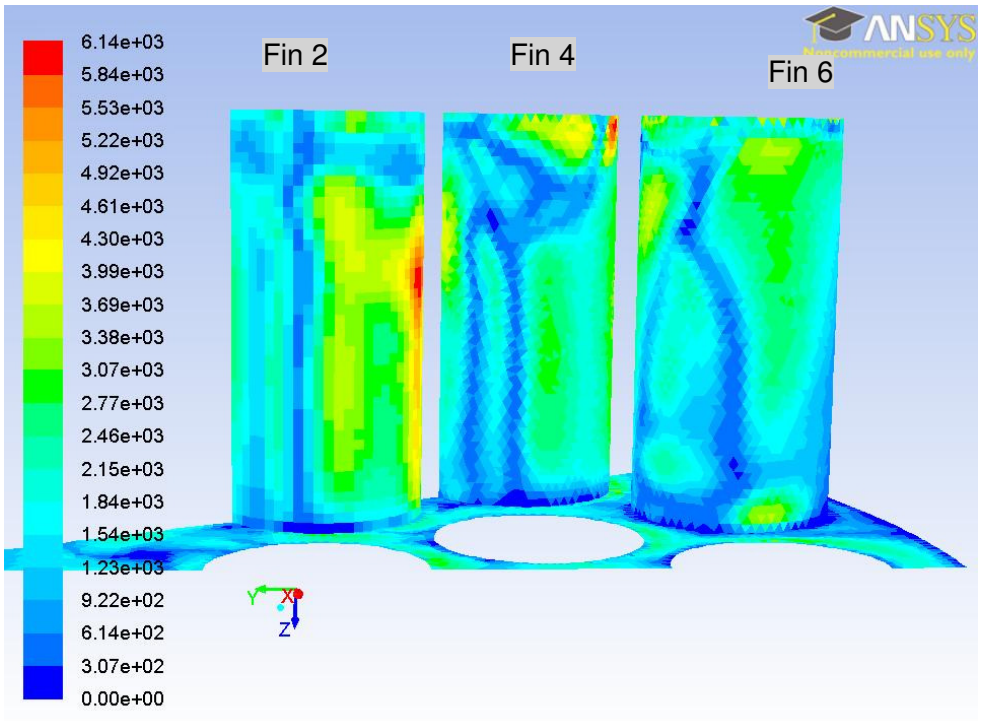

Figure 122. Surface HTC for cooled surface and fins 2, 4, & 6, FR reference case. Scale in units of W/m^2-K.

Simulations allow for the visualization of results using pathlines. The pathlines are created by following simulated massless particles “released” from inlet boundary. The particles follow the velocity field and can be colored by simulation parameters such as temperature or pressure. It should be noted that actual pathlines for a turbulent flow would not follow consistent paths like those shown in subsequent figures. As the RANS solution methods used in FLUENT produce time averaged values of velocity, the use of the term ‘pathlines’ here is for convenience of notation and should be thought of as a method of flow visualization rather than actual pathlines. When using a flow visualization like pathlines, details that are impossible to be captured in the experiment can be examined and insight into the divertor performance can be found. Pathlines colored by pressure are shown in Figure 123 for the FR reference case. As shown, the majority of the pressure drop in the FR configuration is through the inlet/outlet orifice. Since the orifice is not needed for enhancing heat transfer like in the FF configuration, there is an

opportunity for optimization of this design by modifying the inlet/outlet port diameter for reduced pressure drop.

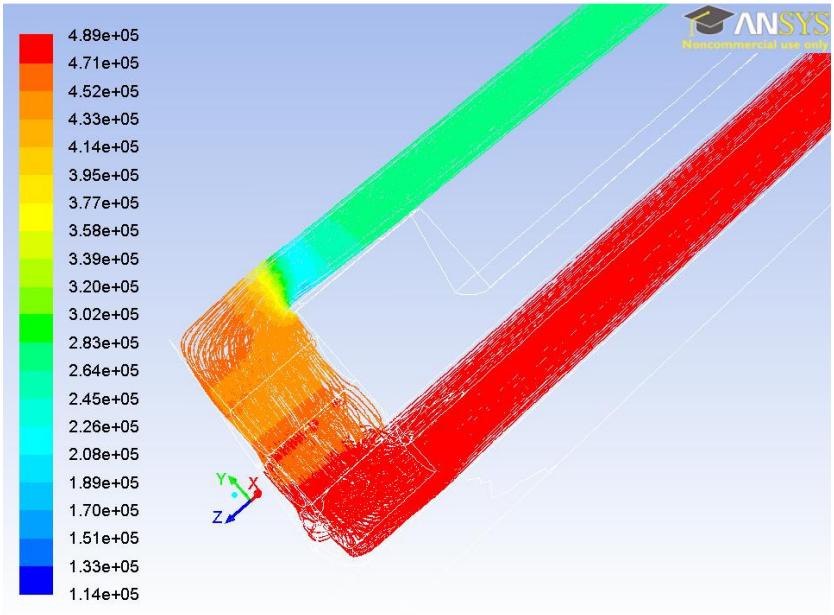

Figure 123. Pathlines colored by pressure, FR reference case.

Figure 124 shows that the temperature increase in the FR configuration does not entirely occur as the air passes through the fins. Some temperature increase is seen before the air reaches the fin array as the inlet air is heated by both the outlet air through conduction through the inlet/outlet tube wall and by conduction up the side of the finger shell. It would be interesting to use a different, less conducting material for the inlet/outlet tube to see the effect on the divertor performance. The actual HEMP divertor will have an inlet/outlet tube made of a steel alloy, which is less conducting than the brass used in these experiments or the tungsten alloy used in the prototypical divertor modules.

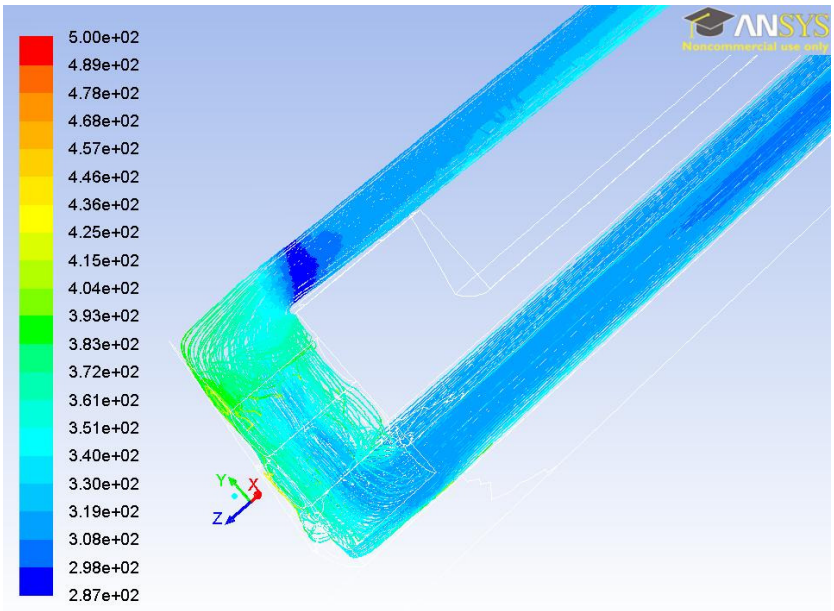

Figure 124. Pathlines colored by temperature, FR reference case.

Figure 125 shows pathlines colored by pressure for the FF reference case. The majority of the pressure drop is seen as the air passes through the inlet/outlet orifice. Also, the stagnation zone of the impinging jet is observed. Another area of low pressure is seen when the air passes through the small gap between fins 1 and 2. A stagnation zone is also observed when the wall jet leaving the stagnation zone of the primary impinging jet impacts fins 1 & 2.

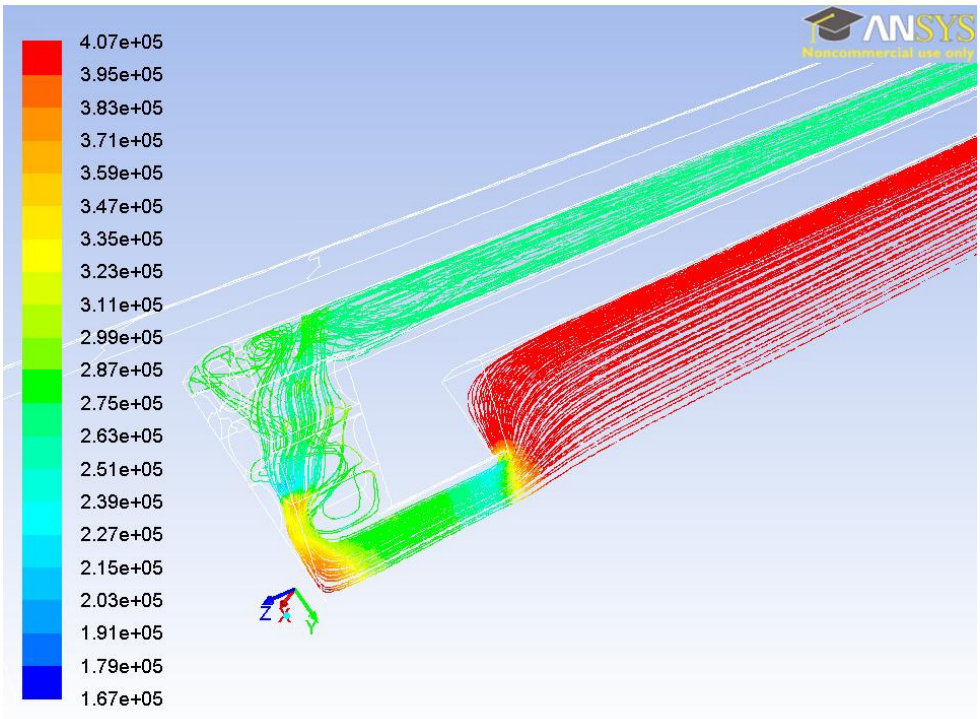

Figure 125. Pathlines colored by pressure, FF reference case. Scale in units of Pa.

As shown in Figure 126, there is less pre-heating of the inlet air stream in the FF configuration as compared to the FR configuration as the inlet stream only receives a small amount of heat from conduction through the inlet/outlet tube. There is some heat added to the outlet stream after it passes through the fin array as the outlet stream removes heat by convection after being conducted along the side of the finger.

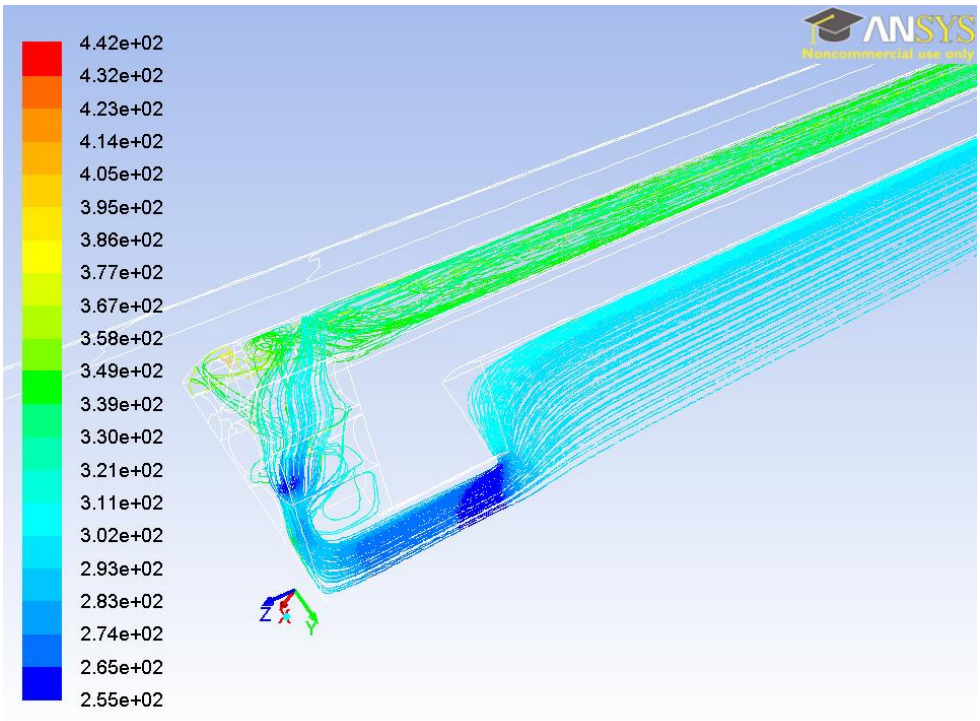

Figure 126. Pathlines colored by temperature, FF reference case. Scale in units of K.

5.2. 3-D Simulations Summary

The FF and FR configurations were modeled using the RKE turbulence model with an adiabatic fin tip condition. Like the BF and BR configurations, the simulations of FF and FR often overpredicted the pressure drop through these HEMP-like divertors. The HTC predicted by the FF model was typically 20-30% higher than that observed experimentally. The FR model typically only overpredicted the effective HTC of the experiments by ~10%.

The results of simulations showed many details regarding the particulars of the finned HEMP-like divertor's behavior. Regarding the FR configuration, the inlet/outlet orifice diameter is likely too small and could be increased without adversely affecting the thermal performance of the FR configuration. The small diameter of the orifice is only useful for the forward flow configurations though it may not be optimal as well. It only adds to the pressure drop unnecessarily for FR. Experiments and simulations for this

type of configuration would be an interesting study for future research. As the FF configuration did not significantly outperform the FR configuration, an optimization of the fin geometry and arrangement should be performed. The optimization should focus on combining more efficiently the impinging jet and the fin array. This optimization could first be performed using CFD and then later verified with experimental study. A CFD study that explores several modifications to the fin array of the FF configuration is documented in the next Section.

Regarding the FF configuration, the height of the fins and the jet-to-wall spacing should be optimized. The dimensions of this particular array were chosen to match the test module. The previous study of a divertor with fin array [28] used a *P/D* of 1.5 compared to the *P/D* of 1.2 for this study, though the height of the fins is consistent with the previous study. The jet-to-wall spacing of this design falls outside of the range of many previous experimental studies. Other jet-impingement divertor designs also call for small jet-to-wall spacing, but an optimization should be performed nonetheless. The height of the fins would obviously need to be matched to the jet-to-wall spacing at least near the location of the jet. The original HEMP design calls for fins of varying heights (and shapes for that matter). As the jet spreads out (decelerates) radially from the center, changing the cross sectional area of the flow path to maintain high velocity may increase thermal performance. Also, the outer diameter of the divertor studied here (12 mm) is somewhat small compared other designs such as the HEMJ (15 mm). Increasing the size of the HEMP-like divertor while maintaining high thermal performance could significantly decrease manufacturing costs and associated assembling complexity. However, use of fins with various cross sections as suggested in the original HEMP design would significantly increase complexity and manufacturing costs.

Regarding the FR configuration, the fin array could also be optimized for using reverse flow. The fin height, diameter and pitch should all be examined. The FR

configuration shows a more uniform effective HTC and temperature distribution. These effects may lessen thermal stresses and should be studied. A more optimized FR configuration may prove just as effective at heat removal compared to an optimized FF configuration. This would also be an interesting study for future researchers.

5.3. Motivation for Fin Array Optimization

The experimentally tested HEMP-like divertor with fins has 48 pin-fins integral to the cooled surface. The experimental and numerical results suggested that the combination of the impinging jet and the fins would not result in a significant performance improvement over using just the fins without the impinging jet (FR). This design was not optimized, however, for combining these two effects. Modifications to the fin array will be made and tested using CFD simulations and a more optimum design will be proposed. The models were constructed and meshed in a similar method to the models used in Section 5.1. All of the designs tested are shown in Figure 127.

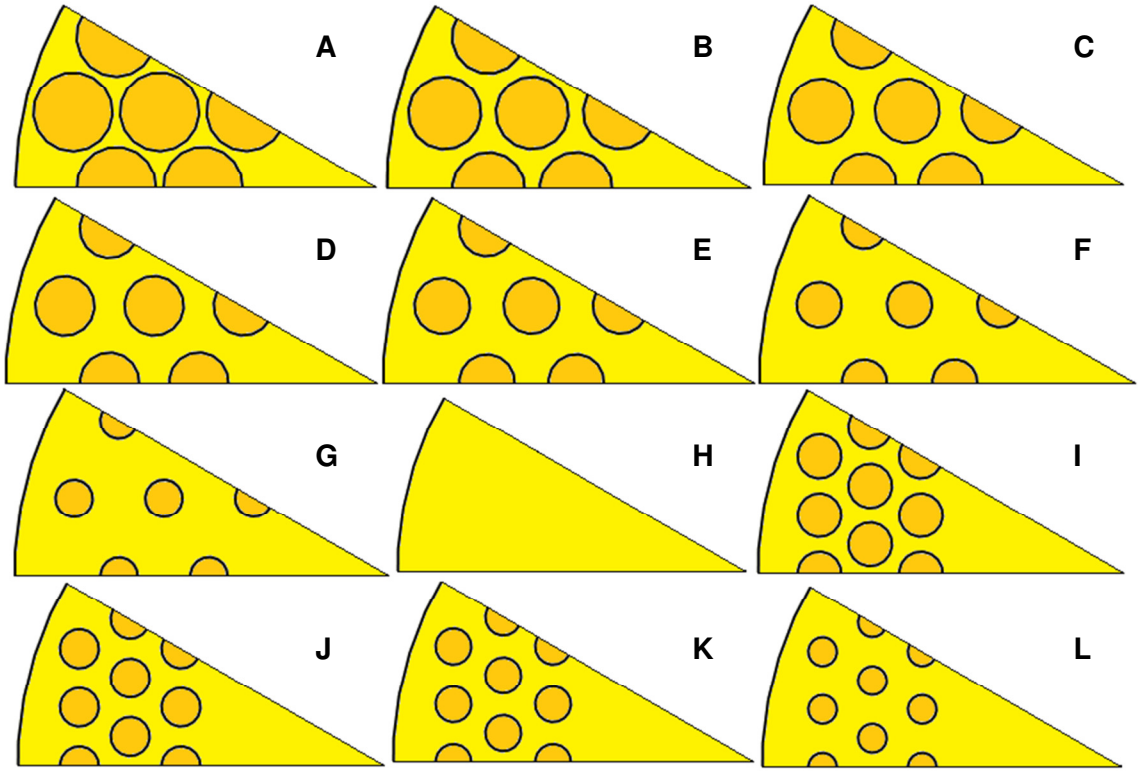

Figure 127. Drawings of the 12 tested fin arrays.

5.4. Baseline Cases

To determine which geometries are to be experimentally tested, any optimization should be performed on prototypical geometries under prototypical conditions. As shown in Figure 17, the HEMP divertor is designed to have a 1 mm thick pressure boundary at the end of the finger. The finned model used in Section 5.1 was modified by removing 5 mm from the 'finger tip' to make the total length of the model 45 mm. Two models, one with the same fin arrangement as experimentally tested (Case **B**) and one without fins (Case **H**) were created using ANSYS 14.0. These models will serve as baseline cases for making comparisons to the other fin geometries.

Each model was composed of approximately 1M unstructured tetrahedral cells with boundary layers near fluid-solid interfaces. Like the models used in Section 5.1, the models had a resolution of 50 μm on the cooled surface and on the fin surfaces.

Boundary conditions were similar to those in Section 5.1 with a uniform heat flux of 10 MW/m^2 applied to the heated surface and adiabatic conditions elsewhere. This is a reasonable assumption as the divertor modules will be in large bundles with little heat losses in the divertor modules themselves. The fingers were given a thermal conductivity similar to that of the WL-10 tungsten alloy. Material properties assumed for this study can be found in Appendix E.

Primarily, two metrics will be used to compare the different fin geometries. The first is the average heated surface (or pressure boundary) temperature, $\overline{T_s}$, and the second is Δp. The WL-10 which composes the pressure boundary must remain within its ductile-brittle transition and recrystallization temperature, 800-1200 ℃. A design which has a low $\overline{T_s}$ will provide more operating temperature margin. As the coolant flow rate can always be decreased, $\overline{T_s}$ can be increased while remaining within the desired operational range. Also, it is desired that the divertor cooling system when operating at normal steady state conditions not consume more than 10% of the power it receives form the fusion reactor. Minimization of Δp will result in a more efficient cooling system.

Each model was tested at the same four flow rates, Re_j = 4.5×10^4, 6×10^4, 7.5×10^4 and 9×10^4. The prototypical flow rate for this design is nearly 7.5×10^4. These flow rates were chosen as they cover a wide range of operating conditions and results will indicate how the different models behave under other operating points.

5.5. Fin Tip Condition

It is important that the design of the divertor have minimal performance variation on account of manufacturing tolerances. As hundreds of thousands of these modules will be required to cover the divertor surface, there will undoubtedly be concerns with reliable and consistent manufacturing. One of these issues is the contact made between the tips

of the fins and the inlet/outlet tube. On account of thermal swelling, neutron induced swelling, and manufacturing tolerances, not all of the fins will make perfect contact with the tube. Two extremes for fin tip to tube contact are perfect contact and no contact (simulated by adiabatic fin tips). As mentioned in Section 5.1, if all of the fins are not the same height, then there will be a small gap where low velocity helium acts essentially as a thermal insulator. Thus the adiabatic condition is somewhat extreme as there will always be some heat transfer from the fin tip (from radiation if nothing else). However, an adiabatic condition should serve as a lower bound to the thermal performance of the finned surface. This means that any predictions made regarding the thermal performance of the HEMP-like divertor at prototypical conditions are, for the purposes of this study, conservative.

The baseline model with fins was setup such that the fins tips were in perfectly conducting contact with the tube (Case **B***). The results of tests at different flow rates show that he change in both $\overline{T_s}$ and Δp is very small (1.3 ℃ and 134 Pa, respectively). The results of the simulations for all of the fin arrays tested are presented in Table 7.

5.6. Forty-Eight Fin Array

The experimentally tested design has 48 one mm OD pin-fins in a triangular array with 1.2 mm pitch. A series of models was created by keeping the pitch the same and changing the diameter of the fins. Seven models (six beyond the experimentally tested design) were created with pitch to diameter ratios (*P/D*) equal to 1.1, 1.2, 1.33, 1.5, 1.6, 2.0, and 2.4. These cases were denoted as Cases **A**-**G** (Case **B** being the experimentally tested array). All simulations were performed at ~10 MPa system pressure with a 10 MW/m^2 incident heat flux. The cases were tested at four flow rates spanning the prototypical flow rate corresponding to Re_j: 4.5×10^4, 6.0×10^4, 7.5×10^4, and

9.0×10^4. The prototypical Re_j is expected to be near 7.5×10^4. The results of the simulations are presented in Table 7.

Both the sides and exposed tips of the fins as well as the area of the cooled surface not covered by the fins is included in the calculation of the cooled surface area, A_C. Though A_C decreases as the *P/D* increases, $\overline{T_s}$ does not necessarily increase. As shown in Table 7, case **C** (with *P/D* = 1.33) had the lowest $\overline{T_s}$ of cases **B**-**G** at the prototypical flow rate. Cases **D**-**F** also had superior performance compared to Case **B** in terms of both $\overline{T_s}$ and Δp.

As the pin diameter decreases, Δp, in general, decreases. For Case **C** Δp was smaller than the experimentally tested design. This means that case **C** will cool both more effectively and efficiently than the experimentally tested case. An improvement of 18.8 ℃ with a 4.5% reduction in Δp is seen over Case **B**. An improvement of 64.7 ℃ and increase of 9.6% in Δp is seen as compared to Case **H**.

Helium is an effective coolant; comparison between the results for Cases **B** and **B*** suggest that most of the heat is removed by the coolant in the portion of the fins closest to the cooled surface. To confirm this hypothesis, the power leaving each fin was integrated axially and normalized to the total power leaving the fin. For Case **D**, this is shown in Figure 128. To make these plots, the power entering the coolant through each individual cell face on the surface of each fin as a percentage of the total power entering the fin through its base was calculated. The cells were arranged according to their distance from the cooled surface and the power percentage from each cell was summed in order moving away from the cooled surface. As shown, at least 75% of the power leaves the fins in the bottom half and 90% of the power leaves in the first 3/4th. Each of the fins is a different color in the figure. As the surfaces of some of the fins are made of quadrilaterals and some of triangles, the trends appear on the graph somewhat different.

The fins with triangles on their surface make for a smooth curve (as none of the cells share the same axial position) whereas the quadrilaterals are all at the same axial position arranged in rows and thus show the staggered behavior.

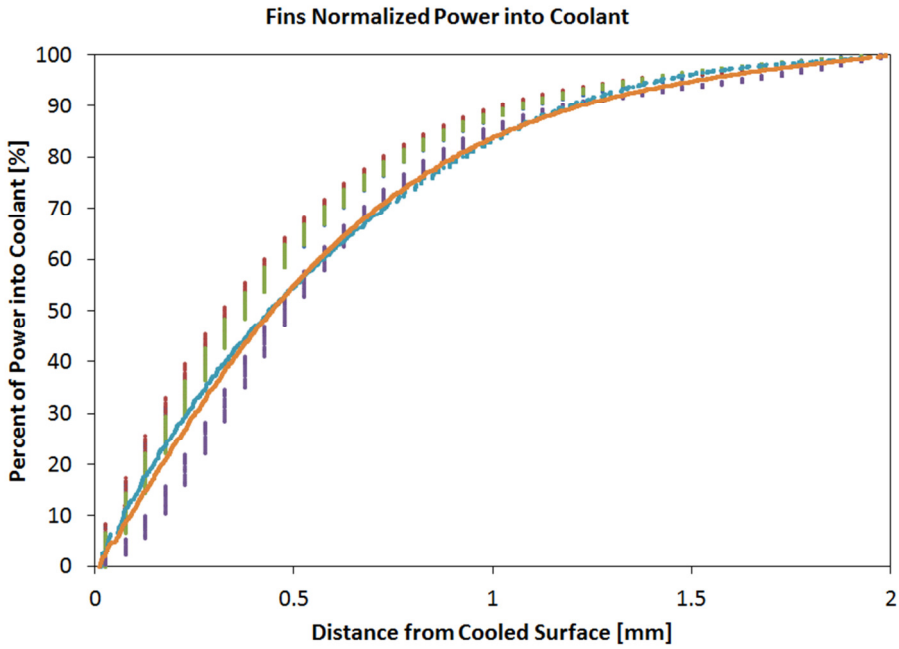

Figure 128. Normalized fin power into coolant for Case **D** at jet Reynolds number of 75,000.

5.7. Eighty-Four Fin Array

As shown in Figure 129, the local HTC of the case without fins (Case **H**) has a maximum 1.2 mm radially outward from the center of the impinging jet. Farther out, the HTC decreases. A design was made assuming that by placing a large number of small fins (thus maintaining A_C) in the area of the jet's least effectiveness, low $\overline{T_s}$ can still be achieved while decreasing Δp and increasing fin efficiency. A design was created with ANSYS 14.0 with 84 pin fins in triangular array with 0.8 mm pitch. Four models were created (denoted **I**-**L**) with *P/D* equal to 1.33, 1.5, 1.6, and 2.0.

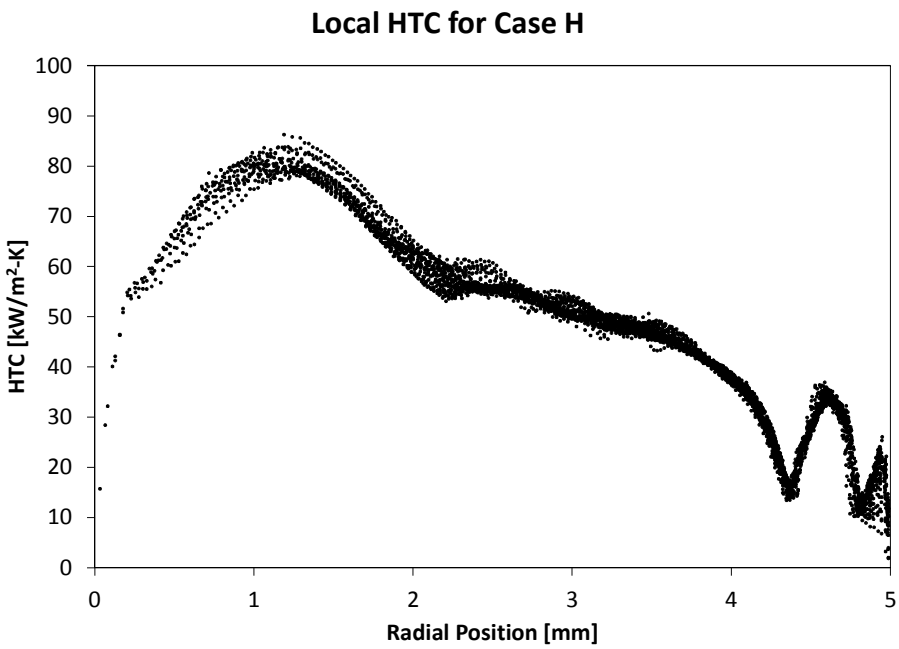

Figure 129. Local HTC for Case **H**.

These arrays were made in the same manner as the experimentally tested design as now described and depicted in Figure 130. Starting with the bare cooled surface, a pin-fin is placed at the center. A pitch is chosen and identical pin-fins are placed in a hexagonal pattern around the center fin. Using the same pitch, successive rings are added until the cooled surface is completely covered by pin-fins. The outermost fins that will be too close or intersect with the finger shell are removed. Finally, the first few rings of fins are removed to make room for the impinging jet.

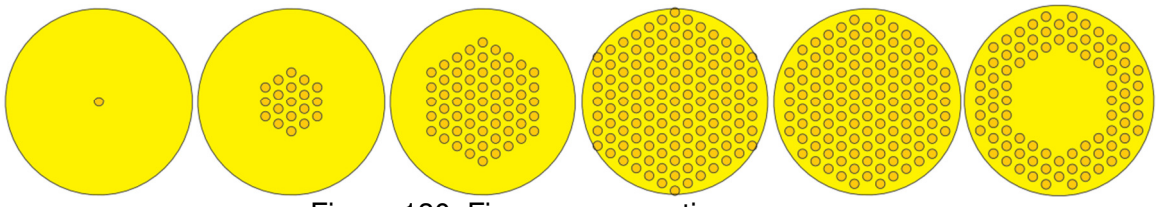

Figure 130. Fin array generation process.

For a pitch of 0.8 mm with *P/D* = 1.6, this amounts to a 0.5 mm OD center fin plus six rings of fins (127 fins total). The fins in the corners intersect the shell of the

finger and are removed (now 119 fins). Then the center fin and the first three rings are removed giving room for the impinging jet leaving 84 fins. The diameters of the pins fins can now be changed to give different *P/D*. A picture of the final fin array cropped to 30° symmetrical segment is shown in Figure 131.

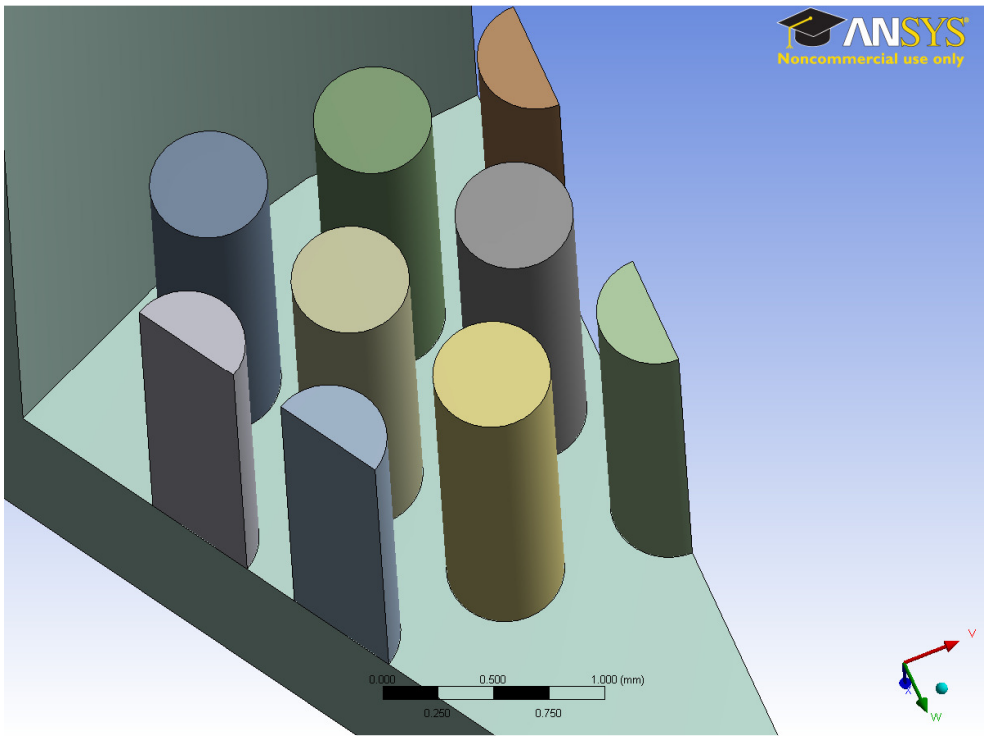

Figure 131. View of model used for case **J**.

The new arrays were tested at the same flow rates as before. As shown in Table 7, for cases **I**-**L** there is a general decrease in Δp for the 84 fin array compared to the 48 fin array maintaining similar values of A_C. Specifically for case **K**, there is a decrease of 13.1 ℃ in $\overline{T_s}$ and 6% in Δp compared to Case **B** at Re_j= 75,000. This improvement comes with an 8% decrease in A_C. Also, there is a decrease of 59.0 ℃ in $\overline{T_s}$ and an increase of 7.9% in Δp compared to the unfinned Case **H** at Re_j= 75,000.

As Case **K** has similar performance at Re_j= 60,000 and 75,000 compared to cases **I** & **J** while using smaller fins (meaning larger inter-fin gaps), it has been chosen

as the most optimum design for the 84-fin array design of those tested. A comparison of the optimum cases for the two fin arrays to the baseline cases for $\overline{T_s}$ is shown in Figure 132. A similar comparison is made comparing Δp as a percent of the Δp for Case **H** in Figure 133. As shown, Case **C** shows the lowest values of $\overline{T_s}$ but has a higher Δp compared to Case **K**. Which of the two optimum designs is most suitable for production depends on which parameter future designers deem more important.

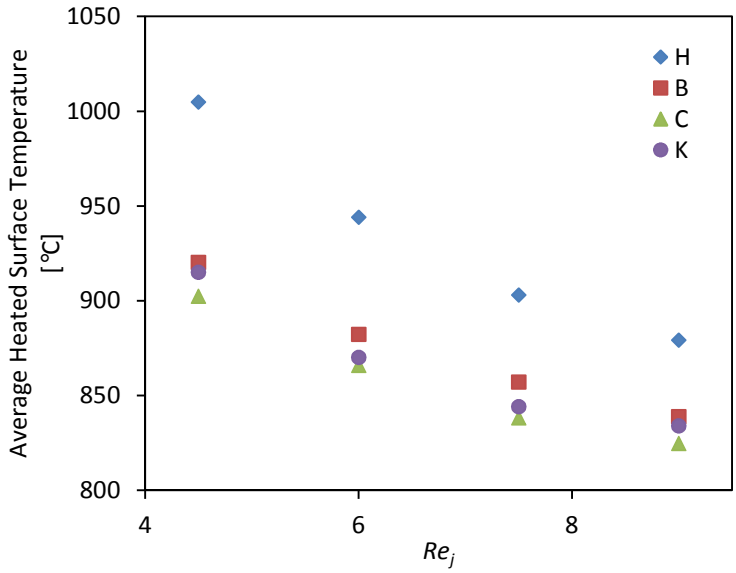

Figure 132. Optimum fin array performance – Average heated surface temperature.

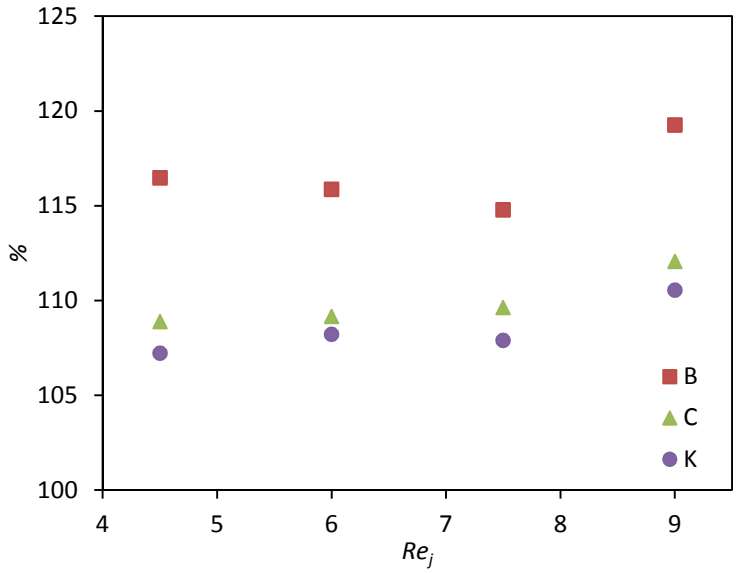

Figure 133. Optimum fin array performance – Pressure drop as percentage of Case **H** pressure drop.

Case **K** thus cools more effectively and efficiently than case **B** and a much smaller increase in Δp than case **B** is predicted comparing Cases **K** and **B** to **H**. Smaller fins may result in machining improvements as well as the small inter-fin gaps are difficult to machine. The small gaps currently present problems for machining techniques like EDM. Improvements in machining techniques are always being developed so perhaps this will not be an issue in the future. However, a larger number of fins may result in an increase in manufacturing complexity, thus negating any improvement as a result of having larger inter-fin gaps. Ultimately, this decision as to which geometry to use (or if fins are to be used at all) has to be an economic decision where any performance improvement is to be compared against the increased complexity and manufacturing costs.

5.8. Fin Optimization Summary

Following the results of an experimental and numerical study on the HEMP-like divertor that the performance of the divertor can be improved by combining impinging

jets with a cooling fin array, the design of the HEMP-like divertor fin array was optimized using CFD models to maximize the effects of these two heat transfer enhancement mechanisms. The OD of the fins in the array with the original pitch was changed to find a more optimum design. Also, a fin array with a new pitch was proposed in an attempt to achieve similar thermal performance with lower pressure drop. The performance of these designs was compared based on the temperature of the heated surface of the pressure boundary and the pressure drop. The minimization of these two quantities near the nominal prototypical flow rate indicated the best performing geometries.

Two optimized designs were found, one using the original array with 48 fins and one using the new array with 84 fins. Both of these designs improve upon both the thermal and hydraulic performance of the experimentally tested cases. Also, the results of these studies provide confidence that there will be minimal impact as a result of manufacturing tolerances and thermal and neutron irradiation induced swelling of the divertor materials. This claim is supported by performing all tests with adiabatic fin tips and by showing that the thermal performance is somewhat insensitive to the fin diameter (i.e., the arrays with fin diameters near the optimum fin diameter do not show a sudden drop in performance).

For instance, one could manufacture the fins in the Case **D** or **E** configuration, assuming that, because of swelling, the fins will eventually more closely resemble those of case **C**. This would provide operators a longer timeframe to operate the HEMP-like divertor (assuming other issues do not cause interruptions).The manufacturer of the fins would also have a wide range of acceptable fin diameters thus increasing yield. Furthermore, pieces manufactured with fins like those of the lower performing designs could be used in regions of lower heat flux.

Since the models used in this optimization and similar to those used in Section 5.1, it's likely that the performance predictions are roughly 10% higher than should be

expected (in terms of overall effective HTC). Also, the predicted pressure drop is likely higher than should be expected. Overall, however, the trends presented should be consistent with actual HEMP-like divertor performance at prototypical conditions.

The two optimized fin arrays are shown with their dimensions in Figure 134. The end of chapter table, Table 7, summarizes the results according to Re_j, $\overline{T_s}$, and Δp. The baseline cases (**B** and **H**) corresponding to the experimentally tested array (FF) and the configuration without fins (BF) are highlighted.

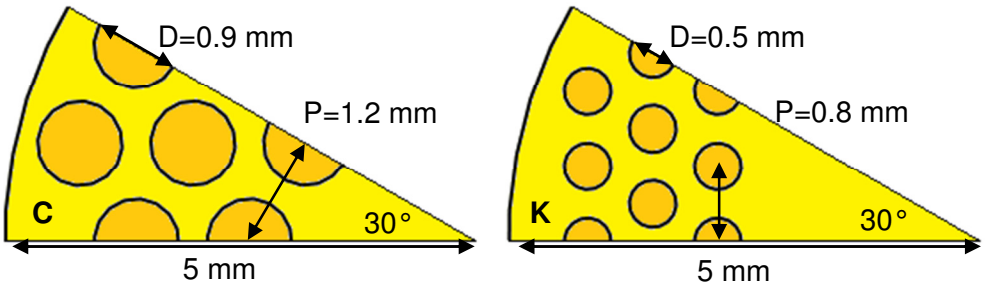

Figure 134. Optimized fin arrays with dimensions. 48 fin array (left), 84 fin array (right).

Table 7. Optimization of HEMP geometry

Case	Fins	*P/D*	A_C [mm^2]	$\overline{T_s}$ [℃]				Δp [kPa]			
				4.5	**6**	**7.5**	**9**	**4.5**	**6**	**7.5**	**9**
A	48	1.1	388.2	882.4	856.2	836.6	828.2	309.4	527.9	803.6	1162.2
B	48	1.2	361.3	920.3	882.4	857.2	839.0	189.7	334.5	525.5	782.1
B*	48	1.2	361.3	917.1	880.7	855.9	838.1	189.8	334.5	525.6	782.4
C	48	1.33	329.3	902.5	866.1	838.4	824.8	177.3	315.1	501.9	735.0
D	48	1.5	303.7	912.0	870.9	849.2	836.3	175.0	312.1	492.0	720.6
E	48	1.6	291.5	923.7	880.2	852.5	837.7	175.0	312.1	492.0	719.6
F	48	2.0	250.5	928.5	883.3	856.2	839.9	176.3	314.2	495.0	722.0
G	48	2.4	223.4	934.0	887.9	860.1	842.8	175.8	313.5	494.2	721.5
H	0	---	78.5	1005.0	944.1	903.1	879.3	162.8	288.7	457.8	655.8
I	84	1.33	379.9	909.0	869.7	844.5	829.1	177.7	316.9	499.5	735.1
J	84	1.5	348.0	909.2	868.8	845.0	832.5	174.6	311.8	492.8	726.0
K	84	1.6	331.9	915.2	870.2	844.1	834.1	174.6	312.4	494.0	725.0
L	84	2.0	282.9	922.7	878.2	854.1	837.9	174.6	312.4	492.0	719.4

CHAPTER 6: CONCLUSIONS & RECOMMENDATIONS

This Chapter highlights the results of the previous Chapters, presenting notable findings and conclusions. Also, recommendations for future work as well as contributions to the state of the art of MFE divertor research will be discussed.

6.1. Summary of HEMP Experimental and Numerical Studies

Four configurations of a HEMP-like finger-type divertor were tested experimentally and numerically, namely, forward/reverse flow with bare/finned surfaces. The 2D simulations used to model the HEMP-like configurations without fins showed close agreement with experiments in terms of temperature and HTC (within ±10% for most cases) predictions at the cooled surface. The pressure drop was typically overpredicted by the 2D models (~40%). The HTC for the bare, forward-flow (BF) configuration (with impinging jet but without fins) was modeled most closely using the Spalart-Allmaras (S-A) turbulence model. The HTC for the bare, reverse-flow (BR) configuration (without impinging jet and without fins) was modeled most closely using the realizable k-ε (RKE) turbulence model.

For the HEMP-like divertor with an array of cylindrical fins, the 3D models typically overpredicted the HTC (compared to the experiments) by ~10% near the prototypical operating flow rate for reverse flow and ~20% for forward flow. Like the 2D simulations, the pressure drop through the finned test section was also overpredicted by the simulations (~40%). There are many possible explanations for this discrepancy, with one possibility being geometric inconsistencies between the experiments and the simulations.

The results of the models were used to expand the understanding of the HEMP-like and other finger-type divertors. In particular, the models showed that a significant portion of the incident heat was removed by the air after being conducted up the walls of the finger and not through the cooled surface as originally assumed. Dynamic similarity in the thermal performance is thus not achievable using just the Reynolds number (Re_j). By analyzing a series of simulations performed on the BF configuration using other gases (He and Ar) and a test section made of a carbon steel alloy (which has a lower thermal conductivity than the brass alloy used in the experiments), it was found that dynamic similarity between experiments with different coolants and test section materials can be achieved by accounting for the thermal conductivity ratio of the structure to the coolant to compensate for the amount of conduction vs. convection heat transfer at the cooled surface. The results of this investigation necessitated the reevaluation of performance predictions made for previously studied finger-type divertors, specifically the investigation of the HEMJ divertor detailed in Chapters 3 & 4.

After verifying the numerical model and extending the performance predictions to near prototypical operating conditions, the performance of the bare HEMP-like divertor was extrapolated to prototypical conditions. Performance curves were created that allow for divertor cooling system and MFE reactor designers to predict the thermal performance of the bare HEMP-like divertor. The results show that for the BF configuration assuming an inlet helium temperature of 600 °C, 18.2 MW/m^2 heat flux incident on the outer pressure boundary surface can be removed at the prototypical Re_j while keeping the average heated surface temperature below 1200 °C. This requires a pumping power fraction of ~13% of the total incident thermal power on the divertor. Accounting for the plasma-facing tungsten armor tile with cross sectional area 1.4 times that of the pressure boundary, the maximum heat flux incident on the divertor tile itself

that can be accommodated by the BF configuration is 13 MW/m^2. This is greater than the currently estimated 10 MW/m^2 requirement necessary for the operation of the divertor.

Further, the results of the experiments and the 3D simulations indicated that improvement in the thermal performance of the HEMP-like divertors could be made by optimizing the combination of the impinging jet and cooling fins. Both the forward and reverse flow finned designs showed very similar thermal-hydraulic performance but it was hoped that the finned array in the forward flow configuration would combine the benefits of an impinging jet and fin array. As the design tested was not optimized for both of these effects, the optimization of the fin array of the HEMP-like divertor was performed using CFD simulations as detailed in the second part of Chapter 5. Also recommended, but not performed, is an optimization of the inlet/outlet port diameter for both forward and reverse flow as the simulations show that it is the location of the majority of the pressure drop through the HEMP-like divertors.

Regarding the fin optimization for the finned design in forward flow, two optimized designs were selected from two sets of fin arrays. The first set used the same 48-fin arrangement used in the experimental test sections but changed the fin diameter. The second set used an array with 84 fins placed further out radially away from the impinging round jet. This new design has a similar overall heat transfer area, but uses a larger number of smaller fins when compared to the experimentally tested array. Also, by placing the fins further away from the impinging jet, the velocity of the coolant is reduced when passing through the small gaps between the fins thus resulting in a lower pressure drop. The optimized fin arrangement of both arrays provided both thermal and hydraulic benefits compared to the experimentally tested designs. This optimization also provides fin array manufacturers with some assurance that small variation in the dimensions of the cooling fins will not significantly impact the performance of the HEMP-like divertor.

These new designs can now be fabricated and tested experimentally for confirmation of these predictions.

Experiments should be performed using gases other than air on the HEMP-like test sections in order to confirm the prediction of the numerical simulations regarding the effect of conductive vs. convective heat transfer. Beyond just using the already constructed brass test section, carbon steel tests sections should be tested in order to cover a wider range of thermal conductivity ratios. Constructing a finned test section out of steel is expensive so numerical simulations should first be performed on the finned configurations to see if the effect of conductive heat transfer is significant. The air-cooled simulations showed that ~70% of the incident power is removed through the cooled surface which is significantly greater than the~40% and ~10% removed in the forward and reverse flow configurations without fins, respectively. The effect of conduction heat transfer is thus not as significant for the finned configurations.

6.2. Summary of the HEMJ Experimental Study

The HEMJ divertor performance was reevaluated covering a wider range of experimental conditions than previously tested by other researchers at Georgia Tech. Using six combinations of coolant and structural materials (air, Ar or He with brass or carbon steel), the impact of the thermal conductivity ratio of the structure to the coolant on the divertor thermal performance was quantified. The thermal conductivity ratios of the six experiments were chosen to cover a wide range including values near the expected prototypical value for tungsten alloy and helium at operating temperatures. The experiments showed that the Nusselt numbers for all six configurations were able to be correlated using the thermal conductivity ratio and Re_j, thereby confirming dynamic similarity.

Also, for the first time, performance curves for the HEMJ were created assuming an inlet helium temperature of 600 ℃. As the HEMJ and HEMP-like divertors share many geometric similarities, the performance curves for the two designs were generated using very similar procedures. The HEMJ is predicted to be able to remove 14.1 MW/m^2 through the pressure boundary while keeping the average pressure boundary temperature below 1200 ℃ and using a pumping power ~8% of the incident thermal power. Accounting for an 18 mm flat-to-flat hexagonal tile, the corresponding heat flux into the tungsten armor tile is 11.4 MW/m^2.

The results of this study verify the prediction made in Chapter 4 regarding the fact that dynamic similarity between the test modules and the actual divertor cannot be achieved by only matching Re_j. Corrections must be made to account for the effect of conduction along the divertor walls on the convective *Nu* for the cooled surface. Following the successful study of the HEMJ, other previously tested divertors (T-Tube and HCFP) should also be examined for effects of convective versus conductive heat removal.

6.3. Contributions to MFE Divertor Design Efforts

The creation of the performance curves for the HEMP-like and HEMJ divertors will significantly improve performance predictions made by cooling system designers regarding the prototypical behavior of these divertors. By creating these curves from experimental data over a wide range of operating conditions, it assures the designers that any the extrapolations predicted are well qualified.

The optimized HEMP-like fin array geometries should provide significant thermal performance enhancements compared to the experimentally tested HEMP-like divertors of Chapter 3. As many thousands of these modules are required to cool the entire divertor surface, these studies provide manufacturers confidence that small machining

inconsistencies inevitable with the manufacture of such a large number of components will not hinder divertor performance significantly.

The methods presented here for both experimental and numerical study of divertor designs can be used by future researchers to quantify/verify the thermal performance of other divertor designs. Specifically, the coupling between experimental results and numerical simulations used to analyze and optimize the HEMP-like divertor is a prime example of the use of verified numerical models.

6.4. Recommendations for Future Work

The results of the numerical study on the HEMP-like divertor indicate that experiments using different gases as coolant should be performed. Combined with test sections constructed of steel, these experiments would provide a much wider base of data on which extrapolations to prototypical conditions can be made. A bare test section should be tested first as the test sections with fins are more expensive to machine. These experiments should be validated with a numerical model like those used in Chapters 4 or 5.

As the optimized fin arrays of the HEMP-like divertor provide significant thermal performance improvements, these optimized designs should be fabricated for testing. As mentioned, steel and brass test sections with the optimized fin arrays with different coolants (e.g. air, argon, and helium) would provide a very wide range of operating conditions to test the HEMP-like divertor. This proposed study would also serve to quantify the deviation from the actual performance of the fin optimization to further validate the adequacy of the numerical models

As a thorough series of experiments on the HEMJ geometry have been performed at laboratory conditions, the HEMJ is now suited for testing at prototypical conditions constructed of prototypical materials. While some of these tests have been

performed, as documented in the literature review of Chapter 2, further tests that specifically verify the performance predictions presented at the end of Chapter 4 are suggested. Using the same facilities as this thesis (once-through helium, air, or argon heated by oxy-acetylene torch) at Georgia Tech would not be appropriate for such a study. A helium-loop that is capable of operating at steady-state conditions for extended periods is recommended for such a study. Also, using an improved heat source to achieve prototypical heat loads would be beneficial as well. This improved heat source may be the current torch but it will need to be augmented with either a larger tip or a heat-flux concentrator like those used in previous divertor studies at Georgia Tech. A helium loop would allow for the use of cartridge heaters like in the studies of previous Georgia Tech researchers, but a new design would be required to achieve heat loads near 10 MW/m^2.

The performance curves generated for the BF HEMP-like and HEMJ designs should be tested in a system code package. Especially since the HEMJ is further along in development, the results of that test in particular would be beneficial for the designers of a MFE reactor. The results of the HEMJ study indicate that the divertor structural material has an appreciable effect on the divertor performance itself, in terms of the heat removal capability based on the convection vs. conduction heat flow paths and this result should be taken into consideration when selecting materials. Estimates should be made to the extent of thermal conductivity degradation due to irradiation over the life time of the divertor and the extent by which such degradation in thermal conductivity can impact the divertor thermal performance over the life of the plant.

It has been shown that previous work on gas-cooled divertors using the dynamic similarity technique should be reexamined to assess the impact of conduction heat transfer on the divertor performance. This recommendation includes the T-Tube and

HCFP divertors. Simulations could first be performed to determine if such effect is significant and then be followed by experimental studies if necessary.

The inlet/outlet port diameter and fin height of the HEMP-like divertor should be optimized. Simulations showed that most of the pressure drop through the divertor occurs at the inlet/outlet port for both the forward and reverse flow configurations. As the port size has no heat transfer enhancement implications for the reverse flow configurations it is likely that such an optimization would greatly enhance the performance predictions of the FR configuration. The BR configuration has very poor thermal performance and can safely be neglected for all future studies. Also, a fin optimization for the FR configuration may prove beneficial as well.

APPENDIX A: HEMP EXPERIMENTAL DATA

The following tables list the pertinent time averaged experimental parameters for each of the cases detailed in Chapter 3. Pressures p_{rot} and p_{in} are given as gauge pressure.

A.1. Bare Forward

Table 8. Bare Forward Recorded Experimental Data

Case #	P_{rot} [kPa]	Δp [kPa]	p_{in} [kPa]	T_h [℃]	T_0 [℃]	T_1 [℃]	T_2 [℃]	T_3 [℃]	T_{in} [℃]	T_{out} [℃]	p_{amb} [kPa]	$\dot{V}$ [cm^3/s]
401	418.0	137.6	413.7	99.8	83.2	81.7	81.8	81.2	20.9	31.5	98.1	1208.2
402	348.1	118.4	344.1	104.7	88.3	86.8	87.2	86.5	20.9	33.4	98.1	1128.0
403	282.4	99.8	278.8	111.3	95.1	93.6	94.0	93.4	21.1	36.0	98.1	1038.3
404	215.0	79.8	212.0	120.2	104.2	102.7	103.0	102.5	21.3	39.6	98.1	939.2
405	145.8	57.7	143.5	133.3	117.8	116.3	116.5	115.9	21.6	44.8	98.1	816.5
406	106.4	44.2	104.5	144.5	129.3	127.8	128.0	127.4	21.9	49.5	98.3	722.1
407	71.2	31.0	69.8	158.6	144.0	142.5	142.5	141.9	22.1	54.9	98.1	618.3
408	49.2	22.0	48.1	173.3	159.0	157.5	157.4	156.8	22.3	61.2	98.1	538.0
409	35.7	16.2	34.9	187.5	173.6	172.1	171.8	171.2	22.6	68.1	98.1	467.2
410	20.8	9.5	20.4	210.8	197.5	195.9	195.5	194.9	22.9	78.5	98.1	368.1
411	7.0	3.3	6.9	261.0	249.0	247.3	246.2	245.8	23.6	100.4	98.1	217.1
412	415.5	130.4	411.8	250.5	205.6	201.6	201.6	197.8	21.9	55.8	97.9	1184.6
413	348.4	112.3	345.0	265.3	220.8	216.8	217.0	213.1	22.1	61.6	97.9	1104.4
414	277.2	92.6	274.2	284.2	240.6	236.5	236.8	232.8	22.3	68.9	97.9	1019.4
415	210.0	73.1	207.6	308.2	265.8	261.7	261.9	257.8	22.5	78.7	97.9	910.9
416	140.7	51.9	139.0	345.3	304.5	300.2	300.1	295.8	22.8	94.6	97.9	778.7
417	107.6	41.2	106.3	373.1	333.1	328.7	328.3	323.9	23.0	106.5	97.9	693.8
418	69.5	28.2	68.6	384.2	348.9	344.8	344.3	340.4	23.3	117.6	97.8	585.2
419	49.4	20.7	48.8	376.4	345.7	342	341.3	338.1	23.6	120.8	97.8	509.7
420	36.0	15.4	35.6	365.6	338.9	335.5	334.9	332.2	23.7	122	97.8	448.4
421	20.2	8.9	20.2	329.7	310	307.3	306.6	305.1	24	117.9	97.8	349.2
484	618.9	186.4	611.4	242.2	196.1	195.6	189.7	187.6	24.4	51.5	97.9	1313
485	624.5	130.2	619.4	255.8	209	208.5	202.7	200.6	24.5	55.8	97.9	1166.7
486	626.5	110.5	622.9	261.6	215.1	214.6	208.9	206.6	24.7	58.3	97.9	1087.6
487	627.9	94.0	625.2	268.1	221.8	221.3	215.6	213.3	24.9	60.8	97.9	1006.5
488	631.6	69.8	630	285.3	239.5	238.8	231.5	227.9	25.1	66.6	97.9	858.2
489	634.9	48.2	634.6	305.3	260.5	259.9	252.4	247.8	25.5	74.6	97.8	692.1
490	636.7	34.0	637.6	328.6	284.9	284.3	276.5	273.1	26	84.4	97.8	549.7
491	640.4	20.9	641.6	372.6	330.3	329.5	321.5	318.4	26.5	103.7	97.8	359.9
492	645.5	9.9	647.5	339.7	313.1	312.5	306.7	305.1	27.1	115.8	97.8	128.5

Table 9. Bare Forward Calculated Experimental Data

Case #	$\dot{m}$ [g/s]	Re_j [/10^4]	$\Delta p'$ [kPa]	K_L [-]	$\overline{q''}$ [MW/m^2]	T'_0 [°C]	T'_1 [°C]	T'_2 [°C]	T'_3 [°C]	$\overline{T_c}$ [°C]	$\overline{h}$ [W/m^2-K]	$\overline{Nu}$ [-]	M [-]
401	3.29	11.53	108.4	1.099	0.316	80.6	79.1	79.2	78.6	78.7	7865.5	599.3	0.684
402	2.85	9.97	79.1	1.092	0.319	85.7	84.2	84.6	83.9	84.1	7285.0	553.5	0.685
403	2.41	8.44	55.5	1.099	0.323	92.5	91.0	91.4	90.8	90.9	6659.6	504.0	0.678
404	1.97	6.88	35.3	1.096	0.324	101.6	100.1	100.5	99.9	100.0	5927.9	446.2	0.666
405	1.50	5.23	18.9	1.092	0.313	115.3	113.8	114.1	113.5	113.6	4905.3	366.4	0.636
406	1.20	4.20	11.6	1.116	0.300	127.0	125.5	125.6	125.0	125.2	4178.2	310.0	0.593
407	0.93	3.23	6.4	1.142	0.274	141.9	140.4	140.4	139.8	140.0	3348.6	246.5	0.529
408	0.74	2.59	3.8	1.144	0.260	157.1	155.5	155.4	154.8	155.0	2825.6	206.2	0.468
409	0.61	2.11	2.5	1.188	0.249	171.8	170.2	170.0	169.4	169.6	2437.1	176.2	0.406
410	0.44	1.52	1.2	1.255	0.219	195.9	194.3	193.9	193.3	193.5	1849.8	131.8	0.314
411	0.22	0.76	0.4	1.625	0.152	247.9	246.2	245.2	244.7	244.9	988.3	68.4	0.168
412	3.21	11.21	103.2	1.105	0.982	198.5	194.5	194.5	190.6	191.6	8331.5	612.9	0.66
413	2.78	9.71	75.8	1.104	0.991	213.7	209.6	209.9	206.0	207.0	7718.9	563.3	0.656
414	2.35	8.18	51.3	1.083	0.987	233.6	229.5	229.8	225.8	226.8	6950.6	502.1	0.655
415	1.89	6.58	32.2	1.098	0.959	259.2	255.1	255.2	251.1	252.2	6013.4	428.6	0.634
416	1.41	4.90	16.8	1.116	0.917	298.3	294.1	293.9	289.6	290.7	4930.5	344.1	0.595
417	1.15	4.01	11.1	1.158	0.878	327.3	322.9	322.5	318.0	319.2	4267.9	293.3	0.554
418	0.87	3.01	5.8	1.192	0.746	344.1	339.9	339.4	335.5	336.5	3427.6	232.2	0.491
419	0.70	2.43	3.6	1.226	0.621	341.7	337.9	337.3	334	334.9	2870.4	193.6	0.435
420	0.58	2.00	2.4	1.252	0.519	335.5	332.1	331.5	328.8	329.6	2441.7	164.4	0.384
421	0.41	1.42	1.2	1.338	0.35	307.6	304.9	304.3	302.8	303.2	1807	122.2	0.294
484	4.49	15.54	211.4	1.098	1.096	188.1	187.5	181.6	179.6	180.6	10097.3	744.7	0.667
485	4.04	13.99	157.1	1.045	1.141	200.7	200.2	194.4	192.3	193.3	9735.6	713.6	0.536
486	3.79	13.13	136.3	1.036	1.147	206.8	206.4	200.6	198.3	199.4	9454.5	690.5	0.484
487	3.54	12.25	117.9	1.033	1.148	213.6	213.1	207.3	205	206.1	9119.2	663.6	0.439
488	3.08	10.64	89.9	1.036	1.149	231.4	230.7	223.3	219.7	221.2	8440.7	609.3	0.365
489	2.55	8.82	63.6	1.035	1.132	252.6	252	244.5	239.9	241.7	7537.1	538	0.292
490	2.10	7.25	45.6	1.040	1.111	277.3	276.7	268.9	265.5	267	6639.5	467.6	0.234
491	1.50	5.17	28.4	1.111	1.055	323.3	322.6	314.5	311.3	312.9	5304.6	364.2	0.163
492	0.77	2.63	13.7	1.179	0.62	308.9	308.3	302.6	301	301.9	3249.7	219.6	0.082

A.2. Fins Forward

Table 10. Fins Forward Recorded Experimental Data

Case #	P_{rot} [kPa]	Δp [kPa]	p_{in} [kPa]	T_h [℃]	T_0 [℃]	T_1 [℃]	T_2 [℃]	T_3 [℃]	T_{in} [℃]	T_{out} [℃]	p_{amb} [kPa]	$\dot{V}$ [cm^3/s]
380	418.0	150.9	413.9	83.3	64.4	62.8	64.1	66.0	21.7	34.0	97.7	1175.1
381	348.1	129.8	344.3	88.4	69.4	67.9	69.2	71.2	21.8	36.5	97.7	1094.9
382	281.9	109.4	278.4	87.4	70.1	68.7	70.0	72.1	22.0	37.8	97.7	1010.0
383	210.4	85.8	207.4	94.6	77.7	76.3	77.6	79.7	22.2	41.7	97.7	901.4
384	141.4	61.8	139.1	104.9	88.5	87.2	88.4	90.5	22.5	47.0	97.7	774.0
385	100.8	46.3	99.0	115.9	99.7	98.4	99.5	101.6	22.7	52.7	97.7	674.9
386	69.9	33.4	68.5	126.9	111.2	110.0	111.0	113.1	23.0	58.9	97.7	589.9
387	48.8	23.9	47.8	140.3	125.0	123.8	124.6	126.7	23.2	66.1	97.7	505.0
388	34.7	17.3	33.9	153.2	138.3	137.3	138.0	140.0	23.5	73.2	97.6	434.2
389	20.7	10.5	20.2	175.7	161.3	160.3	160.7	162.8	23.8	84.7	97.7	344.5
390	7.2	3.9	7.0	227.5	214.4	213.5	213.3	215.1	24.6	107.1	97.7	207.7
391	419.1	145.0	415.7	184.3	136.4	131.7	134.7	134.7	21.7	54.9	98.3	1146.8
392	346.8	123.3	343.7	194.8	147.6	143.0	145.9	146.2	21.9	60.6	98.3	1061.9
393	278.6	102.2	275.7	208.4	161.9	157.5	160.2	160.7	22.1	67.7	98.3	972.2
394	211.6	80.9	209.2	227.1	181.8	177.5	180.0	180.6	22.4	77.8	98.3	877.8
395	140.0	56.9	138.1	257.3	213.5	209.4	211.6	212.2	22.6	93.7	98.3	741.0
396	105.0	44.3	103.5	281.0	238.3	234.2	236.2	236.8	23.0	106.6	98.3	656.0
397	70.1	31.0	69.1	317.9	276.7	272.7	274.4	274.9	23.4	127.6	98.3	556.9
398	49.6	22.8	48.8	300.0	266.0	262.7	264.0	264.7	23.6	127.3	98.3	486.1
399	35.1	16.7	34.6	286.0	257.6	254.8	255.9	256.8	23.8	126.4	98.3	420.0
400	21.5	10.6	21.2	280.5	257.2	255.0	255.7	256.6	24.1	128.0	98.3	335.1
503	624.0	203.0	616.2	225.0	164.7	158.6	161.3	160.6	24.6	60.6	97.9	1269.5
504	633.6	136.9	628.1	236.1	176.2	170.0	172.6	171.8	24.7	66.2	97.9	1099.5
505	644.8	88.3	641.3	253.4	193.9	187.9	190.2	189.4	25.0	75.3	97.9	885.9
506	652.5	61.2	649.5	271.3	212.6	206.5	208.8	208.1	25.6	84.0	97.8	723.8
507	647.1	46.9	645.9	286.5	228.7	222.4	225.2	224.1	25.8	93.2	97.7	613.0
508	655.1	31.0	655.1	315.7	259.3	253.2	255.7	254.7	26.2	109.2	97.6	452.8
509	673.5	14.0	673.2	286.4	249.3	245.3	246.8	246.7	26.8	117.6	97.6	195.8

Table 11. Fins Forward Calculated Experimental Data

Case #	$\dot{m}$ [g/s]	Re_j [/10^4]	$\Delta p'$ [kPa]	K_L [-]	$\overline{q''}$ [MW/m^2]	T'_0 [°C]	T'_1 [°C]	T'_2 [°C]	T'_3 [°C]	$\overline{T_c}$ [°C]	$\overline{h}$ [kW/m^2-K]	$\overline{h_a}$ [kW/m^2-K]	η [-]	$\overline{Nu}$ [-]	M [-]
380	3.20	11.15	116.9	1.234	0.354	61.5	59.8	61.1	63.0	62.5	12.51	3.32	0.872	252.0	0.689
381	2.76	9.63	85.2	1.231	0.365	66.4	64.8	66.2	68.2	67.6	11.48	3.01	0.882	227.4	0.688
382	2.34	8.16	59.6	1.233	0.332	67.4	65.9	67.3	69.3	68.7	10.25	2.65	0.895	199.7	0.683
383	1.87	6.51	36.6	1.245	0.327	75.0	73.6	74.9	77.1	76.4	8.69	2.20	0.911	165.2	0.665
384	1.40	4.88	19.4	1.273	0.310	86.0	84.6	85.9	88.0	87.3	6.87	1.70	0.930	126.7	0.625
385	1.10	3.83	11.5	1.322	0.297	97.3	96.1	97.1	99.2	98.6	5.64	1.38	0.943	101.7	0.573
386	0.88	3.04	6.7	1.333	0.283	109.0	107.8	108.7	110.9	110.2	4.67	1.13	0.953	82.5	0.516
387	0.69	2.40	4.0	1.401	0.267	122.9	121.7	122.5	124.6	124.1	3.81	0.91	0.962	66.0	0.445
388	0.55	1.93	2.6	1.474	0.249	136.4	135.3	136.0	138.1	137.5	3.14	0.75	0.969	53.5	0.380
389	0.40	1.40	1.3	1.589	0.222	159.7	158.7	159.1	161.1	160.6	2.34	0.55	0.977	38.8	0.294
390	0.20	0.71	0.4	2.122	0.154	213.2	212.4	212.2	214.0	213.6	1.17	0.27	0.989	18.7	0.160
391	3.12	10.89	113.8	1.271	0.932	129.2	124.4	127.5	127.5	127.2	12.73	3.36	0.875	247.2	0.658
392	2.67	9.31	81.7	1.275	0.930	140.5	135.9	138.8	139.1	138.8	11.45	2.97	0.888	217.3	0.652
393	2.24	7.80	55.9	1.280	0.920	155.0	150.5	153.3	153.8	153.4	10.09	2.58	0.902	186.6	0.642
394	1.82	6.35	35.2	1.273	0.911	175.1	170.7	173.3	173.9	173.5	8.68	2.18	0.916	155.6	0.627
395	1.33	4.64	18.1	1.322	0.860	207.3	203.1	205.4	206.0	205.7	6.77	1.66	0.936	116.2	0.580
396	1.08	3.76	11.6	1.376	0.824	232.5	228.4	230.4	231.0	230.7	5.71	1.39	0.946	95.2	0.537
397	0.82	2.86	6.4	1.432	0.785	271.4	267.3	269.0	269.5	269.3	4.60	1.10	0.957	73.7	0.473
398	0.66	2.31	4.0	1.476	0.630	261.6	258.3	259.7	260.3	260.1	3.83	0.91	0.964	61.1	0.419
399	0.54	1.86	2.5	1.547	0.503	254.1	251.3	252.4	253.3	253.0	3.16	0.75	0.970	50.0	0.362
400	0.39	1.36	1.4	1.714	0.373	254.6	252.4	253.1	254.0	253.8	2.34	0.55	0.978	36.6	0.283
503	4.36	15.10	228.8	1.238	1.416	154.0	147.9	150.6	149.9	149.9	16.28	4.45	0.844	323.7	0.664
504	3.85	13.33	166.7	1.216	1.443	165.4	159.2	161.8	161.0	161.1	15.24	4.11	0.854	296.9	0.509
505	3.19	11.04	114.1	1.225	1.448	183.3	177.2	179.5	178.7	178.8	13.56	3.58	0.871	255.8	0.383
506	2.69	9.27	81.7	1.222	1.421	202.4	196.2	198.5	197.8	197.8	11.88	3.08	0.888	217.0	0.306
507	2.32	8.01	62.9	1.232	1.420	218.6	212.2	215.1	213.9	214.0	10.86	2.78	0.898	193.7	0.260
508	1.82	6.26	42.7	1.271	1.373	249.8	243.6	246.1	245.1	245.2	9.03	2.26	0.916	154.4	0.197
509	1.00	3.44	20.0	1.379	0.829	243.5	239.5	241.0	240.9	240.8	5.58	1.35	0.948	91.2	0.103

A.3. Bare Reverse

Table 12. Bare Reverse Recorded Experimental Data

Case #	P_{rot} [kPa]	Δp [kPa]	p_{in} [kPa]	T_h [℃]	T_0 [℃]	T_1 [℃]	T_2 [℃]	T_3 [℃]	T_{in} [℃]	T_{out} [℃]	p_{amb} [kPa]	$\dot{V}$ [cm^3/s]
278	415.6	179.8	410.1	129.9	121.0	120.2	119.0	118.8	23.9	31.7	98.4	1288.4
279	349.2	154.2	344.2	137.8	128.8	128.0	126.9	126.8	23.8	33.2	98.4	1189.3
280	274.1	124.4	269.8	150.3	141.3	140.6	139.1	139.1	23.8	35.7	98.4	1085.5
281	208.3	97.5	204.8	159.9	151.2	150.6	149.0	149.0	23.8	38.5	98.3	976.9
282	142.7	69.8	140.0	173.1	164.7	164.2	162.5	162.5	24.0	42.9	98.4	849.5
283	107.2	53.8	105.0	182.8	174.6	174.2	172.3	172.4	24.1	46.6	98.4	755.1
284	70.4	36.0	68.9	197.9	190.0	189.6	187.4	187.6	24.2	52.6	98.3	637.1
285	48.0	24.7	47.0	219.1	211.2	210.8	208.3	208.3	24.4	60.8	98.3	542.7
286	35.6	18.3	34.5	237.4	229.1	228.6	225.8	225.4	24.1	67.2	98.7	476.7
287	21.8	11.2	21.1	252.3	244.5	244.0	241.1	240.8	24.5	78.3	98.7	377.6
288	7.1	3.7	6.4	290.3	283.1	282.4	279.5	278.8	26.0	106.9	98.6	217.1
289	417.0	175.5	411.0	293.0	272.5	270.8	267.7	267.2	23.8	46.1	98.5	1250.7
290	351.9	151.0	346.5	315.1	294.3	292.6	289.3	288.4	23.8	50.3	98.7	1161.0
291	284.7	125.3	280.0	330.2	310.4	308.9	305.2	304.6	23.9	54.9	98.6	1061.9
292	208.5	94.0	205.1	357.8	338.4	337.1	333.1	332.0	24.5	63.1	98.4	934.5
293	135.2	63.9	132.5	392.4	373.9	372.7	368.4	367.9	24.6	76.0	98.4	783.4
294	105.7	51.3	103.4	347.0	332.4	331.5	328.1	328.6	24.7	74.2	98.4	717.4
295	70.2	35.0	68.3	370.3	356.4	355.7	351.8	352.5	25.0	85.9	98.3	599.4
296	51.2	25.8	49.6	337.0	325.5	325.0	321.8	322.8	25.3	86.6	98.3	533.3
297	36.1	18.4	34.8	350.2	339.3	338.7	335.3	336.4	25.6	95.9	98.3	457.8
298	22.8	11.7	21.5	373.4	362.9	362.3	358.7	359.7	26.2	112.5	98.3	363.4
550	666.4	213.4	661.4	396.4	353.4	352.0	343.8	342.2	23.3	49.5	97.8	1362.5
551	671.8	139.9	668.4	365.2	327.9	326.7	319.5	318.3	23.3	49.5	97.8	1170.7
552	677.4	105.6	674.7	379.6	342.7	341.5	334.3	333.2	23.4	52.9	97.8	1022.3
553	684.2	75.7	683.8	366.5	333.2	331.9	325.4	324.5	23.5	54.6	97.8	858.2
554	687.2	54.9	687.2	378.3	346.8	345.3	338.6	337.2	23.7	59.2	97.8	709.9
555	690.4	41.6	691.9	346.0	319.3	318.0	312.2	311.2	23.7	58.9	97.8	593.2
556	692.5	27.6	695.0	370.7	345.1	343.7	337.8	336.8	24.0	67.8	97.8	427.1
557	700.9	14.0	703.6	393.9	372.2	370.8	364.9	364.3	24.5	86.5	97.8	195.8

Table 13. Bare Reverse Calculated Experimental Data

Case #	$\dot{m}$ [g/s]	Re_j [/10^4]	$\Delta p'$ [kPa]	K_L [-]	$\overline{q''}$ [MW/m^2]	T'_0 [℃]	T'_1 [℃]	T'_2 [℃]	T'_3 [℃]	$\overline{T_c}$ [℃]	$\overline{h}$ [kW/m^2-K]	$\overline{Nu}$ [-]	M [-]
278	3.50	11.89	132.9	1.084	0.247	119.0	118.3	117.1	116.9	117.1	3.82	289.7	0.842
279	3.00	10.18	97.6	1.101	0.254	126.8	126.0	124.9	124.8	124.9	3.62	274.0	0.826
280	2.49	8.39	63.9	1.082	0.268	139.2	138.6	137.0	137.0	137.1	3.40	256.6	0.814
281	2.02	6.77	40.0	1.074	0.268	149.1	148.5	146.9	146.9	147.1	3.13	235.2	0.788
282	1.55	5.12	21.5	1.062	0.264	162.8	162.2	160.5	160.6	160.7	2.78	207.3	0.741
283	1.26	4.14	13.7	1.081	0.256	172.7	172.3	170.4	170.4	170.6	2.51	186.8	0.685
284	0.95	3.08	7.2	1.092	0.244	188.2	187.8	185.7	185.8	186.0	2.17	159.7	0.596
285	0.75	2.36	4.1	1.097	0.245	209.4	209.0	206.5	206.6	206.8	1.93	140.8	0.514
286	0.62	1.94	2.7	1.102	0.241	227.4	226.9	224.1	223.7	224.1	1.73	125.3	0.452
287	0.45	1.38	1.5	1.162	0.219	243.0	242.4	239.6	239.2	239.6	1.47	104.3	0.355
288	0.22	0.63	0.4	1.440	0.160	282.0	281.4	278.4	277.7	278.2	0.92	62.6	0.191
289	3.40	11.15	130.8	1.089	0.681	267.8	266.1	263.0	262.5	262.9	4.10	305.1	0.823
290	2.94	9.56	96.8	1.088	0.700	289.5	287.8	284.5	283.6	284.2	3.87	286.4	0.814
291	2.47	7.94	66.8	1.085	0.691	305.8	304.2	300.6	299.9	300.4	3.60	264.4	0.800
292	1.93	6.09	39.0	1.074	0.674	334.0	332.6	328.6	327.6	328.2	3.19	231.8	0.767
293	1.40	4.29	19.1	1.069	0.649	369.7	368.6	364.2	363.7	364.3	2.75	196.2	0.710
294	1.19	3.66	13.0	1.075	0.531	328.9	328.0	324.5	325.1	325.3	2.54	181.7	0.669
295	0.89	2.67	7.0	1.106	0.491	353.2	352.5	348.7	349.3	349.5	2.18	153.3	0.582
296	0.74	2.21	4.4	1.098	0.410	322.8	322.2	319.0	320.1	320.1	2.00	140.6	0.522
297	0.59	1.74	2.7	1.117	0.378	336.8	336.2	332.9	333.9	334.0	1.76	122.4	0.450
298	0.43	1.23	1.5	1.196	0.340	360.7	360.1	356.5	357.4	357.5	1.48	100.4	0.357
550	4.80	15.64	257.7	1.058	1.133	346.0	344.7	336.4	334.8	335.9	5.22	386.5	0.712
551	4.19	13.65	181.1	1.027	0.988	321.3	320.2	312.9	311.8	312.7	4.92	364.1	0.543
552	3.72	12.02	141.7	1.022	0.987	336.2	335.0	327.8	326.7	327.7	4.67	344.4	0.455
553	3.19	10.28	105.2	1.018	0.894	327.3	326.0	319.5	318.5	319.4	4.35	320.0	0.370
554	2.71	8.63	77.8	1.010	0.869	341.1	339.6	332.9	331.4	332.4	4.05	296.0	0.306
555	2.33	7.42	59.9	1.018	0.738	314.4	313.1	307.3	306.3	307.1	3.75	274.1	0.256
556	1.78	5.56	40.3	1.044	0.705	340.5	339.1	333.1	332.2	333.0	3.28	237.0	0.194
557	1.02	3.06	20.9	1.114	0.573	368.6	367.1	361.2	360.6	361.3	2.45	172.5	0.111

A.4. Fins Reverse

Table 14. Fins Reverse Recorded Experimental Data

Case #	P_{rot} [kPa]	Δp [kPa]	p_{in} [kPa]	T_h [℃]	T_0 [℃]	T_1 [℃]	T_2 [℃]	T_3 [℃]	T_{in} [℃]	T_{out} [℃]	p_{amb} [kPa]	$\dot{V}$ [cm^3/s]
261	202.4	97.6	200.2	121.1	103.9	104.0	102.0	105.2	24.1	52.3	98.3	844.8
262	140.9	72.4	139.4	134.0	117.4	117.5	115.5	118.7	24.2	60.7	98.3	722.1
263	105.8	56.7	104.7	146.0	129.7	129.8	127.7	131.0	24.3	68.5	98.2	637.1
264	68.5	38.6	67.8	165.9	150.3	150.4	148.0	151.4	24.6	81.8	98.2	528.6
265	49.1	28.5	48.6	181.0	165.9	166.0	163.3	166.8	24.8	92.4	98.2	453.1
266	34.4	20.5	34.2	191.8	178.0	177.8	175.4	178.5	24.0	100.7	98.7	387.0
267	20.2	12.4	19.8	218.7	206.3	206.2	203.6	206.9	24.9	119.1	98.7	297.3
268	7.8	5.0	7.5	153.6	148.1	148.3	147.2	150.4	25.5	90.0	98.7	198.2
269	272.6	122.5	269.2	117.1	98.7	98.8	97.4	101.3	23.8	48.6	98.7	943.9
270	346.5	149.1	342.6	109.4	90.5	90.6	89.2	93.3	23.6	44.0	98.7	1043.0
271	416.4	178.8	412.1	104.2	85.0	85.1	83.6	87.6	23.6	40.9	98.7	1137.4
272	413.9	174.9	410.4	226.4	181.3	179.0	176.7	180.6	24.1	70.0	98.5	1076.0
273	349.5	149.5	346.4	242.6	198.1	196.1	193.6	197.5	24.1	78.8	98.6	991.1
274	279.4	124.4	276.8	260.4	217.3	215.5	213.0	216.8	24.1	90.0	98.5	892.0
275	214.0	100.6	211.8	283.0	241.2	239.4	236.9	240.5	24.2	104.9	98.5	788.2
276	146.3	74.8	144.5	319.2	278.9	277.1	274.4	277.4	24.4	128.9	98.6	660.7
277	110.3	59.4	108.5	353.1	313.7	312.1	309.2	312.0	24.7	151.3	98.6	585.2
519	666.3	244.7	664.2	223.2	164.9	160.6	162.6	164.1	23.9	56.6	97.7	1269.5
520	671.2	158.3	672.3	235.7	178.0	173.5	175.7	177.2	24.1	62.9	97.7	1069.8
521	675.8	123.3	677.2	245.1	187.7	183.2	185.5	186.9	24.2	67.9	97.7	945.2
522	680.0	88.1	683.0	258.9	202.6	198.0	200.2	201.4	24.3	75.9	97.7	783.1
523	685.0	60.8	688.5	278.0	222.9	218.4	220.3	221.3	24.5	87.7	97.7	615.0
524	690.2	38.8	694.0	307.6	254.1	249.6	251.1	251.8	24.8	107.1	97.7	435.0
525	694.9	20.0	699.1	259.7	225.2	222.0	223.0	223.4	25.1	110.1	97.7	239.3

Table 15. Fins Reverse Calculated Experimental Data.

Case #	$\dot{m}$ [g/s]	Re_j [/10^4]	$\Delta p'$ [kPa]	K_L [-]	$\overline{q''}$ [MW/m^2]	T'_0 [°C]	T'_1 [°C]	T'_2 [°C]	T'_3 [°C]	$\overline{T_c}$ [°C]	$\overline{h}$ [kW/m^2-K]	$\overline{h_a}$ [kW/m^2-K]	η [-]	$\overline{Nu}$ [-]	M [-]
261	1.72	5.56	39.2	1.396	0.436	100.4	100.5	98.5	101.7	101.1	8.16	2.05	0.918	151.1	0.700
262	1.30	4.12	22.0	1.457	0.426	114.0	114.1	112.1	115.4	114.7	6.78	1.68	0.932	122.0	0.651
263	1.05	3.27	14.2	1.513	0.417	126.5	126.6	124.4	127.8	127.2	5.84	1.43	0.942	102.9	0.602
264	0.77	2.34	7.5	1.587	0.400	147.2	147.3	145.0	148.4	147.7	4.67	1.13	0.954	79.7	0.519
265	0.61	1.81	4.8	1.680	0.376	163.1	163.2	160.4	164.0	163.4	3.91	0.93	0.962	65.2	0.450
266	0.49	1.42	3.0	1.768	0.341	175.4	175.3	172.8	176.0	175.4	3.24	0.77	0.968	53.1	0.382
267	0.34	0.95	1.6	1.992	0.292	204.2	204.0	201.5	204.8	204.2	2.35	0.55	0.977	37.2	0.289
268	0.19	0.58	0.5	2.504	0.114	147.2	147.4	146.4	149.6	148.8	1.33	0.31	0.987	21.6	0.167
269	2.15	7.01	63.0	1.384	0.481	94.9	94.9	93.5	97.5	96.6	9.51	2.43	0.904	179.9	0.712
270	2.61	8.62	94.6	1.376	0.479	86.6	86.8	85.3	89.4	88.5	10.64	2.75	0.892	205.3	0.722
271	3.08	10.23	133.0	1.366	0.480	81.0	81.1	79.7	83.7	82.8	11.67	3.06	0.882	229.1	0.744
272	2.89	8.99	130.2	1.390	1.200	172.4	170.1	167.7	171.7	170.9	11.77	3.05	0.887	219.8	0.727
273	2.48	7.57	96.0	1.392	1.227	189.1	187.1	184.6	188.5	187.8	10.79	2.77	0.897	196.9	0.714
274	2.04	6.08	65.7	1.411	1.218	208.6	206.7	204.2	208.0	207.3	9.58	2.42	0.909	169.7	0.703
275	1.63	4.70	42.4	1.441	1.196	232.8	231.0	228.5	232.1	231.4	8.31	2.07	0.922	142.4	0.685
276	1.19	3.29	23.4	1.505	1.141	271.1	269.3	266.5	269.6	269.1	6.71	1.64	0.938	109.6	0.645
277	0.97	2.56	15.2	1.515	1.127	306.2	304.6	301.7	304.4	304.0	5.81	1.41	0.947	91.3	0.612
519	4.49	14.40	289.1	1.290	1.324	155.0	150.6	152.6	154.1	153.6	14.70	3.94	0.859	289.1	0.711
520	3.85	12.17	203.2	1.295	1.351	167.9	163.4	165.7	167.1	166.6	13.65	3.61	0.869	262.6	0.521
521	3.46	10.80	163.9	1.300	1.363	177.7	173.1	175.4	176.8	176.3	12.91	3.39	0.877	244.4	0.443
522	2.93	9.00	121.2	1.311	1.367	192.6	188.0	190.3	191.4	191.0	11.81	3.06	0.888	218.4	0.358
523	2.39	7.15	85.9	1.333	1.367	213.1	208.5	210.5	211.5	211.1	10.55	2.69	0.901	189.3	0.283
524	1.80	5.19	56.2	1.376	1.352	244.6	240.1	241.6	242.4	242.1	8.96	2.25	0.917	153.8	0.211
525	1.16	3.32	29.5	1.429	0.899	218.8	215.5	216.5	217.0	216.8	6.75	1.66	0.936	113.0	0.132

APPENDIX B: HEMJ EXPERIMENTAL DATA

The following tables list the pertinent time averaged experimental parameters for each of the cases detailed in Chapter 5. Pressures p_{rot} and p_{in} are given as gauge pressure.

B.1. Brass Thimble

Some He cases performed with differential pressure transducer not functioning. These values have been filled 'XXX'.

Table 16. Brass Thimble Recorded Experimental Data

Case #	Gas	p_{rot} [kPa]	Δp [kPa]	p_{in} [kPa]	T_0 [℃]	T_1 [℃]	T_2 [℃]	T_3 [℃]	T_4 [℃]	T_5 [℃]	T_{in} [℃]	T_{out} [℃]	T_{rot} [℃]	p_{amb} [kPa]	$\dot{V}$ [cm^3/s]
14	Air	685.6	19.2	677.1	223.8	221.1	214.8	198.2	240.2	252.8	23.3	79.9	22.8	100.7	895.4
15		690.6	16.7	682.8	247.9	243.4	235.7	220.2	263.8	273.2	23.4	88.6	22.9	101.9	826.7
16		682.8	35.3	669.7	277.1	273.0	267.8	244.3	307.4	333.3	23.6	87.9	22.9	101.9	1209.3
17		673.5	73.3	650.5	241.5	237.3	232.0	209.4	271.8	297.1	24.4	71.0	22.8	101.9	1719.4
30		677.3	60.0	663.7	101.1	100.5	98.3	88.2	115.3	128.6	23.2	40.3	23.0	100.8	1552.6
31		692.4	21.7	685.0	117.0	117.2	115.9	104.7	130.8	146.3	23.4	49.0	23.0	100.8	934.6
32		696.9	14.2	690.9	126.2	126.4	125.0	113.7	139.6	154.8	23.4	54.0	23.1	100.8	738.4
33		699.2	9.1	694.4	137.6	137.8	136.4	124.9	150.8	165.6	23.4	60.5	23.1	100.8	561.8
18	He	1365.3	43.2	1348.8	221.3	212.7	205.0	179.0	267.6	304.7	23.8	67.6	25.0	101.2	1278.0
19		1373.1	115.4	1344.4	188.5	176.6	167.3	144.2	237.0	272.1	23.9	52.1	23.8	101.9	2062.8
20		1368.5	76.5	1346.1	202.8	190.8	181.1	157.9	250.6	285.1	24.2	56.6	22.2	101.9	1680.2
22		1351.4	XXX	1307.6	204.0	198.0	185.8	151.5	267.0	312.3	24.7	54.7	28.5	101.2	2736.4
23		1365.6	XXX	1330.9	191.0	196.8	189.3	146.1	259.1	314.2	24.5	54.9	27.3	100.7	2370.0
24		1373.2	XXX	1347.7	210.6	216.9	209.8	164.4	279.7	337.7	25.2	61.0	25.9	100.7	1942.6
25		1391.0	XXX	1373.4	243.1	249.9	242.9	195.3	312.2	372.0	25.5	72.6	24.3	100.7	1454.0
42	Ar	707.6	63.4	693.1	102.4	103.3	100.2	89.6	114.4	125.1	16.6	39.0	12.1	100.3	1562.4
43		699.1	50.0	686.9	103.8	104.6	103.1	92.0	115.8	129.8	14.3	38.7	9.1	100.3	1405.5
44		696.3	38.3	686.2	107.5	108.5	107.0	95.8	119.5	133.8	13.5	40.4	7.4	100.3	1228.9
45		693.7	26.2	686.6	115.3	116.3	114.9	103.5	127.1	141.1	14.5	45.2	7.9	100.3	1013.1
46		690.2	19.8	684.2	121.9	122.7	121.2	109.9	133.4	147.2	15.4	49.2	8.8	100.3	856.1
47		685.9	12.1	681.1	135.4	136.4	134.8	123.1	146.8	160.4	17.6	58.2	10.7	100.3	659.9
48		692.8	7.5	688.8	148.6	149.4	147.8	136.0	159.7	172.9	19.4	67.8	12.7	100.3	483.3

Table 17. Brass Thimble Calculated Experimental Data

Case #	Gas	$\dot{m}$ [g/s]	Re_j [/10^4]	K_L [-]	$\overline{q''}$ [MW/m^2]	T'_0 [℃]	T'_1 [℃]	T'_2 [℃]	T'_3 [℃]	$\overline{T_c}$ [℃]	$\overline{h}$ [kW/m^2-K]	$\overline{Nu}$ [-]	κ [-]
14	Air	2.98	2.15	2.213	0.750	195.5	212.1	218.5	221.1	208.5	6.98	248.3	4923
15		2.76	2.00	2.261	0.800	217.4	232.8	240.6	245.1	230.0	6.68	234.8	4953
16		4.02	2.90	2.165	1.149	240.3	263.9	269.0	273.2	257.9	8.46	297.6	5065
17		5.68	4.09	2.068	1.174	205.2	227.9	233.2	237.3	222.2	10.25	368.2	5030
30		5.14	3.72	2.157	0.392	86.6	96.7	98.9	99.5	94.1	9.53	357.3	4660
31		3.12	2.26	2.287	0.356	103.3	114.5	115.8	115.6	111.3	6.98	258.6	4688
32		2.48	1.79	2.433	0.336	112.4	123.7	125.1	124.9	120.5	5.97	219.9	4701
33		1.89	1.36	2.698	0.311	123.7	135.2	136.6	136.4	131.9	4.94	180.2	4713
18	He	2.15	1.43	2.441	2.156	171.0	197.1	204.9	213.6	191.1	22.25	136.8	839
19		3.49	2.31	2.341	2.256	135.6	158.9	168.2	180.2	154.2	29.89	186.9	825
20		2.85	1.89	2.403	2.108	149.9	173.3	183.0	195.2	168.7	25.19	156.7	832
22		4.56	3.02	XXX	3.130	139.6	174.2	186.6	192.6	166.5	38.08	237.2	832
23		3.98	2.63	XXX	2.760	135.5	179.1	186.7	180.8	167.1	33.40	208.0	832
24		3.27	2.16	XXX	2.680	154.3	200.1	207.2	200.9	187.3	28.53	176.4	841
25		2.47	1.63	XXX	2.665	185.6	233.5	240.5	233.8	220.0	23.65	144.3	853
42	Ar	6.31	3.78	2.211	0.325	88.3	98.9	102.0	101.1	96.3	7.04	396.6	7012
43		5.67	3.43	2.195	0.318	90.7	101.8	103.4	102.5	98.7	6.51	367.9	7055
44		4.97	3.01	2.231	0.307	94.5	105.8	107.2	106.2	102.6	5.95	335.9	7075
45		4.09	2.47	2.290	0.288	102.4	113.7	115.1	114.2	110.5	5.18	290.3	7079
46		3.44	2.07	2.449	0.267	108.8	120.2	121.7	120.8	117.0	4.53	252.1	7079
47		2.63	1.58	2.531	0.246	122.1	133.9	135.4	134.5	130.5	3.76	206.0	7070
48		1.93	1.15	2.943	0.215	135.2	147.0	148.6	147.8	143.7	2.98	160.9	7055

B.2. Steel Thimble

All cases assumed to have constant p_{amb} of 100.7 kPa.

Table 18. Steel Thimble Recorded Experimental Data

Case #	Gas	P_{rot} [kPa]	Δp [kPa]	p_{in} [kPa]	T_0 [°C]	T_1 [°C]	T_2 [°C]	T_3 [°C]	T_4 [°C]	T_5 [°C]	T_{in} [°C]	T_{out} [°C]	T_{rot} [°C]	$\dot{V}$ [cm^3/s]
101	Air	684.8	7.4	679.5	264.2	256.2	248.2	219.8	302.0	370.2	24.9	83.9	24.7	503.0
102		681.7	12.3	674.7	233.6	225.9	219.2	191.7	271.6	339.4	24.8	71.1	24.6	699.2
103		676.2	18.1	667.3	249.7	240.2	232.1	201.1	294.8	377.5	24.7	70.7	24.4	895.4
104		664.3	26.9	652.6	231.6	222.1	215.3	184.3	277.4	361.0	24.2	63.1	23.8	1091.6
105		658.4	37.7	643.4	215.3	206.4	200.6	169.9	261.3	343.2	24.2	57.8	23.9	1287.8
106		652.6	50.6	633.8	202.6	194.1	189.0	158.7	248.6	329.6	24.1	53.7	23.9	1484.0
107		649.3	65.8	626.1	192.4	184.3	179.6	149.8	238.5	318.7	24.1	50.6	23.9	1680.2
108		644.8	85.8	616.5	183.3	175.6	171.9	141.8	229.7	308.9	24.1	47.8	23.9	1876.4
109		643.0	107.0	609.7	176.2	168.7	165.4	135.6	222.6	301.3	24.0	45.7	23.9	2072.6
110	Ar	625.4	68.9	600.6	109.0	106.9	107.1	91.5	128.7	156.1	22.6	38.6	21.0	1719.4
111		618.6	103.3	585.2	198.0	192.6	189.4	158.1	239.8	303.2	22.2	51.8	20.3	2033.3
112		634.2	12.7	626.6	192.4	189.4	187.6	165.4	217.6	251.3	24.4	67.3	23.8	738.4
113		610.0	73.1	585.2	202.3	198.7	185.0	163.2	226.2	285.6	22.0	55.0	17.7	1719.4
114		593.0	6.3	588.3	216.9	211.1	202.3	186.9	227.7	280.9	24.8	76.5	23.2	434.3
115		587.5	17.2	579.0	227.7	223.9	210.7	189.4	245.2	300.8	24.3	71.0	21.6	846.3
116		615.8	25.3	604.7	200.9	197.3	184.8	166.8	216.9	268.3	23.5	62.2	20.4	1042.5
117		613.1	38.2	598.3	183.0	179.5	167.6	150.7	199.2	249.7	21.8	54.9	16.8	1268.1
118	He	1400.8	14.3	1386.9	154.0	137.3	130.1	134.8	176.2	269.4	26.5	52.2	27.3	758.0
119		1411.2	56.4	1384.6	162.5	140.9	138.8	149.8	210.3	364.2	29.1	48.7	30.0	1523.2
120		1402.1	89.7	1366.3	191.7	175.7	156.5	161.7	248.6	397.1	28.9	49.8	29.3	1915.6
121		1364.4	174.1	1307.9	163.8	146.7	136.9	132.2	232.6	421.7	27.1	41.9	27.4	2553.2
122		1334.6	218.1	1268.9	154.7	141.6	131.3	120.5	228.9	415.0	24.4	38.2	24.2	2736.4
123		1347.5	304.3	1264.9	147.0	131.0	117.6	115.8	203.5	368.5	25.6	37.1	25.7	3163.9

Table 19. Steel Thimble Calculated Experimental Data

Case #	Gas	$\dot{m}$ [g/s]	Re_j [/10^4]	K_L [-]	$\overline{q''}$ [MW/m^2]	T'_0 [°C]	T'_1 [°C]	T'_2 [°C]	T'_3 [°C]	$\overline{T_c}$ [°C]	$\overline{h}$ [kW/m^2-K]	$\overline{Nu}$ [-]	κ [-]
101	Air	1.67	1.20	2.760	0.437	215.8	244.1	252.0	260.1	237.4	3.55	125.3	1888
102		2.32	1.67	2.343	0.476	187.4	214.9	221.5	229.1	208.1	4.48	160.9	1970
103		2.96	2.13	2.082	0.604	195.6	226.5	234.5	244.0	219.0	5.37	192.7	1953
104		3.58	2.58	2.053	0.619	178.8	209.6	216.4	225.9	201.9	6.01	218.4	2003
105		4.21	3.03	2.021	0.627	164.4	194.9	200.7	209.6	187.0	6.65	243.0	2043
106		4.83	3.48	1.995	0.633	153.2	183.3	188.4	196.9	175.3	7.23	265.9	2075
107		5.45	3.93	1.966	0.640	144.2	173.9	178.6	186.7	166.0	7.79	287.6	2100
108		6.07	4.38	1.975	0.639	136.3	166.3	170.0	177.6	158.0	8.25	305.7	2122
109		6.70	4.83	1.933	0.646	130.0	159.7	163.1	170.5	151.4	8.75	325.3	2140
110	Ar	6.48	3.82	1.931	0.239	89.5	105.1	104.9	107.0	100.2	5.31	296.9	3350
111		7.64	4.51	1.925	0.520	153.6	184.7	187.9	193.3	175.9	5.84	320.8	3098
112		2.79	1.63	2.165	0.274	162.9	185.1	187.0	190.0	178.7	3.07	164.6	3019
113		6.45	3.81	2.012	0.489	158.9	180.6	194.3	197.8	177.3	5.44	297.6	3082
114		1.59	0.93	3.105	0.189	185.2	200.6	209.4	215.2	198.1	1.89	99.9	2934
115		3.10	1.82	2.192	0.333	186.4	207.7	220.9	224.6	204.3	3.19	170.4	2941
116		3.91	2.30	2.093	0.348	163.7	181.7	194.1	197.8	179.2	3.86	208.5	3042
117		4.77	2.82	2.071	0.363	147.5	164.4	176.3	179.7	162.1	4.46	244.1	3122
118	He	1.29	0.85	2.345	0.757	128.3	123.7	130.8	147.5	127.3	12.95	80.8	366
119		2.58	1.69	2.206	1.156	139.8	128.9	130.9	152.4	133.4	19.14	119.4	364
120		3.24	2.12	2.148	1.556	148.1	143.0	162.0	177.8	149.7	22.23	138.6	359
121		4.28	2.81	2.156	1.446	119.9	124.6	134.3	151.2	125.9	25.26	159.2	370
122		4.57	3.02	2.235	1.437	108.4	119.1	129.3	142.2	118.6	26.34	167.2	375
123		5.29	3.49	2.133	1.393	104.1	105.8	119.1	135.0	109.0	28.84	183.0	378

APPENDIX C: UNCERTAINTY ANALYSIS

The uncertainty in the experimental measurements is an important consideration when analyzing the results of experiments. It's imperative to use an appropriately accurate instrument depending on its purpose. Standard error approximation was used for the experiments presented in Chapters 3-5 and will be summarized herein. These techniques are discussed in more detail in reference materials [61] [62].

C.1. Uncertainty Assumptions

There are several sources of error for a given measurement or calculation. For the purpose of this thesis, the error analysis will follow these guidelines:

- Errors in the manufacture of instruments are inevitable and these values as reported by the manufacturer will be assumed to be valid.
- Error in measurements by the experimenter should be based on the precision of his or her instruments.
- Only half of the smallest gradation of an analog instrument is the limit of that instrument's precision.
- Calibrated instruments assume the uncertainty of the calibration device.
- Uncertainty based on the oscillations of the readings of electronic instruments will be neglected as all reported values are time averaged over a range of 3-5 minutes depending on the experiment.
- Error in machining and placement of sensors was not considered and assumed to be negligible.

- Error as a result of measuring was not considered, that is error in the measured temperature by TCs as a result of the placement of the TCs in the test section. This would be considered a covariance term.

C.2. Uncertainty in Measurements

Details of instrument calibration follow in Appendix D. The OMEGA Type E TCs used in these experiments are rated as having a ±1 ℃ error up to 250 ℃ and an extra error of 0.004 ℃ for every ℃ above 250 ℃.

The Brooks 1110 flow meter used to measure volumetric flow in the experiments has gradations of 1% from 0-100%. This means that only 0.5% precision is achievable (9.8 cm^3/s).

All of the pressure transducers used (differential and total) were calibrated with an analog pressure gauge with gradations of 0.2 psi. This means that only 0.1 psi precision is achievable (689.5 Pa). The atmospheric pressure gauge has gradations of 1 torr so 0.5 torr (66.7 Pa) precision was achievable.

C.3. Uncertainty in Calculations

Uncertainty U in measurements is propagated through the calculation of derived quantities using the standard error approximation (ignoring covariance):

$$U_x(i,j,\dots,n) = \sqrt{U_i^2\left(\frac{\partial x}{\partial i}\right)^2 + U_j^2\left(\frac{\partial x}{\partial j}\right)^2 + \cdots + U_n^2\left(\frac{\partial x}{\partial n}\right)^2} \tag{74}$$

where x is the derived quantity that is a function of either measured or derived quantities $(i,j,\dots,n)$. Examples of the application of this equation follow.

For the HEMJ experiments, the mass flow rate, $\dot{m}$, is calculated from the measured quantities $\dot{V}$, p_{amb}, p_{rot}, and T_{rot}. The uncertainty in $\dot{m}$ is thus $U_{\dot{m}}$:

$$U_{\dot{m}}\left(\dot{V}, p_{amb}, p_{rot}, T_{rot}\right) =$$

$$\sqrt{U_{\dot{V}}^2\left(\frac{\partial \dot{m}}{\partial \dot{V}}\right)^2 + U_{p_{amb}}^2\left(\frac{\partial \dot{m}}{\partial p_{atm}}\right)^2 + U_{p_{rot}}^2\left(\frac{\partial \dot{m}}{\partial p_{rot}}\right)^2 + U_{T_{rot}}^2\left(\frac{\partial \dot{m}}{\partial T_{rot}}\right)^2} \quad (75)$$

The uncertainty can also be calculated from the uncertainty in other derived quantities as long as the uncertainty is based on measured quantities. For example Eq. 75 can be rewritten in terms of the rotameter density, ρ_{rot}, and volumetric flow rate because ρ_{rot} is derived from , p_{atm} , p_{rot} , and T_{rot}:

$$U_{\dot{m}}\left(\dot{V}, \rho_{rot}\right) = \sqrt{U_{\dot{V}}^2\left(\frac{\partial \dot{m}}{\partial \dot{V}}\right)^2 + U_{\rho_{rot}}^2\left(\frac{\partial \dot{m}}{\partial \rho_{rot}}\right)^2} \quad (76)$$

For HEMJ case 19 (He-cooled brass thimble), the calculation is as follows:

$$U_{\dot{V}} = 9.8\ \mathrm{cm^3/s} \quad (77)$$

$$\frac{\partial \dot{m}}{\partial \dot{V}} = \sqrt{\rho_{rot}\rho_{cal}}\ = 1.693\ \mathrm{kg/cm^3} \quad (78)$$

$$U_{\rho_{rot}} = 1.12\ \mathrm{g/m^3} \quad (79)$$

$$\frac{\partial \dot{m}}{\partial \rho_{rot}} = \dot{V}\frac{\sqrt{\rho_{cal}}}{2\sqrt{\rho_{rot}}} = 730.0\ \mathrm{cm^3/s} \quad (80)$$

$$U_{\dot{m}}\left(\dot{V}, \rho_{rot}\right) = 0.0166\ \mathrm{g/s} \quad (81)$$

A similar method was applied to other derived quantities. An example follows. For the case of the HTC, which is derived from the measured values of T_0, T_1, T_2, T_3,

T_{in}, T_{out}, p_{atm}, p_{rot}, $\dot{V}$, and T_{rot}, it is much simpler to use the derived quantity $\overline{q''}$ and the temperature difference $\overline{T_c} - T_{in}$:

$$U_{\overline{h}}\left(\overline{q''}, \overline{T_c} - T_{in}\right) = \sqrt{U^2_{\overline{T_c}-T_{in}}\left(\frac{\partial \overline{h}}{\partial\, \overline{T_c}-T_{in}}\right)^2 + U^2_{\overline{q''}}\left(\frac{\partial \overline{h}}{\partial \overline{q''}}\right)^2} \tag{82}$$

For the same case discussed previously (HEMJ He-Brass case #19), the calculation of the uncertainty in $\overline{h}$ is as follows:

$$U_{\overline{T_c}-T_{in}} = 1.19\ \mathrm{K} \tag{83}$$

$$\left|\frac{\partial \overline{h}}{\partial\, \overline{T_c}-T_{in}}\right| = \frac{A_h}{A_c}\frac{\overline{q''}}{\left(\overline{T_c}-T_{in}\right)^2} = 229.5\ \mathrm{W/(m^2K^2)} \tag{84}$$

$$U_{\overline{q''}} = 113.5\ \mathrm{kW/m^2} \tag{85}$$

$$\frac{\partial \overline{h}}{\partial \overline{q''}} = \frac{A_h}{A_c}\frac{1}{\overline{T_c}-T_{in}} = 0.0132\ \mathrm{1/K} \tag{86}$$

$$U_{\overline{h}}\left(\overline{q''}, \overline{T_c} - T_{in}\right) = 1528\ \mathrm{W/(m^2K)} \tag{87}$$

Data tables of the uncertainty of measured quantities for the HEMP and HEMJ experiments follows on subsequent pages.

C.4. Bare Forward Uncertainty

Table 20. Relevant Bare Forward Uncertainty in Calculated Experimental Data

Case #	$\dot{m}$ [g/s]	Re_j [/10^4]	K_L [-]	$\overline{q''}$ [kW/m^2]	T'_0 [℃]	T'_1 [℃]	T'_2 [℃]	T'_3 [℃]	$\overline{T_c}$ [℃]	$\overline{h}$ [W/m^2-K]	$\overline{Nu}$ [-]
401	0.033	0.122	0.034	41.6	1.087	1.087	1.087	1.087	0.838	1,049.4	80.0
402	0.030	0.112	0.036	36.1	1.073	1.073	1.073	1.073	0.828	835.6	63.5
403	0.028	0.102	0.039	30.6	1.062	1.062	1.062	1.062	0.819	643.6	48.7
404	0.025	0.092	0.042	25.2	1.051	1.052	1.052	1.052	0.811	470.4	35.4
405	0.022	0.080	0.047	19.5	1.041	1.041	1.041	1.041	0.802	311.9	23.3
406	0.020	0.072	0.053	16.0	1.034	1.034	1.034	1.034	0.797	228.7	17.0
407	0.018	0.065	0.062	12.9	1.026	1.026	1.026	1.026	0.791	161.6	11.9
408	0.017	0.061	0.071	11.1	1.022	1.022	1.022	1.022	0.788	123.8	9.1
409	0.016	0.057	0.085	10.2	1.019	1.019	1.019	1.020	0.786	101.7	7.4
410	0.015	0.054	0.120	9.5	1.015	1.015	1.015	1.015	0.783	81.1	5.8
411	0.014	0.050	0.334	10.4	1.008	1.008	1.008	1.008	0.777	67.9	4.7
412	0.032	0.120	0.034	41.7	1.260	1.262	1.262	1.263	0.974	360.2	26.6
413	0.030	0.111	0.036	36.7	1.250	1.251	1.251	1.253	0.966	291.5	21.4
414	0.028	0.101	0.038	31.8	1.235	1.236	1.236	1.237	0.954	228.5	16.6
415	0.025	0.090	0.042	27.0	1.263	1.250	1.251	1.238	0.955	173.0	12.4
416	0.022	0.078	0.049	22.8	1.369	1.355	1.354	1.340	1.034	125.3	8.8
417	0.020	0.072	0.056	21.2	1.455	1.439	1.438	1.423	1.098	105.4	7.3
418	0.018	0.064	0.067	19.2	1.480	1.465	1.463	1.448	1.118	89.6	6.1
419	0.017	0.060	0.079	17.6	1.443	1.429	1.427	1.415	1.091	82.4	5.6
420	0.016	0.057	0.093	16.3	1.400	1.387	1.385	1.374	1.060	77.8	5.3
421	0.015	0.053	0.135	14.1	1.264	1.254	1.251	1.246	0.961	73.1	5.0
484	0.039	0.146	0.031	57.3	1.343	1.344	1.347	1.348	1.039	536.0	39.6
485	0.038	0.140	0.028	52.0	1.345	1.345	1.348	1.349	1.040	451.1	33.2
486	0.037	0.137	0.028	49.1	1.339	1.339	1.342	1.343	1.035	411.9	30.2
487	0.036	0.133	0.028	46.1	1.330	1.330	1.333	1.334	1.029	373.4	27.3
488	0.035	0.128	0.030	41.0	1.314	1.314	1.318	1.319	1.017	306.8	22.3
489	0.034	0.122	0.034	35.6	1.323	1.321	1.301	1.295	0.999	242.0	17.4
490	0.033	0.118	0.041	31.9	1.380	1.378	1.355	1.345	1.038	194.4	13.8
491	0.033	0.114	0.062	29.7	1.500	1.498	1.471	1.461	1.127	152.1	10.5
492	0.032	0.111	0.171	27.7	1.329	1.327	1.306	1.300	1.003	146.0	9.9

C.5. Fins Forward Uncertainty

Table 21. Relevant Fins Forward Uncertainty in Calculated Experimental Data

Case #	$\dot{m}$ [g/s]	Re_j [/10^4]	K_L [-]	$\overline{q''}$ [kW/m^2]	T'_0 [℃]	T'_1 [℃]	T'_2 [℃]	T'_3 [℃]	$\overline{T_c}$ [℃]	$\overline{h}$ [W/m^2-K]	$\overline{h_a}$ [W/m^2-K]	$\overline{Nu}$ [-]
380	0.032	0.120	0.041	40.4	1.095	1.095	1.095	1.095	0.844	1,480.6	384.7	29.2
381	0.030	0.111	0.043	35.0	1.083	1.084	1.083	1.083	0.835	1,146.2	294.4	22.3
382	0.028	0.101	0.046	29.7	1.065	1.066	1.065	1.065	0.821	958.4	243.0	18.3
383	0.025	0.090	0.051	23.9	1.053	1.053	1.053	1.053	0.812	668.1	166.6	12.5
384	0.022	0.078	0.058	18.3	1.041	1.041	1.041	1.041	0.803	427.7	104.6	7.8
385	0.020	0.071	0.068	14.9	1.034	1.034	1.034	1.034	0.797	297.7	71.9	5.3
386	0.018	0.064	0.076	12.5	1.029	1.029	1.029	1.029	0.793	217.2	52.0	3.8
387	0.017	0.060	0.091	10.9	1.024	1.025	1.025	1.024	0.790	163.0	38.7	2.8
388	0.016	0.057	0.112	10.1	1.021	1.021	1.021	1.021	0.787	131.9	31.1	2.2
389	0.015	0.053	0.156	9.8	1.016	1.016	1.016	1.016	0.784	105.8	24.8	1.8
390	0.014	0.050	0.416	11.1	1.009	1.009	1.009	1.009	0.778	84.8	19.6	1.3
391	0.032	0.120	0.042	40.5	1.267	1.270	1.268	1.268	0.978	577.1	149.4	11.0
392	0.030	0.110	0.045	35.2	1.252	1.254	1.252	1.252	0.966	454.4	116.0	8.5
393	0.028	0.100	0.048	30.4	1.234	1.236	1.235	1.235	0.952	349.6	88.0	6.4
394	0.025	0.090	0.052	26.2	1.217	1.219	1.218	1.218	0.939	261.1	64.8	4.7
395	0.022	0.078	0.062	21.9	1.182	1.183	1.182	1.182	0.911	179.6	43.7	3.1
396	0.020	0.071	0.071	20.5	1.160	1.161	1.161	1.160	0.895	146.9	35.4	2.5
397	0.018	0.064	0.085	20.3	1.233	1.219	1.225	1.227	0.946	121.6	29.0	2.0
398	0.017	0.060	0.099	18.3	1.152	1.141	1.145	1.148	0.885	113.2	26.8	1.8
399	0.016	0.057	0.120	16.7	1.091	1.081	1.085	1.088	0.839	106.2	25.0	1.7
400	0.015	0.053	0.172	15.4	1.065	1.056	1.059	1.063	0.819	97.5	22.8	1.5
503	0.038	0.144	0.036	56.4	1.514	1.519	1.517	1.518	1.170	677.0	181.3	13.3
504	0.037	0.137	0.034	50.5	1.507	1.512	1.510	1.511	1.165	559.1	148.0	10.7
505	0.036	0.130	0.035	43.4	1.484	1.489	1.487	1.488	1.147	427.4	111.1	8.0
506	0.035	0.124	0.039	38.5	1.449	1.453	1.452	1.452	1.120	337.8	86.2	6.1
507	0.034	0.121	0.044	35.9	1.433	1.437	1.435	1.436	1.107	287.4	72.5	5.1
508	0.033	0.117	0.056	34.1	1.416	1.402	1.408	1.405	1.084	231.7	57.4	4.0
509	0.033	0.113	0.125	30.0	1.169	1.170	1.169	1.169	0.902	204.6	49.2	3.3

C.6. Bare Reverse Uncertainty

Table 22. Relevant Bare Reverse Uncertainty in Calculated Experimental Data

Case #	$\dot{m}$ [g/s]	Re_j [/10^4]	K_L [-]	$\overline{q''}$ [kW/m^2]	T'_0 [℃]	T'_1 [℃]	T'_2 [℃]	T'_3 [℃]	$\overline{T_c}$ [℃]	$\overline{h}$ [W/m^2-K]	$\overline{Nu}$ [-]
278	0.032	0.118	0.038	44.1	1.075	1.075	1.076	1.076	0.829	683.4	51.8
279	0.030	0.108	0.042	37.9	1.061	1.061	1.061	1.061	0.818	541.7	41.0
280	0.027	0.097	0.045	31.5	1.049	1.049	1.049	1.049	0.809	402.0	30.3
281	0.025	0.086	0.049	25.7	1.039	1.039	1.039	1.039	0.801	302.1	22.7
282	0.022	0.075	0.054	19.9	1.030	1.030	1.030	1.030	0.794	210.8	15.8
283	0.020	0.068	0.062	16.4	1.025	1.025	1.025	1.025	0.790	162.8	12.1
284	0.018	0.060	0.074	12.9	1.020	1.020	1.020	1.020	0.787	115.9	8.6
285	0.017	0.055	0.090	10.9	1.018	1.018	1.018	1.018	0.785	87.4	6.4
286	0.016	0.051	0.108	10.1	1.017	1.017	1.017	1.017	0.784	73.3	5.3
287	0.015	0.047	0.159	9.4	1.014	1.014	1.014	1.014	0.782	63.6	4.5
288	0.014	0.041	0.506	10.9	1.140	1.137	1.125	1.123	0.866	62.6	4.3
289	0.032	0.113	0.044	43.3	1.221	1.215	1.205	1.203	0.928	261.7	19.5
290	0.030	0.104	0.047	37.7	1.293	1.287	1.275	1.272	0.981	209.7	15.5
291	0.028	0.093	0.052	32.1	1.341	1.335	1.322	1.320	1.018	168.1	12.4
292	0.025	0.081	0.060	25.8	1.433	1.428	1.413	1.409	1.087	123.4	9.0
293	0.022	0.068	0.074	20.3	1.557	1.552	1.536	1.534	1.183	86.9	6.2
294	0.020	0.063	0.078	17.5	1.379	1.375	1.362	1.364	1.052	84.7	6.1
295	0.018	0.056	0.100	15.1	1.463	1.460	1.445	1.448	1.117	67.8	4.8
296	0.017	0.052	0.109	13.3	1.332	1.330	1.318	1.322	1.019	65.9	4.7
297	0.016	0.048	0.137	12.8	1.381	1.379	1.366	1.370	1.056	60.4	4.2
298	0.015	0.044	0.209	13.3	1.470	1.468	1.453	1.457	1.124	58.2	4.0
550	0.040	0.141	0.036	61.2	1.640	1.636	1.610	1.605	1.238	283.2	21.0
551	0.038	0.133	0.033	53.6	1.505	1.501	1.478	1.474	1.137	267.8	19.9
552	0.037	0.127	0.035	47.9	1.545	1.541	1.517	1.514	1.168	227.9	16.8
553	0.036	0.121	0.037	41.5	1.480	1.476	1.454	1.451	1.119	203.2	15.0
554	0.035	0.116	0.043	36.0	1.515	1.510	1.486	1.481	1.143	169.0	12.4
555	0.035	0.113	0.049	31.4	1.382	1.378	1.357	1.354	1.044	160.5	11.8
556	0.034	0.108	0.069	26.2	1.464	1.458	1.437	1.433	1.106	123.1	8.9
557	0.033	0.101	0.165	22.8	1.539	1.534	1.512	1.509	1.164	98.0	6.9

C.7. Fins Reverse Uncertainty

Table 23. Relevant Fins Reverse Uncertainty in Calculated Experimental Data

Case #	$\dot{m}$ [g/s]	Re_j [/10^4]	K_L [-]	$\overline{q''}$ [kW/m^2]	T'_0 [℃]	T'_1 [℃]	T'_2 [℃]	T'_3 [℃]	$\overline{T_c}$ [℃]	$\overline{h}$ [W/m^2-K]	$\overline{h_a}$ [W/m^2-K]	$\overline{Nu}$ [-]
261	0.024	0.081	0.080	22.5	1.073	1.073	1.073	1.072	0.827	442.7	109.6	8.1
262	0.022	0.071	0.100	17.8	1.063	1.063	1.063	1.063	0.819	299.6	73.1	5.3
263	0.020	0.064	0.121	15.4	1.057	1.057	1.057	1.057	0.815	228.1	55.2	4.0
264	0.018	0.055	0.160	13.5	1.049	1.049	1.049	1.049	0.809	165.3	39.5	2.8
265	0.017	0.051	0.206	13.0	1.042	1.042	1.042	1.042	0.804	139.7	33.2	2.3
266	0.016	0.047	0.265	12.9	1.035	1.035	1.035	1.035	0.798	125.4	29.6	2.1
267	0.015	0.043	0.438	13.8	1.026	1.026	1.026	1.026	0.791	112.2	26.2	1.8
268	0.014	0.043	0.766	8.8	1.006	1.006	1.006	1.006	0.776	103.4	24.0	1.7
269	0.027	0.092	0.070	27.7	1.093	1.093	1.094	1.093	0.843	573.5	144.0	10.7
270	0.030	0.103	0.062	33.4	1.105	1.105	1.105	1.104	0.851	770.3	195.7	14.6
271	0.032	0.113	0.057	39.1	1.118	1.118	1.119	1.118	0.862	984.1	252.8	19.0
272	0.032	0.104	0.075	38.8	1.363	1.364	1.365	1.363	1.051	397.7	101.6	7.4
273	0.030	0.095	0.085	34.6	1.360	1.361	1.362	1.360	1.049	319.1	80.7	5.8
274	0.027	0.084	0.101	30.5	1.338	1.339	1.340	1.338	1.032	251.3	62.7	4.4
275	0.025	0.074	0.127	27.5	1.312	1.313	1.314	1.312	1.012	199.5	49.2	3.4
276	0.022	0.062	0.179	25.9	1.363	1.358	1.350	1.358	1.047	157.5	38.2	2.6
277	0.020	0.054	0.227	26.7	1.463	1.458	1.449	1.457	1.124	140.9	33.9	2.2
519	0.039	0.134	0.050	57.8	1.470	1.473	1.472	1.471	1.134	663.0	174.6	12.8
520	0.037	0.125	0.049	50.3	1.459	1.462	1.460	1.459	1.125	527.7	137.4	10.0
521	0.037	0.120	0.052	45.9	1.450	1.453	1.451	1.451	1.119	452.4	116.8	8.5
522	0.036	0.113	0.060	40.5	1.433	1.436	1.435	1.434	1.106	365.5	93.3	6.7
523	0.035	0.106	0.075	36.1	1.412	1.415	1.414	1.413	1.090	290.6	73.2	5.2
524	0.034	0.099	0.111	34.2	1.395	1.385	1.388	1.389	1.071	234.1	58.0	4.0
525	0.033	0.096	0.186	29.8	1.200	1.201	1.200	1.200	0.926	228.3	55.5	3.8

C.8. HEMJ Brass Thimble Uncertainty

Some He cases performed with differential pressure transducer not functioning. These values have been filled 'XXX'.

Table 24. Relevant Brass Thimble Uncertainty in Calculated Experimental Data

Case #	Gas	$\dot{m}$ [g/s]	Re_j [/10^4]	K_L [-]	$\overline{q''}$ [kW/m^2]	T'_0 [℃]	T'_1 [℃]	T'_2 [℃]	T'_3 [℃]	$\overline{T_c}$ [℃]	$\overline{h}$ [W/m^2-K]	$\overline{Nu}$ [-]
14	Air	0.033	0.024	0.093	20.4	1.005	1.005	1.005	1.005	0.588	195.5	7.0
15		0.033	0.024	0.108	19.8	1.005	1.005	1.005	1.005	0.588	169.5	6.0
16		0.033	0.025	0.055	26.9	1.008	1.079	1.099	1.116	0.621	202.9	7.2
17		0.033	0.026	0.031	36.3	1.012	1.012	1.012	1.012	0.592	322.7	11.6
30		0.033	0.026	0.037	32.4	1.011	1.010	1.010	1.010	0.591	802.7	30.1
31		0.033	0.024	0.087	20.0	1.005	1.005	1.005	1.005	0.587	402.5	14.9
32		0.033	0.024	0.135	16.2	1.004	1.004	1.004	1.004	0.587	296.1	10.9
33		0.033	0.024	0.226	13.0	1.003	1.003	1.003	1.003	0.586	213.8	7.8
18	He	0.017	0.012	0.054	71.6	1.042	1.040	1.040	1.039	0.609	754.7	4.6
19		0.017	0.012	0.027	113.5	1.100	1.096	1.094	1.092	0.641	1528.1	9.6
20		0.017	0.012	0.036	92.9	1.068	1.065	1.064	1.063	0.623	1129.5	7.0
22		0.016	0.013	XXX	148.0	1.161	1.151	1.148	1.147	0.675	1829.4	11.4
23		0.016	0.013	XXX	129.1	1.127	1.117	1.116	1.117	0.655	1587.8	9.9
24		0.017	0.012	XXX	106.8	1.088	1.081	1.080	1.081	0.633	1156.2	7.2
25		0.017	0.012	XXX	82.0	1.053	1.049	1.048	1.049	0.614	741.3	4.5
42	Ar	0.040	0.026	0.037	20.6	1.005	1.005	1.005	1.005	0.588	457.5	25.8
43		0.040	0.026	0.044	18.6	1.005	1.004	1.004	1.004	0.587	390.4	22.1
44		0.040	0.026	0.054	16.3	1.004	1.004	1.004	1.004	0.587	325.8	18.4
45		0.040	0.025	0.075	13.6	1.003	1.003	1.003	1.003	0.586	251.7	14.1
46		0.039	0.024	0.102	11.6	1.002	1.002	1.002	1.002	0.586	203.6	11.3
47		0.039	0.024	0.163	9.3	1.002	1.002	1.002	1.002	0.586	147.4	8.1
48		0.039	0.024	0.297	7.6	1.002	1.001	1.001	1.001	0.586	109.7	5.9

C.9. HEMJ Steel Thimble Uncertainty

Table 25. Relevant Steel Thimble Uncertainty in Calculated Experimental Data

Case #	Gas	$\dot{m}$ [g/s]	Re_j [/10^4]	K_L [-]	$\overline{q''}$ [kW/m^2]	T'_0 [°C]	T'_1 [°C]	T'_2 [°C]	T'_3 [°C]	$\overline{T_c}$ [°C]	$\overline{h}$ [W/m^2-K]	$\overline{Nu}$ [-]
101	Air	0.033	0.024	0.278	13.5	1.004	1.004	1.029	1.061	0.589	111.5	3.9
102		0.033	0.024	0.147	16.0	1.007	1.007	1.007	1.007	0.589	153.3	5.5
103		0.032	0.024	0.092	19.7	1.011	1.012	1.012	1.012	0.591	177.9	6.4
104		0.032	0.024	0.065	23.1	1.016	1.017	1.018	1.018	0.595	228.3	8.3
105		0.032	0.025	0.049	26.8	1.023	1.024	1.024	1.025	0.599	288.4	10.6
106		0.032	0.025	0.038	30.6	1.030	1.032	1.032	1.033	0.603	353.7	13.0
107		0.032	0.025	0.032	34.4	1.039	1.041	1.041	1.042	0.608	424.0	15.7
108		0.032	0.026	0.027	38.3	1.048	1.051	1.051	1.052	0.614	498.6	18.5
109		0.032	0.026	0.023	42.2	1.059	1.061	1.062	1.063	0.620	576.9	21.5
110	Ar	0.037	0.024	0.030	21.1	1.014	1.014	1.014	1.014	0.593	475.9	26.6
111		0.037	0.025	0.024	24.9	1.020	1.021	1.021	1.021	0.597	283.5	15.6
112		0.037	0.022	0.131	9.8	1.002	1.002	1.002	1.002	0.586	111.6	6.0
113		0.037	0.024	0.031	21.1	1.013	1.014	1.014	1.014	0.593	238.3	13.1
114		0.036	0.021	0.370	6.7	1.000	1.000	1.000	1.000	0.585	68.1	3.6
115		0.036	0.022	0.102	10.8	1.002	1.002	1.002	1.002	0.586	105.5	5.6
116		0.037	0.023	0.070	13.1	1.004	1.004	1.004	1.004	0.587	148.1	8.0
117		0.037	0.023	0.050	15.8	1.007	1.007	1.007	1.007	0.589	197.3	10.8
118	He	0.017	0.011	0.128	42.8	1.060	1.059	1.060	1.061	0.619	747.8	4.7
119		0.017	0.012	0.039	83.9	1.227	1.223	1.224	1.231	0.716	1407.0	8.8
120		0.017	0.012	0.028	105.2	1.345	1.343	1.352	1.360	0.786	1521.1	9.5
121		0.016	0.013	0.019	138.6	1.536	1.539	1.546	1.559	0.900	2445.6	15.4
122		0.016	0.013	0.018	147.8	1.587	1.596	1.604	1.614	0.932	2735.3	17.4
123		0.016	0.014	0.015	171.2	1.741	1.743	1.755	1.770	1.020	3578.5	22.7

APPENDIX D: INSTRUMENT CALIBRATION

Many instruments were used over the course of the investigations presented in Chapters 3-5. The calibration procedure for these instruments as well as calibration data will be provided in this Appendix.

D.1. Flow Meter Theory

The flow meter used for most of the experiments is the Brooks 1110 Series variable area flow meter (Rotameter) with tapered, rib-guided glass tube R-8M-25-2 and float 8-RS-8 which has a maximum rated flow rate of 4.18 SCFM. The calibration density for the flow meter is dry air at 14.7 psia and 70℉ (101.325 kPa, 21.1℃) or 1.20 kg/m^3. Some of the He-cooled HEMJ experiments used the 8-LJ-48 float which has a maximum rating of 13.01 SCFM at the same calibration density. The 250 mm scale used ranged from 0-100%.

Variable area meters are constructed such that the scale has a linear response to changes in volumetric flow. The ribbed guide tube in the flow meter changes in inner diameter along its length. The rate of change of this area is precisely defined to achieve the desired linear response. To properly use this type of flow meter, it must be oriented vertically with the gas flowing vertically upward through it.

The variable area flow meter can be described assuming incompressible flow using the following analysis: Three forces are acting on the float, two upward (F_d drag; F_b, buoyancy) and one downward (F_g, gravity). When taking a reading of the volumetric flow rate, the float is stationary so these forces sum to zero.

$$F_g = m_f g \tag{88}$$

$$F_b = \rho_g V_f g \tag{89}$$

$$F_d = \frac{1}{2} C_d \rho_g A_f v_g^2 \tag{90}$$

$$F_g + F_b + F_d = 0 \tag{91}$$

where subscripts f and g indicate the float and the gas respectively, m_f is the mass of the float, g is the acceleration due to gravity, ρ_g is the density of the gas, V_f is the volume of the float, C_d is the drag coefficient of the float, A_f is the frontal area of the float and v_g is the velocity of the gas. As the steel float is several thousand times more dense than the gas (even though it is compressed) the contribution of F_b will be ignored. (This may not be the case for denser fluids like water flowing over less dense floats of plastic or glass.) The resulting force balance is thus:

$$\frac{1}{2} C_d \rho_g A_f v_g^2 = g\left(m_f + \cancel{\rho_g V_f}\right) \tag{92}$$

The velocity of the gas is based on both the volumetric flow rate of the gas, $\dot{V}_g$, and the cross sectional area of the tube, A_t, at the position of the float, z_f :

$$v_g = \frac{\dot{V}_g}{A_t(z_f)} \tag{93}$$

By solving for $\dot{V}_g$, the force balance equation becomes

$$\dot{V}_g = A_t(z_f)\sqrt{\frac{2gm_f}{C_d \rho_g A_f}} \tag{94}$$

This equation shows that the $\dot{V}_g$ is proportional to the area of the tube at z_f as the other terms are constant or can be determined. If the tube is designed to linearly increase in

area along its axis, then the volumetric flow reading will be linearly dependent on the actual volumetric flow of the gas. Also, this shows that the volumetric flow rate is inversely proportional to the square root of the gas density. As this particular flow meter was calibrated using dry air at 101.325 kPa and 21.1℃, a correction must be applied when using the flow meter with gasses at other pressures and temperatures.

When reading the flow meter, a standard volumetric flow rate $\dot{V}_s$ is recorded. This is based on the calibration density of 1.20 kg/m^3. The actual volumetric flow rate is $\dot{V}_a$. As shown above, the volumetric flow rate is inversely proportional to the square root of the density of the gas. This implies the equality:

$$\dot{V}_s\sqrt{\rho_s} = \dot{V}_a\sqrt{\rho_a} \tag{95}$$

Or

$$\dot{V}_a = \dot{V}_s\sqrt{\frac{\rho_s}{\rho_a}} \tag{96}$$

The actual mass flow rate, $\dot{m}_a$, is thus:

$$\dot{m}_a = \rho_a\dot{V}_a = \dot{V}_s\sqrt{\rho_s\rho_a} \tag{97}$$

D.2. Flow Meter Calibration

The flow meter was calibrated using a Lambda Square Venturi flow meter, SN# 27872. A Venturi flow meter is a low pressure loss device that measures volumetric flow based on small pressure changes as the gas passes through a converging/diverging nozzle. The volumetric flow rate, $\dot{V}$, can be calculated from the pressure drop, Δp, from the inlet to the throat of the nozzle, assuming incompressible flow:

$$\dot{V} = A_1 C \sqrt{\frac{2\Delta p}{\rho\left(\left(\frac{A_1}{A_2}\right)^2 - 1\right)}} \tag{98}$$

Or the mass flow rate $\dot{m}$:

$$\dot{m} = \frac{\pi D_1^2}{4} C \sqrt{\frac{2\rho\Delta p}{\left(\left(\frac{D_1}{D_2}\right)^4 - 1\right)}} \tag{99}$$

where D_1 and D_2 are the inlet and throat diameters, respectively, and C is the combined discharge coefficient. For this particular flow meter, these values as provided by the manufacturer are 0.824", 0.34", and 0.870 respectively. Note that the discharge coefficient is specific to the flowing gas.

To calibrate the variable area flow meter, a flow line was constructed placing the Venturi flow meter after the variable area flow meter with instrumentation to measure the pressure and temperature of the gas at the Venturi meter, the differential pressure across the Venturi meter, and the pressure at the outlet of the variable area meter. As an incompressible assumption is required, the line was operated with compressed air at ~600 kPa to reduce the velocity (and thus Mach number) of the flow. Gauge pressure at the two flow meters was measured with a pair of HEISE CC-8734 pressure gauges with 0.2 psi (1.38 kPa) gradations. Pressure difference across the Venturi was measured with either an incline (Dwyer) or up right (Dwyer) manometer depending on the flow rate. The incline manometer measured up 3.4 in.w.c (<1 kPa) and the upright manometer up to 9 in.w.c (2.24 kPa).

The Venturi meter came from the manufacturer with calibration information and was thus used to calibrate the variable area flow meter. By placing the two flow meters in series, the mass flow rate should be the same (barring any leaks). A calibration curve

for the variable area meter was constructed and is shown in Figure 135. The value of the uncalibrated volume flow rate calculated from the reading of the variable area meter is shown versus the calibrated volume flow rate of the Venturi meter. This calibration curve was used to correct the volumetric flow reading of the variable area meter.

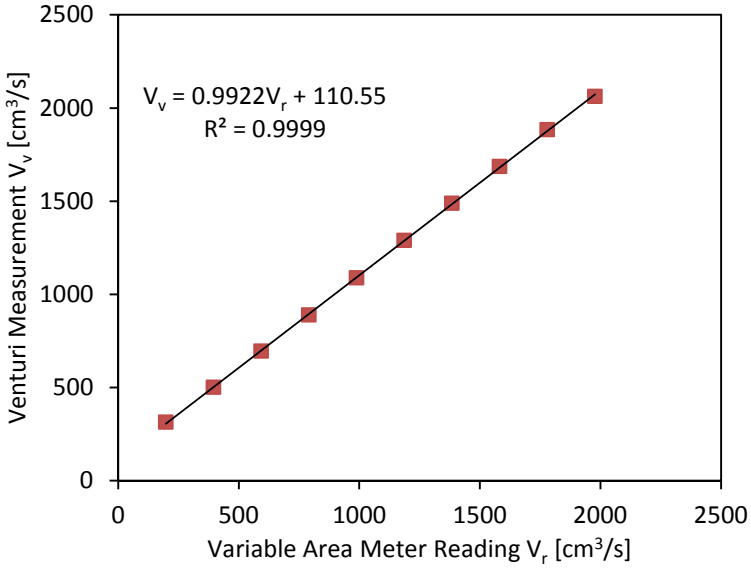

Figure 135. Variable area meter calibration curve.

As mentioned previously, some of the He-cooled HEMJ experiments used a larger float in the variable area meter. As helium is less dense than air at the same temperature and pressure, to achieve the same Re_j through the test section as the air experiments more volumetric flow is required. Instead of performing another calibration, the reading of the larger float was calibrated to the reading of the smaller float (and thus to the Venturi meter). The result of this calibration is shown in Figure 136.

As shown, the uncalibrated values simply offset from the calibrated values. This is because the larger float is rather tall and was not reading zero when there was no flow. Therefore this float was only used when flow rates exceeding the range of the smaller float were expected.

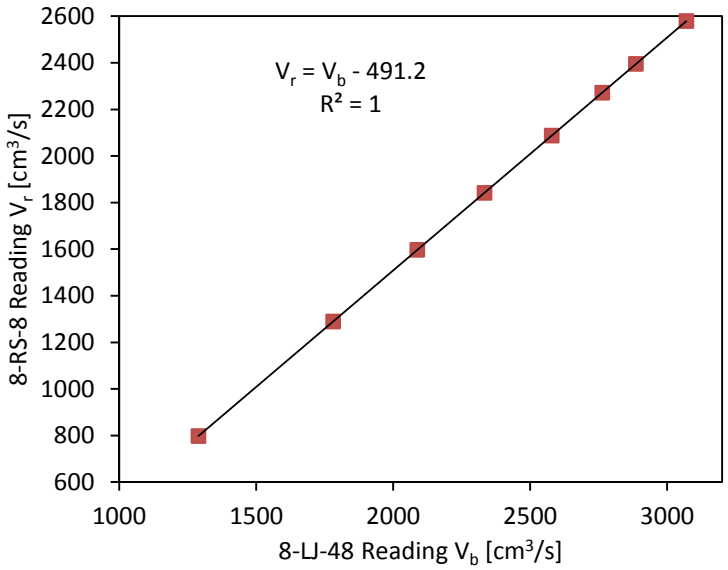

Figure 136. Calibration curve for 8-LJ-48 variable area meter float.

D.3. Pressure Transducer Calibration

The three in-line pressure transducers (OMEGA PX302-300AV, OMEGA PX302-2KGV, and Keyence AP-15SK) used for these experiments were calibrated to the same pressure gauge, HEISE CC-8734. The mV readout of the OMEGA transducers and the mA readout of the Keyence transducer were correlated to the pressure indicated by the gauge. These electrical signals were read using the Agilent 34970A Data Acquisition system connected to a computer just as it was for the experiments. The calibration curves are shown in Figure 137 and Figure 138. The fit for the PX302-2KGV is:

$$P(psi) = 20126.71146 \times \mathrm{V} + 10.5576043 \qquad (100)$$

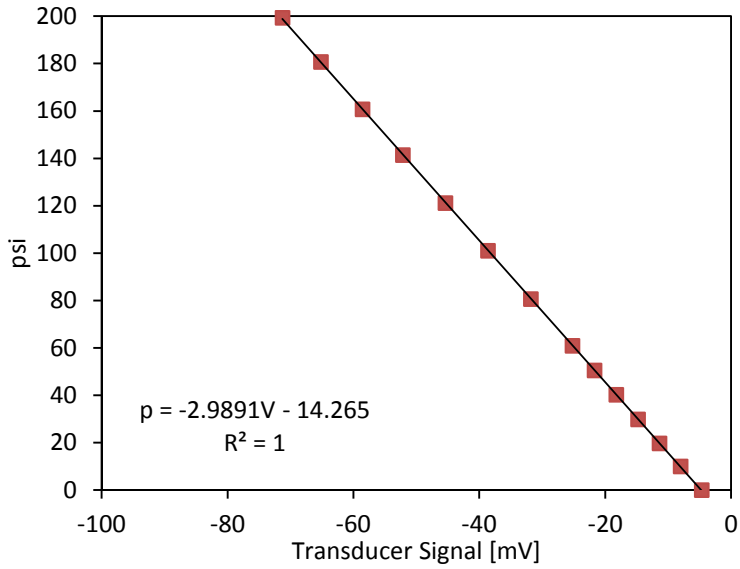

Figure 137. Calibration curve for OMEGA PX302-300AV.

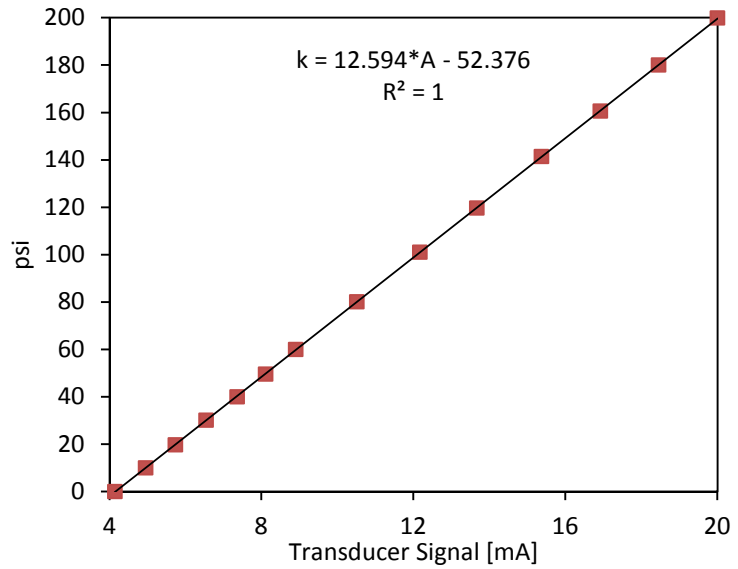

Figure 138. Calibration curve for Keyence AP-15SK.

The differential pressure transducers OMEGA PX26-30DV and PX26-100DV were calibrated using the same pressure gauge as the other pressure transducers. It was noticed that the PX26 exhibits a small pressure bias as the inlet pressure increases even if there is no flow through the test section. Therefore, two calibrations were required. First, a calibration was performed using one side of the PX26 open to the

atmosphere and increasing the pressure on the sealed side. Then this calibration was corrected by connecting both ends of the PX26 up to the same pressure source and measuring the voltage bias. A bias of ~1.5 psi was observed when both sides of the PX26 were connected to a 200 psi source. This bias has large implications on the measured pressure drop through the test section at low flow rate and high pressure. This was accounted for using a second linear fit depending on the system pressure. The calibration is shown in Figure 139.

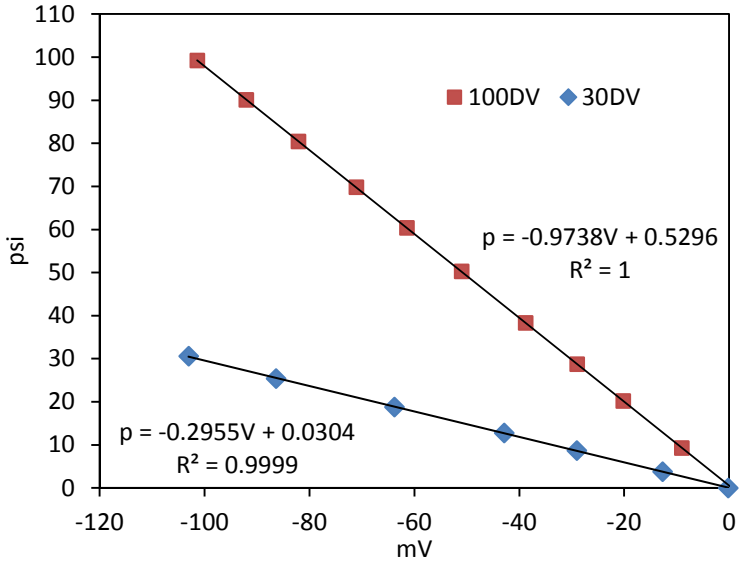

Figure 139. Calibration curve for PX26.

APPENDIX E: MATERIAL PROPERTIES

Accurate materials properties are an important tool to analyzing experimental data and making extrapolations and running numerical simulations. The following data tables and equations detail all the material properties used in the analyses of this thesis. For the solid materials thermal conductivity, often a correlation equation is used instead of a data table as the equations are easier to implement in the integrals of conduction models. No integration was required of the gasses' thermal properties so their properties are left in tabular form.

E.1. Solid Properties

Three solid materials were used in the experimental and numerical studies: C36000 brass, AISI 1010 steel, and WL-10 tungsten alloy. The correlations presented should not be used beyond their range of determination as indicated on the figures. The values for C36000 and AISI 1010 came from [4]. The data for WL-10 comes from [63]. The following correlation equations were used throughout the thesis:

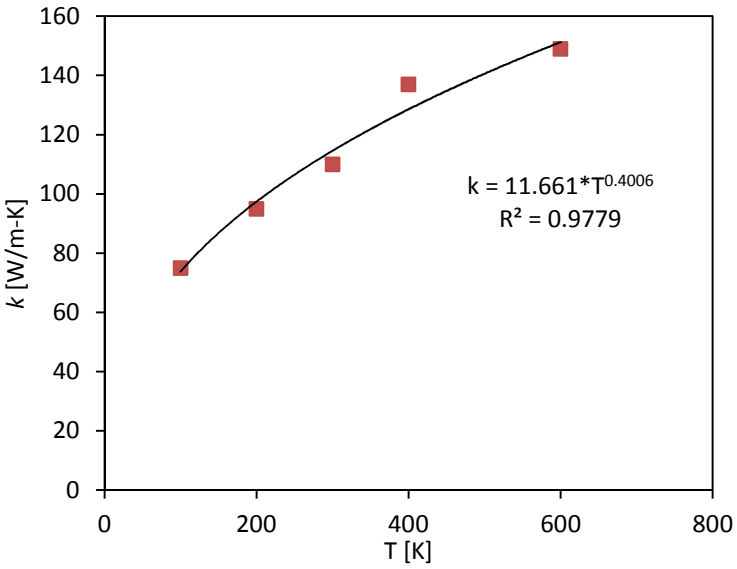

Figure 140. Thermal conductivity of C36000 brass.

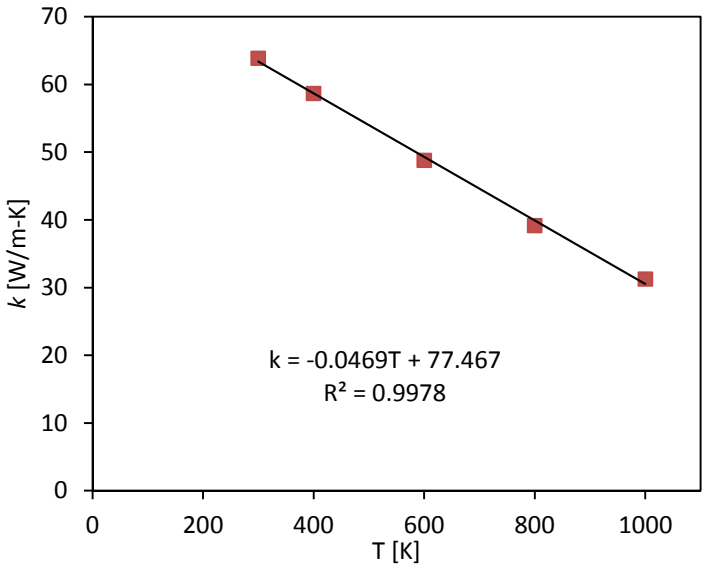

Figure 141. Thermal conductivity of AISI 1010 steel.

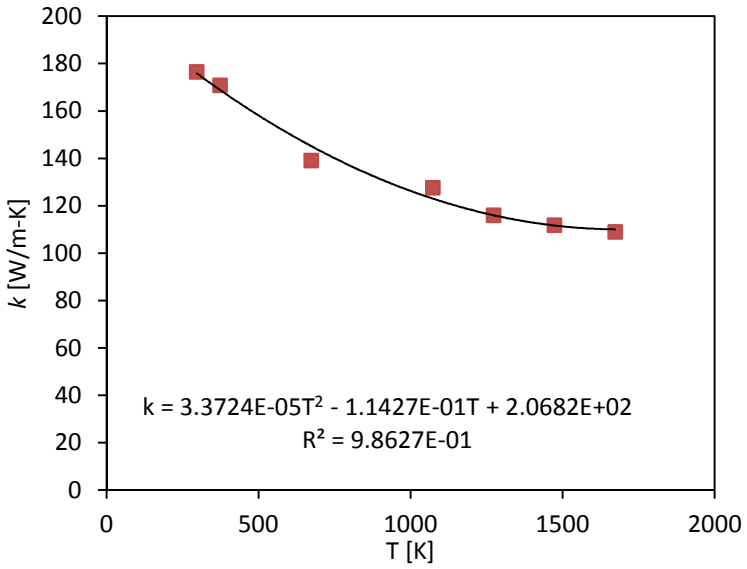

Figure 142. Thermal conductivity of WL-10 tungsten alloy.

E.2. Gas Material Properties

Tabular data was kept for the gas material properties. Air properties from Incropera and Dewitt [4]. Ar and He properties from NIST [64].

Table 26. Air material properties.

T [K]	k [W/m-K]	μ [Pa-s]	c_P [J/kg-K]
250	0.0223	0.000016	1006
300	0.0263	0.0000185	1007
350	0.03	0.0000208	1009
400	0.0338	0.000023	1014

Table 27. Argon material properties.

T [K]	k [W/m-K]	μ [Pa-s]	c_P [J/kg-K]
260	0.015698445	0.0000200925	522.0460479
280	0.016719191	0.0000214005	521.759262
300	0.017714456	0.0000226760	521.5380642
320	0.018685766	0.0000239208	521.3639566
340	0.019634524	0.0000251368	521.2245148
360	0.020562026	0.0000263255	521.1111475
380	0.021469467	0.0000274885	521.0177628
400	0.022357949	0.0000286272	520.9399454

Table 28. Helium material properties.

T [K]	k [W/m-K]	μ [Pa-s]	c_P [J/kg-K]
250	0.137536452	0.0000176025	5193.024633
275	0.146877863	0.0000187807	5193.00365
300	0.155974324	0.0000199297	5192.990957
325	0.164851712	0.0000210534	5192.983528
350	0.173531414	0.0000221538	5192.979511
375	0.182031371	0.0000232328	5192.977735
400	0.190366822	0.0000242923	5192.977445
425	0.198550858	0.0000253338	5192.97814
450	0.206594824	0.0000263587	5192.979486
475	0.214508645	0.0000273681	5192.981254
500	0.222301059	0.0000283631	5192.983286
525	0.229979818	0.0000293445	5192.985476
550	0.237551836	0.0000303132	5192.987746
575	0.245023315	0.0000312699	5192.990044
600	0.252399846	0.0000322152	5192.992335
625	0.259686491	0.0000331498	5192.994593
650	0.266887853	0.0000340741	5192.9968
675	0.274008134	0.0000349887	5192.998947
700	0.28105118	0.0000358941	5193.001026
725	0.288020527	0.0000367905	5193.003032
750	0.294919433	0.0000376786	5193.004966
775	0.301750911	0.0000385584	5193.006825
800	0.30851775	0.0000394306	5193.008611
825	0.315222543	0.0000402952	5193.010325
850	0.321867703	0.0000411526	5193.011969
875	0.328455483	0.0000420031	5193.013546
900	0.334987988	0.0000428469	5193.015058
925	0.341467191	0.0000436843	5193.016508
950	0.347894943	0.0000445154	5193.017899
975	0.354272984	0.0000453405	5193.019232
1000	0.360602952	0.0000461598	5193.020512
1025	0.366886393	0.0000469734	5193.021739
1050	0.373124767	0.0000477816	5193.022918

Table 29. Important Gas Constants

Gas	M [g/mol]	R [J/kg-K]	γ
Air	28.96	287.1	1.4
Ar	39.948	208.1	1.66
He	4.0026	2077.3	1.67

APPENDIX F: PEER-REVIEWED JOURNAL ARTICLES

As a result of the work presented in this thesis, several journal articles were published. Five of the six articles were presented as oral presentations or in poster sessions at Technology of Fusion Energy (TOFE) conferences sponsored by the American Nuclear Society (ANS). What follows is a listing of all articles with contributions by this author followed by the articles where this author is the first author as they appeared in their respective journals.

<u>As first author</u>:

Verification of Thermal Performance Predictions of Prototypical Multi-Jet Impingement Helium-Cooled Divertor Module, J. D. Rader, B. H. Mills, D. L. Sadowski, M. Yoda, and S. I. Abdel-Khalik. Presented at Technology of Fusion Energy 2012 conference, Nashville, TN. To be published in *Fusion Science and Technology*, 2013.

Optimization of Pin-Fin Arrays for Helium-Cooled Finger-Type Divertor, J. D. Rader, B. H. Mills, D. L. Sadowski, M. Yoda, and S. I. Abdel-Khalik. Presented at Technology of Fusion Energy 2012 conference, Nashville, TN. To be published in *Fusion Science and Technology*, 2013.

Experimental and Numerical Investigation of Thermal Performance of Gas-Cooled Jet-Impingement Finger-Type Divertor Concept, J. D. Rader, B. H. Mills, D. L. Sadowski, M. Yoda, and S. I. Abdel-Khalik. *Fusion Science and Technology*, **60**(1), 223-227, 2011. Presented at Technology of Fusion Energy 2010 conference, Las Vegas, NV.

As co-author:

An Experimental Study of the Effects of Solid-to-Coolant Thermal Conductivity Ratio in Helium-Cooled Divertor Modules, B. H. Mills, J. D. Rader, D. I. Sadowski, M. Yoda, and S. I. Abdel-Khalik. Presented at Technology of Fusion Energy 2012 conference, Nashville, TN. To be published in *Fusion Science and Technology*, 2013.

Dynamically Similar Studies of the Thermal Performance of Helium-Cooled Finger-Type Divertors With and Without Fins, B. H. Mills, J. D. Rader, D. L. Sadowski, M. Yoda, and S. I. Abdel-Khalik. *Fusion Science and Technology*, **62**(3), 379-388, 2012.

Experimental Investigation of Fin Enhancement for Gas-Cooled Divertor Concepts, B. H. Mills, J. D. Rader, D. L. Sadowski, S. I. Abdel-Khalik, and M. Yoda. *Fusion Science and Technology*, **60**(1), 190-196, 2011. Winner of Best Student Paper Award and presented at Technology of Fusion Energy 2010 conference, Las Vegas, NV.

VERIFICATION OF THERMAL PERFORMANCE PREDICTIONS OF PROTOTYPICAL MULTI-JET IMPINGEMENT HELIUM-COOLED DIVERTOR MODULE

J. D. Rader, B. H. Mills, D. L. Sadowski, M. Yoda, and S. I. Abdel-Khalik

G. W. Woodruff School of Mechanical Engineering, Georgia Institute of Technology, Atlanta, GA 30332-0405 USA
said.abdelkhalik@me.gatech.edu

An experimental investigation of the thermal performance of the Helium-Cooled Multi-Jet (HEMJ) modular divertor design developed by the Karlsruhe Research Center (FZK) was previously performed at Georgia Tech using air at Reynolds numbers (Re) spanning those at which the actual He-cooled divertor is to be operated. More recently, another experimental investigation was performed by the Georgia Tech group for a similar finger-type divertor module using both air and He as coolants. The results of these experiments suggest that, in addition to matching Re, dynamic similarity between the air and He experiments requires that a correction be made to account for the differences in the relative contributions of convection and conduction (through the divertor walls) to the overall heat removal rate by the module. This correction factor depends on the thermal conductivity ratio of the solid to the coolant. Experiments similar to those previously conducted have therefore been performed using air, argon, or He as coolant for test sections constructed of brass or steel thus covering a wide range of thermal conductivity ratio. The resultant correlation between Re, the heat removal rate, and the thermal conductivity ratio from these experiments can be used to predict the thermal performance of HEMJ-like divertors at prototypical operating conditions.

I. INTRODUCTION

Several gas-cooled divertor designs have been investigated as part of the ARIES research program including the helium-cooled multi-jet[1] (HEMJ), the He-cooled flat plate[2] (HCFP), and the He-cooled modular design with integrated fin array[3] (HEMP). The purpose of these thermal-hydraulic and thermo-mechanical studies is to ensure that these designs can withstand the anticipated heat fluxes (~10 MW/m^2) when operating in a magnetic fusion energy power plant without exceeding temperature and stress limits dictated by material properties.

The research group at Georgia Tech has utilized dynamic similarity to evaluate the thermal-hydraulic performance of the proposed divertor designs by performing a large number of low-temperature, low-pressure experiments. In general, test sections duplicating the geometry of the prototypical design are constructed out of brass (instead of tungsten and tungsten alloys) and cooled with air (instead of He). The experiments are conducted at non-dimensional mass flow rates (Reynolds number, *Re*) that span the expected operating *Re* value. The test modules are heated either electrically or, more recently, by an oxy-acetylene torch. Heat transfer coefficients (HTCs) are determined from calculated incident heat flux values and measured temperature readings from thermocouples embedded in the test section, and used to determine non-dimensional Nusselt numbers (*Nu*). The measured pressure drop across the test section is used to calculate a non-dimensional pressure loss coefficient (K_L). By correlating *Nu* and K_L to *Re*, parametric design curves are constructed that describe the thermal-hydraulic behavior of the design at prototypical conditions. For a given coolant inlet temperature and pressure, and a specified maximum allowable temperature for the pressure boundary, the maximum allowable incident heat flux and the corresponding pumping power fraction are determined based solely upon thermal-hydraulic (*vs.* thermal stress) considerations.

II. THE HEMJ AND HEMP DIVERTORS

Most recently, two modular finger-type divertors, the HEMJ and HEMP, designed by Karlsruhe Research Center (FZK), have been studied at Georgia Tech. The HEMJ divertor cools the inner surface of the divertor tiles using an array of twenty-five round jets (Fig. 1). Hot He enters the inner tube at ~600°C and 10 MPa, passes through the array of round jets thus cooling the inner surface of the endcap (i.e. the pressure boundary), thereby removing the incident heat flux on the divertor tiles, and exits at ~700 °C. The HEMJ is designed to accommodate 10 MW/m^2 incident heat flux while keeping the tungsten alloy endcap peak temperature below 1300°C.

Previously, experimental research on the HEMJ was performed at Georgia Tech[4–6] using a brass test section

electrically heated at heat fluxes up to 0.9 MW/m^2 cooled with air entering the test section at ~20 °C and ~700 kPa. Although these earlier experimental results were not extrapolated to prototypical conditions, numerical simulations using a model validated against the experimental results were used to predict the behavior of the brass HEMJ when tested at the HEBLO test facility at FZK near-prototypical pressures (8 MPa) at incident heat fluxes up to 5 MW/m^2.

Experiments[7-9] performed by FZK with the HEMJ using He at elevated inlet temperature (~600 °C) and pressure (~10 MPa) indicated that the HEMJ could withstand heat fluxes as great as 12 MW/m^2 at the nominal He mass flow rate (6.8 g/s). Further tests[10] on a bundle of nine HEMJ fingers at the Efremov Institute in Russia confirmed these results.

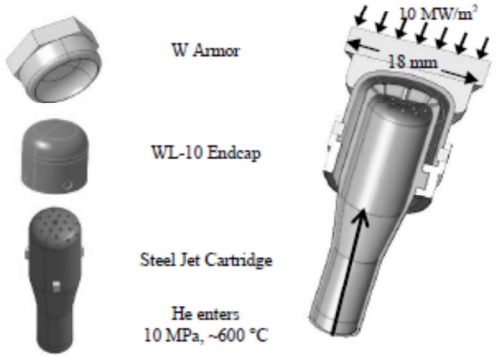

Fig. 1. The HEMJ divertor.[9]

The HEMP (Fig. 2), in contrast, utilizes the heat transfer enhancement effect of an array of fins integral to the inner surface of the divertor pressure boundary instead of impinging jets. Hot He at ~600 °C and 10 MPa enters in an annular channel before flowing radially inward through the array of fins over the cooled surface and then exits axially through a central port at ~700°C. Fabricating the HEMP fin array in tungsten alloys has proven difficult[8] and thus experiments like those on the HEMJ at prototypical conditions have yet to be performed.

Earlier experimental and numerical studies on a HEMP-like divertor[11,12] predicted the performance of the HEMP under prototypical conditions. However, as described by Mills *et al.*,[13] predicted prototypical divertor performance based on non-dimensional Nu and K_L values obtained from an air-cooled brass test module may not be accurate because these predictions do not account for the differences in the relative contributions of convection and conduction through the divertor walls.

The previous experiments performed on an electrically heated HEMJ module cooled with air were therefore re-examined by accounting for the difference in the relative contributions of convection and conduction, characterized by the ratio of the thermal conductivities of the solid and the coolant, to the overall heat removal capability of the divertor module. To this end, additional experiments have been performed using two HEMJ test sections made of brass and steel, respectively, heated with an oxy-acetylene torch at incident heat fluxes up to 3 MW/m^2 and cooled by air, Ar, or He. By varying both the coolant and divertor thermal conductivities, these experiments at different thermal conductivity ratios are designed to verify that these experiments can, by accounting for this effect, give accurate predictions of the thermal performance of the HEMJ design at prototypical conditions.

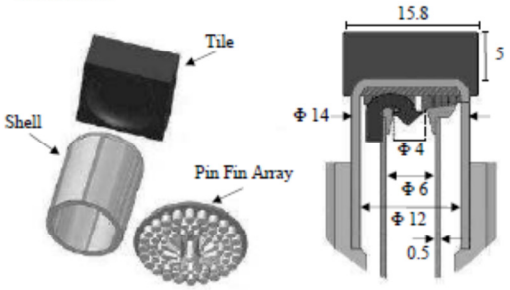

Fig. 2. Exploded view [left] and cross-section [right] of the HEMP divertor.[11] Dimensions in mm.

III. EXPERIMENT

The torch-heated test sections are composed of two primary components: a jet cartridge, which creates round jets, concentric with and inside a thimble that simulates the pressure boundary. Two thimbles were machined, one of C36000 brass alloy and one of AISI 1010 carbon steel. Two jet cartridges were also machined, both out of C36000 brass. The jet cartridges have 24 0.6 mm diameter jets arranged in groups of six placed on four concentric circles with radii of 2.22 mm, 3.52 mm, 4.77 mm, and 6.49 mm projected to a plane at the top of the jet cartridge centered about one 1 mm diameter jet. The thimble and the jet cartridge are separated by a 0.9 mm gap. Schematic drawings of the jet cartridge and thimble are shown in Fig. 3.

The volumetric flow rate of coolant into the test section is measured using a Brooks variable area flow meter (Model 1110) and used along with the density of the coolant calculated using temperature and pressure measurements from an OMEGA type E TC and OMEGA PX302-2KGV pressure transducer at the exit of the flow meter to determine the mass flow rate, $\dot{m}$. The temperature of the coolant was measured at the inlet, T_i, and outlet, T_o, of the test section by two OMEGA type E

TCs and used to calculate the total incident power on the thimble, and hence, the average heat flux over the heated surface, $\overline{q''}$:

$$\overline{q''} = \frac{\dot{m}\overline{c_P}(T_o - T_i)}{A_h} \quad (1)$$

where $\overline{c_P}$ is the constant pressure specific heat capacity of the coolant evaluated at the average of T_i and T_o, and A_h is the area of the heated surface, 227 mm^2. For insulation, the thimble assembly is placed in Marinite® blocks, while the piping near the test section is insulated with a combination of mineral wool and foam. Heat losses in the electrically heated experiments were estimated by comparing the electric power to the power absorbed by the coolant and were typically about 10%. Since numerical simulations showed that the majority of these losses occurred in the large heater block, *vs.* the thimble, heat losses were assumed to be negligible.

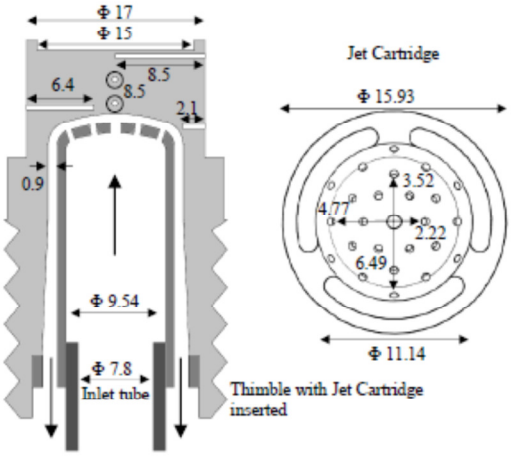

Fig. 3. Diametric cross-section of HEMJ thimble and jet cartridge showing locations of 5 of 6 TCs [left] and top view of jet cartridge showing array of round jets [right]. TCs in the center of the thimble (circled) are normal to viewing plane and inserted 8.5 mm. The sixth TC, which is not shown here, is inserted 4.2 mm normal to this plane. Dimensions in mm.

The temperature distribution in the thimbles was measured using six 0.5 mm embedded type E OMEGA TCs (Fig. 3). The readings from the four TCs nearest the cooled surface spaced 90° apart and radially located 6.4, 4.3, 2.1, and 0 mm at axial locations 8.26, 6.88, 6.36, and 6.25 mm relative to the top of the thimble are used to determine the HTC. These TC readings are extrapolated through 0.5 mm of brass or steel to the cooled surface using $\overline{q''}$ assuming 1-D conduction. The extrapolated temperatures are then area averaged over the projected cooled surface area, A_c = 132 mm^2, resulting in an average cooled surface temperature, $\overline{T_c}$.

The pressure drop, across the divertor Δp was measured using an OMEGA PX26 differential pressure transducer. The inlet pressure was measured with an OMEGA PX302-300AV pressure transducer.

A total of seven experimental configurations were studied: the torch-heated brass thimble cooled with air, Ar, or He; the torch-heated steel thimble cooled with air, Ar, or He; and the electrically heated brass thimble cooled with air, from previous experiments.[5,6] Data from a total of 60 experiments are presented here.

IV. EXPERIMENTAL RESULTS

The area-averaged HTC, $\overline{h}$, was calculated from $\overline{q''}$, $\overline{T_c}$, T_i, and the area ratio A_h/A_c:

$$\overline{h} = \frac{\overline{q''}}{\overline{T_c} - T_i}\frac{A_h}{A_c} \quad (2)$$

The above equation assumes that all of the power incident on the thimble is removed by convection at the cooled surface, i.e. it ignores conduction through the annular walls of the thimble. The area averaged Nu, $\overline{Nu}$, and the Re of the central jet, Re_j, were calculated as follows:

$$\overline{Nu} = \frac{\overline{h}D_j}{\overline{k}} \quad \text{and} \quad Re_j = \frac{\dot{m}D_j}{A_j\mu_j} \quad (3a \text{ \& } 3b)$$

where D_j is the diameter of the central jet (1 mm), $\overline{k}$ is the gas thermal conductivity based on the average of T_i and T_o, A_j is the total area of all 25 jets (7.57 mm^2), and μ_j is the dynamic viscosity of the coolant at T_i.

Fig. 4 presents $\overline{Nu}$ as a function of Re_j, for all seven experimental conditions. Experimental uncertainty for both $\overline{Nu}$ and Re_j was calculated using standard techniques[14] and ranges from 2%-12% for $\overline{Nu}$ and 1% - 3% for Re_j. The largest uncertainties for $\overline{Nu}$ are seen for the smallest values of $T_o - T_i$.

As shown in Fig. 4, the seven experimental data sets each follow their own trend instead of conforming to a global $\overline{Nu}$ relation based solely on Re_j. This means it is incorrect to assume that $\overline{Nu}$ can be predicted by just Re_j – more specifically that all of the heat incident on the divertor is removed by convection at the cooled surface [Eq. (2)]. Since the HEMJ and HEMP divertor are both 'finger-type' and share many general features, it's reasonable to assume that their thermal performance can be generally characterized in the same manner. As shown in Figs. 1-3, the designs remove heat by both convection through the cooled surface and conduction down the walls of the divertor. Using a similar method presented in more detail in Ref. 13 regarding experimental and numerical

studies on a HEMP-like divertor, an additional non-dimensional parameter k_s/k_g, or κ, was required to account for the change in conduction and convection heat removal rates at the cooled surface based on the different combinations of structure and coolant thermal conductivities.

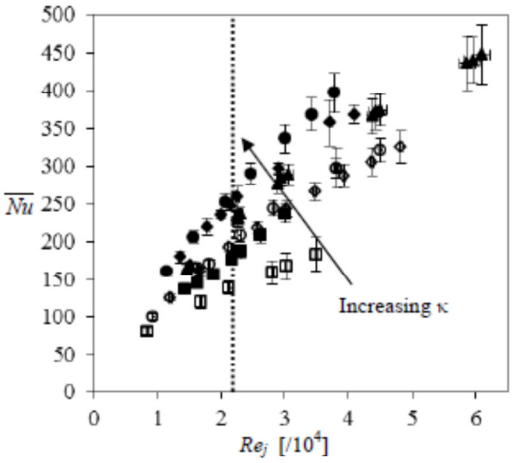

Fig. 4. $\overline{Nu}$ versus Re_j for all seven experimental configurations. Solid symbols for brass thimbles (air ♦, Ar ●, He ■, and electrically heated air ▲) and open symbols for the steel thimble (air ◊, Ar ○, and He □). Prototypical Re_j of 2.16×10^4 is denoted by the vertical dotted line. Error bars give the experimental uncertainty.

As indicated on Fig. 4, the trends of $\overline{Nu}$ to Re_j are layered according to κ. By relating both Re_j and κ to $\overline{Nu}$, and assuming a power law correlation, each of the seven experimental data sets is now shown to follow a global trend (Fig. 5). Nearly all of the data points fit within the range of ±10% of the correlation as shown by the dashed lines. A dotted line indicates the prototypical operating point. The values of the fitting parameters are given by Eq. (4):

$$\overline{Nu} = 0.059\, Re_j^{0.669}\, \kappa^{0.190} \tag{4}$$

The approximate value of κ for each experimental setup is shown in Table I and varies from ~370 for the He-cooled steel thimble experiments to ~7000 for the Ar-cooled brass thimble experiments. Given that the prototypical value of κ is about 340, the lowest value of κ in these experiments is just above the prototypical value. Nevertheless, given the wide range of κ used to obtain Eq. (4), we expect that this correlation can be extrapolated to the prototypical value.

The pressure loss coefficient, K_L, was also calculated for each experiment and is plotted versus Re_j in Fig. 6. The density, ρ_L, and velocity, V_L, used in calculating K_L are determined using the outlet pressure and inlet temperature:

$$K_L = \frac{\Delta p}{\rho_L V_L^2 / 2} \tag{5}$$

A curve fit assuming a power law plus a constant trend for K_L is given by Eq. (6):

$$K_L = 1.39\,(Re_j/10^4)^{-0.50} + 1.32 \tag{6}$$

Since K_L represents the "hydraulic" characteristics of the module, it is appropriately correlated by only matching Re_j (and geometry). The loss coefficients from the electrically heated experiments are not included as those experiments did not use an accurate differential pressure measurement technique.

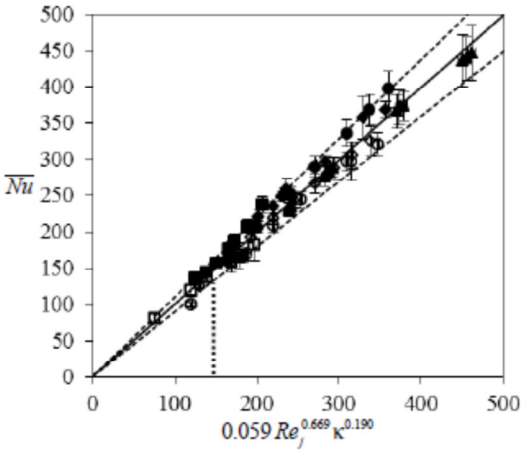

Fig. 5. Correlation of Eq. (4) for all the experimental data. Eq. (4) is given by the solid line, along with ±10% dashed lines. Filled symbols denote brass thimbles (air ♦, Ar ●, He ■, and electrically heated air ▲); open symbols denote steel thimble (air ◊, Ar ○, and He □). Prototypical value for correlation of 140 for Re_j = 2.16×10^4 and κ =340 is given by the vertical dotted line.

TABLE I. Approx. values of κ for different conditions

Case	Approx. k_s [W/m-K]	Approx. k_g [W/m-K]	Approx. κ [-]
Ar Brass	135	0.018	7000
Air Brass	135	0.027	5000
Ar Steel	56	0.018	3000
Air Steel	56	0.027	2000
He Brass	135	0.16	850
He Steel	56	0.16	370
Prototypical	**115**	**0.33**	**340**

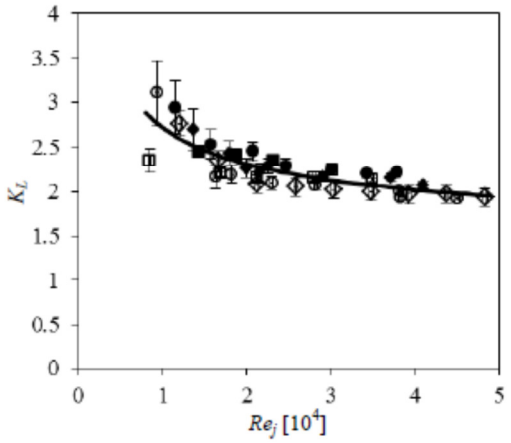

Fig. 6. K_L versus Re_j with associated curve fit. Solid symbols for brass thimbles (air ♦, Ar ●, and He ■) and open symbols for steel thimble (air ◊, Ar ○, and He □). Error bars give the uncertainty in K_L.

V. PROTOTYPICAL CONDITIONS

Using the performance correlations of Eqs. (4) and (6), predictions of the behavior of the HEMJ at prototypical conditions (i.e. 10 MPa He inlet pressure, and 600 °C He inlet temperature) are made. Performance predictions are presented in terms of the average pressure boundary heated surface temperature, $\overline{T_s}$, the heat flux $\overline{q''}$, and the pumping power fraction β, i.e. the ratio between the pumping power and the incident thermal power:

$$\beta = \frac{\dot{m}\Delta p}{\overline{\rho}\,\overline{q''}A_h} \tag{7}$$

where $\overline{\rho}$ is the average coolant density between the inlet and outlet.

Lines of constant $\overline{T_s}$ are constructed by calculating $\overline{q''}$ from $\overline{T_s}$ and Re_j, by way of Eqs. (1), (2-4). First a guess is made for T_o and $\overline{T_c}$ allowing for the calculation of κ and thus $\overline{Nu}$ by Eq. (4) and $\overline{h}$ by Eq. (3a). Then, a thermal resistance analogy for the conduction through the Δz = 1 mm pressure boundary allows for the calculation of $\overline{q''}$:

$$\overline{q''} = \frac{\overline{T_s} - T_i}{\frac{A_h}{A_c}\frac{1}{\overline{h}} + \frac{\Delta z}{k_s\left(\frac{\overline{T_s}+\overline{T_c}}{2}\right)}} \tag{8}$$

where k_s is calculated based on the average of $\overline{T_c}$ and $\overline{T_s}$. This new value of $\overline{q''}$ gives new guesses for both T_o by Eq. (1) and $\overline{T_c}$ by Eq. (2). The process repeats until the values of T_o, $\overline{T_c}$, and $\overline{q''}$ converge.

Lines of constant β are calculated using Eqs. (5-7) as follows: as ρ_L and V_L depend on Δp, an iterative process is applied to Eq. (5) using K_L calculated with Eq. (6) from an assumed Re_j. With this value of Δp, $\overline{q''}$ is calculated based on a fixed value of β using Eq. (7). This also requires iteration since ρ depends on $\overline{q''}$.

As shown in Fig. 7, at the prototypical Re_j of 21,600, the HEMJ is predicted to withstand $\overline{q''}$ of ~14.1 MW/m^2 with $\overline{T_s}$ of 1200 °C while having a β value of ~8% based on a heated surface area of 227 mm^2. This corresponds to a heat flux of ~11.4 MW/m^2 for a hexagonal tile area of 280.6 mm^2 corresponding to a tile flat-to-flat distance of 18 mm (Fig. 1). Although these correlations were all developed for this specific variant of the HEMJ design, the thermal-hydraulic performance reported here is similar to that reported for similar finger-type divertors with different hole diameters and jet-wall spacing.[7-10]

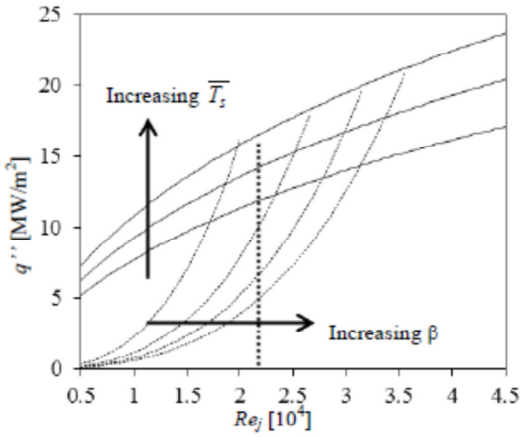

Fig. 7. Prototypical design curves for the HEMJ showing solid lines of constant $\overline{T_s}$ = 1100°C, 1200°C, 1300°C and dashed lines of constant β = 5%, 10%, 15%, 20%). The prototypical Re_j of 2.16×10^4 is denoted by the vertical dotted line.

VI. CONCLUSIONS

As the HEMJ divertor design has been shown to withstand over 10 MW/m^2 incident heat flux at its nominal mass flow rate, an experimental investigation was undertaken to characterize the divertor's behavior under a wide range of operating conditions. These experiments used air, argon, and helium over a range of nondimensional mass flow rates or Reynolds numbers Re_j (8×10^3-6×10^4) and pressures (0.6-1.4 MPa) to cool divertor test sections made of brass and steel that were heated with an oxy-acetylene torch at heat fluxes ranging from 0.5 MW/m^2 to 3 MW/m^2. Using dimensional

analysis and dynamic similarity, the results of these experiments were extrapolated to prototypical conditions, where the divertor is cooled by helium at an inlet temperature of 600°C and pressure of 10 MPa, to produce performance curves. These curves enable designers to estimate the thermal-hydraulic behavior of HEMJ and finger-type divertor designs fabricated in different materials for various steady-state coolant flow rates (i.e. Re_j, coolant inlet temperatures, and incident heat flux values. For example, the maximum incident heat flux that can be tolerated by the divertor for a given maximum temperature of the pressure boundary (usually determined by materials limitations) can be determined for a given coolant flow rate, and the corresponding pumping power fraction can then be estimated as well for these operating conditions.

ACKNOWLEDGEMENTS

This work was performed as a part of the ARIES study. We thank the U.S. DOE Office of Fusion Energy Sciences for their support through contract number DE-FG02-01ER54656. We are also grateful to undergraduate researchers A. J. Polkinghorne and L. H. Stokes for their contributions.

REFERENCES

1. T. IHLI, et al., "An advanced He-cooled divertor concept: Design, cooling technology, and thermohydraulic analyses with CFD," *Fusion Engineering and Design*, **75-79**, 371 (2005).
2. S. HERMSMEYER and S. MALANG, "Gas-cooled high performance divertor for a power plant," *Fusion Engineering and Design*, **61-62**, 197-202 (2002).
3. E. DIEGELE, et al., "Modular He-cooled divertor for power plant application," *Fusion Engineering and Design*, **66-68**, 383 (2003).
4. J. B. WEATHERS, et al., "Development of modular helium-cooled divertor for DEMO based on the multi-jet impingement (HEMJ) concept: Experimental validation of thermal performance," *Fusion Engineering and Design*, **83**, 1120 (2008).
5. J. B. WEATHERS, "Thermal Performance of Helium-Cooled Divertors for Magnetic Fusion Applications," *M.Sc. Thesis*, Georgia Institute of Technology (2007).
6. L. CROSATTI, "Experimental and Numerical Investigation of the Thermal Performance of Gas-Cooled Divertor Modules," *Ph.D. Thesis*, Georgia Institute of Technology (2008).
7. P. NORAJITRA, et al., "He-cooled divertor for DEMO: Experimental verification of the conceptual modular design," *Fusion Engineering and Design*, **81**, 341 (2006).
8. T. CHEVTOV, et al., "Status of He-cooled Divertor Development (PPCS Subtask TW4-TRP-001-D2)," P. NORAJITRA, Ed., Forschungszentrum Karlsruhe, Karlsruhe (2005).
9. T. IHLI, "He-cooled Divertor Development in the EU: The Helium Jet cooled Divertor HEMJ," *ARIES Meeting*, San Diego (2005).
10. P. NORAJITRA, et al., "Progress of He-cooled divertor development for DEMO," *Fusion Engineering and Design*, **86**, 1656 (2011).
11. B. H. MILLS, et al., "Experimental Investigation of Fin Enhancement for Gas-Cooled Divertor Concepts," *Fusion Science and Technology*, **60**, 190 (2011).
12. J. D. RADER, et al., "Experimental and Numerical Investigation of Thermal Performance of Gas-Cooled Jet-Impingement Finger-Type Divertor Concept," *Fusion Science and Technology*, **60**, 223 (2011).
13. B. H. MILLS, et al., "Dynamically similar studies of the thermal performance of helium-cooled finger-type divertors with and without fins," *Fusion Science and Technology*, **62**, 379 (2012).
14. S. KLINE and F. MCCLINTOCK, "Describing the uncertainties in single sample experiments," *Mechanical Engineering*, **75**, 3 (1953).

OPTIMIZATION OF PIN-FIN ARRAYS FOR HELIUM-COOLED FINGER-TYPE DIVERTOR

J. D. Rader, B. H. Mills, D. L. Sadowski, M. Yoda, and S. I. Abdel-Khalik

G. W. Woodruff School of Mechanical Engineering, Georgia Institute of Technology, Atlanta, GA 30332-0405 USA
said.abdelkhalik@me.gatech.edu

The helium-cooled modular divertor concept with integrated pin array developed by the Karlsruhe Research Center (FZK) is unusual among helium-cooled tungsten divertor designs in that it relies upon an array of pin fins on the back of the cooled surface, instead of jet impingement, to cool the plasma-facing surface. The Georgia Tech group experimentally studied a similar design constructed of brass which combined jet impingement with an array of identical cylindrical pin fins using air at nondimensional coolant mass flow rates, i.e. Reynolds numbers, which spanned the range expected under prototypical conditions. The results suggested that the pin-fin array, at least for the particular geometry studied, provides little, if any, additional cooling beyond that provided by jet impingement.

Given that this earlier study considered only one pin-fin array geometry, however, a numerical study was performed to investigate whether changes in the array geometry could improve performance. Specifically, numerical simulations using the commercially available computational fluid dynamics software package ANSYS® 14.0 was used to examine how varying the pitch-to-diameter ratio for the fin array and the height of the fins affected average pressure boundary temperature and the pressure drop across the divertor. These results can, with appropriate experimental validation, be used to determine whether pin-fin arrays can be used to improve the thermal performance of helium-cooled tungsten divertors.

I. INTRODUCTION

Several gas-cooled divertor designs have been studied as part of the ARIES project including the helium-cooled multi-jet[1] (HEMJ), helium-cooled flat plate[2] (HCFP), and the helium-cooled divertor with multi-pin array[3] (HEMP). All these divertors are designed to remove heat fluxes of at least 10 MW/m^2 incident on the plasma-facing tungsten tiles while remaining within temperature and thermal stress limits dictated by material properties. The HEMJ and HCFP designs use impinging round or planar jets as the primary means of removing heat from the pressure boundary, and hence the plasma-facing tiles. The HEMP, however, was designed to use cooling fins integral to the inside surface of the pressure boundary as a way to increase heat removal effectiveness of the coolant. As the relatively complicated fins of the original HEMP design proved difficult to manufacture,[4] a simpler design with an array of identical cylindrical pin fins was constructed and experimentally tested at Georgia Tech.[5,6] Following these experiments, a numerical study was performed that included searching for a more optimal fin layout to enhance the divertor module cooling effectiveness without adversely impacting the required coolant pumping power.

II. THE HEMP DIVERTOR

The HEMP divertor is shown in Fig. 1. Helium at 600 °C and 10 MPa enters via an annular channel and flows radially inward through an array of cooling fins before exiting axially through a central port at ~700 °C. Nearly 4×10^3 of these modules are required to cool the 100 m^2 area of the plasma-facing surface of the divertor.

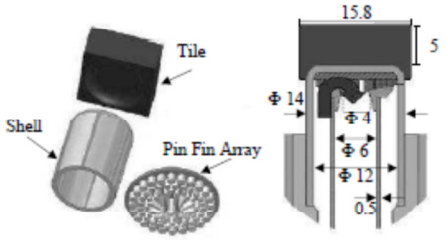

Fig. 1. Exploded view [left] and cross-section [right] of the HEMP divertor.[5] Dimensions in mm.

A design similar to the HEMP divertor module was studied experimentally[5,6] and numerically[7] at Georgia Tech using a test section constructed from brass heated with an oxy-acetylene torch at heat fluxes up to 2 MW/m^2, and cooled with air, argon (Ar), or helium (He) entering at nearly ambient temperatures and pressures up to 1.4 MPa (Fig. 2). These experiments were designed so that the coolant flow was either "forward flow" or "reverse flow." In reverse flow, the coolant, similar to the

original HEMP design, reaches the outer edge of the cooled surface of the pressure boundary via an annular channel, then flows radially inward through the pin-fin array. In forward flow, the coolant impinges on the cooled surface as a round jet that exits the central port, and then flows radially outward through the fin array. The earlier studies conducted at Georgia Tech concluded that the forward flow configuration had a cooling performance similar to, but a pressure drop greater than, the reverse flow configuration at prototypical conditions, due to the increase in pressure drop associated with the impinging jet. More recent estimates[6] show, however, that the forward flow configuration, with its combination of two cooling methods (fins and impinging jet) does, in fact, have superior cooling performance, increasing the maximum heat flux that can be accommodated by the divertor by about 19% compared to the case without fins.

However, the combination of the impinging jet and the pin-fin array increased the pressure drop by about 16% compared with the case without fins. The objective of this numerical investigation was therefore to determine if there were other pin-fin array configurations that would also enhance cooling performance with minimal increase in the pressure drop.

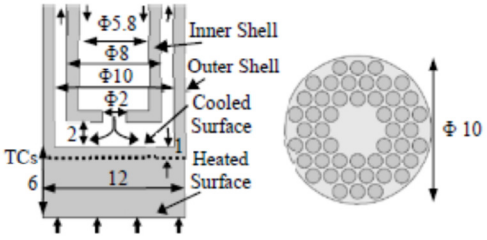

Fig. 2. Diametric slice [left] of the test section studied in previous experiments and a top view [right] of the 48 pin-fin array with diameter D = 1 mm fins on a P = 1.2 mm pitch.[5] The axial extent of the test section is 50 mm; the dimensions in the Figure are given in mm.

III. NUMERICAL MODEL

Experimental testing of divertor modules with different fin configurations is quite costly because of machining costs. This study therefore focused on a numerical approach, which enabled rapid and cost-effective evaluation of a large number of different configurations. A series of 12 numerical models with different pin-fin configurations were chosen to cover a wide range of parameters (Fig. 3). All the computational fluid dynamics (CFD) simulations were performed using ANSYS® FLUENT® 14.0 (Ref. 8).

All 12 models were 45 mm in axial extent; all other model dimensions were identical to those shown in Fig. 2 except that the axial distance between the inner and the outer surfaces of the pressure boundary was 1 mm (Refs. 1, 3) (*vs.* the 6 mm shown in Fig. 2). The test was assumed to be constructed from a W-1% La_2O_3 alloy, WL-10, which has been proposed as a high-temperature structural material for several divertor designs.[4] Only a 30° "slice" of the module was considered because of its twelve-fold radial symmetry. In each case, He enters the inner channel at 600 °C and ~10 MPa and a boundary condition of a uniform heat flux of 10 MW/m^2 is imposed at the heated outer surface of the pressure boundary.

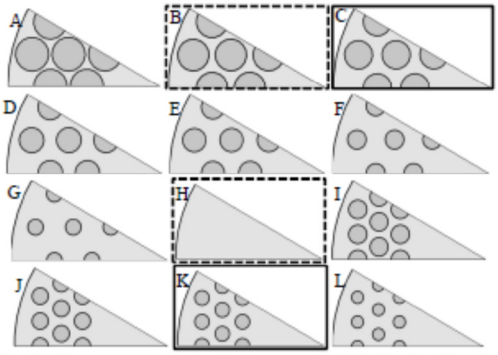

Fig. 3. Fin arrangement of all cases tested. Dashed border indicates baseline case. Solid border indicates the best performing cases for the individual arrays.

Each configuration was simulated at the same four flow rates corresponding to jet Reynolds numbers, Re_j, of 4.5×10^4, 6.0×10^4, 7.5×10^4, and 9.0×10^4: $Re_j = 4\dot{m}/\pi D_j \mu_i$ where $\dot{m}$ is the mass flow rate, D_j is the jet diameter (2 mm), and μ_i is the dynamic viscosity based on the inlet temperature of 600 °C. The realizable k-ε turbulence model[9] with enhanced wall treatment was used in all the simulations based on previous simulations performed on this and similar geometries that suggested that predictions using this model were in good agreement with experimental data, albeit at lower temperatures and pressures.[6,7] A fine numerical mesh comprised of ~3×10^6 unstructured tetrahedral cells was used in order to accurately resolve the heat transfer between the fin surfaces and the coolant, as well as in the small gaps between the fins.

The performances of the two "baseline cases" indicated by the dashed rectangles in Fig. 3 were compared to the other configurations. The first baseline case, the configuration without any fins, should have the worst thermal performance. The second baseline case, which closely resembles the experimentally tested divertor configuration, has 1 mm OD fins arranged in a

1.2 mm pitch hexagonal array – a total of 48 fins over the entire cooled inner surface of the divertor (Fig. 2 [right]).

The thermal-hydraulic performance of each model subject to the same incident heat flux of 10 MW/m^2 was based upon two metrics. The first is the average temperature of the heated side of the pressure boundary, $\overline{T_s}$. Given that the WL-10 alloy needs to operate between 800-1200°C, i.e. between its ductile-brittle transition and recrystallization temperatures,[4] designs with the lowest $\overline{T_s}$ (exceeding 800 °C) are desirable as they provide the greatest operating temperature margin.

The second metric used to evaluate the thermal-hydraulic performance is the pressure drop, Δp. Minimizing Δp for each divertor module will result in significant operating cost savings by reducing pumping power requirements. The divertor cooling system operating at nominal prototypical flow rates under normal, steady-state conditions should have pumping power requirements that are at most 10% of the incident thermal power from the fusion plasma. It should be noted that this study only considers the thermal-hydraulic performance of these pin-fin configurations; additional studies would be needed to confirm that these configurations do not exceed thermal stress limits.

IV. SIMULATIONS

To evaluate the effect of the boundary condition at the tips of the fins, results were compared for otherwise identical simulations of the second baseline case for adiabatic and conducting fin-tip boundary conditions to model the effect of non-contacting and perfectly contacting fin tips. The maximum difference in $\overline{T_s}$ was about <2°C and the value of Δp was nearly identical over the entire ranged of Re_j. Given that the boundary condition at the fin tips appears to have almost no effect on the simulations, the remaining configurations were simulated with a conducting fin-tip boundary condition, corresponding to the assumption that the fin tips are in perfect contact with the inlet tube.

This result implies that the upper portions of the fins have little effect on the heat transfer, since the simulations (results not shown) also suggest that the coolant interacts primarily with the part of the fins near the cooled surface. Fins that occupy most, if not all, of the jet-wall gap, do, however force the coolant to pass between (*vs.* over) the fins and interact with the next row of fins.

A series of models was constructed using fins of varying diameters D, while maintaining the same pitch P = 1.2 mm and number of fins (48) as the baseline case. Cases A-G had P/D = 1.1, 1.2, 1.33, 1.5, 1.6, 2.0, and 2.4. For these cases, the total cooled surface area, A_c, which includes the area on the "sides" and tips of the fins uncovered by the inlet tube, as well as the area of the cooled surface not covered by the fins, increases as D increases, resulting in a larger heat transfer area. Increasing A_c does not necessarily lead to improved performance, however, as shown in Table I, which compares numerical predictions at the prototypical value of Re_j = 75,000 (Ref. 5). This may be due in part to the turbulent wakes behind the fins, which effectively reduce the heat transfer coefficients (HTCs) over much of the back half of the fins. Increasing D may therefore only lead to a small increase in the surface area of each fin with high HTC. More complex fin designs that minimize wake interactions, such as the design proposed for HEMP, may further improve performance, although these are beyond the scope of the current study.

The case with the lowest $\overline{T_s}$ = 824 °C at this Re_j is case C, the configuration where P/D = 1.33, which has a pressure drop of 506 kPa. In general, for a given pitch, an array of fins with smaller D (for a given number of fins) has smaller Δp values, presumably because there is a larger gap between the fins.

TABLE I. 48 Fin Array, P = 1.2 mm, Re_j = 75,000

Case	P/D	A_c [mm^2]	Δp [kPa]	$\overline{T_s}$ [°C]
A	1.1	388	729	836
B	1.2	361	531	848
C	**1.33**	**329**	**506**	**823**
D	1.5	304	498	828
E	1.6	291	500	836
F	2.0	250	502	839
G	2.4	223	501	842
H	Bare	79	459	875

As shown in Fig. 4, the peak HTC at the prototypical flow rate for the baseline case without fins occurs near r = 1.25 mm. When fins are located too close to the peak, they interfere with the spreading of the impinging jet and thus increase Δp. If a new fin array still has as large a A_c as the array with fins closer to the jet, then by locating fins just outside this zone, the effect of the fins can be maximized by producing a lower Δp.

A similar study as performed on the 48 pin array was conducted using a triangular array with a smaller pitch P = 0.8 mm. Reducing the pitch increases the total number of fins to 84 over the inner surface of the pressure boundary, or four half and five whole pin fins per 30° segment as shown in Fig. 3. Four Cases I-L with P/D = 1.33, 1.5, 1.6, and 2.0 were evaluated. Though these fins have a smaller D, the fin array still has A_c similar to that for cases A-G simply because there are more fins. As shown in Table II, cases J&K with P/D = 1.5 and 1.6 have the lowest $\overline{T_s}$ = 838 °C with a similar Δp at the nominal flow rate. Since the fins for case K are smaller and thus potentially easier to machine, it is preferred over case J.

As shown in Table II, moving the fins outward resulted in a modest decrease in Δp for cases I-L even though A_c is similar to the cases presented in Table I.

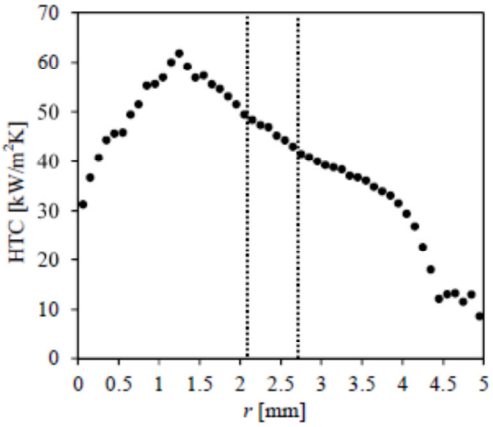

Fig. 4. Local HTC versus radial position r for the case without fins at Re_j = 75,000. Locally averaged values are dark circles (•). The location of the center of closest fin for the two arrays tested is shown by the dotted lines.

Comparing $\overline{T_s}$ and Δp of the best performers, namely cases C and K, with the two baseline cases in Figs. 5 and 6, respectively, shows that both $\overline{T_s}$ and Δp are lower for cases C and K at all Re_j tested (25°C & 5% and 10°C & 6%, respectively at the prototypical Re_j), indicating that these new pin-fin array configurations should cool more effectively and efficiently than the experimentally tested array. Compared to the case without fins at the prototypical flow rate, case C reduces $\overline{T_s}$ by 52°C with a 10% increase in Δp while case K reduces $\overline{T_s}$ by 37 °C with a 9% increase in Δp. The geometric details of the two optimum fin arrangements are shown in Fig. 7.

TABLE II. 84 Fin Array, P = 0.8 mm, Re_j = 75,000

Case	P/D	A_c [mm²]	Δp [kPa]	$\overline{T_s}$ [°C]
H	Bare	79	459	875
I	1.33	380	499	845
J	1.5	348	500	838
K	**1.6**	**332**	**499**	**838**
L	2.0	283	497	842

The gap between the fins in both of the optimum designs is 0.3 mm and it may be difficult to consistently fabricate a pin-fin array with such small gaps. These results suggest cases D and L with slightly larger P/D, which would increase the gap width, has a thermal performance, at least in terms of $\overline{T_s}$ and Δp, nearly as good as the optimal cases C and K, respectively. As demonstrated here, this divertor design can be improved by adding an array of pin-fins to the cooled surface even if their specifications are not exactly as the specified optimum designs.

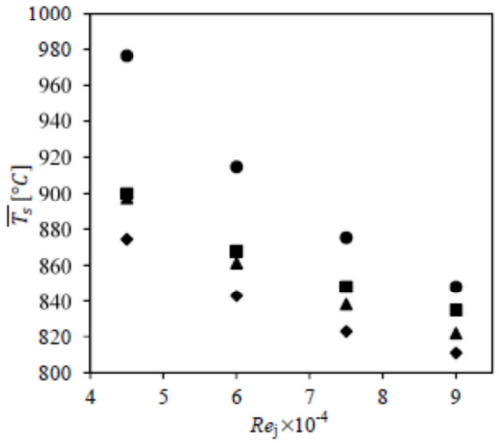

Fig. 5. $\overline{T_s}$ vs. Re_j for optimized cases. Bare (•), experimentally studied array P/D = 1.2 (■), 48 fin array P/D = 1.33 (♦), and 84 fin array P/D = 1.6 (▲).

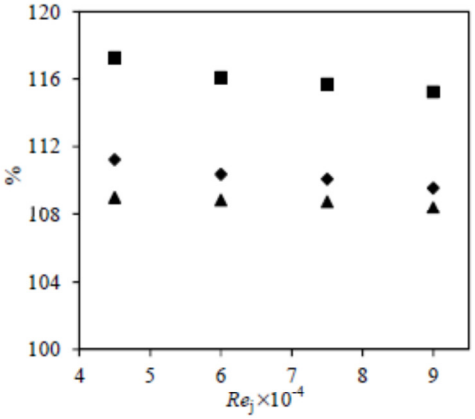

Fig. 6. Δp as a percent of bare Δp vs. Re_j. Experimentally studied array P/D = 1.2 (■), 48 fin array P/D = 1.33 (♦), and 84 fin array P/D = 1.6 (▲).

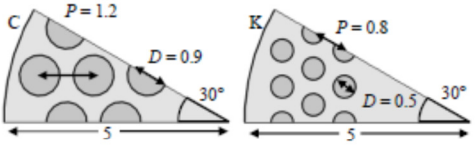

Fig. 7. Details of the optimum array geometries for 48 fin array [left] and 84 fin array [right]. Dimensions in mm.

V. CONCLUSIONS

Previous experimental studies of a HEMP-like divertor module design showed that using the combination of an impinging jet and a pin-fin array consisting of 48 fins with a diameter of 1 mm and a pitch of 1.2 mm could enhance divertor thermal performance.

However, only one pin-fin array configuration consisting of identical cylindrical fins was studied in this experiment, and no attempt was made to optimize the array geometry in these earlier studies. Numerical simulations using a commercial CFD software package were therefore performed to determine a pin-fin array design (consisting of identical cylindrical fins) that would optimize the thermal performance. These simulations considered two cylindrical fins of varying diameter at two different pitch values P = 0.8 mm and 1.2 mm, corresponding to a total of 84 and 48 fins, respectively. An optimum fin diameter D was determined for each value of P. These studies showed that the boundary condition at the fins tips, and hence the type and extent of the contact between the fins and the end of the inner tube, had a negligible effect on the thermal performance. This result suggests that the performance of these fins is fairly robust with respect to minor geometric variations in the fin height due, for example, to manufacturing tolerances.

For 48 fins at P = 1.2 mm, the optimum design with P/D = 1.33 predicts decreases in both the average heated surface temperature of the pressure boundary, $\overline{T_s}$, and pressure drop, Δp, compared to the original experimentally tested array over a range of flow rates spanning the prototypical flow rate of $Re_j = 7.5\times10^4$. This optimized pin-fin array reduces $\overline{T_s}$ by 52 °C, but increases Δp by 10%, compared to the same divertor without fins.

For an array of 84 fins at P = 0.8 mm, the optimum design with P/D = 1.6 also predicts decreases in $\overline{T_s}$ and Δp compared to the experimentally tested array over the same range of flow rates. The optimum design for the 84 fin array also reduces $\overline{T_s}$ by 37 °C and increases Δp by 9% compared to the same divertor without fins at the prototypical flow rate.

When comparing the two optimum designs, though the decrease in Δp is predicted to be slightly larger for the 84 fin design at the prototypical flow rate, the 48 fin design predicts a more significant decrease in $\overline{T_s}$. Also, as the 0.3 mm gap between the fins for both optimum designs may yet still be too small to consistently machine, the results of these studies indicate that designs with slightly smaller fins and thus a larger inter-fin gap may still provide significant performance improvements over both the experimentally tested design with fins and the design without fins. The performance of the fin array should therefore also be fairly robust with respect to small variations in the fin diameter and pitch as well as the pin height.

Also, these simulations should be viewed as merely a guide and not as making exact performance predictions. We have confidence in the results as similar techniques as those used in this report were used to accurately predict the performance of previous experiments. Furthermore, as the simulations were performed using a consistent methodology, the trends shown are expected to be real. Experimental studies are the only true proving ground for any divertor design and in light of this, we plan next to fabricate and experimentally test these "optimal" pin-fin arrays.

ACKNOWLEDGMENTS

This work was performed as a part of the ARIES study. We thank the U.S. DOE Office of Fusion Energy Sciences for their support through contract number DE-FG-02-01ER54656.

REFERENCES

1. T. IHLI, et al., "An advanced He-cooled divertor concept: Design, cooling technology, and thermohydraulic analyses with CFD," *Fusion Eng. Des.*, **75-79**, 371 (2005).
2. S. HERMSMEYER and S. MALANG, "Gas-cooled high performance divertor for a power plant," *Fusion Eng. Des.*, **61-62**, 197 (2002).
3. E. DIEGELE, et al., "Modular He-cooled divertor for power plant application," *Fusion Eng. Des.*, **66-68**, 383 (2003).
4. P. NORAJITRA, et al., "Status of He-cooled Divertor Development (PPCS Subtask TW4-TRP-001-D2)," P. NORAJITRA, Ed., Forschungszentrum Karlsruhe, Wissenschaftliche Berichte, FKZA 7100 (2005).
5. B. H. MILLS, et al., "Experimental investigation of fin enhancement for gas-cooled divertor concepts," *Fusion Sci. Technol.*, **60**, 190 (2011).
6. B. H. MILLS, et al., "Dynamically similar studies of the thermal performance of helium-cooled finger-type divertors with and without fins," *Fusion Sci. Technol.*, **62**, 379 (2012).
7. J. D. RADER, et al., "Experimental and numerical investigation of thermal performance of gas-cooled jet-impingement finger-type divertor concept," *Fusion Sci. Technol.*, **60**, 223 (2011).
8. ANSYS® FLUENT®, Release 14.0, ANSYS, Inc.
9. T.-H. SHIH, et al., "A new *k-e* eddy-viscosity model for high Reynolds number turbulent flows - model development and validation," *Computers Fluids.*, **24**, 227 (1995).

EXPERIMENTAL AND NUMERICAL INVESTIGATION OF THERMAL PERFORMANCE OF GAS-COOLED JET-IMPINGEMENT FINGER-TYPE DIVERTOR CONCEPT

J. D. Rader, B. H. Mills, D. L. Sadowski, M. Yoda, S. I. Abdel-Khalik

Woodruff School of Mechanical Engineering, Georgia Institute of Technology, Atlanta, GA 30332-0405, rader@gatech.edu

As a part of the ARIES study, a modular, helium-cooled, jet-impingement, finger-type divertor design that can accommodate an incident heat flux of 10 MW/m^2 has been proposed. An experimental and numerical investigation was undertaken to quantify the thermal performance of a design that closely resembles previously studied finger-type divertors (e.g. HEMJ and HEMP). Experiments were conducted using air in a test module heated with an oxy-acetylene torch to achieve incident heat fluxes as great as 2 MW/m^2. These experimental results were compared to numerical predictions.

The numerical studies documented here were performed using a commercial computational fluid dynamics (CFD) software package. Simulations were carried out for two different test sections with and without a hexagonal array of cylindrical fins and otherwise identical dimensions and for two different flow directions, reverse flow corresponding to radial inward flow, and forward flow corresponding to jet impingement followed by radial outward flow. The numerical predictions for effective heat transfer coefficients (HTC) are in reasonable agreement with the experimental results for the test section without fins. The numerical predictions overpredict the HTCs for the cases with fins, and resolving this discrepancy is the subject of ongoing work.

I. INTRODUCTION

Magnetic fusion reactor studies, including the ARIES Advanced Tokamak study, have shown that the divertor must be able to withstand an incident heat flux of 10 MW/m^2 without exceeding limits on material temperatures, thermal stresses, or coolant pumping power. Previous studies of gas-cooled divertors[1-3], have reported that such designs can accommodate such high heat loads while remaining below specified peak temperatures. A validated computational fluid dynamics (CFD) model of a given divertor design can be used to "test" this design at heat fluxes beyond 10 MW/m^2, *i.e.*, off-normal conditions, to ensure reliable and robust operation under nominal operating conditions.

This study examined finger-type divertor module designs akin to the He-cooled modular divertor with pin array[4,5] (HEMP) or the He-cooled modular divertor with jet array[6,7] (HEMJ), concepts. The objective of these initial studies was to quantify how the addition of pin fins to the cooled surface of the pressure boundary would affect the thermal performance of these concepts. The aim of this work is to develop a validated numerical model of finger-type divertor designs to explore a variety of modifications that could improve the thermal-hydraulic performance of such designs. This work was motivated by a previous study at Georgia Tech that showed that adding an array of cylindrical fins to the cooled surface of a helium-cooled flat-plate (HCFP) divertor could increase the maximum incident heat flux to as much as 18 MW/m^2 under prototypical conditions. Four different divertor configurations were examined both experimentally[8] and numerically to quantify the thermal performance of these configurations under prototypical conditions. This paper first briefly reviews the experiments, then details the numerical simulations.

II. EXPERIMENTS

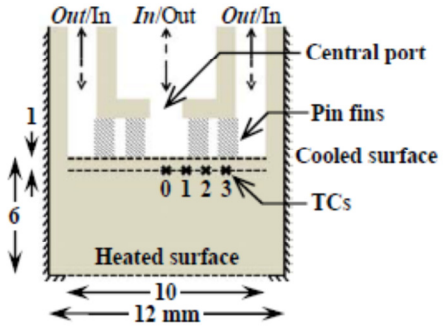

Fig. 1. A diametric slice of the test section.

The experiments were carried out in a brass C36000 alloy test section heated with an oxy-acetylene torch and cooled by air (Fig. 1). As detailed in Ref. 8, two different test sections with and without a hexagonal array of 48 cylindrical pin fins (diameter 1 mm, length 2 mm, pitch 1.2 mm), referred to as the finned and bare test sections, respectively, were studied. In these initial studies, the fin array geometry—*i.e.*, neither the fin diameter and width,

nor the pitch of the fins—was optimized. Two different types of flow were investigated: (1) "forward" flow where the coolant issued from a central port, impinged on and cooled the inner surface of the pressure boundary, then flowed radially outwards (In(coming) and Out(going) flow directions given by bold italic font and dashed lines on the Figure), and (2) "reverse" flow where the coolant flowed radially inwards and exited through the central port (flow directions given by plain font and solid lines). The two flow directions combined with the two test sections gave four different configurations.

The test sections were instrumented with four thermocouples (TCs) (0, 1, 2 and 3) embedded in the brass alloy 1 mm from the cooled surface and at a radial distance of 0, 1, 2, and 3 mm from the central axis of the divertor, respectively. The readings from these TCs are used to calculate the average heat transfer coefficient (HTC) over the cooled surface for a given incident heat flux. During each experiment, the coolant volume flow rate, temperature T_i and pressure were measured at the inlet of the test section. These parameters were used to determine the coolant mass flow rate $\dot{m}$. The pressure drop across the test section and the coolant temperature T_o and pressure at the exit of the test section were also measured.

II.A. Heat Flux Calculation

The heat flux incident on the divertor was calculated from an energy balance based on the mass flow rate determined from the experiments as shown in Fig. 1:

$$\bar{q}'' = \dot{m}\, c_p(\bar{T})\,(T_o - T_i)/A_C \qquad (1)$$

where $c_p(\bar{T})$ is the constant-pressure specific heat of the air evaluated at the average of the inlet and outlet air temperature $\bar{T} \equiv (T_i + T_o)/2$, and A_C is the area of the cooled surface. Although this energy balance gives an accurate estimate of the total power incident on the divertor module, $\bar{q}''$ represents an upper bound on the average heat flux incident on the cooled surface because the balance does not consider any heat removed by the coolant through surfaces other than the cooled surface.

III. NUMERICAL SIMULATIONS

The numerical simulations described in this Section were all performed with the computational fluid dynamics (CFD) software packages ANSYS GAMBIT® 2.4.6 and ANSYS FLUENT® 12.1. The renormalized group (RNG) k-ε turbulence model was used with non-equilibrium wall functions.[9] This model was used because it gave values of the average cooled surface temperature $\bar{T}_C$ that were closer to the experimental values compared with the standard k-ε turbulence model.

III.A. Geometry, Meshing, and Boundary Conditions

Three different numerical models were used in these studies. The bare test section was modeled by both a 2D axisymmetric (Fig. 2*a*) and a 3D model of a 30° section (Fig. 2*b*). Simulations of the 2D axisymmetric model required the least computational time, and the 2D model also gave the finest spatial resolution within the limits of our computational resources. Finally, the finned test section was modeled by a 3D model of a 30° segment of the test section (Fig. 2*c*), which was sufficient to capture the 12-fold symmetry of the hexagonal fin array. The numerical model of the finned test section was essentially that for the bare test section with two cylindrical fins and four half fins added.

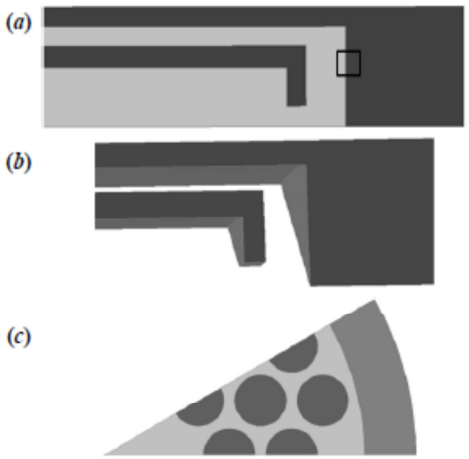

Fig. 2. Illustrations of the (*a*) 2D axisymmetric and (*b*) 3D models of the bare test section, and (*c*) a top view of the 3D model of a 30° segment of the finned test section.

TABLE I. Numerical Model Properties

Model	Number of Cells	Minimum Grid Spacing [μm]	Cell Shape
2D	269,864	40 μm	Triangular
3D Bare	297,058	100 μm	Tetrahedral
3D Fins	1,011,447	40 μm	Tetrahedral

Table I summarizes the mesh parameters for the results presented here. As expected, the numerical model of the finned test section required more than three times the number of cells that for bare test section to resolve the flow in the 0.2 mm gaps between the cylindrical fins. The finest mesh for the 3D model of the finned test section was limited to a maximum of 2×10^6 cells, by the computational resources available. From mesh

convergence studies of the numerical models of the bare test section, it was found that the simulations results for both the 2D and 3D models were essentially converged for mesh sizes of 100 μm and less. The spatial resolution of the 2D model was therefore set to be that of the 3D model of the finned test section. Fig. 3 shows the finest meshes used with a dimension of 40 μm for (*a*) the 2D model of the bare test section and (*b*) the 3D model of the 30° segment of the finned test section.

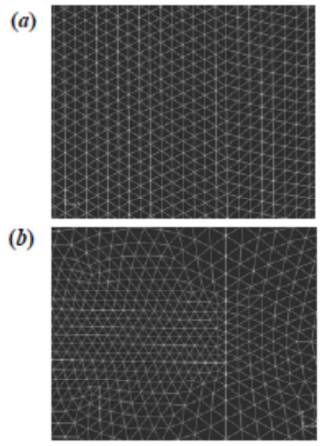

Fig. 3. Numerical models for (*a*) the 2D model of the bare and (*b*) the 3D model of the finned test sections. Both views are of the location in the test section denoted by the rectangle shown on Fig. 2*a*.

In the numerical models of the test sections, the mass flow rate $\dot{m}$ and temperature T_i at the inlet, as determined from the experiments, were specified as boundary conditions; at the exit, the pressure p_o from the experiments was used as the boundary condition. An adiabatic boundary condition was imposed over all the other exterior surfaces of the model, which were insulated in the experiments with Marinite®, rock wool and foam, except at the heated surface, where the boundary condition was imposed that the heat flux was uniform and equal to $\overline{q}''$ (Eq. 1).

III.B. Fins and Fin Tip Boundary Condition

In the experiments, it was unclear how much of the fin tips actually contacted the surface containing the central port due to machining imperfections and mis-alignment.[9] For all the simulations presented here, the fins were therefore assumed to make perfect contact with the inlet/outlet tube. Simulations were also performed assuming an adiabatic boundary condition at the fin tips. Though not presented here (*cf.* Ref. 9), the results suggest that varying the fin tip boundary condition can significantly change the FLUENT® results. Accurately modeling the fin tip boundary condition is the focus of ongoing work.

III.C. Cooled Surface Temperatures

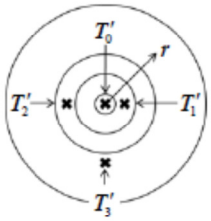

Fig. 4. End view of cooled surface showing the locations of TCs 0, 1, 2 and 3 and the areas used to weight the TC readings T_0', T_1', T_2', and T_3', respectively.

In the experiments, the average cooled surface temperature was determined from the TCs embedded just below the cooled surface. The TC readings were first extrapolated to the cooled surface assuming conduction through 1 mm of the brass alloy using the calculated heat flux of Eq. 1. Since any non-uniformity in the incident heat flux will be significantly reduced by conduction through the 5 mm thickness of the brass pressure boundary, these extrapolated temperatures were area averaged over concentric circular and annular areas corresponding to the different TCs (Fig. 2) to give an average cooled surface temperature:

$$\overline{T}_C = \frac{2\pi \int_C T'(r) r\, dr}{A_C} \approx \frac{T_0'}{100} + \frac{2T_1'}{25} + \frac{4T_2'}{25} + \frac{3T_3'}{4} \qquad (2)$$

where the primes denote the TC readings extrapolated to the cooled surface. For a radial coordinate r measured from the center, the reading for TCs 0, 1, 2 and 3 were averaged over $r \le 0.5$ mm, 0.5 mm $< r <$ 1.5 mm, 1.5 mm $< r <$ 2.5 mm, and 2.5 mm $< r <$ 5 mm, respectively.

In the numerical studies, $\overline{T}_C$ is the average of the nodal temperatures at the cooled surface/air interface. Fig. 5 shows color maps of the temperature distribution over the cooled surface for the case of reverse flow for 3D models of the test sections with (*a*) bare ($\dot{m}$ = 1.92 g/s or $Re = 6.87 \times 10^4$; $\overline{q}''$ = 0.96 MW/m^2) and (*b*) finned ($\dot{m}$ = 2.03 g/s or $Re = 7.28 \times 10^4$; $\overline{q}''$ = 1.35 MW/m^2) surfaces. Note that the planar section shown in Fig. 5*b* "cuts" through the fins at their base. Clearly, the fins greatly reduce the average surface temperature (the incident heat flux for Fig. 5*b* is 75% higher than that for Fig. 5*a*), with the minimum cooled surface temperature at the base of the fins.

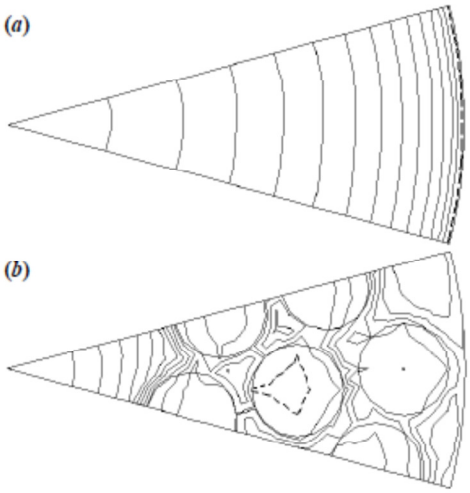

Fig. 5. Contour plots of the temperature over the cooled surface (contours spaced 1 °C apart) for reverse flow for the (*a*) bare and (*b*) finned test sections. The dashed line denotes the contour at the lowest temperature T_{min} = 260°C for (*a*) and 175°C for (*b*).

III.D. Heat Transfer Coefficient

The effective HTC over the cooled surface:

$$h_{eff} = \overline{q}'' / \left(\overline{T}_C - T_i \right) \qquad (3)$$

The area A_C used to calculate $\overline{q}''$ (*cf.* Eq. 1) is the same for the test sections with and without fins. In other words, A_C is the *projected* cooled surface area, and is hence independent of the fin geometry. For the bare surface cases, h_{eff} is therefore identical to the actual HTC. The effective HTC represents the HTC for a surface without fins to have the same surface temperature as a surface with fins subject to the same incident heat flux. The implications of this are discussed in more detail in Ref. 9. As defined, h_{eff} provides a direct method for comparing the average cooled surface temperatures $\overline{T}_C$ since the values of $\overline{q}''$ and T_i are determined from the experiments.

IV. RESULTS

IV.A. Forward Flow Results

Fig. 6 compares h_{eff} as a function of the coolant Reynolds number $Re = 4\dot{m} / (\pi D_o \mu_o)$ where D_o = 2 mm and μ_o are the diameter and coolant dynamic viscosity at the central port calculated from the experimental and numerical results for forward flow. The *Re* corresponding to the prototypical operating conditions for the forward flow cases $Re_P = 7.6 \times 10^4$. When the experimental data were extrapolated to these operating conditions, the pumping power for the finned test section was 17% greater, and h_{eff} was ~5% less, than that for the bare test section.[8] The finned cases have a consistently higher effective HTC than the otherwise identical bare cases at a given *Re*. The numerical predictions of h_{eff} (●, ♦) are in reasonable agreement with the experimental values for the bare cases (▲), especially at higher *Re*. As expected, the predictions obtained with the 3D model (●) are in better agreement with the experimental values, and are slightly lower than those for the 2D model (♦). We conjecture that the 2D model cannot capture the 3D turbulent fluctuations due to the radial outflow. The 2D model is therefore probably a poor choice for simulating the forward flow cases.

For the case with fins, however, the numerical prediction for h_{eff} (★) is 28% greater than the experimental value (■) at Re_P. We suspect that this discrepancy is due to our difficulties in accurately modeling the heat transfer and contact at the fin tip, the inability of the *k*-ε turbulence model to resolve strongly anisotropic flows,[10] and perhaps to an underresolved mesh in the region between the fins.

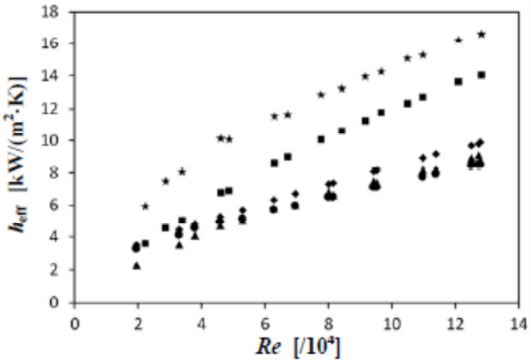

Fig. 6. Effective HTCs from FLUENT® and the experimental results for forward flow as a function of coolant *Re* number for the bare and finned test sections.

IV.B. Reverse Flow Results

Fig. 7 shows a similar comparison for reverse flow, where $Re_P = 7.0 \times 10^4$. When the experimental data were extrapolated to these operating conditions, the pumping power for the finned test section was 28% greater, and h_{eff} was 69% less, than that for the bare test section.[8] Like forward flow, the finned cases have a consistently higher h_{eff} than the otherwise identical bare cases at a given *Re*. For the bare cases, the 2D (◇) and 3D (○) models give nearly identical results, suggesting that the turbulent fluctuations are less of an issue for radial inflow and that the 2D model can be used for reverse flow. The numerical results for h_{eff} for the bare surfaces are 23-24% higher than the experimental values at Re_P, although the

numerical and experimental results are in reasonable agreement for $Re > 10^5$. As observed for forward flow, the numerical predictions (--) are greater than the experimental values (□) for the effective HTC by 29% near Re_P. Understanding these discrepancies for both forward and reverse flow remains the subject of ongoing work.

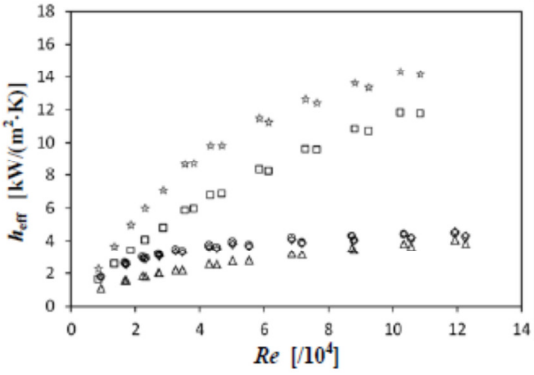

Fig. 7. Similar to Figure 6, but for reverse flow.

V. SUMMARY

As part of the ARIES study, an experimental and numerical investigation was carried out of a design that closely resembles previously studied finger-type divertors such as HEMJ and HEMP. Both forward flow, which involves a single jet impinging upon and cooling the underside of the pressure boundary, and reverse flow, where the coolant flows inwards along the cooled surface, were studied in otherwise identical test sections with and without a hexagonal array of cylindrical pin fins. In the numerical part of the study reported here, the predictions for effective heat transfer coefficient from simulations performed using a commercial CFD software package were compared with the experimental results reported in Ref. 9. For the test section without fins, the simulations give predictions for effective heat transfer coefficient (HTC) that are in reasonable agreement with the experimental values for both forward and reverse flow. The 3D numerical model gives better agreement with the experimental results for the forward flow cases.

For the test section with fins, the numerical studies give consistently higher HTCs than the experiments for both forward and reverse flow. We conjecture that these discrepancies are due to inconsistencies in the boundary conditions at the fin tips between the experiments and simulations, and possibly also due to a lack of mesh spatial resolution in the numerical models in the region between the fins as well as the well-known inability of the k-ε turbulence model to resolve the strongly anisotropic flows between the fins and near the impinging jet. Resolving these discrepancies is the focus of ongoing research.

Nevertheless, both the numerical simulations and experimental results show that the test section with fins has a significantly higher effective HTC than that without fins under otherwise identical conditions. The qualitative trends of how the effective HTC depends upon coolant mass flow rate, given here by the nondimensional Reynolds number, are also consistent between the simulations and the experiments.

ACKNOWLEDGMENTS

This work was performed as a part of the ARIES study. We thank the U.S. DOE Office of Fusion Energy Sciences for their support through contract number DE-FG02-01ER54656.

REFERENCES

1. L. CROSATTI, "Experimental and Numerical Investigation of the Thermal Performance of the Gas-Cooled Divertor Modules," *Ph.D. Thesis*, Georgia Institute of Technology (2008).
2. E. GAYTON, ET AL., "Experimental and Numerical Investigation of the Thermal Performance of the Gas-Cooled Divertor Plate Concept," *Fusion Sci. Technol.* **56**, 75 (2009).
3. M. HAGEMAN, "Experimental Studies of the Thermal Performance of Gas-Cooled Plate-Type Divertos," to appear in *Fusion Sci. Technol.* (2011).
4. E. DIEGELE, ET AL., "Modular He-Cooled Divertor for Power Plant Application," *Fusion Eng. Design* **66-68**, 383 (2003).
5. P. NORAJITRA, ET AL., "Development of a Helium-Cooled Divertor Concept: Design-Related Requirements on Materials and Fabrication Technology," *J. Nucl. Mater.*, **329-333**, 1594 (2004).
6. P. NORAJITRA, ET AL., "Status of He-Cooled Divertor Development for DEMO," *Fusion Eng. Design* **75-79**, 307 (2005).
7. V. WIDAK and P. NORAJITRA, "Optimization of He-Cooled Divertor Cooling Fingers using CAD-FEM Method," *Fusion Eng. Design* **84**, 1973 (2009).
8. B. MILLS, ET AL., "Experimental Investigation of Fin Enhancement for Gas-Cooled Divertor Concepts," submitted to *Fusion Sci. Technol.* (2010).
9. G. BISWAS *Turbulent Flows. Fundamentals, Experiments and Modeling* pp. 339-366, G. BISWAS, V. ESWARAN, Eds. CRC Press LLC, Boca Raton, Florida (2002).
10. T-H SHIH, ET AL., "A New k-ε Eddy Viscosity Model for High Reynolds Number Turbulent Flows," *Comput. Fluids*, **24**, 227 (1995).

REFERENCES

[1] R. Nave, "Nuclear Binding Energy," HyperPhysics, [Online]. Available: http://hyperphysics.phy-astr.gsu.edu/hbase/nucene/nucbin.html. [Accessed 10 January 2013].

[2] ITER Organization, "ITER - the way to new energy," 2011. [Online]. Available: http://www.iter.org. [Accessed 19 July 2011].

[3] T. Ihli, A. R. Raffray, S. I. Abdel-Khalik and S. Shin, "Design and performance study of the helium-cooled T-tube divertor concept," *Fusion Engineering and Design,* vol. 82, pp. 249-264, 2007.

[4] F. P. Incropera, D. P. Dewitt, T. L. Bergman and A. S. Lavine, Fundamentals of Heat and Mass Transfer, Hoboken: John Wiley & Sons, Inc., 2007.

[5] D.-Y. Lee and K. Vafai, "Comparative analysis of jet impingement and microchannel cooling for high heat flux applications," *International Journal of Heat and Mass Transfer,* vol. 42, no. 9, pp. 1555-1568, 1999.

[6] H. Martin, "Heat and Mass Transfer between Impinging Gas Jets and Solid Surfaces," *Advances in Heat Transfer,* vol. 13, pp. 1-60, 1977.

[7] C. Meola, "A New Correlation of Nusselt Number for Impinging Jets," *Heat Transfer Engineering,* vol. 30, no. 3, pp. 221-228, 2009.

[8] P. Norajitra, T. Chehtov, A. Gervash, R. Giniyatulin, T. Ihli, R. Kruessmann, V. Kuznetsov, A. Makhankov, I. Mazul, I. Ochinnikov, J. Weggen and B. Zeep, "Status of He-cooled Divertor Development (PPCS Subtask TW4-TRP-001-D2)," Forschungszentrum Karlsruhe in der Helmholtz-Gemeinschaft, Karlsruhe, 2005.

[9] J.-Y. San and M.-D. Lai, "Optimum Jet-to-Jet Spacing of Heat Transfer for Staggered Arrays of Impinging Air Jets," *International Journal of Heat and Mass Transfer,* vol. 44, pp. 3997-4007, 2001.

[10] C. Cornaro, A. S. Fleischer and R. J. Goldstein, "Flow visualization of a round jet impinging on cylindrical surfaces," *Experimental Thermal and Fluid Science,* vol. 20, no. 2, pp. 66-78, 1999.

[11] R. E. Chupp, H. E. Helms, P. W. McFadden and T. R. Brown, "Evaluation of Internal Heat-Transfer Coefficients for Impingement-Cooled Turbine Airfoils," *Jounral of*

Aircraft, vol. 6, no. 3, pp. 203-208, 1969.

[12] M. S. Tillack, A. R. Raffray, X. R. Wang, S. Malang, S. Abdel-Khalik, M. Yoda and D. Youchison, "Recent US Activities on Advanced He-cooled W-alloy Divertor Concepts for Fusion Power Plants," *Fusion Engineering and Design,* vol. 86, no. 1, pp. 71-98, 2011.

[13] K. Kleefeldt and S. Gordeev, "Performance Limits of a Helium-Cooled Divertor (Unconventional Design)," Forschungszentrum Karlsruhe in der Helmholtz-Gemeinschaft, Karlsruhe, 2000.

[14] T. Ihli, R. Kruessmann, I. Ovchinnikov, P. Norajitra, V. Kuznetsov and R. Giniyatulin, "An advanced He-cooled divertor concept: Design, cooling technology, and thermohydraulic analyses with CFD," *Fusion Engineering and Design,* Vols. 75-79, pp. 371-375, 2005.

[15] T. Ihli, "He-cooled Divertor Development in the EU: The Helium Jet cooled Divertor HEMJ," in *ARIES Meeting*, San Diego, CA, 2005.

[16] L. Crosatti, "Experimental and Numerical Investigation of the Thermal Performance of Gas-Cooled Divertor Modules," *Ph. D. Thesis, Georgia Institute of Technology,* 2008.

[17] J. B. Weathers, L. Crosatti, R. Kruessmann, D. L. Sadowski and S. I. Abdel-Khalik, "Development of modular helium-cooled divertor for DEMO based on the multi-jet impingement (HEMJ) concept: Experimental validation of thermal performance," *Fusion Engineering and Design,* vol. 83, pp. 1120-1125, 2008.

[18] J. B. Weathers, "Thermal Performance of Helium-Cooled Divertors for Magnetic Fusion Applications," *M. Sc. Thesis, Georgia Institute of Technology,* 2007.

[19] L. Crosatti, J. B. Weathers, D. L. Sadowski, S. I. Abdel-Khalik, M. Yoda, R. Kruessmann and P. Norajitra, "Experimental and Numerical Investigation of Prototypical Multi-Jet Impingement (HEMJ) Helium-cooled Divertor Modules," *Fusion Science and Technology,* vol. 56, pp. 70-74, 2009.

[20] T. Ihli, S. Hermsmeyer, C. Koehly and P. Norajitra, "Integration of an advanced He-cooled divertor in a DEMO-relevant tokamak geometry," *Fusion Engineering and Design,* vol. 81, pp. 121-126, 2006.

[21] R. Kruessmann, G. Messemer, K. Zinn, L. Crosatti, D. L. Sadowski and S. I. Abdel-Khalik, "Experimental and numerical investigation of a full-scale helium-cooled divertor finger mock-up," *Fusion Engineering and Design,* vol. 84, pp. 1119-1124, 2009.

[22] P. Norajitra, S. Antusch, R. Giniyatulin, V. Kuznetsov, I. Mazul, H.-J. Ritzhaupt-Kleissl and L. Spatafora, "Progress of He-cooled divertor development for DEMO," *Fusion Engineering and Design,* vol. 86, pp. 1656-1659, 2011.

[23] V. Widak and P. Norajitra, "Optimization of He-cooled divertor cooling fingers using a CAD-FEM method," *Fusion Engineering and Design,* vol. 84, pp. 1973-1978, 2009.

[24] E. Diegele, R. Kruessmann, S. Malang, P. Norajitra and G. Rizzi, "Modular He-cooled divertor for power plant application," *Fusion Engineering and Design,* Vols. 66-68, pp. 383-387, 2003.

[25] R. Kruessman, P. Norajitra, L. V. Boccaccini, T. Chehtov, R. Giniyatulin, S. Gordeev, T. Ihli, G. Janeschitz, A. O. Komarov, W. Krauss, V. Kuznetsov, R. Lindau, I. Ovchinnikov, V. Piotter, M. Rieth, R. Ruprecht, V. Slobodtchouk, V. A. Smirnov and R. Sunyk, "Conceptual Design of a He-cooled Divertor with Integrated Flow and Heat Transfer Promoters (PPCS Subtask TW3-TRP-001-D2)," Forschungszentrum Karlsruhe in der Helmholtz-Gemeinschaft, Karlsruhe, 2004.

[26] S. Hermsmeyer and S. Malang, "Gas-cooled high performance divertor for a power plant," *Fusion Engineering and Design,* Vols. 61-62, pp. 197-202, 2002.

[27] X. R. Wang, S. Malang, A. R. Raffray and the ARIES Team, "Design Optimization of the High Performance Helium-cooled Divertor Plate Concepot," *Fusion Science and Technology,* vol. 56, pp. 1023-1027, 2009.

[28] M. D. Hageman, "Experimental Investigation of the Thermal Performance of Gas-cooled Divertor Plate Concepts," *M. Sc. Thesis,* no. Georgia Institute of Technology, 2010.

[29] M. D. Hageman, D. L. Sadowski, M. Yoda and S. I. Abdel-Khalik, "Experimental Studies of the Thermal Performance of Gas-Cooled Plate-type Divertors," *Fusion Science and Technology,* vol. 60, pp. 228-232, 2011.

[30] E. F. Gayton, "Experimental and Numerical Investigation of the Thermal Performance of the Gas-cooled Divertor Plate Concept," *M. Sc. Thesis,* no. Georgia Institute of Technology, 2008.

[31] E. Gayton, L. Crosatti, D. L. Sadowski, S. I. Abdel-Khalik, M. Yoda and S. Malang, "Experimental and Numerical Investigation of the Thermal Performance of the Gas-cooled Divertor Plate Concept," *Fusion Science and Technology,* vol. 56, pp. 75-79, 2009.

[32] S. I. Abdel-Khalik, L. Crosatti, D. L. Sadowski, S. Shin, J. B. Weathers and M. Yoda, "Thermal-hydraulic Studies in Support of the ARIES-CS T-Tube Divertor Design,"

Fusion Science and Technology, vol. 54, pp. 864-877, 2008.

[33] L. Crosatti, D. L. Sadowski, S. I. Abdel-Khalik and M. Yoda, "Thermal Performance of a Prototypical Gas-cooled T-Tube Divertor Module with Single-sided Heating," *Fusion Science and Technology,* vol. 56, pp. 96-100, 2009.

[34] L. Crosatti, D. L. Sadowski, J. B. Weathers, S. I. Abdel-Khalik and M. Yoda, "Experimental and Numerical Investigation of the Thermal Performance of Gas-cooled T-Tube Divertor Modules," *Fusion Science and Technology,* vol. 52, pp. 531-538, 2007.

[35] T. Ihli and A. R. Raffray, "ARIES CS Report: Helium cooled divertor design study," UCSD-CER-06-04, San Diego, CA, 2005.

[36] A. R. Raffray, S. Malang and X. Wang, "Optimizing the Overall Configuration of a He-cooled W-alloy Divertor for a Power Plant," *Fusion Engineering and Design,* vol. 84, pp. 1553-1557, 2009.

[37] O. Reynolds, "On the Dynamical Theory of Incompressible Viscous Fluids and the Determination of the Criterion," *Philosophical Transactions of the Royal Society of London. A.,* vol. 186, pp. 123-164, 1895.

[38] J. O. Hinze, Turbulence, New York: McGraw-Hill Publishing Co., 1975.

[39] B. E. Launder and D. B. Spalding, Lectures in Mathematical Models of Turbulence, London, England: Academic Press, 1972.

[40] V. Yakhot and S. A. Orszag, "Renormalization Group Analysis of Turbulence I. Basic Theory," *Journal of Scientific Computing,* vol. 1, no. 1, pp. 1-51, 1986.

[41] T.-H. Shih, W. W. Liou, A. Shabbir, Z. Yang and J. Zhu, "A new k-epsilon eddy viscosity model for high Reynolds number turbulent flows," *Computers Fluids,* vol. 24, pp. 227-238, 1995.

[42] B. E. Launder and D. B. Spalding, "The Numerical Computation of Turbulent Flows," *Computer Methods in Applied Mechanics and Engineering,* vol. 3, pp. 269-289, 1974.

[43] S.-E. Kim and D. Choudhury, "A Near-Wall Treatment Using Wall Functions Sensitized to Pressure Gradient," in *ASME FED Vol. 217, Separated and Complex Flows*, ASME, 1995.

[44] H. C. Chen and V. C. Patel, "Near-Wall Turbulence Models for Complex Flow Including Separation," *AIAA Journal,* vol. 26, no. 6, pp. 641-648, 1988.

[45] M. Wolfshtein, "The Velocity and Temperature Distribution in One-Dimensional Flow with Turbulence Augmentation and Pressure Gradient," *International Journal of Heat and Mass Transfer,* vol. 12, pp. 301-318, 1969.

[46] T. Jongen, "Simulation and Modeling of Turbulent Incompressible Flows," in *PhD Thesis*, EPF Lausanne, Lausanne, Switzerland, 1998.

[47] B. A. Kader, "Temperature and Concentration Profiles in Fully Turbulent Boundary Layers," *International Journal of Heat and Mass Transfer,* vol. 24, no. 9, pp. 1541-1544, 1981.

[48] F. M. White and G. H. Christoph, "A Simple New Analysis of Compressible Turbulent Two-dimensional Skin Friction under Arbitrary Conditions," University of Rhode Island, 1971.

[49] P. G. Huang, P. Bradshaw and T. J. Coakley, "Skin Friction and Velocity Profile Family for Compressible Turbulent Boundary Layers," *AIAA Journal,* vol. 31, no. 9, pp. 1600-1604, 1993.

[50] P. R. Spalart and S. R. Allmaras, "A One-Equation Turbulence Model for Aerodynamic Flows," in *AIAA-92-0439*, Reno, NV, 1992.

[51] K. Abe, T. Kondoh and Y. Nagano, "A new turbulence model for predicting fluid flow and heat transfer in separating and reattaching flows-I. Flow field calculations," *International Journal of Heat and Mass Transfer,* vol. 37, no. 1, pp. 139-151, 1994.

[52] K. Abe, T. Kondoh and Y. Nagano, "A new turbulence model for predicting fluid flow and heat transfer in separating and reattaching flows-II. Thermal field calculations," *International Journal of Heat and Mass Transfer,* vol. 38, no. 8, pp. 1467-1481, 1995.

[53] O. Redlich and J. N. S. Kwong, "On the Thermodynamics of Solutions. An Equation of State. Fugacities of Gaseous Solutions.," *Chemical Reviews,* vol. 44, no. 1, p. 233, 1949.

[54] T. J. Barth and D. Jespersen, "The design and application of upwind schemes on unstructured meshes," in *Technical Report AIAA-89-0366*, AIAA 27th Aerospace Sciences Meeting, Reno, Nevada, 1989.

[55] S. V. Pantankar, Numerical Heat Transfer and Fluid Flow, Washington, DC: Hemisphere, 1980.

[56] J. P. Vandoormaal and G. D. Raithby, "Enhancements of the SIMPLE Method for Predicting Incompressible Fluid Flows," *Numerical Heat Transfer,* vol. 7, pp. 147-

163, 1984.

[57] J. R. Turner and T. R. Yoos, "Pressure Loss Calculation Procedures for High Speed Gas Flow in Ducts," Dynatech Corporation, Cambridge, MA, 1961.

[58] ANSYS FLUENT 14.0.

[59] J. Dacles-Mariani, G. G. Zilliac, J. S. Chow and P. Bradshaw, "Numerical/Experimental Study of a Wingtip Vortex in the Near Field," *AIAA Journal,* vol. 33, no. 9, pp. 1561-1568, 1995.

[60] W. C. Reynolds, "Fundamentals of turbulence for modeling and simulation," *Lecture Notes for Von Karman Institute Agard Report No. 755,* 1987.

[61] S. J. Kline and F. A. McClintock, "Describing the uncertainties in single sample experiments," *Mechanical Engineering,* pp. 3-8, 1953.

[62] J. P. Holman, Experimental Methods for Engineers, Boston: McGraw-Hill, 2001.

[63] M. Roedig, W. Kuehnlein, J. Linke, D. Pitzer, M. Merola, E. Rigal, B. Schedler and E. Visca, "Post irradiation testing of samples from the irradiation experiments PARIDE 3 and PARIDE 4," *Journal of Nuclear Materials,* Vols. 329-333, pp. 766-770, 2004.

[64] National Institute of Standards and Technology, "Thermophysical Properties of Fluid Systems," 2011. [Online]. Available: http://webbook.nist.gov/chemistry/fluid/. [Accessed 23 August 2012].

VITA

Jordan D. Rader was born in Tuscaloosa, AL in 1986 to David and Janet Rader. He graduated Salutatorian from Union High School in Tulsa, OK in 2004 and received his Bachelor of Science degree with Highest Honor in Nuclear & Radiological Engineering in 2008 and his Master of Science degree in Nuclear Engineering in 2009, both from the Georgia Institute of Technology. His M.S. research focused on accident analysis in a pressurized water nuclear fission reactor.

In his spare time, he enjoys all kinds of sports and outdoor activities. He currently lives in Marietta, GA with his wife, Emily.

This thesis was typed by Jordan D. Rader